ISSN 0915-6348

NATIONAL INSTITUTE FOR FUSION SCIENCE

Physics and Applications of Extreme Energy-Density State

Nov. 25-26, 1999
NIFS

(Eds.) K. Yatsui and W. Jiang

(Received - Feb. 28, 2000)

NIFS-PROC-45 Mar. 2000

RESEARCH REPORT
NIFS-PROC Series

NAGOYA, JAPAN

Physics and Applications of Extreme Energy-Density State

Edited by K. Yatsui and W. Jiang

November 25-26, 1999
National Institute for Fusion Science
Toki, Japan

Abstract

This is the proceedings of "Symposium on Physics and Applications of Extreme Energy-Density State" held at National Institute for Fusion Science. Recent experimental and theoretical research results on high-power particle beams, z-pinches, pulsed-power technologies, and industrial applications are presented.

Keywords: high energy-density state, pulsed particle beam, pulsed power, z-pinch, pulsed laser, pulsed x-ray, high power microwave

PREFACE

This publication contains 30 papers presented at "Symposium on Physics and Applications of Extreme Energy-Density State" held at National Institute for Fusion Science (NIFS) on November 25-26, 1999. This symposium was supported by a collaborative research program of the NIFS and was attended by 53 researchers from more than 20 research groups all over Japan.

The main topics of the symposium are high-power particle beams, z-pinches, pulsed power technologies, and industrial applications. Recent research progresses on these topics were reported and discussed on the symposium.

The editors would like to thank all the authors of the papers, all attendees of the symposium, and the NIFS for their support on the symposium and the proceedings.

Kiyoshi Yatsui
Weihua Jiang
Nagaoka University of Technology

Contents

List of Attendees

H. Akamatsu	Himeji Institute of Technology
H. Akiyama	Kumamoto University
N. Akiyama	Nihon University
R. Ando	Kanazawa University
E. Baronova	Kurchatov Institute
Y. Doi	Toyama University
S. Furuya	Nagaoka University of Technology
N. Harada	Nagaoka University of Technology
D. Hasegawa	Kanazawa University
Y. Hashimoto	Kobe City College of Technology
M. Hirai	Nagaoka University of Technology
S. Hirata	Toyama University
K. Horioka	Tokyo Institute of Technology
K. Ikuta	Nagaoka University of Technology
G. Imada	Nagaoka University of Technology
K. Imasaka	Kyushu University
H. Ishihawa	Tokyo Institute of Technology
S. Ishii	Tokyo Institute of Technology
W. Jiang	Nagaoka University of Technology
K. Kamada	Kanazawa University
S. Katsuki	Kumamoto University
Y. Kawasaki	Tokyo Institute of Technology
S. Kawata	Utsunomiya University
T. Kikuchi	Nagaoka University of Technology
Y. Kinemuchi	Nagaoka University of Technology
R. Kodera	Osaka City University
H. Maeda	Gunma University
Y. Maetsubo	Toyama University
H. Maruyama	Gunma University
K. Masugata	Toyama University
H. Matsuzawa	Yamanashi University
T. Miyamoto	Nihon University

A. Muravich	Nihon University
K. Murayama	Yatsushiro National College of Technology
Y. Nakagawa	Osaka City University
T. Namihira	Kumamoto University
H. Nozawa	Tokyo Institute of Technology
Y. Ono	Gunma University
M. Onoi	Himeji Institute of Technology
M. Sato	Gunma University
N. Shimomura	The University of Tokushima
M. Shiotani	Toyama University
T. Suzuki	Nagaoka University of Technology
T. Takaki	Iwate University
K. Takao	Toyama University
K. Takasugi	Nihon University
T. Tazima	National Institute for Fusion Science
Y. Teramoto	Kumamoto University
V. Vikhrev	Kurchatov Institute
K. Yatsui	Nagaoka University of Technology
M. Yatsuzuka	Himeji Institute of Technology
T. Yamamoto	Fukushima National College of Technology
T. Yanagidaira	Gunma University
T. Yoshida	Nihon University

INITIAL BEHAVIOR OF GAS-PUFF Z-PINCH PLASMA PRODUCED BY IPP GENERATOR AND ITS CHARACTERISTICS

K. Imasaka, T. Masaki, K. Kawazoe, J. Suehiro and M. Hara

Department of Electrical and Electronic Systems Engineering, ISEE, Kyushu University,
6-10-1, Hakozaki, Higashi-ku, Fukuoka, 812-8581, Japan

ABSTRACT

It is necessary to supply fast-high current to the gas-puff z-pinch plasma in order to produce the stable pinched plasma. In this study, fast-high current generated by an inductive pulsed power generator which has 400ns rising time and 60kA peak value of a current is supplied to the gas-puff z-pinch plasma. Behavior of the pinching process of the plasma during initial phase of the discharge is observed by framing photography. The photograph shows Zipper effect and cathode spot generation on the cathode surface during initial phase of the pinching process. The result also reveals that cathode spot influences the pinching process and hot spots formation.

1. Introduction

Gas-puff z-pinch has a compact configuration and easily produces high energy density plasmas, which emits soft x-rays. Soft x-rays have a longer wavelength than hard x-rays and are comparatively safe to handle. Recently, soft x-rays have drawn attention in diverse area including x-ray lithography semiconductor processing, microscopy and so on [1-3]. A gas-puff z-pinch device utilizing a plasma compression phenomenon emits relatively high-intensity soft x-rays with a compact design and is seen as a promising new source of soft x-ray radiation [1-3]. In applications of gas-puff z-pinch plasma as a soft x-ray source, control over not only the output of soft x-ray radiation but also the spatial stability of hot spots is critical in improving soft x-ray directivity. For this purpose, fast-high current must be supplied to the z-pinch plasma as quickly as possible during the several microsecond pinch phenomenon before MHD instabilities appear [4,5]. Conventional gas-puff z-pinch has used fast bank (FB) system operated by capacitor discharge, but the slow rise of the delivered current makes it difficult to generate pinched plasma efficiently and to reduce instabilities. The inductive energy storage pulsed power (IPP) system which stores the primary energy from a capacitor in an inductor and supply fast-high current to the z-pinch plasma by using an opening switch. Previous results of the pinching behavior during maximum compression of the z-pinch plasma using IPP system show that more uniform plasma column and stabilization of spatial distributions of hot spots are obtained in comparison with FB system [6]. Gap length dependece of the pinching plasma behavior has been also studied [7]. Pinch time,

which is the time from discharge onset to emission of soft x-ray from the pinched plasma, is shorter than that of FB system. These results are advantage of the fast-high current supplied from IPP generator. However, pinch time has dispersion under the same experimental conditions.

The object of the present research is to investigate pinching phenomenon during initial phase of the discharge and discuss a cause of dispersion of pinching time. Behavior of the pinching process is observed by using an image-converter camera.

2. Experimental setup and method

Experimental setup is same as shown in Ref.[6], [7]. Argon gas is filled into a gas-puff valve plenum at 0.1MPa and is puffed through a gas-puff nozzle between electrodes. The nozzle is tilted inwardly. The external and internal diameters of the nozzle exit are 8mm and 4mm, respectively. Cathode is a conical-shaped rod, which has 4mm in diameter at the tip.

Rogowsky coils are used to measure generator and z-pinch currents. Current flowing through a coil to drive a fast solenoid valve is measured by a B-dot probe. A PIN-photo diode (Hamamatsu photonics co., S1722 Japan) with an aluminum foil filter of 18μm thickness is used for soft x-ray detection. Behavior of the z-pinch plasmas during compression is observed by framing photographs using a high-speed image converter camera (Hadland Inc., IMACON468 England). The camera is expressed by an abbreviation of ICC in this paper. 7 frames are captured during a single shot discharge. Exposure and inter-frame time of each frame are individually changeable. In order to know a time sequence of the exposure, shutter pulse signals from the ICC are displayed on an oscilloscope together with current waveforms and soft x-ray signals.

Delay time, which is a timing between the gas injection and generator current onset, is defined as the time elapsed from the rise of current flowing through the coil used for fast solenoid valve operation until the rise of generator current.

In the present research, experiments are performed under the condition that the delay rime and the gap length between z-pinch electrodes are 1.20ms and 10mm, respectively. The charging voltage of capacitor is set to 25 kV in FB system and 28 kV in IPP system so that one can obtain an identical peak value of the z-pinch current with different rising rates in both systems.

3. Experimental results

3.1 Behavior of the gas-puff z-pinch plasma

Fig.1 (a) shows the time sequence of the observation by framing photography that is monitored as the shutter pulses of ICC. I_g and $I_{L\text{-}IPP}$ are generator and z-pinch current waveforms respectively. Horizontal axis is the time from beginning of I_g onset. ICC captures 7 flames in a shot and therefore behavior of the z-pinch plasma during initial phase of the discharge (2.25-2.90μs) is observed divided into three parts of [I], [II] and [III] as shown in Fig. 1. Exposure and inter-frame time of the each frame in [I], [II] and [III] are 10ns and 20ns, respectively. Several

voltage shots are discharged in [I], [II] and [III]. Reproducibility of current waveforms and framing photographs is confirmed in these voltage shots by the previous experiments. **Fig. 1(b)** shows the framing photographs. [I], [II], [III] and the times indicated in the figure agree with those in Fig. 1 (a). Emission of light from the discharge of Ar is observed at $I_{L\text{-}IPP}$ onset and cathode spot is generated at the cathode surface (2.30μs). The plasma sheath is expanded in the radial direction between electrodes and the cylindrical plasma is also formed in the expanded plasma sheath. The expanded plasma sheath is compressed by Lorentz force inwardly near the nozzle exit when IL-IPP increases at 2.39μs. The compression of the plasma sheath progresses toward the cathode surface gradually together with the increase of $I_{L\text{-}IPP}$. The behavior is called Zipper effect. Plasma diameter near the nozzle exit at 2.62μs in [III] is about 4mm that is the half of the initial diameter. After that, the plasma sheath is drastically compressed and the diameter of the plasma becomes tenth of the initial diameter at 2.73μs. Fast-high current $I_{L\text{-}IPP}$ is completely transferred from the IPP generator to the z-pinch plasma at this time. However, the pinched plasma column is produced only half size of the gap length. The uniform pinched plasma is produced between electrodes at 2.79μs by Zipper effect. Plasma diameter that is measured at the nozzle exit by using Fig.1(b) and $I_{L\text{-}IPP}$ are shown in **Fig. 2**. These are compared with the results in case of FB system. It is found that the plasma diameter in case of IPP system is compressed much faster than FB system because the rising rate of $I_{L\text{-}IPP}$ is much higher than that of FB system.

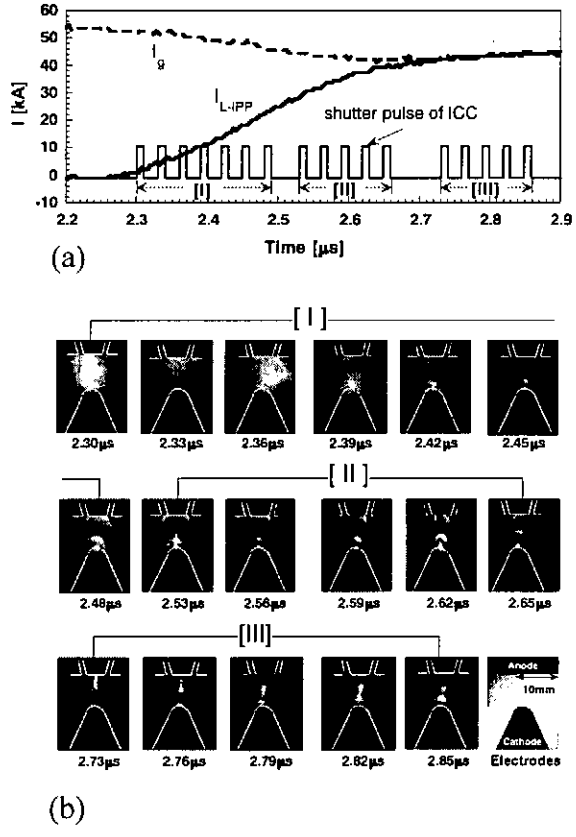

Fig. 1. Behavior of the gas-puff z-pinch plasma during initial phase of the discharge in IPP system. (a) : Time sequence of the observation that is monitored as the shutter pulse of ICC and currents waveforms. (b) : Framing photographs captured by ICC.

By the way, cathode spot generated on the cathode surface moves toward the anode side

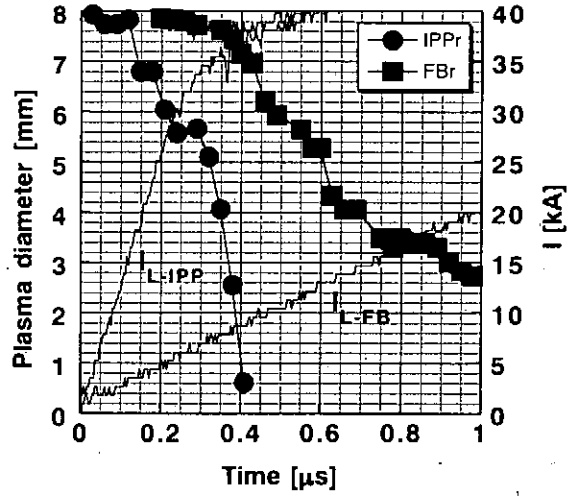

Fig. 2. Plasma diameter and z-pinch current waveforms in IPP and FB systems.

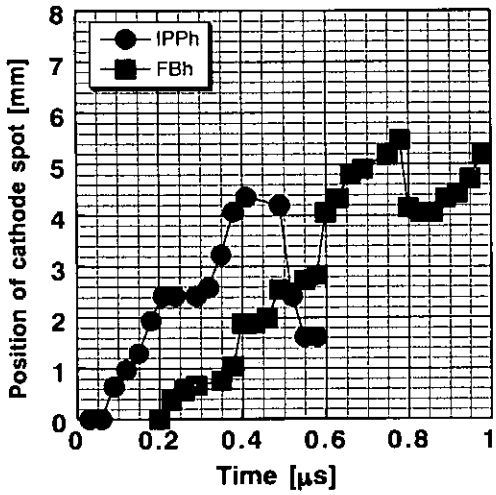

Fig. 3. Behavior of cathode spot in IPP and FB systems.

when time passes as shown in Fig. 1(a) and this behavior will affect the pinching phenomenon. **Fig. 3** shows the position of cathode spots from the cathode surface along the z-axis between electrodes in case of both systems. Cathode spot rises until 0.4μs and the maximum height from the cathode surface is 4.5mm in case of IPP system. Then, the cathode spot falls down. Rising of the cathode spots is due to the electric force. In Fig. 3, the time of 0.4μs agrees with the time of 2.73μs in Fig. 1(b). Since the strong compression of the plasma sheath progresses from the center of the gap toward the cathode surface after 2.73μs as shown in Fig. 1(b), the cathode spot can not rise further and then fall down. Behavior of cathode spot in case of FB system also has a same tendency as IPP system.

3. 2 Relationship between number of soft x-ray pulses and behavior of the pinching plasma.

Characteristics of the z-pinch such as soft x-ray output, pinch time and number of soft x-ray pulses have dispersion under the same experimental conditions. In this subsection, we describe some results obtained under the condition that delay time is 1.20ms and gap length is 10mm with respect to number of soft x-ray pulses and the dispersion of pinch time. Pinch time, t_p is defined as the time between z-pinch current onset and detection of soft x-ray emitted from the pinched plasma with PIN-photodiode. This definition of t_p is shown in **Fig. 4**. The incidence of soft x-ray pulses detected in 100 voltage shots is shown in **Fig. 5**. It is found that soft x-ray pulses are 1 to 5 in number and the incidence of more than 2 pulses is higher rather than single pulse. Especially, the incidence of 2 pulses is highest and the incidence of more than 3 pulses decreases. In this experiment, the incidence of the multiple pulses is about 80%. **Fig. 6** shows

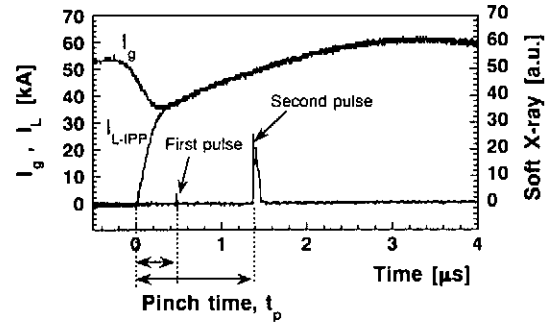

Fig. 4. Definition of pinch time.

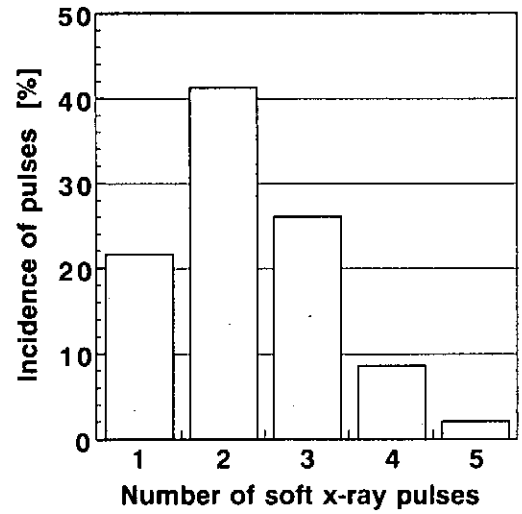

Fig. 5. Incidence of soft x-ray pulses in IPP system.

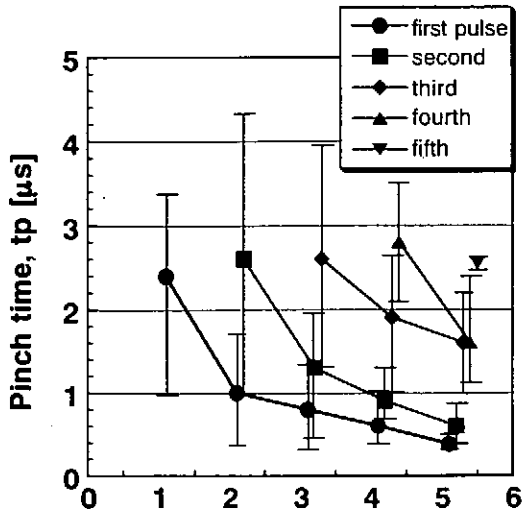

Fig. 6. Relationship between pinch time and number of soft x-ray pulses.

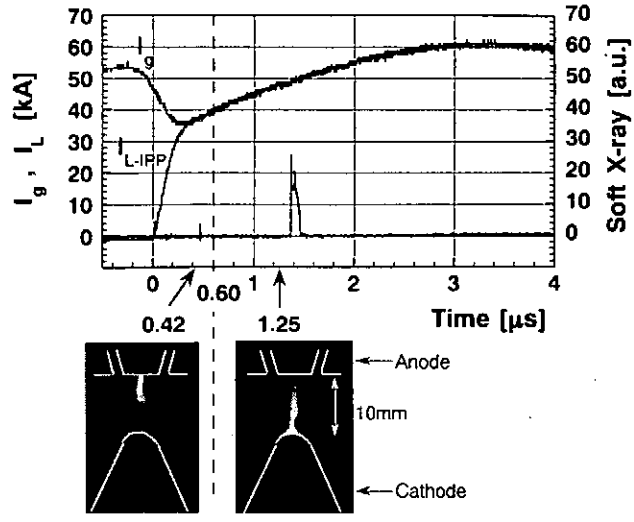

Fig. 7. Framing photographs of the pinched plasma when soft x-rays are emitted

the dependence of t_p on number of soft x-ray pulses. Although t_p has some dispersion in same number of the pulses, the dispersion decreases when number of the pulses is increases. When multiple pulses such as 2 to 5 are observed, a pulse detected at shorter time in those pulses has smaller scatter in comparison with the other pulses that have longer t_p.

4. Discussion

It is said that the pinch time depends on the z-pinch current and the shape of the pinched plasma column under the fixed experimental condition as for delay time, gap length and pressure of the injected gas and so on. Therefore, we discuss the incidence of the pulses and pinch time by using the z-pinch current and behavior of the pinching plasma in case of IPP system.

Soft x-ray and currents waveforms are shown in **Fig. 7**. Framing photographs of the z-pinch plasma at 0.42 and 1.25μs after $I_{L\text{-}IPP}$ onset is also shown in the figure. Exposure time of the photographs is 10ns. During 0.40μs from $I_{L\text{-}IPP}$ onset, the plasma sheath is compressed by Zipper effect from the anode side and the compression progresses toward the cathode side as shown in Fig. 1. At 0.42μs as shown in Fig. 7, the pinched plasma column is produced between the anode and the center of the electrodes by Zipper effect and the rising of the cathode spot. Just after that, first soft x-ray pulse that has small output is detected. It is thought that the soft x-ray pulse at 0.45μs is emitted from the pinched plasma column. The compression of the plasma sheath is immediately progresses between the center of the electrodes and the cathode surface after 0.6μs, and then the entire plasma column on which a hot spot is produced by sausage instability is generated finally at 1.25μs. It is thought that second soft x-ray pulse at 1.40μs is emitted from the hot spot. If you consider that the size of the pinched plasma column at around 0.42μs is the same as that in soft x-ray emission and first soft x-ray pulse is detected before

0.6μs, the current value and pinched plasma size after 0.6μs satisfy the condition to emit soft x-ray. This result indicates that soft x-ray can be emitted any time after 0.6μs until 4.0μs when the z-pinch current reaches peak value and therefore there is the scatter of t_p as shown in Fig. 6. From $I_{L\text{-}IPP}$ waveform, it is expected that MHD instability is easy to occur because the rising rate of $I_{L\text{-}IPP}$ after 0.4μs becomes very low. As a result, several hot spots are produced on the pinched plasma column and multiple soft x-ray pulses are detected.

5. Conclusion

Behavior of the compressing gas-puff z-pinch plasma produced by the inductive pulsed power generator is observed by using ICC during initial phase of the z-pinch current rising. It is revealed that Zipper effect compress the plasma sheath and behavior of cathode spot affect the pinch phenomenon. The incidence of the soft x-ray pulses and pinch time depend on the z-pinch current value, rising rate of the current and the shape of the pinched plasma. Emission of multiple soft x-ray pulses and the dispersion of pinch time result from the low rising rate of the z-pinch current in IPP system after transmission of the generator current to the z-pinch plasma.

References

[1] J. Bailey, Y. Ettinger, A. Fisher, and R. Feder : "Evaluation of the gas puff z pinch as an x-ray lithograhy and microscopy source", Appl. Phys. Lett., Vol. 40, No. 1, 1982, pp. 33-35.

[2] J. Davis, R. Clark, J. P. Apruzese, and P. C. Kepple : "A z-pinch neonlike x-ray laser", IEEE Trans. on Plasma Sci., Vol. 16, No. 5, 1988, pp. 482-490.

[3] I. N. Weingerg and A. Fisher : "Elemental imaging of biological speciments using a z pinch", Appl. Phys. Lett., Vol. 47, No. 10, 1985, pp. 1116-1118.

[4] D. L. Book, E. Ott, and M. Lampe : "Nonlinear evolution of the sausage instability", Phys. Fluids., Vol. 19, No. 12, 1976, pp. 1982-1986.

[5] W. W. Hsing and J. L. Porter : "Measurements of axial nonuniformities in gas-puff implosions", Appl. Phs. Lett., Vol. 50, No. 22, 1572-1574, pp. 1572.

[6] K. Imasaka, S. Hara, K. Kawauchi, J. Suehiro, and M. Hara : "Soft x-ray emission from the gas-puff z-pinch plasma produced by an inductive pulsed power generator", Proc. of 11th Pulsed Power Conf., Vol. 1, 1997, pp. 845-848.

[7] K. Kawazoe, T. Masaki, K.Imasaka, J. Suehiro and M. Hara : "Gap length dependence of soft x-ray emission from gas-puff z-pinch plasma produced by inductive pulsed power generator", Proc. of 1998 K-J Joint Sympo. on ED and HVE, 1998, 175-178.

ELECTROSTATIC POWDER INJECTION SYSTEM FOR Z-PINCH PLASMAS

H. Ishihara, Y. Kawasaki, H. Nozawa, J. Kuroda, S. Ibuka, Y. S. Liu, K. Yasuoka and S. Ishii

Department of Electrical and Electronic Engineering
Tokyo Institute of Technology
2-12-1 O-okayama, Meguro-ku, Tokyo 152-8552, Japan

ABSTRACT

Electrostatic powder injection system for the proposed new scheme of Z-pinch, powder Z-pinch, is discussed. Characteristic of the prototype powder injection system with a pair of parallel-plate electrodes was improved by introducing a focusing electrode. The focusing electrode enabled to focus powder flow and increase injected total powder mass. In this study, we examined issues of the electrostatic control of powder injection system for the Z-pinch, namely, the powder shape and driving pulsed voltage waveform. The efficient pre-ionization system for stable powder Z-pinch is to avoid off-axis discharges is briefly discussed.

I. Introduction

Z-pinch can easily create high energy density and high temperature plasmas, and it has many applications such as soft X-ray sources and nuclear fusion[1]. Z-pinch can be produced in various ways. The typical examples are a gas-puff Z-pinch and a wire array Z-pinch. The advantage of the gas-puff Z-pinch is that dense plasmas can be created in a reproducible manner at a high repetition rate. Since puffing material must be gaseous state, solid materials are not applicable to the gas-puff Z-pinch. The wire array Z-pinch can also generate high-density plasma from solid matter. However, it is difficult to set the wires in the proper position between the main electrodes. We have proposed a new scheme of Z-pinch by solid powder injection that has both advantages of high repetition rate operation and having a high initial mass density. The principle of this scheme is that dense plasmas are created from powder accelerated and injected between the Z-pinch electrodes. When a high current pulse is applied to the Z-pinch electrodes, the powder is evaporated and ionized. High repetition rate operation is possible in the powder Z-pinch. Since almost every material becomes powder, emission spectra in the soft X-ray region from the powder Z-pinch are expected to have extremely wider range than those from gaseous plasmas.

Control of the powder number density for the Z-pinch has been established by using an electrostatic control method. This method is useful for applied electrostatics in handling powder and or small particles, and has the advantage of easiness, compactness, good reproducibility, and to be operated in vacuum. In the previous paper, results of the particle trajectories in high electric field obtained by numerical analysis have shown that the additional electrode enhances focusing effect in parallel-plate electrodes powder injection system[2]. Moreover, it is possible to obtain desired particle trajectories for the Z-pinch, when the electric field distribution between the acceleration electrodes is carefully designed.

The paper is organized as follows. In section III, we examined issues of the electrostatic control of powder injection for the Z-pinch: the powder shape and driving pulsed voltage waveform. The efficient pre-ionization system for stable powder Z-pinch is to avoid off-axis

discharges is briefly given in section IV.

II. Experimental Setup

(1) Powder Injection System

Spatial and temporal control of powder injection is required for the powder Z-pinch plasmas. The powder must be injected in a pulsed mode as synchronizing with Z-pinch discharge. In addition, it is desirable that the powder injection system is small-sized and driven by a simple electrical circuit. The prototype powder injection system was designed to have parallel-plate electrodes with a focusing electrode in order to examine controllability of the powder number density. Fig.1 shows a schematic diagram of the powder injection system of pulsed parallel-plate electrodes with a focusing electrode, which are the circular shaped aluminium plates with a diameter of 90mm. A polyacetal cylinder with 5mm in height and the inner diameter of 20mm was used for an insulating spacer for the electrodes. The upper electrode and focusing one have a hole with the diameter of 2mm and 6mm, respectively. The powder used in this study consisted of the fine copper particles with the diameter of 75 and 150μm.

When the pulsed voltage of 8kV (HV1) and 6kV (HV2) are applied to lower and focusing electrodes, respectively, the powder (d=150μm) detaches from the lower electrode by Coulomb force F_e, which is greater than the gravitational force F_g ($F_e > F_g$). F_e force drives the powder toward the upper electrode[3]. The pulsed voltages were generated by a relay switching circuit composed of a high voltage power supply (Matsusada Precision, HB-25P) and a high voltage relay switch (Kilovac, K81A-2PM). The pulse width was set voluntarily by using the function generator (Iwatsu Electric, FG-350). The injection experiments were conducted in the air.

The powder number density was obtained by measuring light attenuation of a He-Ne laser beam (λ=632.8nm) passing through the injected powder flow region as shown as Fig.1[4]. The laser beam position was at 3mm apart from the upper electrode surface. When we measure the transmitted light intensity I_2 and I_1 through the region with and without powder, these intensities obey the Bouguer (Lambert-Beer) law,

$$I_2 = I_1 \exp\left(-nzA_pQ_{ext}\right)$$

Where n, A_p, z and Q_{ext} are the powder number density, projected area of a particle ($A_p = \pi d^2/4$, d: particle diameter), beam path length in the powder, and the extinction coefficient, respectively. From the Mie theory we assumed Q_{ext}=2 for particles with the diameter of 75-150μm larger than the wavelength of the laser light of λ=632.8nm.

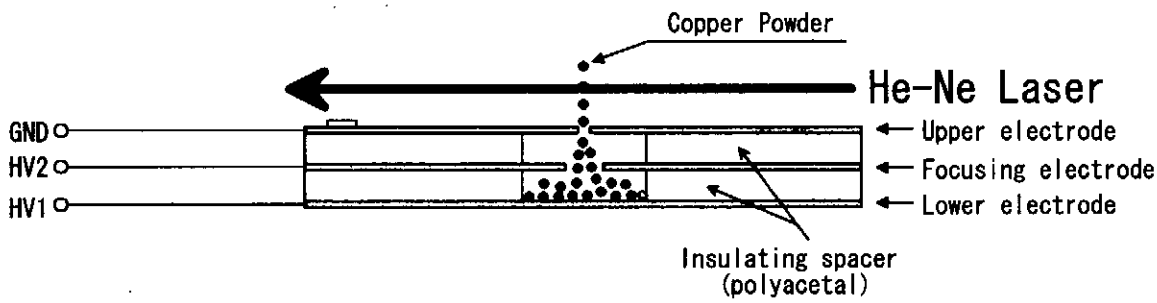

Fig.1: Experimental setup for the pulsed parallel-plate electrodes with a focusing electrode powder injection system. The He-Ne laser beam is from right to left. The upper electrode and focusing one have a hole with the diameter of 2mm and 6mm, respectively.

(2) Pre-ionization system

Since the injected powder particles are located separately, it is hard for powder to develop discharge between the electrodes. The situation is quite different from that of solid fibers. The discharge with powder is unstable like vacuum spark discharges of which characteristics are influenced by electrode surface condition and slight distortion of the electric field. It is difficult to generate the powder plasma with reproducibility because the electrode is wasted hard and may be destroyed by local arc currents. To obtain stable and uniform high current pulse discharges, the pre-ionization system was employed to supply sufficient amount initial electrons between the electrodes. Therefore a third electrode for pre-ionization near the anode was employed as shown in Fig.2. When a high voltage pulse is applied to the main electrode, a surface discharge is generated between the third electrode and anode, to provide initial electrons between the main electrodes. Furthermore, this pre-ionization restricts discharge region and enables to generate stable plasma from injected. The framing photographs of the plasma injection for pre-ionization were taken by an image converter camera (Hadland Photonics, Imacon 468).

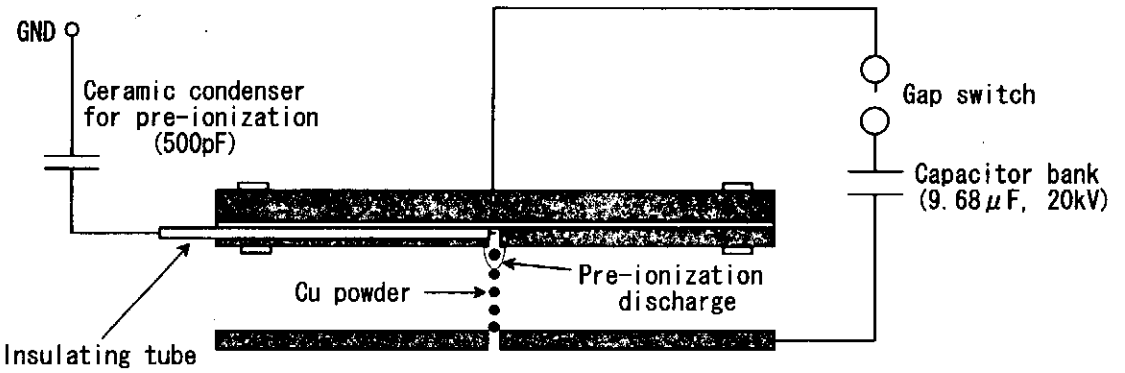

Fig.2: Schematic cross sectional view of the pre-ionization triggered anode. The anode has a hole with the diameter of 2mm for the pre-ionization.

III. Results and Discussion

III-I. Powder Injection System

(a) Dependence of the powder shape

Fig.3 shows the photograph of the dendritic Cu powder flow near the injection hole illuminated by a He-Ne laser beam. Thanks to the focusing electrode diverging powder flow was focused. However, the injected powder mass did not increase as comparing with case of no focusing electrode. Such the dendritic powder contains particles with various sizes and shapes, reproducibility of the discharges was not good. Fig.4 shows the microscope photograph of the dendritic powder taken by a digital microscope (Keyence VH-7000). There exist particles with the diameter less than 150μm even in the dendritic powder of the class 100 meshes. It is difficult to get particles with the similar diameter in dendritic powder.

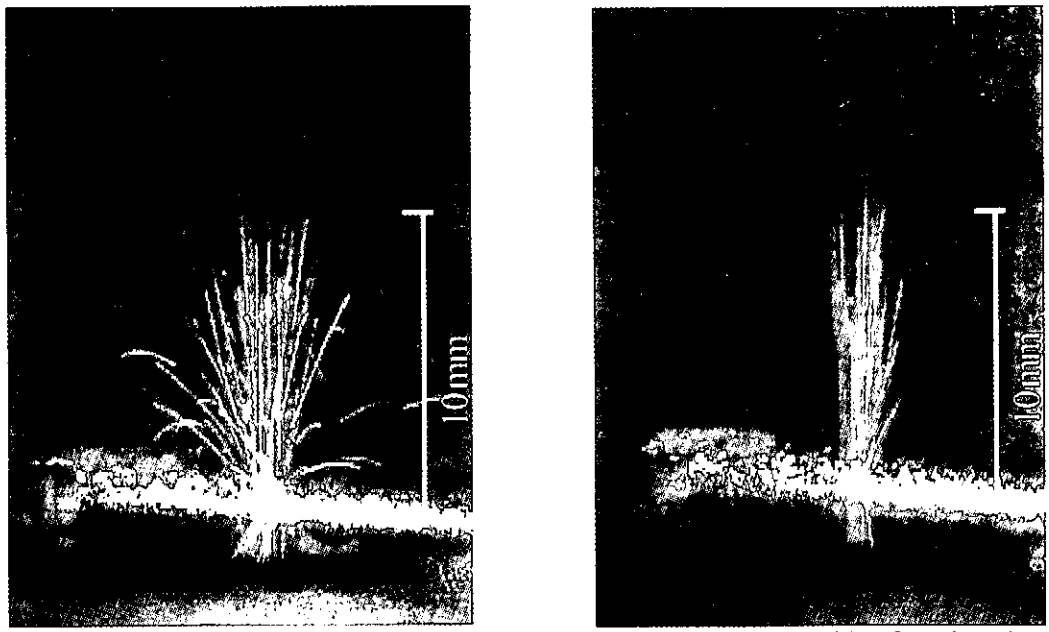

(a) Parallel-plate electrodes (b) Parallel-plate electrodes with a focusing electrode

Fig.3: Photograph of the dendritic Cu powder (d=150μm, -100mesh) flow near the injection hole illuminated by a He-Ne laser beam. The pulsed voltage of 8kV (HV1) and 6kV (HV2) were applied to lower and focusing electrodes, respectively.

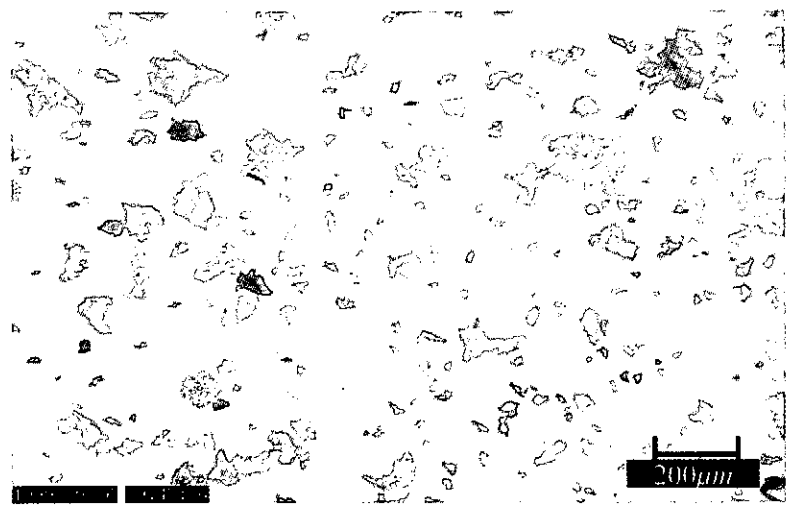

Fig.4: Microscope photograph of the dendritic Cu powder (d=150μm, 100mesh). There exist particles with the diameter less than 150μm even in the dendritic powder of the class 100 meshes.

We then employed the spherical powder shown in Fig.5 in place of the dendritic powder. Injected powder flow patterns with and without focusing electrodes are shown in Fig.6. The powder flow expanded in the case of no focusing electrode as shown in Fig.6 (a) and the injected powder mass was smaller. The focusing electrode enabled to focus the powder flow and enhanced the injected powder mass. Since the shape and diameter of particles in the spherical powder are almost similar, generalization of the experimental data is possible.

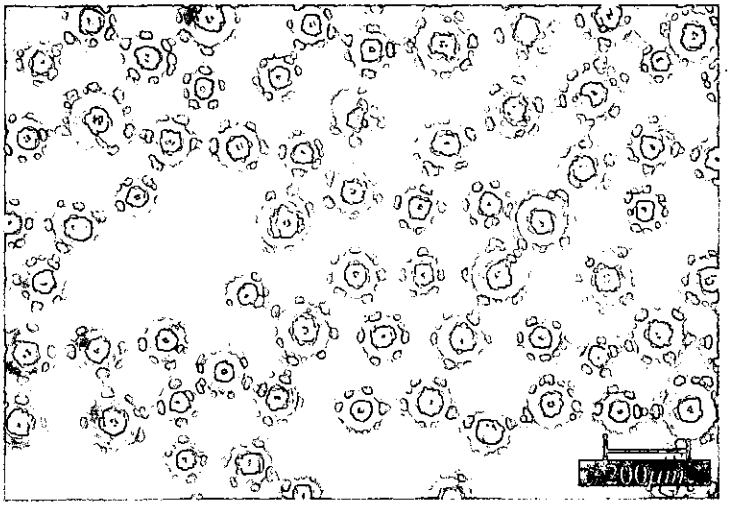

Fig.5: Microscope photograph of the spherical Cu powder (d=150μm).
The shape and diameter of particles in the spherical powder are almost similar.

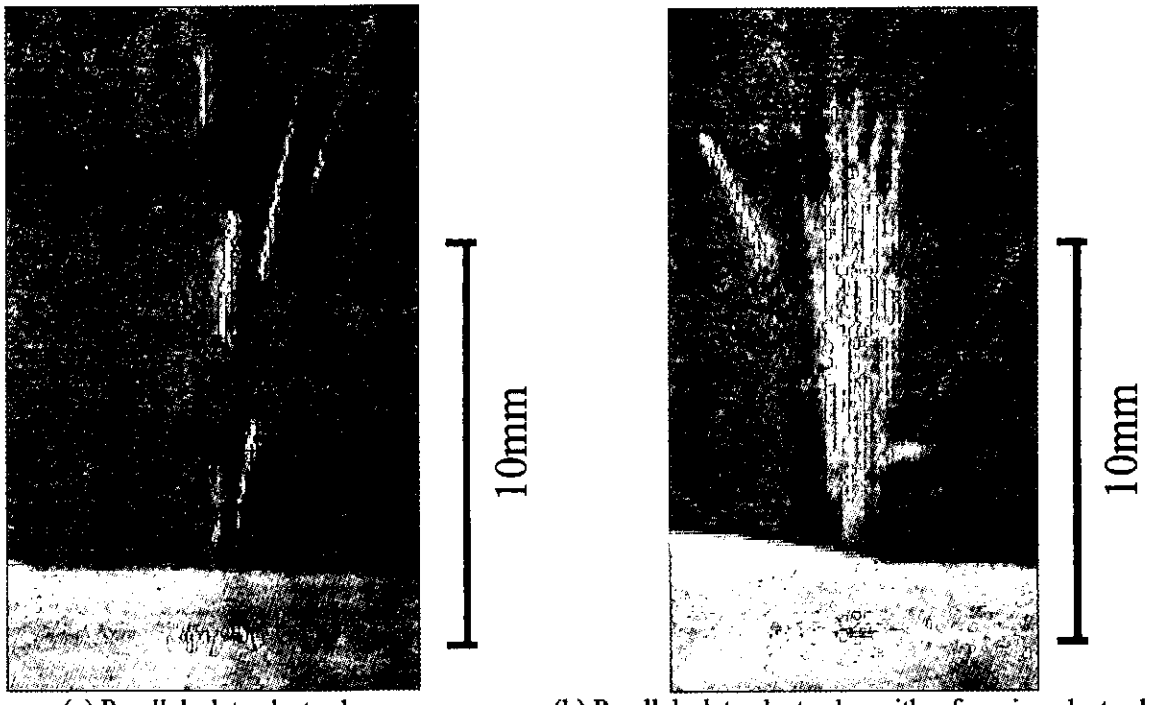

(a) Parallel-plate electrodes (b) Parallel-plate electrodes with a focusing electrode

Fig.6: Photograph of the spherical Cu powder (d=150μm) flow near the injection hole illuminated by a He-Ne laser beam. The pulsed voltage of 8kV (HV1) and 6kV (HV2) were applied to lower and focusing electrodes, respectively.

(b) Dependence on the driving pulse voltage waveform

In the previous study, we used the *CR* discharge circuit to drive powder acceleration. Since the pulsed voltage decayed exponentially, the powder was not fully accelerated and the injected powder mass was not enough to get reproducibility of the powder plasma. Thus it was necessary to improve the waveform of the applied pulse voltage from the exponential one to the rectangular one as shown in Fig.7. As the pulse width became longer, the injected powder number density increased. One can control the powder number density by changing

the pulse width. The powder number densities are summarized in Table 1, when the pulse width changed from 40 to 140ms.

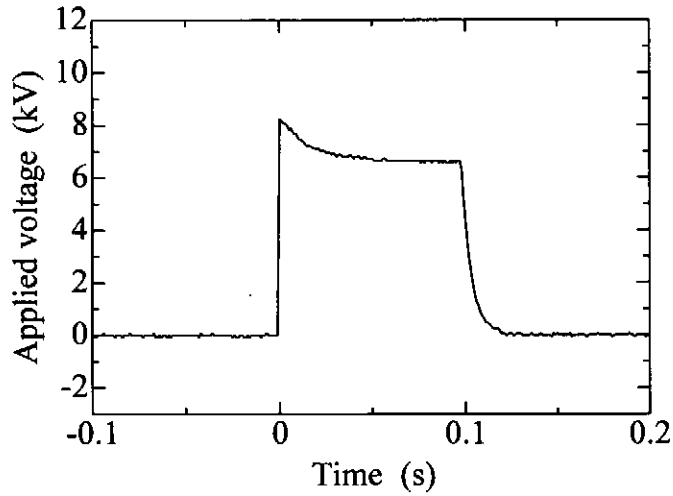

Fig.7: The rectangular waveform of the pulsed applied voltage (τ=100ms). The pulse width is possible to set voluntarily by using the function generator.

Table 1: Powder number density by laser beam attenuation measurement. The pulsed voltage of 8kV (HV1) and 4.5kV (HV2) were applied to lower and focusing electrodes, respectively. The Cu powder in this measurement was the diameter of 75μm.

Pulse width (ms)	Transmittance (%)	Powder number density (m^{-3})
40	97.8	4.84×10^{8}
60	96.2	8.84×10^{8}
120	93.8	1.44×10^{9}
140	92.9	1.66×10^{9}

III-II. Pre-ionization system

In Fig.8, the framing photographs of the pre-ionization discharge (a) and the induced pulsed plasma (b). The pre-ionization plasma expanded to the cathode. Afterward, a blight plasma channel develops. The peak value of discharge current reaches 83kA in 4us. Consequently, it was confirmed to create the powder Z-pinch by electrostatic injection.

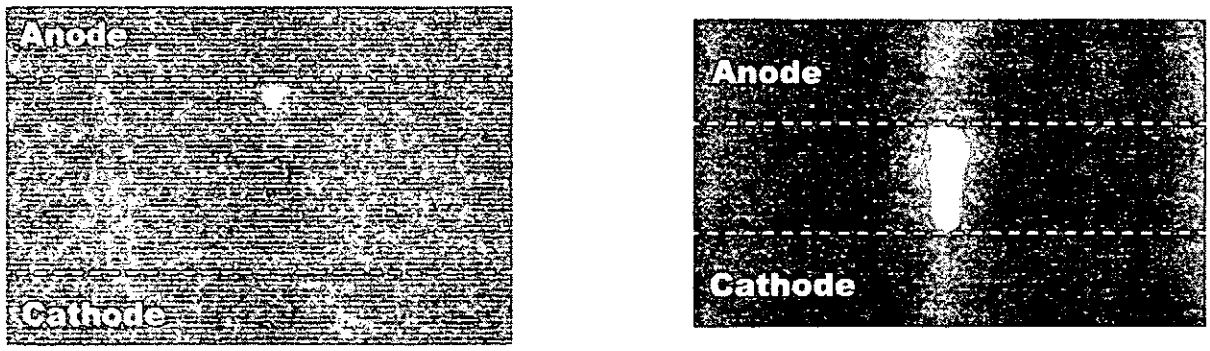

(a) Pre-ionization (exposure 300ns) (b) Pulsed plasma (exposure 200ns)

Fig.8: The framing photographs of the pre-ionization discharge and the induced pulsed plasma.

IV. Conclusions

The accurate control of powder for the Z-pinch has been established by using electrostatic control method. The focusing electrode enabled to focus the powder flow and enhanced the injected powder mass. In this study, we examined issues of the electrostatic control of powder injection system for the Z-pinch, namely, the powder shape and driving pulsed voltage waveform. The efficient pre-ionization system for stable powder Z-pinch is to avoid off-axis discharges is briefly discussed. Therefore, it was confirmed to create the powder Z-pinch by electrostatic injection.

References

1) T. Miyamoto, J. Plasma Fusion Research: Vol.74 (8), pp. 855-76 (1998) [in Japanese].
2) H. Ishihara, Y.Kawasaki, M.Sonoda, S.Suzuki, Y.S.Liu, K.Yasuoka and S. Ishii: NIFS-PROC-42, pp.134-143 (1998).
3) L. Dascalescu, M. Mihailescu and R. Tobazéon: IEEE Trans. Ind. Appl., Vol.34 (1), pp. 66-74 (1998)
4) G. M. Colver and L. J. Ehlinger: IEEE Trans. Ind. Appl., vol.24 (4), pp.732-39 (1988).

HIGH-SPEED OBSERVATION OF THE SOFT X-RAYS FROM THE PLASMA FOCUS

Yasushi Ono, Takeshi Yanagidaira, Haruhisa Maruyama,
Katsuji Shimoda, and Katsumi Hirano

Department of Electronic Engineering, Gunma University Kiryu, Gunma 376-8515, Japan

ABSTRACT

Emission from pinched plasma generated with plasma focus device with neon puffing is observed. Using the spatially and temporally resolved diagnostics such as the filtered photodiode array, image converter camera, framing mode x-ray camera and imaging Bragg spectrometer, we obtained the results that x-ray are emitted before disruption of plasma column. The electron temperature was between 0.6 and 0.7 keV at the hot spots, while the temperature of the surrounding region was 0.4 keV.

Ⅰ. Introduction

Intense source of soft x-rays have been required for many purposes such as x-ray microscopy, x-ray laser pumping and x-ray lithography. In the z pinch plasmas, x-ray sources which emit an intense soft x-ray are easily generated [1-3]. They are well known as hot spots or micropinches.

Spatially and temporally resolved diagnostics of the soft x-ray emission in the Z-pinch device make it possible to clarify the structure and time variation of the x-ray source generated in the pinched plasma. A spectroscopic method has frequently been employed in soft x-ray bands. The electron temperature have been evaluated using the intensity ratios of particular lines. However, spectral measurements are often made with time integrated spectroscopy, and so the evaluation of the plasma parameter such as electron density, temperature, and the size of emitting region of particular lines has been surveyed unsatisfactory with exception of a few papers [4, 5].

In this paper, we intend to clarify the mechanism of plasma heating by evaluating the detailed spatial distribution of electron temperature and simultaneous measurement with an imaging Bragg spectrometer, a high speed imaging system for visible, infrared and soft x-rays in streak mode, an image converter camera of visible light, a soft x-ray framing camera which is able to take four successive frames and so on.

Ⅱ. Apparatus

1. Plasma focus facility with gas puff

A Mather type plasma focus facility was used to generate a current sheet to compress puffed high Z gases. The outer electrode of the facility is squirrel cage type. The diameters of the inner and the outer electrode were 50 and 100 mm, respectively. Their lengths were 280 and 230 mm, respectively. The condenser bank consisted of 28×1.56 μ F, 80 kV capacitors. The facility was operated at the bank voltage of 45 kV and the bank current was estimated to be $\sim$ 1 MA in this experiment.

Neon was puffed with a fast acting valve through the inner electrode immediately before

each discharge. The hydrogen base pressure of 5 Torr. and neon plenum pressure of 3 atm were employed.

The schematic diagram of the plasma focus facility and the diagnostic tools are shown in Figure 1.

2. Three channel imaging system in streak mode

The imaging system [6] with one-dimensional resolution has three channels, that is a visible, an infrared and an x-ray channel in streak mode. The system, which consisted of 15-channel arrayed p-i-n diode detectors (International Radiation Detectors, AXUV-10EL), was operated to compose streak mode images. Combination filters were used for detector; glass (4.3 mm in thickness) and visible light pass filter (Kureha Chemical Industry, UCF-02) for visible light channels, glass (4.3 mm in thickness) and infrared pass filter (Fuji optical film, IR88) for infrared channels, and Al foil (1.5 um in thickness) for x-ray channels. The spectral response of the visible light channels, infrared channels and x-ray channels are from 450 to 650 nm, from 750 to 1000 nm and from 2 to 15 Å, respectively. The viewing field of each elements was 3 mm for axial and 15 mm for radial direction of the coaxial electrode of the plasma focus facility. The viewing field of the adjacent channels in the arrayed detector are designed to overlap each other. Therefore, the arrayed system enabled continuous detection over the whole area where the sources are generated. The rise time of the detection system was 1 ns. The analog signals from each channels were recorded at a sampling rate of 2 G samples/s in storage oscilloscope (Hewlett-Packard 54542A and 54542C). The oscilloscope can store analog signals from each channels into DOS-compatible files.

3. Image converter camera for visible light

An image converter camera (Hadland Photonics, IMACON700) operated in streak mode was employed in order to observe the macroscopic behavior of the plasma. The camera viewed the region of 2 mm from the inner electrode surface through a slit, 100 μ m in width and mounted perpendicular to the electrode axis.

4. Framing mode x-ray camera

An x-ray imaging camera available for taking four successive frames was developed to observe macroscopic behavior during the soft x-ray emission from the pinched plasma [7]. The camera consisted of a pinhole array with four pinholes, a Be foil filter, a MCP and a charge coupled device (CCD) camera with which the soft x-ray images of the plasma are recorded. The x-ray images are projected on four strip lines which were made from a thin gold coat on the MCP. These strip lines can be gated independently by four pulses. The inter-frame time and the exposure time were 2.5 ns and 0.22 ns, respectively. The spatial resolution of the camera system including the CCD camera was 120 μ m. The combination of the Be foil filter (50 μ m in thickness) and the MCP provides a pass band between 3 and 14 Å which accepts He-like and H-like spectral series of neon. Characteristics of the framing camera are described more precisely in a previous paper [7].

5. Imaging Bragg spectrometer

An imaging Bragg spectrometer was constructed to analyze the soft x-rays emitted from the pinched plasma. A RAP (rubidium acid phthalate, 2d=26.12 Å) convex crystal with the diameter of 12.5 mm was employed in this spectrometer [8]. For the imaging, an entrance slit

of 100 μ m and 5 mm in width and length was used. The spectrometer was capable of collecting x-ray spectra in a 3-20 Å region with the resolution power of $\sim$ 600 and the dispersion of $\sim$ 0.11 Å/mm. In this spectrometer, a pinhole was installed on the slit plane, so that precise identification of the wavelength was carried out, in spite of fluctuation of the x-ray source location from shot to shot. A Kodak TRI-X film was employed as a recording medium.

6. Auxiliary tools

The soft x-rays were monitored in the radial direction by a pin diode, which was also coupled with a Be filter (25 μ m in thickness). The hard x-rays were also monitored in order to detect the generation of electron beam from pinched plasma. The plasma light were monitord to know the appearance of plasma by an optical fiber mounted on the slit.

Ⅲ. Results and Discussion

1. Correlation of Streak image and soft x-ray

Figure 2 (a)-(e) shows an example of the streak image and soft x-ray taken in a single shot. In this figure, (a) is streak photographs taken with the image converter camera by visible light through the slit mounted at 2.0 mm from the inner electrode surface. The plasma is constricted toward the electrode axis with the radial velocity of $\sim$ 2.0×10^7 cm/s and the diameter become less than 1.5 mm at pinch phase. The plasma column lasts for $\sim$ 20 ns after formation of the plasma column along the electrode axis. In the figure, (b), (c) and (d) shows the signal of the plasma light taken by an optical fiber mounted on the slit, the signal of the hard x-rays and the signal of the pin diode, respectively. The signal of plasma light shows that plasma light was enhanced during t1-t2 when plasma was compressed by current sheet, and that the x-ray emission took place at t3. Therefore x-ray are emitted during a period when the plasma formed plasma column. The plasma light was enhanced at t4. This is not the scintillation of the optical fiber by hard x-rays. This is ascribed to the turbulence of the plasma before disruption.

Figure 2 (e) corresponds to the rise of the analog signal from monitor photodiode as shown in figure 2 (d). The x-ray framing images did not show obvious change for each frames although we had reported the growth of the instability in the framing photographs in the previous paper. But these frames showed difference at 12 mm from the inner electrode surface. The x-ray source recorded on frame (2) which corresponds to the peak of the pin diode had brightest intensity and reduced its intensity without drastic changing of its shape as shown in frame (3) and (4).

2. Correlation of visible, infrared and x-ray

The result for neon puff pinch is shown in figure 3. Emission in visible range from locations around z $\sim$ 15 mm last until t=80 ns. This is ascribed to emission from plasma which flowed from plasma column. X-ray source is generated at t=t1, z=0-5 mm, and after the peak emission in visible range. In the previous paper, we reported temporal and spatial resolved x-ray images that show x-ray emitted by a spot-like x-ray emissions. This figure shows the zippering effect on the formation of spots. X-ray emission in this shot seems to have started in the process of heating during the pinch phase. This electron temperature can be achieved by the process of heating during the pinch phase, as the electron temperature of neon puffing was estimated about 0.4 keV by the Bennet relation.

Immediately after x-ray emission, the peak emission in the visible range was observed at t=t2, z=0-5 mm. The peak emission in visible range cannot be ascribed to line radiation because at temperature around 0.4 keV, neon is highly stripped and there would be only a small fraction of ion which corresponds to line spectra in visible range. Therefore this peak is ascribed to bremsstralung and plasma oscillation excited in turbulent plasma.

3. Evaluation of the plasma parameter

Figure 4 (a) shows a typical example of the time integrated spectrogram taken in the shot #5413 with neon puffing. In order to identify wavelengths in the spectrogram, the photographic film was scanned with a scanner (EPSON FS-1200WINP). The soft x-ray intensity is displayed in a linear scale at figure 4 (b).

The H-like Rydberg transitions in NeX 1s-np series were observed for $2 < n < 7$ in this shot, whereas He-like $1s^2$-$1sn^1p$ series were observed for $2 < n' < 6$ as shown in Figure 4 (a). The upper detectable limits in both series gives an electron density estimate of $n_e \sim 10^{22}$ cm^{-3} according to the series merging technique based on Inglis-Teller theory.

The recorded around 9 Å for shot #5413 image was identified to be the direct exposure of x-rays without reflecting at the crystal for this shot by an irregular setup of the spectroscope.

The image of Lyman-α contained mainly four spots and the sizes were about $\sim$ 250 μ m. The recombination radiation were recognized around 10 Å at z=0.87 mm and 8.78 mm. The continua appeared at the position closer to the inner electrode surface from the spots, and correspond to the position of microscopic disruption. Therefore we thought the plasma compressed by the growth of instability moved off toward the inner electrode from hot spot, then the electron caused recombination radiation.

Figure 5 (a) shows the spatially resolved electron temperature and figure 5 (b) shows variation of the temperature scanned along the inner electrode axis. This temperature was calculated from the ratio between intensity of Lyman-α, intensity of resonance line and intercombination line. For the calculation of the temperature, the photographic density of the film was linearized. These figures show that the electron temperature was between 0.6 and 0.7 keV at hot spots, while the temperature at the surrounding region was 0.4 keV. The electron temperature estimated from intensity integrated for all region of the source does not correctly represent the plasma parameter of the hot spots and it is necessary to calculate the temperature from intensity except the surrounding region.

Figure 6 shows the radial distribution of electron temperature at z=0.686 mm, where recombination radiation was observed. This spot have highest electron temperature on the electrode axis, and was estimated at 0.571 keV.

Ⅳ. Conclusion

Using the spatially and temporally resolved diagnostics of the visible, infrared and soft x-ray emission, we obtained the results that x-ray are emitted from the hot spots and surrounding region.

References

1) N. J. Peacock, R. J. Speer and M. G. Hobby: J. Phys. B 2 (1969) 798.

2) P. G. Burkhalter, G. Mehlman, D. A. Newman, M. Krishnan and R. R. Prasad: Rev. Sci. Instrum. 63 (1992) 5052.

3) H. Kitaoka, T. Yamamoto and L. Hirano: J. Phys. Soc. Jpn. 67 (1998) 481.

4) T. Nash, C. Deeney, P. D. LePell, R. Prasad and M. Krishnan: Rev. Sci. Instrum. 65 (1994) 3761.

5) J. M. Bayley, G. Decker, W. Kies, M. Malzig, F. Muller, P. Rowekamp, J. Westheide and Y. V. Sidel'nikov: J. Appl. Phys. 69 (1991) 613.

6) T. Yanagidaira and K. Hirano: Rev. Sci. Instrum. 68 (1997) 3074.

7) B. Shan, T. Yanagidaira, K. Shimoda and K. Hirano: Rev. Sci. Instrum. 70 (1999) 1688.

8) K. Hirano, N. Hisatome, T. Yamamoto and K. Shimoda: Rev. Sci. Instrum. 65 (1994) 3761.

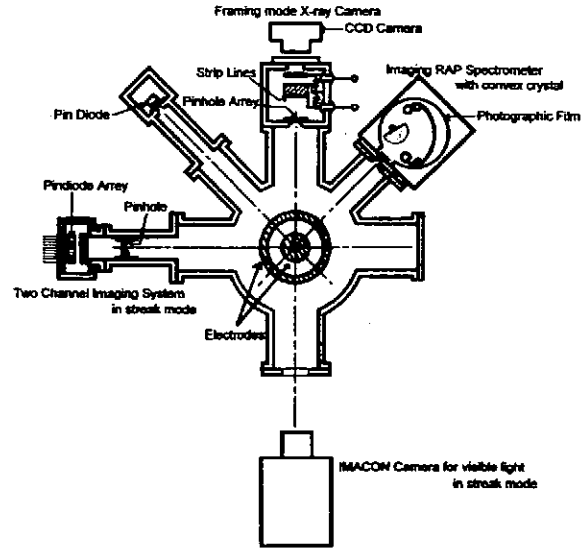

Figure 1. Plasma focus facility and diagnostic tools.

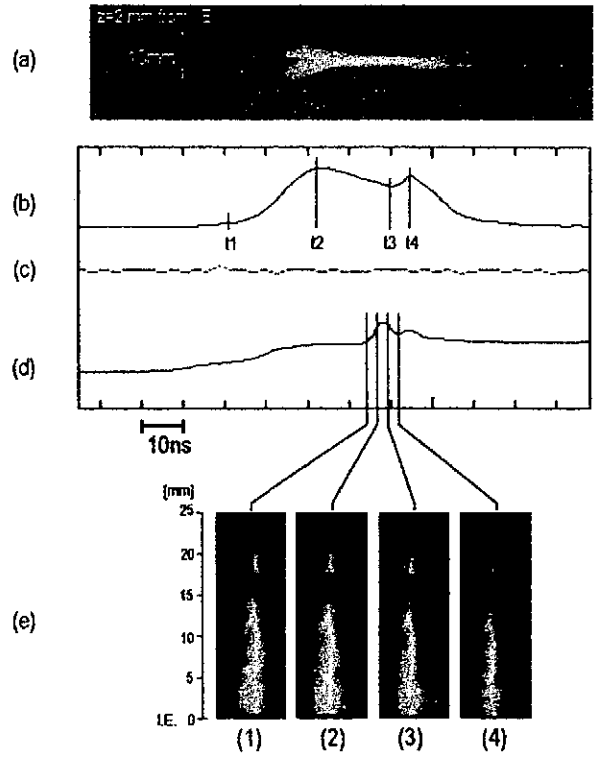

Figure 2. Streak image and framing images.

(a) Streak image(z=2.0 mm from I.E.). (b) Signal of the plasma light. (c) Signal of the hard x-rays. (d) Signal of the pin diode. (e) Framing images.

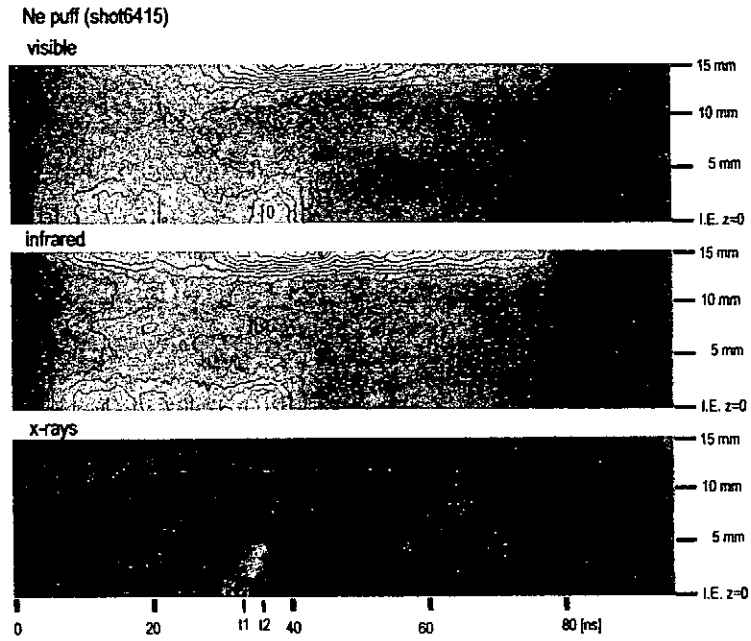

Figure 3. Experimental results for neon puff.

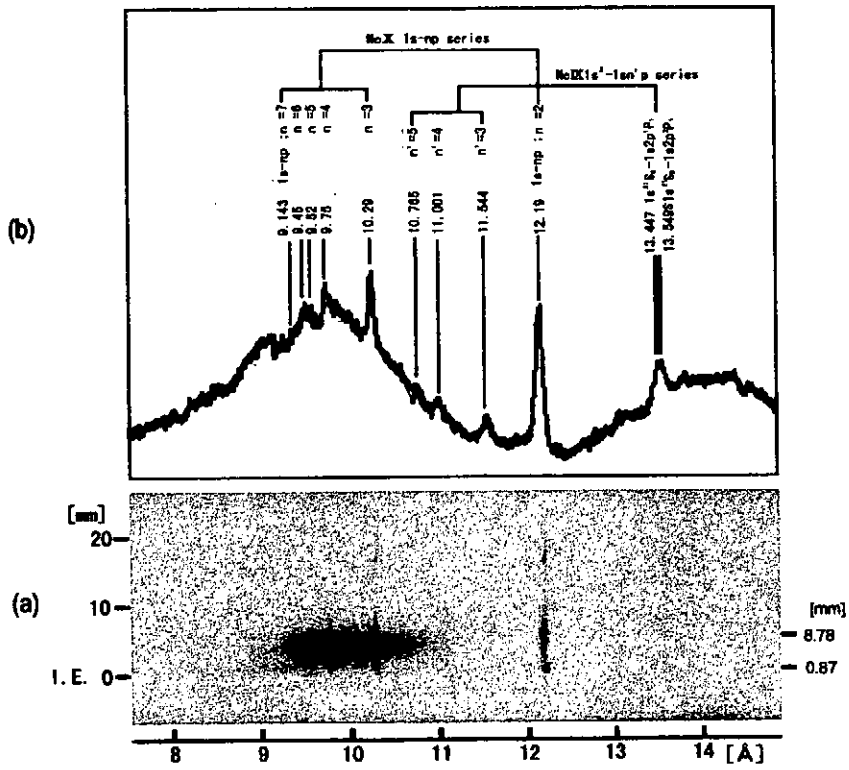

Figure 4. Spectrum of neon plasma.

(a) Imaging spectrogram of neon focused plasma.

(b) Neon spectrogram obtained by scanning of (a).

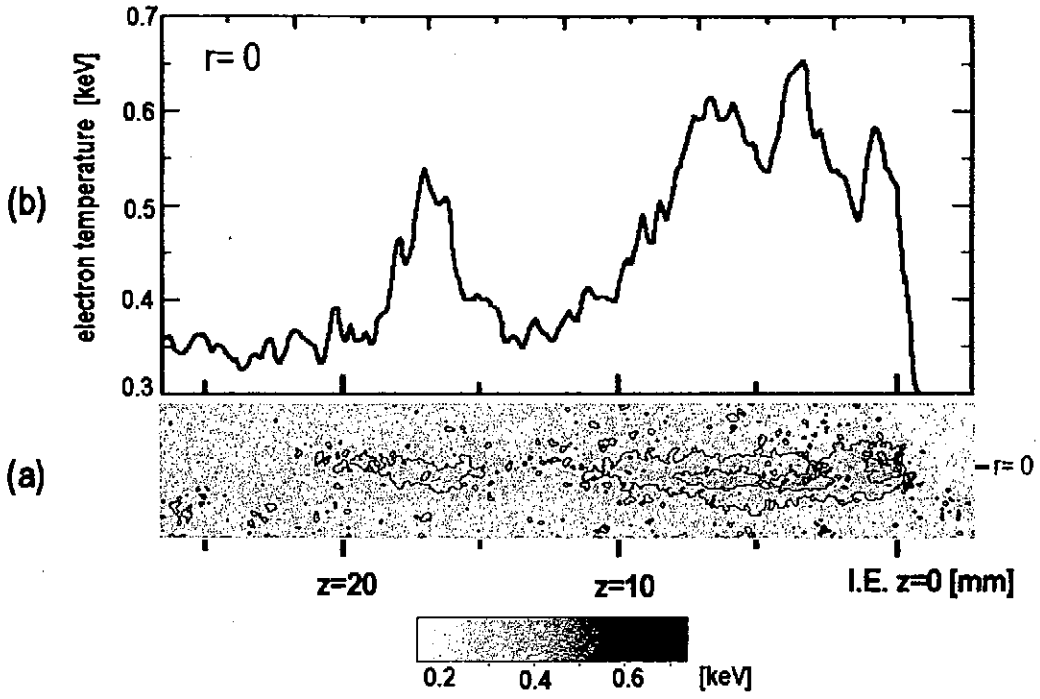

Figure 5. Spatial resolved electron temperature.

(a) Spatial distribution of electron temperature.

(b) Electron temperature scanned at r=0.

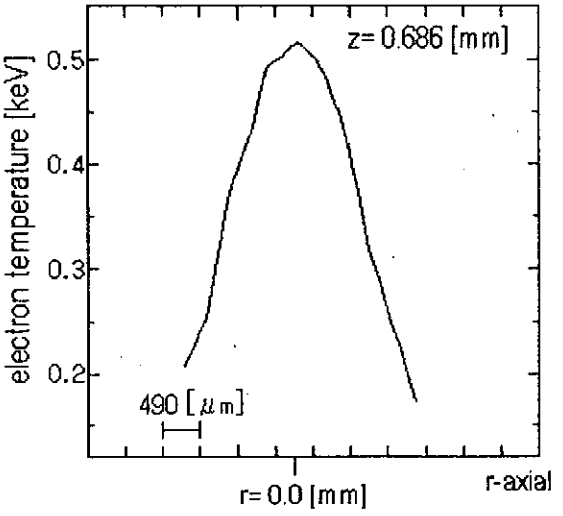

Figure 6. The radial distribution of electron temperature at z=0.686 mm.

HEATING OF GAS-PUFF TARGET IN PLASMA FOCUS

T. Yanagidaira, F. Wen, Y. Ono, and K. Hirano

Department of Electronic Engineering, Gunma University,
1-5-1 Tenjin-cho, Kiryu, Gunma 376-8515, Japan

ABSTRACT

The evolution of the plasma focus with neon gas puffing was investigated experimentally and numerically. By using a simulation code based on the finite volume method, the dynamics and the heating of plasma driven by shock wave were calculated for different initial densities of the current sheet. The temperature was calculated to be 0.2- 0.4 keV at the maximum compression, whereas the experimental result from x-ray spectra was 0.5 keV. Assuming an initial density for collapse phase, the reflection of the shock wave does not cause a rapid expansion of the pinch column even in a calculation without radiation loss and the calculated sustaining time agree with the experimental result.

Ⅰ. Introduction

There are an increasing number of applications of soft x-rays in fields such as x-ray microscopy, x-ray lithography and laser excitation. Plasma focus device with gas puffing is an intense and impulsive source of soft x-rays. The device is capable of compressing and heating arbitrary gas by a collapsing current sheet of hydrogen. The plasma produced in gas puff pinch with pulse power generator is generally more stable than the gas embedded pinch. When high Z gas such as neon and argon is puffed, an intense soft x-ray from highly ionized plasma is observed.[1] In experiments with neon gas puffing, x-rays were emitted during pinch.[1,2] Therefore, we expect that the soft x-ray yield can be increased by increasing the sustaining time of the plasma column. However, heating mechanism and the dynamics have not clarified satisfactorily yet. For example, Potter[3] developed a model which describes the radial structure of plasma parameter between piston and shock. However, the reflection of the shock wave was not considered. In this paper, we examined the mechanism by which the puffed gas is heated, by comparing experimental results and a numerical simulation of pinch based on FVM (finite volume method) which enables description of the propagation and reflection of the shock wave. And we considered instability growth rates for different initial

conditions for optimization for soft x-ray source.

Ⅱ. Plasma focus facility with gas puff

A Mather type plasma focus facility was used to generate a current sheet to compress puffed high Z gases. The diameters of the coaxial inner and the outer electrode were 50 and 100 mm, respectively. The length of the inner and the outer electrodes were 280 and 230 mm, respectively. The capacitor bank consisted of 28 x 1.56 μF, 80 kV capacitors. The device was operated at the bank voltage of 45 kV and the peak of discharge current was $\sim$ 1 MA. Immediately before each discharge, a high Z gas such as neon was puffed through a hole in the inner electrode. In plasma focus, an extremely rapid rising current can be applied to the collapsing plasma column at the start of the radial collapse phase because the plasma already carries a heavy current at the beginning of this phase. The puffed gas does not affect the acceleration of the current sheet, and so the density of the puffed gas can be set independent of hydrogen pressure. An embedded hydrogen base pressure of 5.5 Torr was employed. Approximately 5 cc at 3 atm. of neon was puffed by each operation. The experimental setup and the arrangement of diagnostic tools is shown in Fig. 1. The pressure distribution of the puffed gas at the start of the discharge was measured with a pressure transducer as shown in Fig. 2.

Ⅲ. Modeling of plasma focus with gas puff

In order to examine the stability of the plasma at pinch and to evaluate the instability growth rate, the pinch plasma with neon gas puffing was simulated numerically. We assumed infinite conductivity, and the heating of hydrogen and puffed gas was calculated by compression and imploding shock wave driven by the current sheet on the surface of the plasma. Joule heating was not included because the skin effect prevents the current from penetrating into puffed gas. In order to simulate heating process in plasma focus driven by a fast capacitor bank, it is important for simulation code that it can calculate the propagation and the reflection of the shock wave in radially imploding plasma. Therefore, we developed FVM (Finite Volume Method) 1D (cylindrical) fluid code in Lagrangian coordinate, which traces cells in which plasma is contained. The cells interact each other and move with plasma flow. An artificial viscosity that is proportional to the relative velocity for adjacent cells was employed to avoid numerical difficulty. The parameters for each time step were calculated with 2nd-order accuracy. To reduce CPU time, the time step was controlled automatically so that the rate of volume change for each step is around 1 %. We used the average charge of neon [4] which is given as a function of the temperature.

In the collapse phase, the current sheet is accelerated toward electrode axis. However, not all the hydrogen embedded between electrodes converges on the x-ray-emitting region at

the same time because of geometry of the current sheet. The time of maximum compression depends on the distance from the inner electrode owing to the geometry and axial velocity of the current sheet. Then the pressure gradient makes plasma move away from compressed region by an axial flow. In order to examine the effect of density of the current sheet on final pinch, we calculated pinch evolution, changing initial density of the plasma sheet as parameter. We defined a standard density ρ_s as the density of current sheet when all the hydrogen between electrodes were collected in a cylindrical region with same length as the anode diameter. The instability growth rate was also evaluated from the radius and the temperature calculated at maximum compression.

IV. Results and discussion

Figure 3 shows the correlation between the macroscopic behavior of the plasma and x-ray emission.[2] Figure 3 (a) is the streak image in visible light observed through a slit mounted at 9 mm from the inner electrode. The plasma is constricted toward the electrode axis with the velocity of $\sim 10^5$ m/s. The pinch was sustained for $\sim$ 30 ns and there was no remarkable change of visible light intensity during the period. Figure 3 (b) shows the x-ray emission observed with the P-I-N photodiode. The peak of soft x-ray was observed during the sustaining time. The framing pictures shown in Fig. 3 (c) were recorded with a gated MCP system[5] and taken from four shots on the basis of reproducibility and arranged according to the time sequence. These x-ray pictures show that there were drastic changes of soft x-ray source by growth of instabilities even in the period when the pinch seemed to be stable.[2]

The results for 1D simulation of pinch with neon puffing are shown in Fig. 4. Fig. 4 (a), (b) and (c) shows results for initial densities of $\rho_s/1$, $\rho_s/2$ and $\rho_s/10$, respectively. For $\rho_s/1$ and $\rho_s/2$, the plasma diameter begins to rapidly increase at t_2 after the current sheet was pushed by the shock wave which is reflected on the electrode axis at t_1. However, in the case of $\rho_s/10$, the reflection of the shock wave at t_1 does not cause a rapid expansion of the plasma column although energy loss by radiation is not included. The pinch is sustained until the growth of instability disrupts the plasma column at t_3. The calculated radial velocity and pinch diameter in this case agree with the experimental results shown in Fig. 3 (a).

There are several factors affecting the life time of pinch and the x-ray yield. As shown in the simulation, there is a criterion of initial density for final pinch to be in steady state. The other factor is the growth time for the instability which is in order of $\tau = a / (2kT_i/m_i)^{1/2}$, where a is the pinch radius, T_i is the ion temperature and m_i is the ion mass. If no instability is grown, the plasma is calculated to be compressed again by bouncing at $t = t_4$. However, the value of τ was calculated according to the simulation to be $\sim$ 40 ns ($t = t_3$)

which is shorter than the bounce time and was consistent with the sustaining time in Fig. 3 (a).

Puffed neon is heated by shock wave to several hundred eV depending on the initial density at the beginning of the sustaining time. The temperature at t_2 for $\rho_s/1$, $\rho_s/2$ and $\rho_s/10$ are 0.4 keV, 0.33 keV and 0.21 keV, respectively. Without gas puffing, the ion temperature was calculated to exceed 1 keV at the maximum compression. The growth time can be extended by the lowering of T_i and the increase of m_i by a gas puffing. The axial flow of plasma also lowers the temperature.

Generation of the localized hot spots observed in the latter phase of the sustaining time [1,2] is ascribed to another mechanism for further heating, such as turbulence by the growth of instability. In plasma focus, part of energy attained in collapse phase is converted to kinetic energy of the axial flow and contribute heating later. Further simulations are in progress using 2D FVM code (Fig. 5) to obtain precise information for optimization for x-ray yield.

References

1. T. Yanagidaira, T. Yamamoto and K. Hirano: J. Phys. Soc. Jpn., 68 (1999) 839.
2. T. Yanagidaira, K. Shimoda, Y. Ono and K. Hirano: Phys. Plasmas, 6 (1999) 4679.
3. D. Potter: Nucl. Fusion, 18 (1978) 813.
4. M. Arnaud and R. Rothenflug: Astron. Astrophys. Suppl. Ser., 60 (1985) 425.
5. B. Shan, T. Yanagidaira, K. Shimoda and K. Hirano: Rev. Sci. Instrum., 70 (1999) 1688.

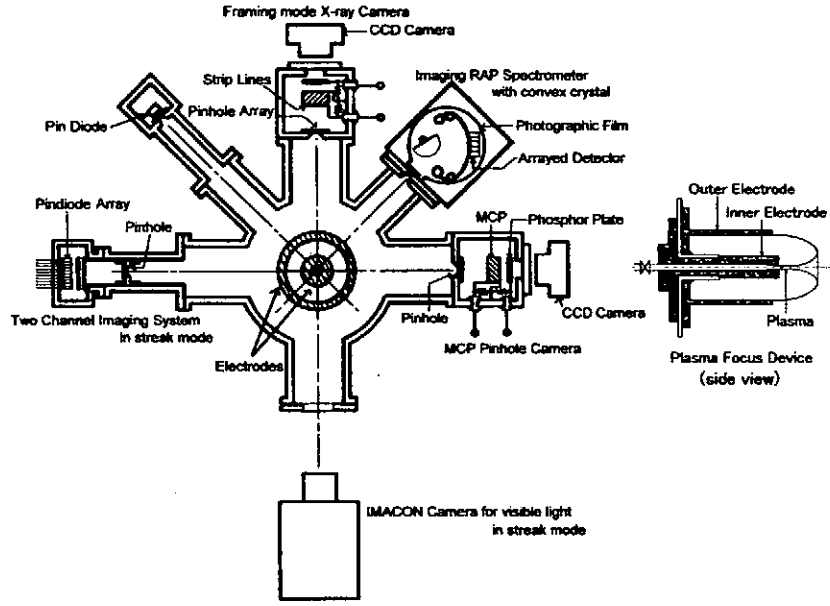

Fig. 1: Plasma focus device and diagnostic tools

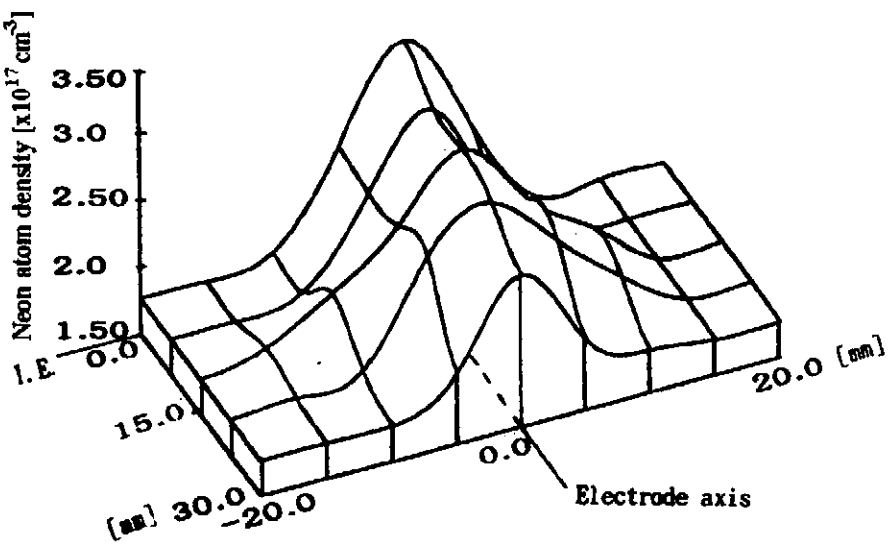

Fig. 2: Density profile of puffed neon at the plasma focus discharge.

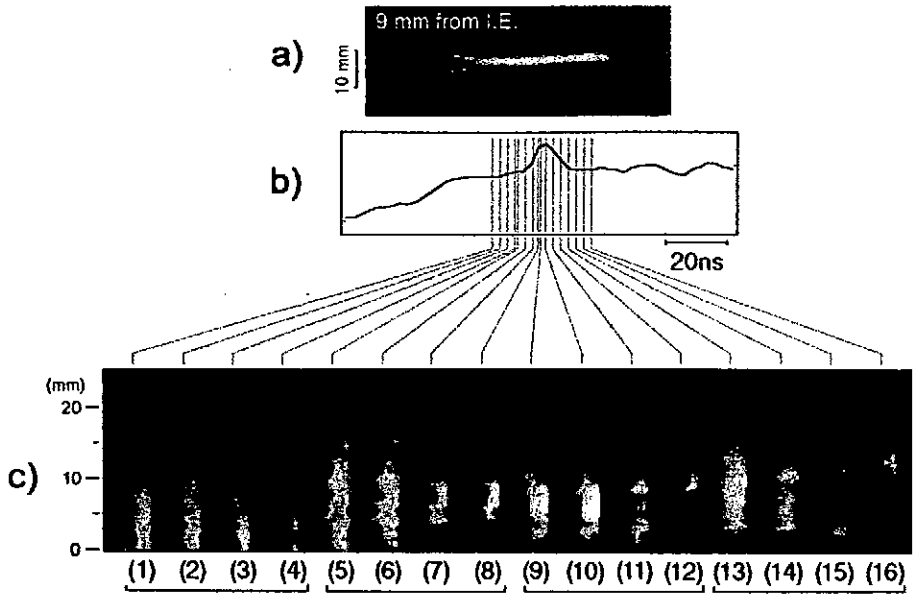

Fig. 3: a) Streak photograph in visible light, b) Signal from P-I-N photodiode and c) X-ray photographs taken with the gated MCP system. The inter-frame time is 2.5 ns.

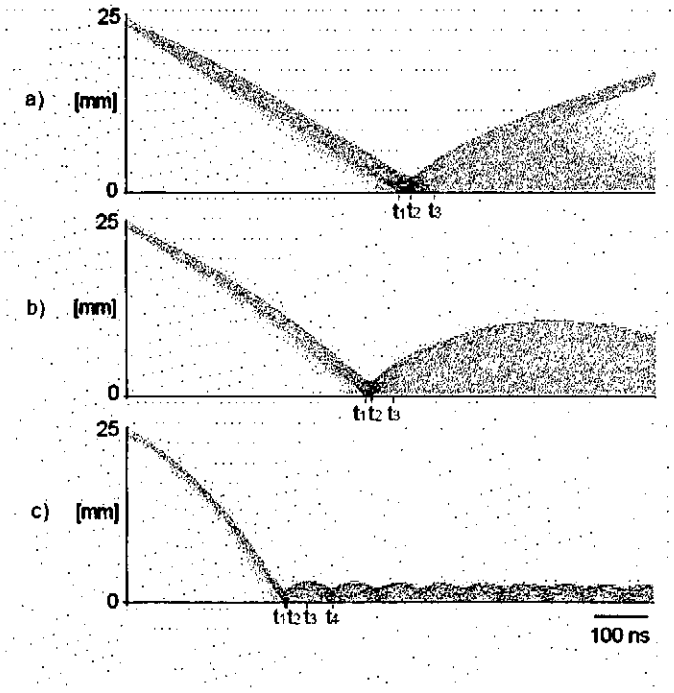

Fig. 4: (a)-(c) Pinch evolution with neon puffing calculated for different initial plasma sheet densities. t1, t2, t3 and t4 corresponds to the reflection of the shock wave, the maximum compression, sustaining time and the bounce time.

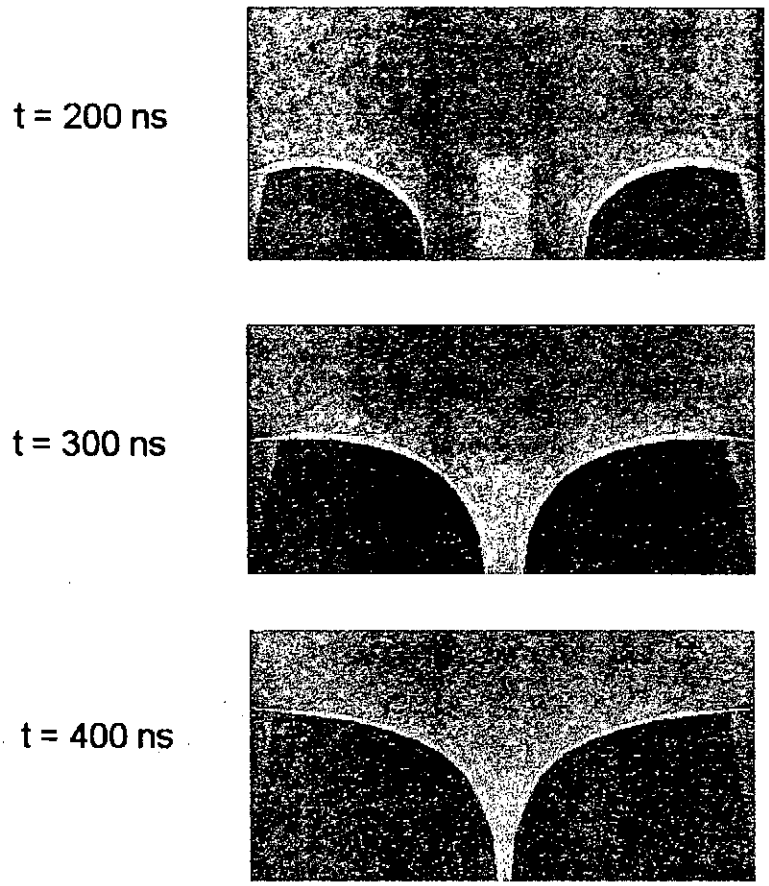

Fig. 5: An example for 2D FVM simulation. Each image shows pinch region in fromt of the inner electrode face (100 mm x 50 mm).

Nanosecond Generation of Intense Electron Pulses through a High-T_c Superconducting Tube

Hidenori Matsuzawa, Yoshinori Watanabe, Koji Mikami, and Kenjirou Fukasawa

Faculty of Engineering, Yamanashi University, Kofu 400-8511, Japan

Abstract: When a high-voltage pulse was applied to a diode consisting of a cold cathode and a high-critical temperature (T_c) superconducting tube anode (supertron), an intense electron beam pulse was generated which was ~340 keV, ~2 kA, with a duration of ~1.5 nanosecond at 80 K. The anode was composed of an inner 1.5-mm-thick Bi-based sintered pipe and an outer 1-mm-thick Y-based melt-processed pipe, with a 17-mm innermost diameter and a 55-mm axial length including a funnel-type inlet. The pulse widths increased with temperatures. Modifications to the anode tube were proposed for compressing electron pulses to subnanoseconds.

In the course of experiments on a high-critical temperature (T_c) superconducting tube lens [1, 2] for charged particle beams, we found that intense electron pulses with a full-width at half-maximum (FWHM) of ~1.5 ns were readily generated using the lens. The novel method is simple as compared with other short-pulse generators [3, 4] such as a multi-stage autoaccelerator [5, 6]. If the method is improved, it would generate subnanosecond electron pulses. Therefore, this paper outlines the experimental results [7].

Figure 1 shows the experimental setup used. The device consisted of a beam diode, a Faraday cup, and a Rogowski coil. A high-T_c superconductor tube lens was glued onto the inner surface of a copper-made heat sink with silver paste. The sink thus prepared played a role of anode of the diode. The superconductor tube used was double-layered: The outer 1-mm-thick pipe was made from yttrium (Y)-based melt-processed materials [8] with a T_c of ~90 K, composed of grains of more than some millimeters. The inner 1.5-mm-thick pipe was shaped from bismuth (Bi)-based sintered materials with a T_c of 103 K, consisting of grains of ten or less micrometers. These two pipes were cemented each other with electrically conductive resin. The latter pipe had a 17-mm inner diameter. The tube thus assembled was 55 mm in axial length, including a funnel-type inlet made from Y-based melt-processed superconductor with an opening of 55-mm diameter.

The double-layered structure was tried for the confirmation of the idea [9] that such a tube will focus and guide electron beams ranging from continuous to single short-pulsed currents. The idea came to us from a ferrite-core model [10] proposed previously for explaining the operation of Bi-based sintered tubes. The melt-processed pipe should be outside the sintered one. This is because the self-magnetic fields of

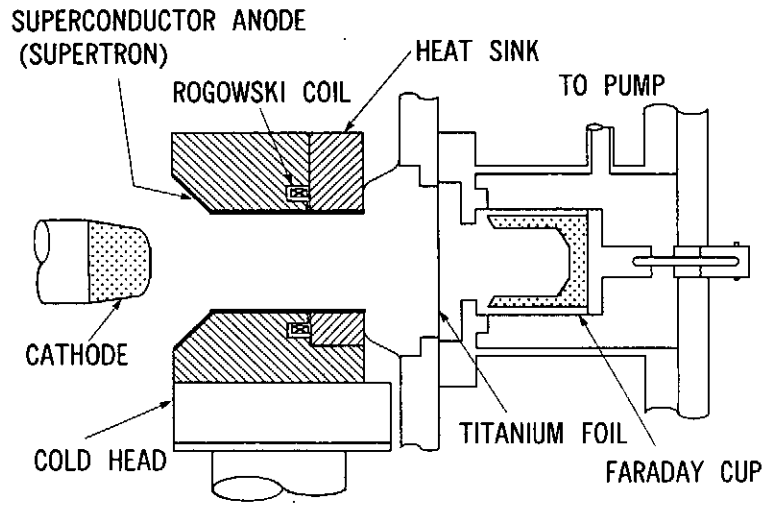

Fig. 1. Experimental setup. Electron beams were field emitted from a cold cathode by applying high-voltage pulses to the diode consisting of the cathode and high-T_c superconductor tube anode (supertron). The Faraday cup detected the electron currents focused with the supertron. The Rogowski coil observed self-magnetic fields of net electron currents.

single short electron pulses are confined by the inner sintered pipe and because the fields of continuous electron currents diffuse through grain boundaries of the inner pipe and then are blocked by the outer melt-processed pipe.

Just before operating the device, we introduced neon gas of the order of 0.1 Torr into the diode space for neutralizing space charges of the intense electron pulses and consequently for focusing the electron beams easily. The Faraday cup was isolated from the diode space with a 20-μm-thick titanium foil and was kept at a pressure less than 10^{-4} Torr. Thus, the cup detected electron currents of kinetic energies higher than 60 keV. The Rogowski coil received the magnetic fields that were induced by the electron beams propagating down the bore of the tube and then diffused through the double-layered wall. The signals from the Rogowski coil were delayed by 26 ns behind those from the Faraday cup with an additional 5-m-long cable. Temporal waveforms were displayed on a high-speed oscilloscope (Tektronix SCD 1000, 1 GHz). The heat sink was cooled with a compact helium-gas refrigerator. Operation temperatures were monitored with thermocouples at the inlet and exit of the heat sink.

The first and second peaks in Fig. 2 show, respectively, waveforms of the electron pulses and of the magnetic fields at temperatures of (a) 200 and (b) 80 K. Figure 2(c) shows a waveform at 100 K for a slow sweep of 50 ns/div. The second peaks of magnetic fields in Fig. 2 were induced by the net electron currents consisting of primary intense electron currents and secondary plasma electron currents. Figure 3 indicates the electron pulses for the temperatures 200 to 80 K. The high-frequency oscillations imposed on the waveforms are probably parasitic ones induced by the measurement system. In Fig. 4 we plotted the average values of the electron pulse widths (FWHM) at respective temperatures for more than ten shots. Near the T_c's of

the tube materials, the pulse widths were compressed steeply. Here we comment on the T_c's. The tube used had a zone of T_c of 90 to ~100 K. This is because the tube was composed of the two different pipes. In addition, operating temperatures of the inner pipe were different from those of the outer pipe, because the two pipes were cooled through the thermal conduction from the refrigerator. The present data are plotted as a function of temperature of the inner pipe.

Radial profiles of the electron beams were observed at the exit of the tube. The radial FWHM of the profile at 80 K was ~ 3 mm and increased with temperatures. Namely, the focusing ability of the double-layered tube decreased with increasing temperatures as was the case of Bi-based single tubes in the previous experiments [1, 2].

The electron pulses at 80 K were ~2 kA, ~340 keV, with a FWHM less than 1.5 ns. The present experiments were not optimized for achieving the shortest pulses.

The mechanism of the pulse compression is not clear yet. However, we picture the following primitive scheme. When the front of electron beams approaches the inlet of the double-layered tube, the corresponding shielding currents are induced in surface of the inner Bi-based tube in the direction opposite to the incident beams. As was explained by the ferrite-core model [10], the shielding currents respond rapidly to the injection of the beams because of the small grain size and hence of small time constants (low Q-values) of the circuit of the induced currents in grains. On the other hand, the shielding currents in the outer Y-based pipe increase slowly because the self-magnetic fields of the electron beams arrive at the outer pipe after diffusing through the wall of the inner pipe and because the circuit of the induced currents in the outer pipe has large

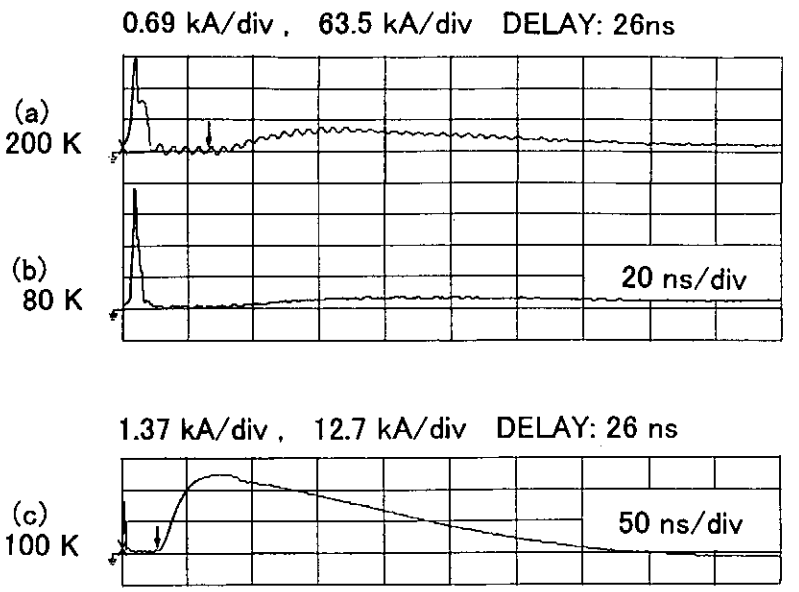

Fig. 2. Temporal behaviors of electron current pulses detected with Faraday cup (first peaks) and of magnetic fields that were induced by net electron currents and arrived at Rogowski coil after diffusing through superconductor tube wall (second peaks). The second peaks were delayed by 26 ns behind the first ones. (a) 200 K and (b) 80 K. (c) The slow horizontal sweep 50 ns/div. at 100 K shows a time evolution of second peak of magnetic fields.

time constants (high Q-values) due to the large grain size. Thus, the beam front is compressed by the repulsive force between the beam-front charges and the shielding currents induced in the Bi-based pipe. This process of compression continues while the beam front propagates down the sintered pipe. When the tail of the beams leaves the double-layered tube, the expelling (repulsive) force between the beam tail and the currents induced in the Y-based pipe kicks the tail out of the tube. This is because the currents induced in small grains of the Bi-based pipe respond quickly to the beam tail, turn their direction of flow easily, and decay promptly owing to the low Q-values of the current circuit. Contrarily, the currents induced in large Y-based grains persist in flowing in the same direction as they were induced, probably because the currents cannot turn their direction of flowing owing to the high-Q values of the current circuit even when the beam tail leaves the pipe. Thus, both the front and tail of the beams are compressed. We can say that this model was already partially supported by the

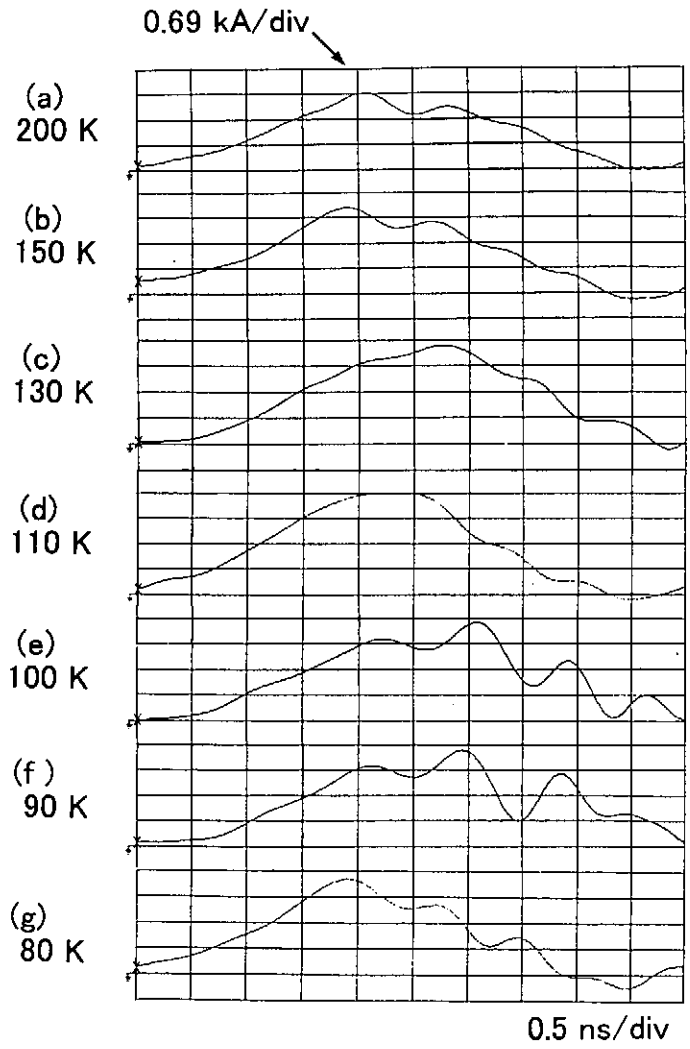

Fig. 3. Temporal behaviors of electron current pulses for 200 to 80 K. Pulse widths decreased with lowering temperatures.

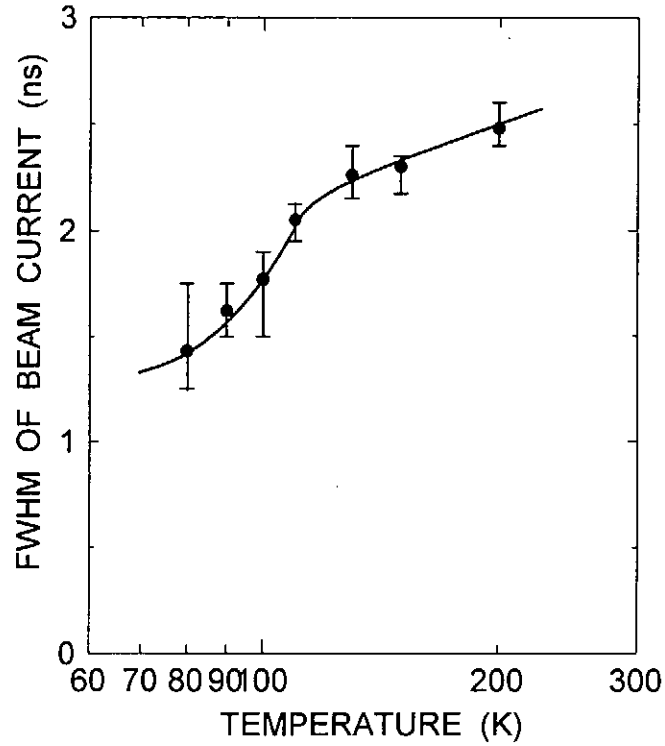

Fig. 4. Full-widths at half-maximum (FWHM) of electron pulses as a function of operation temperatures. The FWHM's decreased steeply below a T_c zone of the tube materials.

experimental results [7] that the FWHM's for the present experiments were narrower than those for either of Bi-based and Y-based single-layer tube lenses.

According to the model, minor modifications will be necessary to the structure of the present tube for achieving more effective compression of the pulses: The inner Bi-based pipe should be thick near the entrance of the tube and decrease gradually in thickness with the axial distance. On the contrary, the outer Y-based pipe should be thin near the entrance and be thicker with the distance. If a longer tube is used, electron pulses may be compressed more because of longer duration of the interaction time between the beams and tube.

In conclusion, we reported a novel method for generating intense electron pulses of ~1.5 ns using a high-T_c superconducting double-layered tube. The improvements in configuration of the tube will provide electron pulses with a duration of subnanoseconds.

References

[1] For a review, see H. Matsuzawa, J. Appl. Phys. **74**, R111 (1993) [Erratum: J. Appl. Phys. **76**, 624 (1994)]. Other papers on the lens (supertron) to the end of 1993 are listed in this article.

[2] H. Matsuzawa, A. Matsushita, P. Roth, H. Matsubara, Y. Ueda, and S. Suganomata, Jpn. J. Appl. Phys. **36**, 98 (1997).
[3] R. B. Miller, *An Introduction to the Physics of Intense Charged Particle Beams* (Plenum, New York, 1982).
[4] S. Humphries, Jr., *Charged Particle Beams* (John Wiley, New York, 1990).
[5] M. Friedman, Appl. Phys. Lett. **41**, 419 (1982).
[6] D. Hasegawa, K. Kamada, K. Shimizu, M. Miyamoto, R. Ando, and M. Masuzaki, *Proc. of the 12th Intern. Conf. on High-Power Particle Beams* (Haifa, Israel, June 7-12, 1998).
[7] H. Matsuzawa, Y. Watanabe, K. Mikami, and K. Fukasawa, Jpn. J. Appl. Phys. **39**, 47 (2000).
[8] For a review of melt-processed materials, see M. Murakami, Supercond. Sci. Tech. **9**, 1015 (1997).
[9] H. Matsuzawa, Y. Watanabe, K. Fukasawa, and K. Mikami, *Advances in Supercond. XI*, edited by N. Koshizuka and S. Tajima (Springer, Tokyo, 1999) pp. 1309-1312.
[10] H. Matsuzawa, H. Kobayashi, H. Mochizuki, N. Yoneyama, A. Ohshima, S. Hirano, E. Mori, G. Horigome, Y. Ishida, and Y. Chino, Jpn. J. Appl. Phys. **33**, 2526 (1994) [Erratum: Jpn. J. Appl. Phys. **33**, 4799 (1994)].

POWER FLOWS THROUGH GEOMETRICAL DISCONTINUITY IN MAGNETICALLY INSULATED TRANSMISSION LINES

Kazuki Hiraoka, Mitsuo Nakajima and Kazuhiko Horioka
Department of Energy Sciences, Tokyo Institute of Technology
Nagatsuta 4259, Midoriku Yokohama, Japan 226-8502

ABSTRACT

MITLs (Magnetically Insulated Transmission Lines) under high power operation are dominated with space charge current flowing between anode and cathode. When MITL has a geometrical discontinuity, the interaction between the disturbed electrons and the non-linearly coupled electromagnetic field makes their behavior difficult to predict. The results of particle simulations show that the space charge electrons tend to maintain the effective impedance of the transmission lines, by changing their distribution and the boundary of electron cloud. Although a fraction of the space charge flow shunt the gap at the discontinuity when the discontinuity is larger than a critical value, the total upstream current is still preserved. To discuss this impedance adjustment process and the critical value, we propose a laminar flow model with constant current density.

1. Introduction

In high-power transmission lines the high power electromagnetic pulse is inevitably accompanied by high electric field. The power density of electromagnetic wave is described by the Poynting vector $S=ExH$. When we think of a TEM mode in vacuum, the magnitude of this vector is $|S|=|E|^2/377(\Omega)$, which means that high power density is inevitably accompanied by high electric fields. For example, a power density of 1TW/cm^2 arises from a 20 MV/cm electric field. Generally, when the local electric field on the cathode surface exceeds 200kV/cm[1], electrons explosively emitted from the cathode shunt the high voltage gap. Consequently, ordinary transmission lines have a limit of energy flux at ~100MW/cm^2. However, when the current flowing the line grows to large enough, the self-magnetic field overcome the electric field and insulate the gap(Fig.1). Thus the magnetic insulation is of essential technology for high energy density power transportation[2].

Magnetically insulated transmission lines (MITLs) under high power operation are dominated with space charge current flowing between the gap. The relativistic electrons coupled to the strong electromagnetic field transport significant fraction of the power in MITLs. The energy conservation relation for a system of relativistic charged particles and fields is expressed as follows[3],

$$(\partial/\partial t)(\mu_0 \boldsymbol{H}^2/2+\varepsilon_0 \boldsymbol{E}^2/2+\boldsymbol{T}/q) = -div(\boldsymbol{E}\mathrm{x}\boldsymbol{H}+\boldsymbol{JT}/q) \qquad (1)$$

where the left-hand side is time variation of energy density as the sum of field energy and kinetic energy of charged particles, and the right-hand side expresses the outflow of them from the unit volume. μ_0 and ε_0 are the vacuum permeability and the vacuum permittivity respectively, E is the electric field, H is the magnetic field, q is the charge of particle, ρ is the charge density, J is the current density, and T is the relativistic kinetic energy of charged

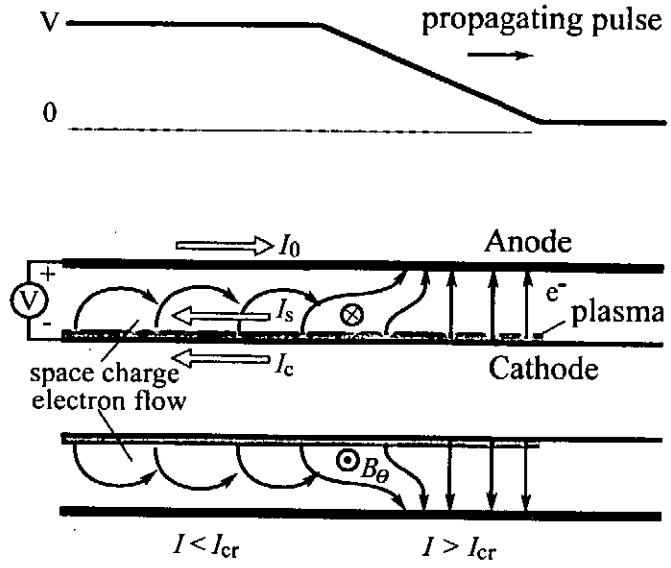

Fig.1 Schematic Diagram of Magnetically Insulated Transmission Line

particles. In other words, the energy per unit length W_L of MITLs is composed of the electric field energy W_E, the magnetic field energy W_H and the kinetic energy of particles W_{KE}, as follows;

$$W_L = W_E + W_H + W_{KE}. \quad (2)$$

As shown in Fig.2, when the transmission line has a geometrical discontinuity, the space charge electron flow suffers disturbance from the variations of fields due to the geometrical change. The change of electron flow influences the electric and magnetic fields, and the disturbed fields exert an effect on the behavior of electron flow. In ordinary transmission lines, the power is carried only by the electromagnetic field (W_E+W_H). Hence the field distribution is determined uniquely by the geometrical shapes of transmission lines and the power flow is analytically predictable. On the other hand, in MITLs with geometrical discontinuity, the space charge electrons can form arbitrary distribution between the gap. Then the non-linearly coupled electrons and fields make the power flow difficult to predict[4]. Some attempts to model these disturbed electron flows based on particle simulations were done in the study of multigap inductive voltage adders with positive polarity[5,6]. However, their solutions can be obtained in a particular situations. In actual MITLs, negative polarity and geometrical changes are often needed in order to connect with the load[7,8], match the line impedances[9-11] and install diagnostic apparatus[12].

The purpose of this paper is; to reveal how the distribution of the space charge electron flow is determined when the electromagnetic energy interacting with charged particles propagates through a geometrical discontinuity; and to show how the disturbance influences the power transportation. In this paper, to understand the behavior of electron flows in coaxial MITLs which increase geometrical impedance toward the downstream, the electromagnetic 2.5D PIC(Particle-in Cell) code MAGIC[13] is used. To discuss the behavior of space charge electrons and the efficiency of the power transport in MITLs, we propose a new analytical model, based on the simulation results.

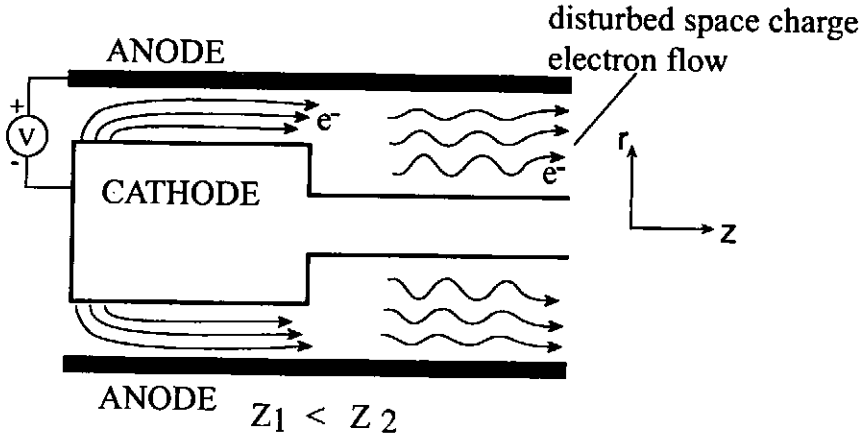

Fig.2 Space Charge Flow through Geometrical Dsicontinuity

2. Particle simulations

2.1 Conditions of calculations

The particle simulations are conducted under the self-limited condition[14]. Geometrical parameters are as follows; the length of the line is 1m, the anode (outer conductor) radius r_a is constant and the cathode radius r_c decreases along the z axis at z=15cm. The cell size is 0.5~1mm in r-direction and 2.5~5mm in z-direction. The time step is 2~3ps, and the number of macro particles is typically 0.5~2million.

The applied electric potential is 2MV at the input-side boundary (z=0). We assume that the source impedance matches to the geometrical line impedance (Z_0) at the input-side. As the space charge layer reduces the impedance, the voltage of 1.5MV is actually applied to the MITL gap. The voltage pulse is injected from the input boundary at t=0, and rises to a peak value at t=0.5ns then keeps the value. Because the space charge layer is fully developed at a few cm from the input-side, we defined the input-power at z=5cm. At the output-side boundary (z=100cm), the electromagnetic wave and particles go out of the calculation area without any reflection. The anode and the cathode are assumed to be ideal conductors and the electron emission is only from the cathode. The threshold value of the local electric field for the emission is 0.23MV/cm, and once electrons are emitted, the space charge limited condition is assumed on the cathode surface. The initial velocity of electrons is set to the thermal velocity (5×10^6m/s).

The total current I_0 is estimated from the magnetic field just inside the anode, the conduction current on the cathode Ic is from inside the cathode surface and the space charge electron current Is is defined as the difference of Ic and I_0. The voltage between the gap V_0 is the integral of the local electric field in the radial direction, and the power P is the product of I_0 and V_0. The definition of the effective line impedance is $Zef = V_0 / I_0$. Mean values of them at t=7.5~8ns are used in the following discussions of the power transport.

2.2 Behavior of space charge electrons

Figure 3 demonstrates the response of space charge electrons to the radial geometrical change. As shown in Fig.3(a) and (b), the boundary of space charge electrons (r_b) gradually spreads toward the anode at the discontinuity with increase of downstream geometrical

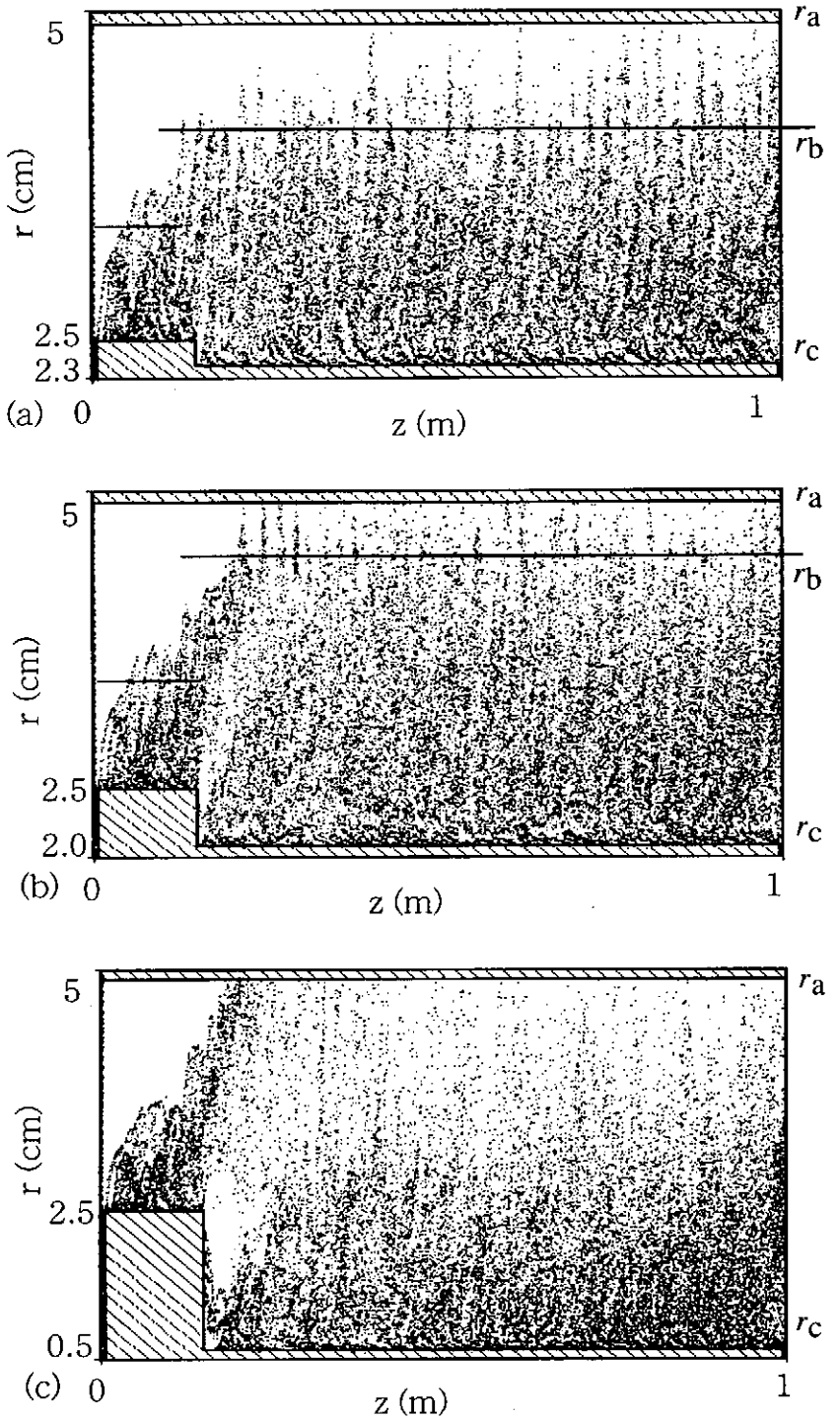

Fig.3 Responce of Space Charge Electrons to Geomerical Disturbance

impedance Z_{0d}. When Z_{0d} exceeds a critical value, a fraction of space charge electrons leaks into the anode conductor (Fig.3(c)). From the point view of transport efficiency, it is important to know how the power flow is affected by the geometrical change. Fig.4 shows the time history of the current and voltage in the case of Fig.3(a). Being different from ordinary transmission lines, the reflection toward the upstream due to the geometrical change is not observed. In spite of the geometrical discontinuity, the total current and the voltage at the downstream are the same values as the upstream. In other words, the effective impedance of downstream line $Zef(=V_0/I_0)$ is adjusted by the behavior of electron cloud.

The behavior of electron flow in the case of Fig.3(a) and (b) is as follows. About a half of total current is carried by the space charge electrons, and the ratio of the space charge current $Is(=I_0-Ic)$ to total current I_0 increases from about 50% at upstream to more than 60% at downstream. Current density profiles of the upstream and downstream side in the case of Fig.3(a) are shown in Fig.5(a) and (b) respectively. These plots indicate that the electron cloud spreads toward the anode and makes uniform profile of current density in the downstream side. Electrons accelerated to near the anode at the geometrical discontinuity carry larger fraction of the current because of the larger drift velocity. As an additional electron emission occurs in the downstream side of the discontinuity, the space charge current Is increases while the conduction current of the cathode Ic decreases. The voltage is adjusted to the same value as the upstream by the counteraction of electron cloud against the reflection of electromagnetic wave. In this way, the disturbed electrons can reduce the effective impedance in the downstream side and adjust it to the same value as the upstream.

Next, consider a case that the electron flow is strongly disturbed at the discontinuity as Fig.3(c). Fig.6 shows time history of the current and voltage in the case of Fig.3(c). In this case, because a fraction of electrons strongly disturbed at the step discontinuity leaks into the anode conductor, the current value at the downstream is smaller than the upstream. Here, total power of electrons restore to the conductor agrees with the power difference between the upstream and the downstream[4]. Therefore, we can conclude that the disturbed electrons result in the power loss when the discontinuity is larger than the critical value. However even in this case, because of the formation of parallel current path at the discontinuity, upstream and downstream line voltages are kept the same value and no reflection is observed in spite of the considerable geometrical impedance change.

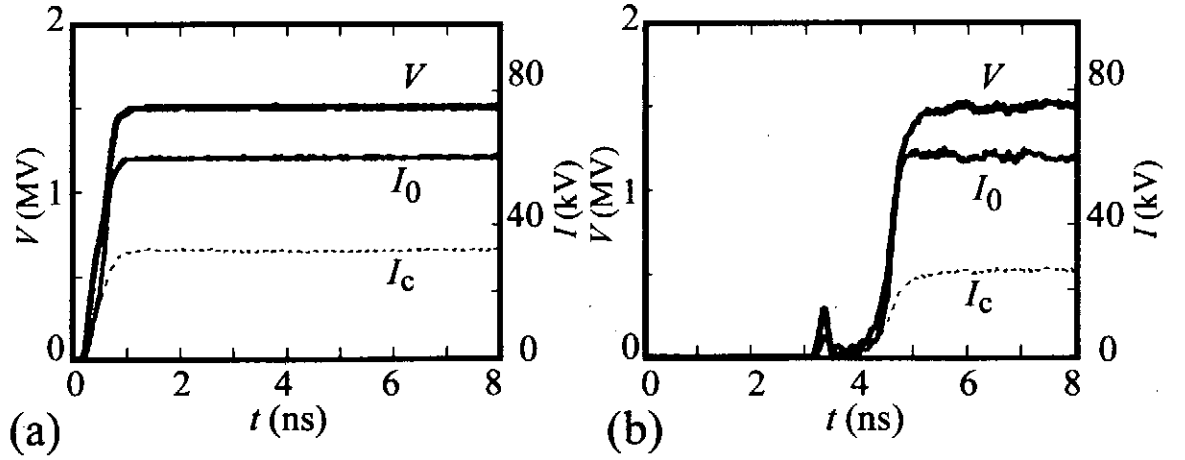

Fig.4 Time History of Current and Voltage in Case of Fig.3(a)

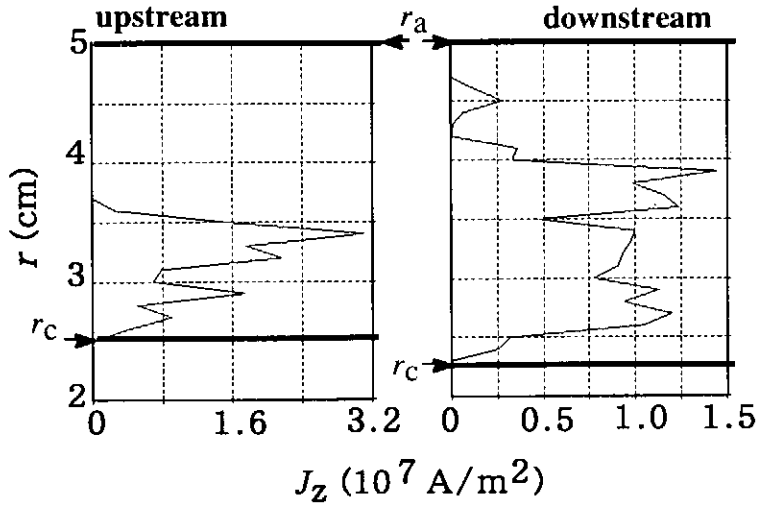

Fig.5 Typical Current Profiles

2.3 Effective impedance of MITL with disturbed electron flow

The effective line impedance Z_{ef} at downstream the discontinuity is surveyed over a wide range of parameters. The relationship between Z_{0d} and Z_{ef} is shown in Fig.7. Here, input voltages (2, 4, 8MV) and geometrical shapes (step and tapered line) are employed as the simulation parameter. As shown, in spite of the parameter change, every plot has the same tendency. It shows that the downstream Z_{ef} keeps constant value (same as the upstream value) when Z_{0d} is less than a critical value, but once it exceeds the critical value, the current loss begins and Z_{ef} increases in proportion to Z_{0d}. Since the voltage between the gap is always constant, the increase of Z_{ef} means the decrease of total current and the power loss.

Thus the behavior of an MITL with a geometrical discontinuity which increases the impedance toward the downstream side can be summarized as follows: the space charge electron flow tends to compensate the influence of the discontinuity by the radial spread of boundary, but when it can not adjust the geometrical disturbance, its boundary touches the anode conductor, and causes a current loss. However, even in the case, the line voltage is regulated at the upstream value.

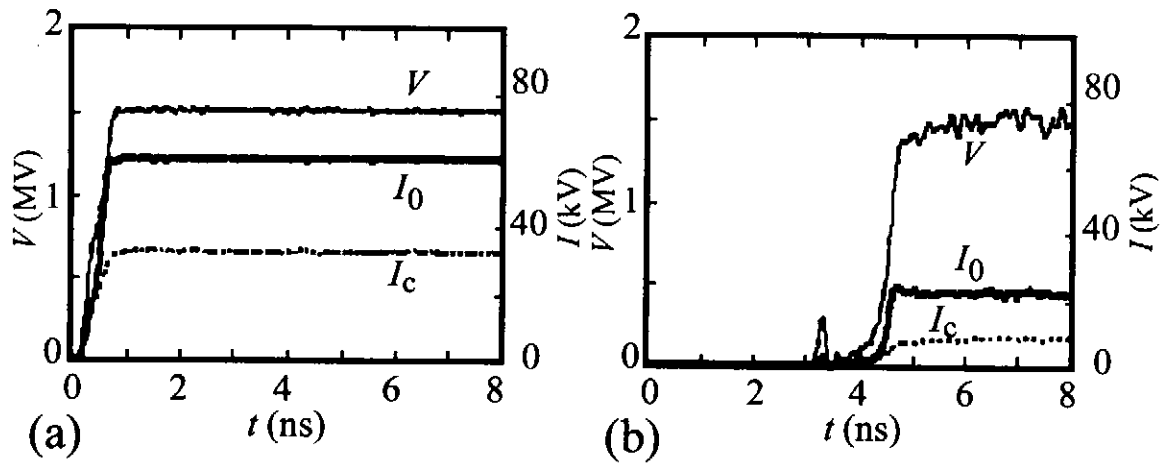

Fig.6 Time History of Current and Voltage in Case of Fig.3(c)

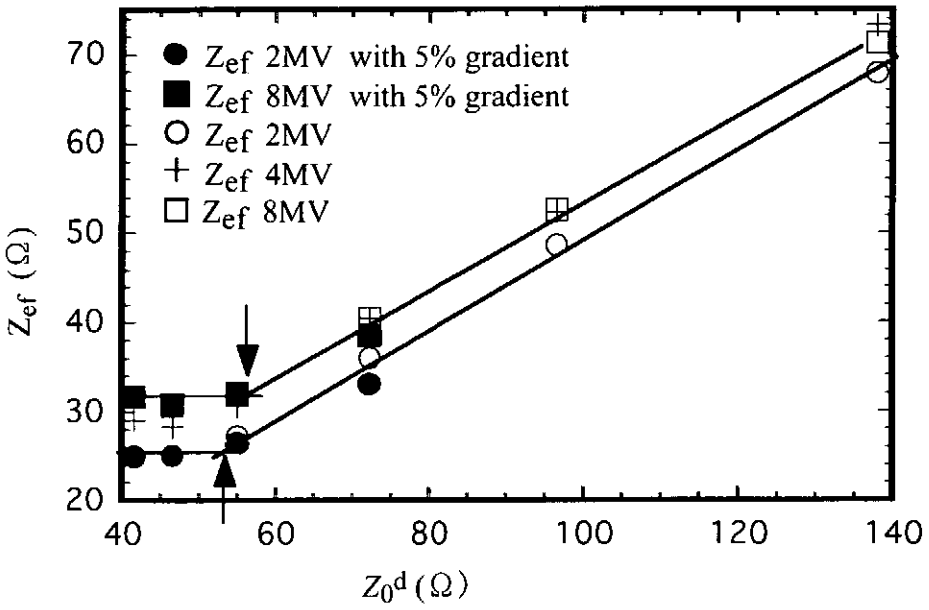

Fig.7 Effective Impedance Z_{ef} vs Geometrical Line Impedance Z_0^d

3. Constant current density model for space charge flow

Although the behaviors of MITLs are essentially nonlinear and it is somewhat inevitable depending on the numerical simulations to predict them, we need an analytical model to get insight into the nature of MITLs. We propose a constant current density laminar flow model to deal with such disturbed electron flows in the downstream side[15]. This model assumes a laminar flow with constant current density profile as shown in Fig.8(a) and is based on the assumption of nonzero canonical momentum and total energy for the space charge electron flow[15]. Here in the near-cathode region of $r_c<r<r_{c1}$, we assumed a truncated current region to fit the simulation results.

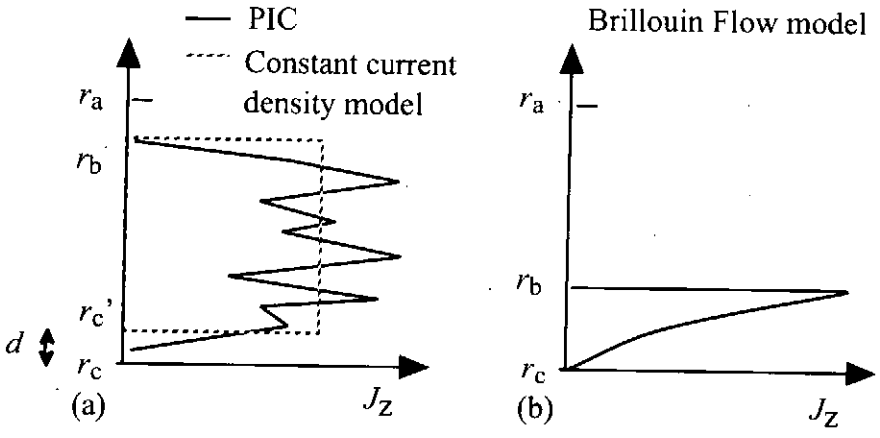

Fig.8 Schematic of Constant Current Density Model

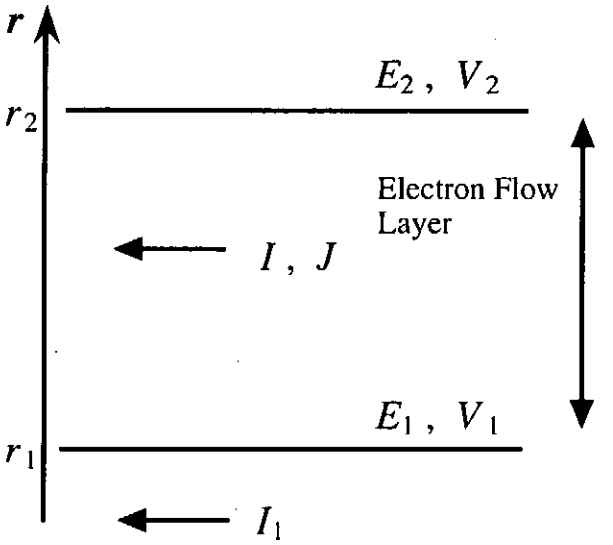

Fig.9 Notation of Electron Flow Model

The current density profile analytically obtained by the relativistic Brillouin flow model[2,17,18] is shown in Fig.8(b). This profile resembles that of the PIC results at upstream the discontinuity (Fig.5), but there is a large difference in the downstream side. Obviously, the Brillouin solution cannot describe the disturbed electron flow at downstream the discontinuity.

Figure 9 shows a schematic diagram of the model. As shown in Fig.9, a sheath region($r_1<r<r_2$) with constant current density is assumed.

The behavior of electrons is described by the equation of motion

$$d\boldsymbol{p}/dt = -e(\boldsymbol{E}+\boldsymbol{v}\times\boldsymbol{B}), \tag{3}$$

where $\boldsymbol{p} = \gamma m_e \boldsymbol{v}$ is the relativistic momentum, and by the stationally Maxwell equations,

$$div\boldsymbol{E} = (\rho / \varepsilon_0), \tag{4}$$

$$rot\boldsymbol{B} = \mu_0 \boldsymbol{J}, \tag{5}$$

$$\boldsymbol{J} = \rho \boldsymbol{v} = \text{const.} \tag{6}$$

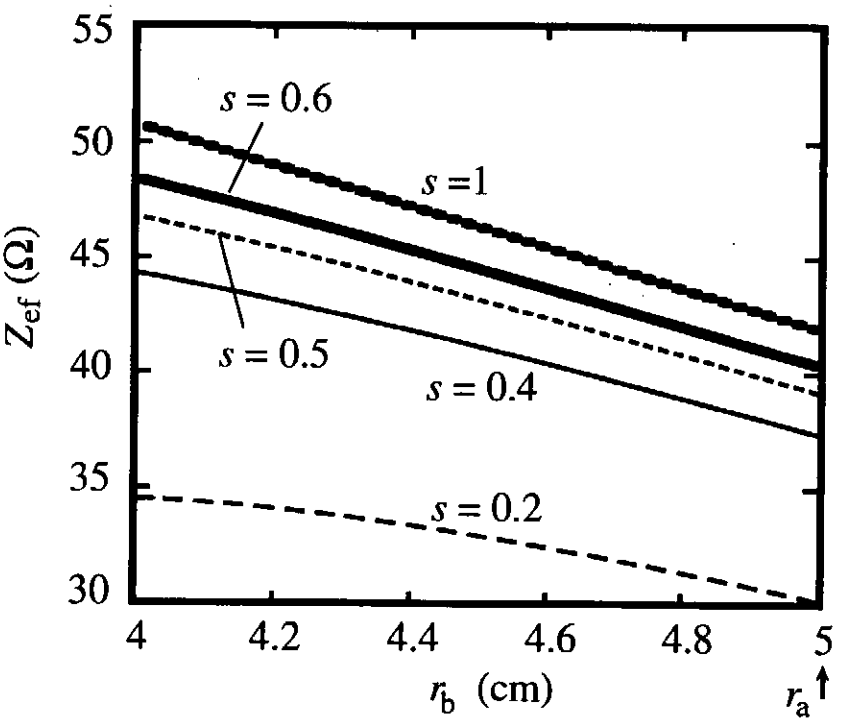

Fig.10 Effect of I_c/I_s and r_b on Effcetive Impedance Z_{ef}

Using steady state condition (dp/dt=0) and the laminar flow approximation, the drift velocity of space charge electrons is given by

$$v_z = (E_r/B\theta). \tag{7}$$

Under the assumption of coaxial geometry, Eqs. (5) and (6) result in

$$B\theta(r) = (\mu_0/2\pi r)(I_c + (r^2-r_c^2)I_s/(r_b^2-r_c^2)) \tag{8}$$

and the solution of E_r is given by,

$$E_r = K[L+r^2+(M/r^2)]^{1/2}, \tag{9}$$

where,

$$K = I/\{2\pi(r_b^2-r_c^2)\}(\mu_0/\varepsilon_0)^{1/2} \tag{10}$$

$$L = 2I_1(r_b^2-r_c^2)/I-2r_1^2 \tag{11}$$

$$M=r_1^2\{4E_1^2\pi^2\varepsilon_0(r_2^2-r_1^2)^2/\mu_0 I^2 - 2(r_2^2-r_1^2)I_1/I + r_1^2\} \tag{12}$$

Eq,(13) says that the solution E_r requires,

$$L + r^2 + (M/r^2) > 0\,. \tag{13}$$

The solution of Er exists when,

$$s > \{(r_a/r_c)^2-1\}^{-1}. \tag{14}$$

From the gap voltage above derived, we can derive the effective impedance Z_{ef} for MITL power flow with constant space charge current density profile.

For example in a case of rc1 rc (d 0) and, Z_{ef} is expressed as

$$Z_{ef} =[4\pi(1+s)]^{-1}(\mu_0/\varepsilon_0)^{1/2}\{(1+2s)^{1/2}(2\ln(r_a/r_b)+1) + (sr_b^2-sr_c^2-r_c^2)/(r_b^2-r_c^2)\ln[(1+s+(1+2s)^{1/2})/s]\}. \tag{15}$$

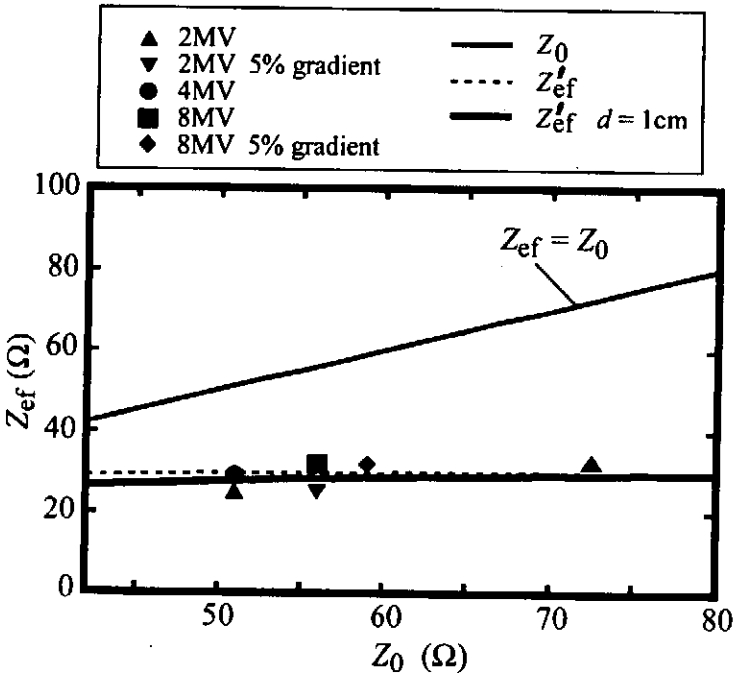

Fig.11 Comparison of Analytically Estimated Effective Impedance with PIC Simulation

Equation (24) indicates that Z_{ef} is sensitive to s; the ratio of space charge current and the boundary of the electron layer (rb). Figure10 shows the effect of s and space charge layer boundary rb on Z_{ef}, when the anode radius r_a=5cm and the cathode radius r_c=2cm (Z_0=55 Ω). For example, the Z_{ef} value decreases about 5 Ω if r_b spreads 1cm toward the anode or the ratio I_c/I_s decreases from 1 to 0.4. The lowest effective impedance Z_{ef}' is given by putting r_b=r_a in Eq.(15) as,

$$Z_{ef}' = 30/(1+s)[(1+2s)^{1/2}+\{s-((r_a/r_b)^2-1)^{1/2}\}\ln((1+s+(1+2s)^{1/2})/s)]. \quad (16)$$

However, in this model, Ic/Is can take arbitrary values. Here, another condition that determines s value is needed. We redefine the condition of Z_{ef}' takes the lowest value as that the electron flow fully spreads toward r direction (r_b=r_a) and its current value(I_s) takes the allowed largest ratio to coduction current (I_c). The latter case corresponds to that s(=I_c/I_s) takes the smallest value. It can be obtained by the condition (21). Consequently, the lowest value Z_{ef}' is derived by substituting r_b=r_a and

$$s = \{(r_a/r_c)^2-1\}^{-1} \quad (17)$$

into (25), as follows;

$$Z_{ef}' = 30\{1-(r_a/r_c)^4\}^{1/2}. \quad (18)$$

Figure 11 shows the Z_{ef}' of the constant current density model (18) and the critical impedance Z_{0c} obtained by the particle simulations. The lowest Z_{ef} of the model Z_{ef}' and the critical impedance Z_{0c} by PIC simulations have good agreement and it indicates Zef adjustment is due to the radial spread toward the anode of the electron flow and increase of Is. This result shows that the limit of the impedance adjustment when Z_0 increases in the downstream side can be predicted by Z_{ef}' derived from the constant current density model. It also indicates that when the downstream geometrical impedance Z_{0d} is large (>40 Ω), Z_{ef}' takes virtually constant value (about 30 Ω). This means that when the upstream effective impedance Z_{ef}^{u} is larger than 30 Ω, the space charge electron compnsates the geometrical discontinuity.

4. Conclusion

In this paper we have discussed the power flow in coaxial MITLs with geometrical discontinuity. In order to understand the behavior of space charge electrons, we simulated MITLs with various operating paremeters using the electromagnetic PIC code MAGIC. Based on the simulation results, we developed a constant current density model for the disturbed space charge flow. From the derived analytical expressions, we can define an effective impedance for the power flow in the MITLs.

For concluding remarks, we can say that for negative polarity MITLs operating at self-limited condition;

1) The space charge electrons tend to compensate the influence of the geometrical discontinuity, by changing their distribution, boundary of the electron cloud, and the ratio of space charge current to conduction current.

2) The electron flow has the Brillouin like profile upstream the discontinuity, however, at the downstream, it moves boundary to the anode and changes current density distribution to a constant profile.
3)This behavior adjusts the downstream impedance of the MITLs at the upstream value upto a critical value.
4) By using analytically estimated effective impedance based on the constant current density model, we can predict the critical value; the limit of efficient power transport through the MITLs.

References

[1] R. B. Miller: *An Introduction to the Physics of Intense Charged Particle Beams,* (Plenum Press, New York, 1982)
[2] M. S. Di Capua: IEEE TRANSACTIONS ON PLASMA SCIENCE, PS-11 No.3 , p.205-215 (1983)
[3] M. Y. Wang: Appl. Phys. Lett. 33(4) p.284 (1978)
[4] K. Hiraoka, M. Nakajima, K. Horioka and M. Shiho: J. Plasma and Fusion Research, Vol.75-5 CD p.57-74 (1999) (in Japanese)
[5] C. W. Mendel, Jr. and S. E. Rosenthal: Phys. Plasmas 2 (4) p.1332-1342 (1995)
[6] B. W. Church and R. N. Sudan: Phys. Plasmas 2 (6) p.1837-1845 (1995)
[7] D. D. Ryutov and R. N. Sudan: *Proc. 10th Int. Conf. High Power Particle Beams,* p.144-149 (1994)
[8] K. Horioka, K. Hiraoka, M. Nakajima and T. Aoki: NIFS-PROC-23 p.118 (1994)
[9] P. Hoppe, W. Bauer, et al.: Proc. 12th Int. Conf. High Power Particle Beams, Vol.1, p.218-221, (1998)
[10]S. E. Rosenthal: IEEE Trans. Plasma Sci. 19 No.5 p.822-830 (1991)
[11]M. G. Mazarakis et.al: Appl. Phys. Lett. 70 No.7 p.832-834 (1997)
[12]J. P. VanDevender: J. Appl. Phys. 50 No.6 p.3928-3934 (1979)
[13]B.Goplen, L. Ludeking, D. Smith and G. Warren: Computer Physics Communications, 87 Nos. 1&2 p.54-86 (1995)
[14]R. I. Lawconnel and J. Neri: Phys. Fluids B2 (3) p.629-639 (1990)
[15]K.Hiraoka, M.Nakajima, M.Shiho and K.Horioka, Jap. J. Appl. Phys., (to be published)
[16]A. V. Gordeev, A. S. Chuvatin and H. Ghalila: Proc. 12th Int. Conf. High Power Particle Beams, Vol.1, pp.189-192, (1998)
[17]J. M. Creedon: J. Appl. Phys. 46 No.7 p.2946-2955 (1975)
[18]M. Y. Wang: Appl. Phys. Lett. 33(4) p.284 (1978)

UNSTABLE BEHAVIOR OF CURRENTS IN EXPLODING WIRE ARRAY

N. Shimomura, M. Nagata, Y. Teramoto* and H. Akiyama*

Department of Electrical and Electronic Engineering, The University of Tokushima,
2-1 Minamijosanjima, Tokushima, 770-8506, Japan
*Department of Electrical and Computer Engineering, Kumamoto University,
2-39-1 Kurokami, Kumamoto, 860-8555, Japan

ABSTRACT

Although considerable investigations have been reported on z-pinches to achieve nuclear fusion, little attention has been given from the point of view of how a wire array consisting of many parallel wires explodes. In this paper, the unstable behavior of a wire array is investigated. The instability occurs by the deviation from the homogeneous current flow through many wires. The expressions discriminating between the stability and the instability are derived. Using the resistivity variation of the wire, the unstable behavior during the explosion of the wires is predicted and the strength of the tendency to an unstable behavior is evaluated. The unstable region on a map of resistivities is independent of the wire number while the strength of the tendency to the unstable behavior depends on the wire number.

I. Introduction

Recently, z-pinches have been expected to achieve power generation by nuclear fusion [1)-4)]. Wire arrays are exclusively used as a z-pinch plasma source. The behavior of the plasma produced from a wire array and the wire explosion have been investigated by numerical analyses and experiments. It has been reported that the initial mass distribution of the plasma has a significant influence on the development of the Rayleigh-Taylor instability [4),5)]. On the other hand, the unstable behavior of parallel two exploding wires has been investigated from the viewpoint of an opening switch [6),7)]. However, little attention has been given to the point of view of how a wire array consisting of numerous parallel wires explodes. When the wires of the array do not explode simultaneously, owing to an unstable behavior, an inhomogeneous mass distribution of the plasma, as well as a deviation of the

current flow, may be yielded.

The discussion of unstable behaviors in two parallel wires is extended to the case of a wire array with n–wires. The instability in the system is determined by the deviation of the current distribution on wires and the expressions discriminating between the stability and the instability are derived. The combination of the expressions and resistivity variation of the wire is used to predict the unstable behavior of parallel exploding wires.

II. Formalization of unstable behavior

A. Model

A wire array system consisting of n–wires with identical dimensions is considered. The equivalent circuit of the system is shown in Fig. 1(a). The currents i_1 to i_n flow through wires having resistances of R_1 to R_n, respectively. Here, in order to estimate the unstable behavior of a single wire on other wires, it is presupposed that the other wires simultaneously explode and therefore have the same resistance. The circuit of Fig. 1(a) is re-drawn like Fig. 1(b) by the adoption of R_0 and i_0 as a package of (n-1)–wires. The inductance in the system is disregarded in order to consider the essential behavior of the wire array.

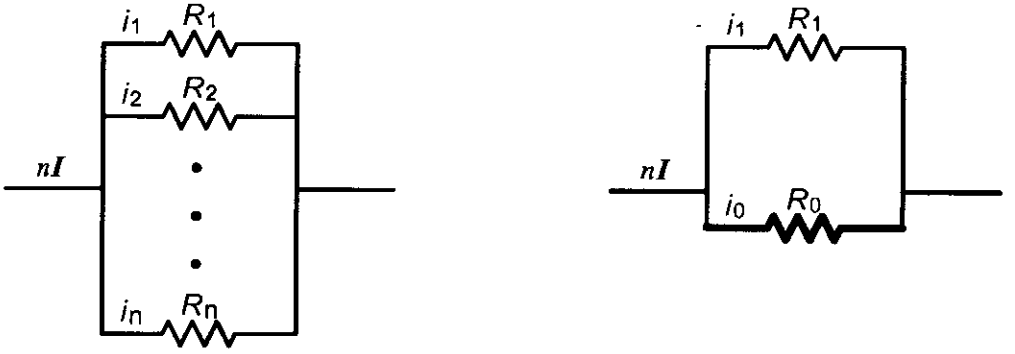

Fig. 1. Circuit model of n-wire array.

B. Discrimination between stability and instability and estimation of the strength of tendency to the unstable behavior

In a two wire system, the advancement of the deviation between currents through two wires showed the instability [6]. A similar method is applied to the n–wire system here. Since the unstable behavior of a wire on others is treated, the current deviation α is defined as

$$\frac{i_1}{i_0/(n-1)} = \alpha = \frac{(n-1)R_0}{R_1}. \tag{1}$$

The equilibrium corresponds to α=1, since the currents on n-1 wires are identical under the

presupposition. The right term of Eq. (1) is obtained by using the resistances of wires instead of currents, because the wires are connected to each other in parallel and the applied voltage is the same. Defining $\beta = \log \alpha$, the unstable condition is represented as

$$\begin{cases} \dfrac{\partial \beta}{\partial t} < 0, & (\text{in the case of } \beta < 0), \\ \dfrac{\partial \beta}{\partial t} > 0, & (\text{in the case of } \beta > 0), \end{cases} \tag{2}$$

by adopting a differential of β. Furthermore, $\partial\beta/\partial t$ is rewritten as following:

$$\begin{aligned} \frac{\partial \beta}{\partial t} &= \frac{1}{R_0}\frac{\partial R_0}{\partial t} - \frac{1}{R_1}\frac{\partial R_1}{\partial t} \\ &= \frac{1}{(n-1)^2}\left(\frac{dR}{dE}\right)_{(n-1)R_1}\left(\frac{R_1}{R_0+R_1}nI\right)^2 - \left(\frac{dR}{dE}\right)_{R_1}\left(\frac{R_0}{R_0+R_1}nI\right)^2 \\ &= \left(\frac{n}{(n-1)R_0+(n-1)R_1}\right)^2\left[{R_1}^2\left(\frac{dR}{dE}\right)_{(n-1)R_0} - \{(n-1)R_0\}^2\left(\frac{dR}{dE}\right)_{R_1}\right]I^2, \end{aligned} \tag{3}$$

where

$$\frac{\partial R_1}{\partial t} = \frac{dR_1}{\partial E_1}{R_1 i_1}^2 = \left(\frac{dR}{dE}\right)_{R_1}{R_1 i_1}^2,$$

$$\frac{\partial R_0}{\partial t} = \frac{dR_0}{\partial E_0}{R_0 i_0}^2 = \frac{1/(n-1)}{n-1}\left(\frac{dR}{dE}\right)_{(n-1)R_0}{R_0 i_0}^2,$$

R and E are the resistance of a general exploding wire and the energy deposited in it, respectively.

To exclude the influence of the wire dimensions and of the magnitude of the current, the parameter γ is introduced. For the case of $\beta < 0$,

$$\gamma = \left(\frac{n}{(n-1)\rho_0+(n-1)\rho_1}\right)^2\left[{\rho_1}^2\left(\frac{d\rho}{dE}\right)_{(n-1)\rho_0} - \{(n-1)\rho_0\}^2\left(\frac{d\rho}{dE}\right)_{\rho_1}\right], \tag{4a}$$

for the case of $\beta > 0$,

$$\gamma = \left(\frac{n}{(n-1)\rho_0+(n-1)\rho_1}\right)^2\left[\{(n-1)\rho_0\}^2\left(\frac{d\rho}{dE}\right)_{\rho_1} - {\rho_1}^2\left(\frac{d\rho}{dE}\right)_{(n-1)\rho_0}\right], \tag{4b}$$

where ρ is the resistivity of the wires and it's subfix has the same notation as that of the resistance. The positive and negative values of γ mean stability and instability, respectively. Furthermore, the absolute value shows the strength of the tendency to the stable and the

unstable behavior.

III. Prediction of unstable behavior and discussions

Eqs. (4a) and (4b) can show whether the wire array system is stable or unstable. The variation in the resistivity was obtained experimentally and was shown in Fig. 7 of reference [6]. The wire was made of copper and exploded in water. The values of ρ and $d\rho/dE$ are substituted for those in Eqs. (4a) and (4b), and the contour maps of γ are obtained by the sweep of ρ_1 and ρ_0, as shown in Fig. 2 (a) and (b). The abscissa and the ordinate of Fig. 2 show the resistivity of one wire and the normalized resistivity of n-1 wires. Figs. 2 (a) and (b) are for the case of $n = 2$ and $n = 10$, respectively. Since the positive values of γ are plotted as zero, the hatched areas with negative γ mean unstable regions and the depth represents the strength of the tendency to the unstable behavior. The exploding state of the wire array moves on the diagonal from the left-down corner to the right-up corner, when all wires explode simultaneously, that is, an equilibrium is achieved. When the trace point exists in the unstable region, it deviates furthermore from the diagonal. On the contrary, when it exists in the stable region, it approaches to the diagonal. When the rapid increase of $d\rho/dE$ occurs, the unstable regions appear. A large $d\rho/dE$ means that a small deposited energy by small current produces a larger resistivity variation. Even though the energy deposited in the wire is the same, $d\rho/dE$ is not constant owing to the complicated exploding phases. Since the unstable regions lie near the diagonal, where the state on the diagonal is neither stable nor unstable, it is no wonder that the wire array system will become unstable even when all wires are exploding simultaneously.

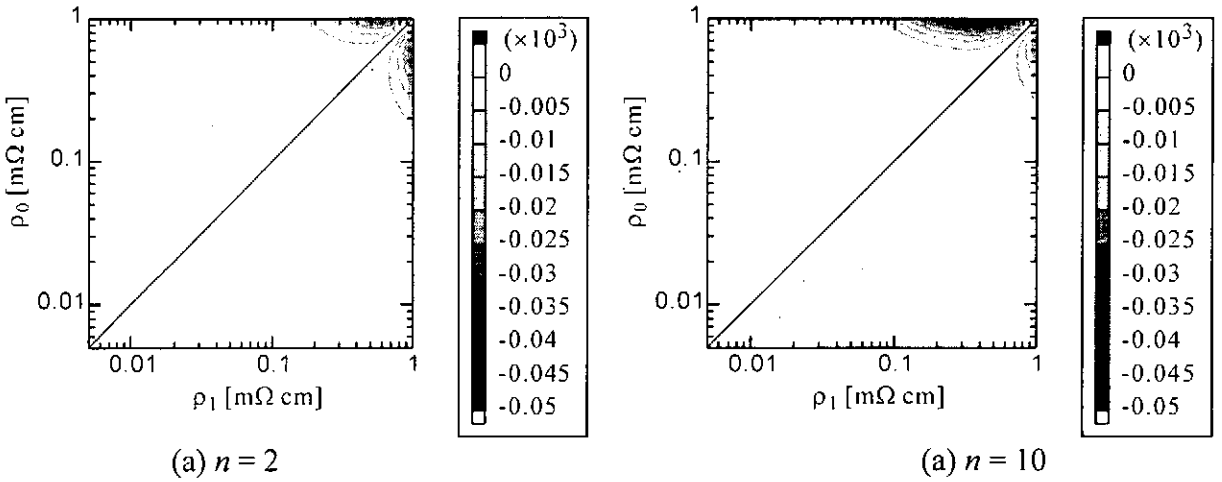

Fig. 2. The contour maps of the instability in exploding; the unstable strength is represented as minus magnitude and stability is represented by zero (white-painted).

It should be noted that the distributions of the unstable regions on the map are independent of the wire number n while the strength of the tendency to the unstable behavior is dependent on n. Eqs. (4a) and (4b) are rewritten as a product of two functions.

$$\gamma = f_m(n, \rho_1, (n-1)\rho_0) \cdot f_d(\rho_1, (n-1)\rho_0). \tag{5}$$

Here,

$$f_m(n, \rho_1, (n-1)\rho_0) = \left(\frac{n}{(n-1)\rho_0 + (n-1)\rho_1} \right)^2,$$

$$f_d(\rho_1, (n-1)\rho_0) = \pm \rho_1^2 \left(\frac{d\rho}{dE} \right)_{(n-1)\rho_0} \mp \{(n-1)\rho_0\}^2 \left(\frac{d\rho}{dE} \right)_{\rho_1}.$$

The function f_m depends on the wire number n but its value is always positive. On the other hand, the function f_d is independent of n and its sign is not restricted. Therefore, f_m and f_d can be regarded as the functions that give the strength of the tendency to the unstable and the stable behavior and the discrimination between the instability and the stability, respectively. Accordingly, the distribution of the unstable regions does not change with the wire number and is symmetrical about the diagonal.

In the case of $n = 2$, the distribution of γ is symmetrical about the diagonal, since a bundle of n-1 wires is just one wire. In the case of $n = 10$, the strength of the tendency to the unstable behavior on the left hand side of the diagonal is larger than that on the right hand side of it, although it is not clear on Fig. 2(b) because of the rough separation of the depth of the gray scale. Also, the same tendency occurs for the stable behavior as known from Eq.(5), although positive value of γ is not indicated in the Fig. 2(b). The distribution of γ is no longer symmetrical about the diagonal. Furthermore, the strength of the tendency to the unstable and the stable behavior increases with increasing the wire number. The enhancement of the strength of the tendency to the unstable behavior at the left hand side of the diagonal implies that one wire explodes later than the others and the current concentrates into the wire. Since it is a probabilistic phenomenon, all systems do not behave like this and this situation is, so to speak, more prevalent.

Tungsten wires have been used frequently as a z-pinch plasma source. Although the unstable behavior in the wire array is predicted according to the resistivity variation of a copper wire, the behavior of the wire arrays in various materials seems unstable. This is because the rate of the resistivity variation is not constant. The phenomena described in this paper occur as long as the current per unit cross section of the wire is the same value, even though the cross section of the wire is changed.

IV. Summary

The unstable phenomena in the *n*-wire array system were discussed by extension of two wire system. The expressions for the discrimination between the instability and the stability were derived, and then the contour maps expressing the strength of the tendency to the unstable behavior were obtained by adopting the resistivity variation of a copper wire. Since the exploding process of the wire array must travel the unstable regions, it is inevitable that the system behaves unstably more or less. While the distribution of the unstable regions on the map is independent of the number of the wires, the strength of the tendency to the unstable behavior depends on the number of the wires. The strength of the tendency to the unstable behavior is enhanced with the increase of the number of wires. Frequent observations of the current concentration into one wire are predicted. These phenomena were frequently observed in experiments. The high uniformity of the wire arrays might help the suppression of the unstable behavior.

Acknowledgement

The authors would like to thank Prof. Reuben Hackam for helpful discussions and valuable suggestions.

References

1) M. K. Matzen, "Z pinches as intense x-ray sources for high-energy density physics applications", *Phys. Plasmas*, **4**, 1519-1527 (1997).
2) J. H. Brownell, R. L. Bowers, K. D. McLenithan, and D. L. Peterson, "Radiation environments produced by plasma z-pinch stagnation on central targets", *Phys. Plasmas*, **5**, 2071-2080 (1998).
3) R. B. Spielman, C. Deeney, et al., "Tungsten wire-array Z-pinch experiments at 200 TW and 2 MJ", *Phys. Plasmas*, **5**, 2105-2111 (1998).
4) T. W. L. Sanford, R. C. Mock, R. B. Spielman, M. G. Haines, J. P. Chittenden, K. G. Whitney, J. P. Apruzese, D. L. Peterson, J. B. Greenly, D. B. Sinars, D. B. Reisman, and D. Mosher, *Phys. Plasmas*, **6**, 2030-2038 (1999).
5) I. V. Lisitsyn, S. Katsuki, and H. Akiyama, "Two-dimensional implosion of liners", *Phys. Plasmas*, **6**, 1389-1292 (1999).
6) N. Shimomura, M. Nagata, C. Grabowski, and H. Akiyama, "Mechanism of Unstable Behavior of Parallel Fuses as an Opening Switch", *IEEE Transactions on Plasma Science*, **23**, 860-864 (1995).
7) N. Shimomura, M. Nagata, C. Grabowski, K. Murayama, and H. Akiyama, "Effects of Wire-Shape on Unstable Behavior of Parallel Fuses", *IEEE Transactions on Plasma Science*, **24**, 1192-1193 (1996).

TEMPORAL OBSERVATION OF GAS-PUFF Z-PINCH PLASMAS BY USING LASER INTERFEROMETER

K. Murayama, T. Nishi†, S. Katsuki†, H. Akiyama†

Yatsushiro National College of Technology,
Hirayamashinmachi 2627, Yatsushiro, 866-8501, Japan
† *Department of Electrical and Computer Engineering, Kumamoto University*
Kurokami 2-39-1, Kumamoto, 860-8555, Japan

ABSTRACT

Spatial distribution of the incident gas significantly influences on the pinch process in gas-puff z pinch schemes. This paper shows the dependence of the plasma formation on the distribution of the gas puffed into the discharge region. Temporary and spatially resolved gas density between the z-pinch electrodes was measured by using a high-sensitive multi-channel laser interferometer. Also plasma density distribution was measured by using a pulsed laser interferometer. The gas, which was puffed from the anode nozzle toward the center axis, quickly spread out to the radial direction and formed a conical shape. This resulted in the significant gas density gradient along z-axis. The pulsed laser interferometer showed a discharge took place at the contour of the gas distribution. The pinch process was significantly influenced by the initial gas distribution. In addition, the double layer structure was observed before implosion.

I. Introduction

Intense soft x-rays radiated from z-pinch devices has a potential to be used for several industrial applications, for example lithography in the semiconductor device processing[1], x-ray microscopy etc. since it is quite simple, small and cheap in comparison with the synchrotron obituary radiation (SOR). Above all, gas-puff z-pinch scheme[2-4] has an advantage with respect to repetitive operation. Almost applications request the reproducibility of x-ray radiation in terms of photon energy, intensity and position where to radiate[5, 6]. Spatial distribution of the incident gas is one of the significant factors to influence on the implosion process in gas-puff z pinch schemes. Therefore, the gas-puff valve and electrodes have to be optimized to produce the homogeneous plasma columns along the z-axis.

The purpose of the paper is to measure the gas density distribution and to understand the pinch process dependent on the gas distribution before the discharge. A high-sensitive laser interferometer [7-9] was employed to measure the temporary and spatially resolved gas density between the z-pinch electrodes. In addition, the time evolution of the z pinch plasma columns was investigated by using a pulsed laser interferometer. Two kinds of cathodes, a brass solid and a stainless steel mesh, were used as examples of the measurement.

II. Experimental setups and procedure

A. Z-pinch device

Z-pinch device consists of a columnar anode that is equipped with a circular nozzle for gas-puff and a cathode that is faced to the anode. The inner and outer diameters of the nozzle are 4 and 8 mm,

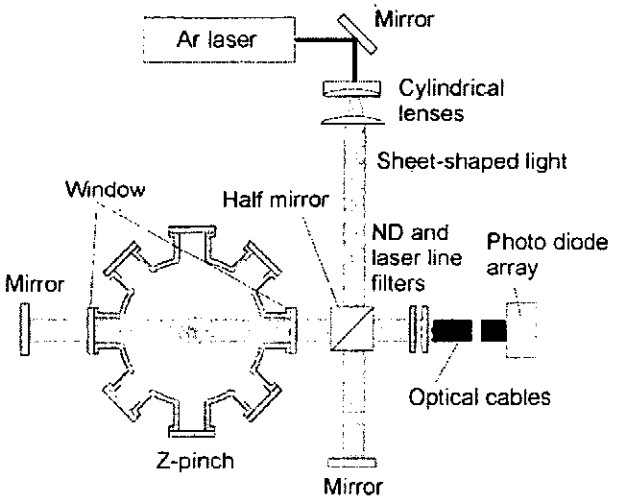

Figure 1. Schematic diagaram of the high-sensitive multi-channnel laser interfermeter for gas density measurement.

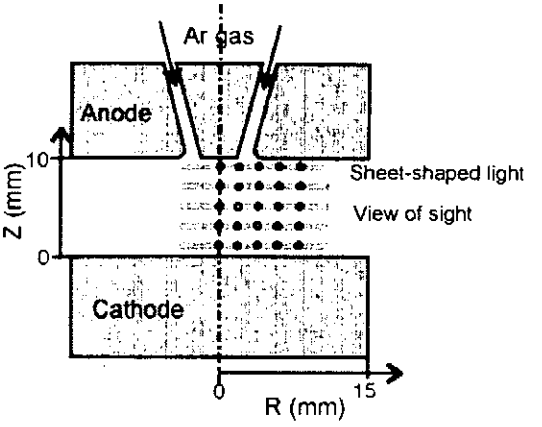

Figure 2. View of the high-sensitive laser interferometer.

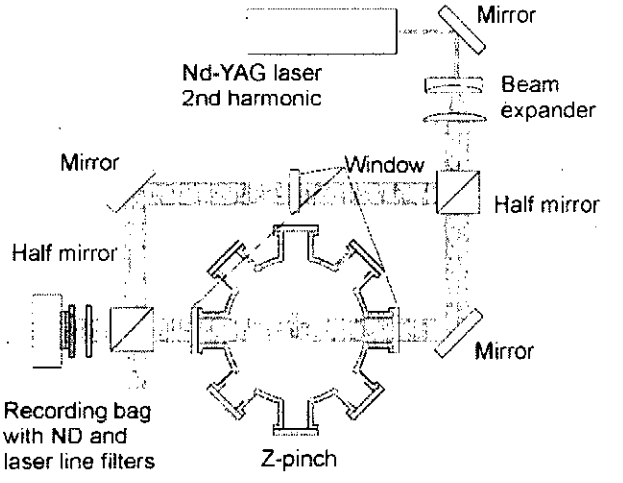

Figure 3. Schematic diagram of the pulsed laser interferometer for plasma density measurement.

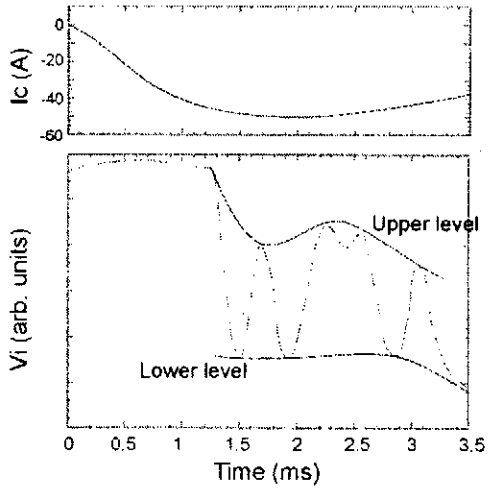

Figure 4. The driving current for the gas-puff valve and the interferometer signal caused by both the puffed gas and the mechanical vibration.

respectively. The nozzle is slightly directed to the z-axis to be expected to suppress the diffusion in the radial direction. Two kinds of cathodes, a solid brass and a stainless steel mesh, were used in this measurement. Edge of the solid cathode is inclined. The transparency of the mesh cathode is 81%. Ar gas is puffed from the anode nozzle about 1.3 ms after the gas-puff actuator starts operating.

The plasma current is provided from a 6 μF capacitor, which is charged up to 25 kV. The current starts flowing with triggering a field distortion gap switch and reaches 170 kA at 1.3 μs (quarter period) after the beginning of the current.

B. Gas density measurement

Since the interaction between the laser and an usual neutral gas in low pressure is small, the interference fringe shifts due to the gas expected to be less than a half period. A high sensitive laser

interferometer has been developed by several researchers who involve the plasma opening switch (POS) studies [4,5,6]. The interferometer in this experiment was extended their scheme to multi-channel acquisition system. Figure 1 shows the schematic arrangement of the laser interferometer. The coherent light from Ar laser (NEC, 488 nm, 300 mJ) was formed into a thin sheet-shaped profile by using two cylindrical lenses and goes through the space between electrodes. The sheet-shaped interference light is guided to a shield room by using optical cables and detected by using a five-channels PIN photo diode array. This enables simultaneous acquisition of the radial density distributions. This technique can be extended to two-dimensional measurement if you afford the number of acquisition channels and the laser power. Figure 2 shows the view of sight for the interferometer between the electrodes. The density was scanned along the z-axis by shifting the sheet-shaped light.

C. Plasma density measurement

Figure 3 shows the schematic arrangement of the pulsed laser interferometer. Second harmonic wave (532 nm) of the Nd-YAG laser (Continuum, Surelite-II, 600 mJ) was used. The interference image was recorded on instant films after passing through a neutral density (ND) and a laser line filter. A window was inserted in the reference arm of the interferometer to improve the contrast in the interference images.

III. Experimental results and discussions

A. Gas density measurement

Figure 4 shows typical waveforms of the current provided to the gas-puff valve and of the interference signal at the cathode surface in the case of the solid brass cathode. The sudden drop on the interference signal indicates the Ar gas coming out of the nozzle. Appearance of the gas is delayed 1.3 ms after the gas-puff actuator starts operating. The line density of the gas gradually increases until 2.4 ms and decays out after that. The interference signal oscillates 1.1 period (2.2π), which corresponds to the line density of 3×10^{18} cm^{-2}. However, the practical x-ray generation experiment needs a delay time about 1.5 ms, where the density is much lower. The signal contains contributions not only from the gas but also from the mechanical vibrations of the optical system. It is difficult to completely get rid of the vibration. The mechanical vibrations of the optics cause the

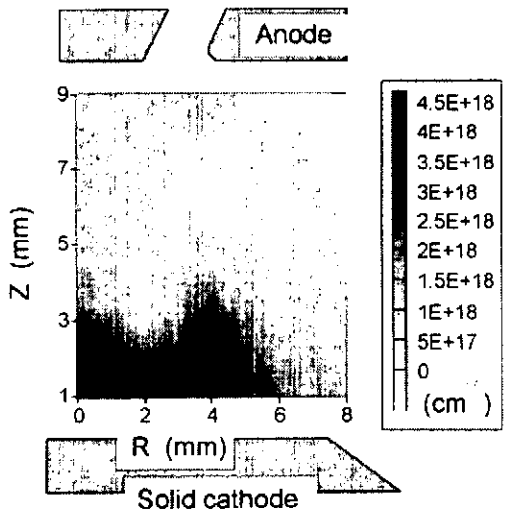

Figure 5. Ar gas density distribution at 1.4 ms in the case of using the stainless steel mesh cathode. The numbers beside the color bar indicate the line-integrated density in cm^{-2}.

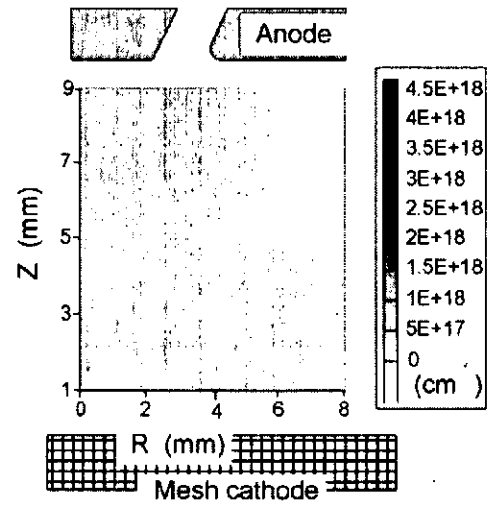

Figure 6. Ar gas density distribution at 1.4 ms in the case of using the solid brass cathode. The numbers beside the color bar indicate the line-integrated density in cm^{-2}.

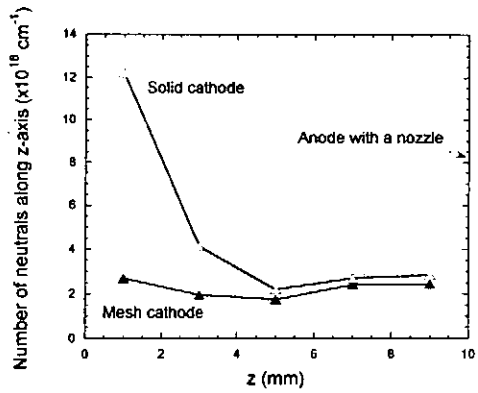

Figure 7. The number of Ar neutrals per unit length along z-axis. These were obtained by integrating the density in Fig. 6 along the radial directions.

variation in the amplitude of oscillations as shown in Fig. 4. Typical frequency of the vibrations is 1 kHz that is not slow enough to neglect. The upper and lower level curves as shown in Fig. 4 are obtained by connecting the upper and lower tips of the oscillation, respectively. The line-integrated gas density can be obtained by conducting the geometrical calculations using these two curves and the interference signal.

Figures 5 and 6 show the gas density distributions between electrodes in the cases of using solid brass and stainless mesh cathodes, respectively. Both were at 1.4 ms after gas-puff actuator was triggered. Figs. 5 and 6 shows the gas density near the nozzle on the anode is high. In the case of using the solid cathode the gas is stagnated near the cathode. The stagnation was reduced by using the mesh cathode, but still exists. Figure 7 shows the number of Ar neutrals per unit length along z-axis in two cases. The curves in Fig. 7 were obtained by integrating the density in Fig. 6 along the radial directions. The mesh cathode helps distribute the gas along z-axis more uniformly. However. the uniformity is still 30%.

B. Plasma density measurement

Since the gas distribution in the case of the solid cathode is too complicated to investigate and not adequate for our purpose, only the mesh cathode was used here. Figure 8 shows the view of the pulsed laser interferometer. A half area around the electrodes is well covered by the stripe due to the interference. A series of images in Fig. 9 shows the interference images at different times. Each

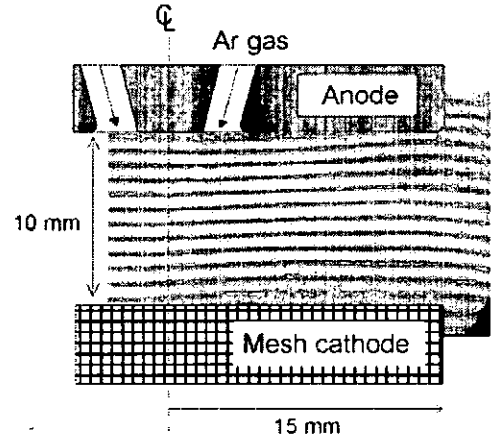

Figure 8. View of the pulsed interferometer.

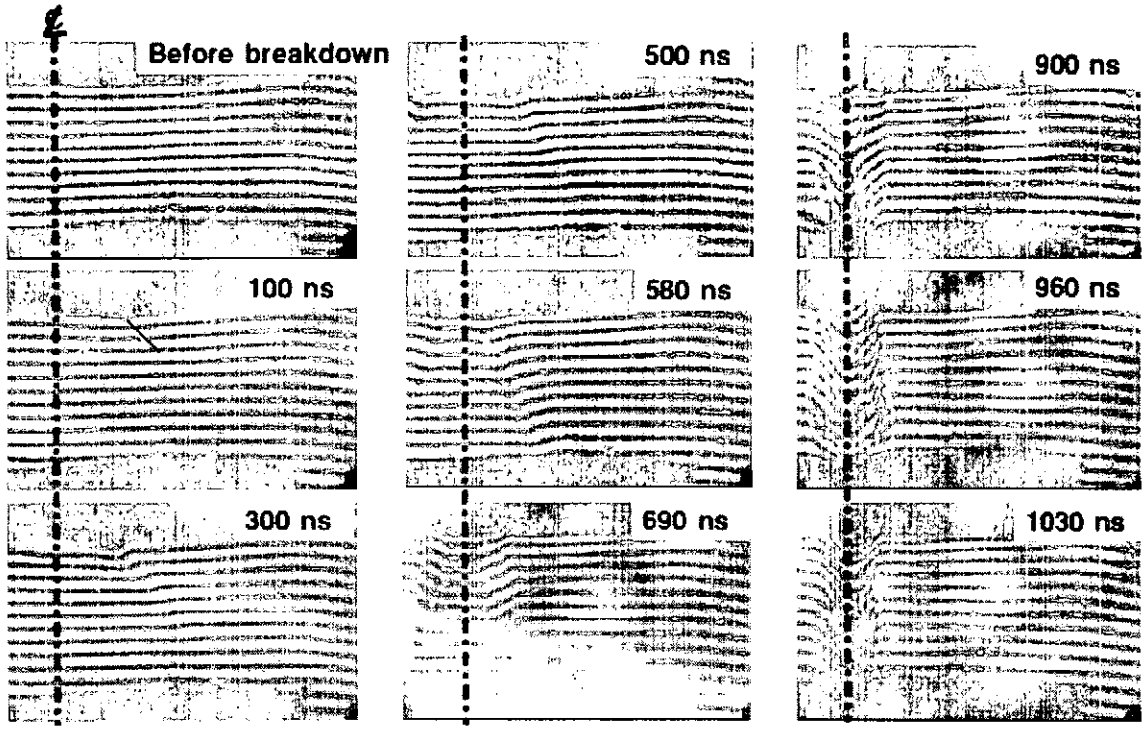

Figure 9. Time evolution of z-pinch plasma column. Each image was obtained in different shot. The number in each image show the time after the current starts to flow.

image was obtained in different shot. The first image shows the scene just before the plasma formation. Since the gas-puff valve had opened at 1.5 ms before the time of the scene, the gas was expected to exist in the scene. However, the sensitivity of the interferometer is not high enough to detect the gas density. The stripe around the nozzle is slightly distorted in the image at 100 ns. The distortion indicates the discharge occurring at slightly outer the nozzle position on the anode side. The image in 300 ns shows more clearly. The discharge was shaped conical, which corresponded to the contour shape of gas density distribution. In addition, the plasma was localized on the edge, where the current flow through. The images from 300 to 900 ns show the clearly show the pinch process. The behavior of the current layer until 1 ms was reproducible in this experiment. The radius of the plasma column near the anode does not change so much while that near the cathode is dynamically reduced, despite the current layer with less radius receives more magnetic force to move inward. This is due to the gas distribution along z-axis, which is shown in Fig. 7. The higher gas density near the nozzle might sustain the plasma radius until 900 ns. Finally the plasma radius along z-axis became almost uniform. Double layer structure came out around 600 ns, and inner layer moved faster than outer layer. After the inner layer meets at the z-axis, something complex started expanding. In this experiment, the instability of the outer layer always started growing after meeting the inner structure.

VI. Conclusions

Measurement of the gas and the plasma density were conducted by using a high-sensitivity and a pulsed laser interferometer, respectively. Incident gas spreads away quickly and its distribution forms a conical shape. Plasma formation occurs at the edge of the gas distribution. The pinch process is influenced by gas density distribution along z-axis.

Only one feature of anode nozzle was presented in this paper. A different shape of nozzle were designed and now being tested.

REFERENCES

1) E. W. Becker, W. Ehrfeld, P. Hagmann, A. Maner and D. Munchmeyer: Microelectron. Eng., 4 (1986) 35.
2) M. Bàdaye, R. Stempork and R. P. Gupta: Rev. Sci. Instrum., 61 (1990) 1457.
3) J. Du, T. Ohata, K. Shimoda and K. Hirano: Jpn. J. Appl. Phys., 64 (1995) 4185.
4) K. Takasugi, H. Suzuki, K. Moriyama and T. Miyamoto: Jpn. J. Appl. Phys., 35 (1996) 4051.
5) I. Okada, Y. Saitoh, S. Itabashi and H Yoshihara: J. Vac. Sci. & Technol., B4 (1986) 243.
6) K. Murayama, T. Shinkai, S. Katsuki and H. Akiyama: Jpn. J. Appl. Phys., 37 (1998) 2676
7) B.V. Weber, S.F. Fulghum: Rev. Sci. Instrum., 68 (1997) 1227.
8) B.V. Weber, D.D. Hinshelwood: Rev. Sci. Instrum., 63 (1992) 5199
9) I. V. Lisitsyn, S. Kohno, S. Katsuki and H. Akiyama: Rev. Sci. Instrum., 69 (1998) 1584.

MEASUREMENT OF SOFT X-RAYS RANGED IN WATER WINDOW REGION GENERATED WITH GAS-PUFF Z-PINCH PLASMA

H. Maeda, K. Shimoda and M. Sato

Department of Electronic Engineering, Gunma University,
1-5-1 Tenjin-cho, Kiryu, 376-8515, Japan

ABSTRACT

The soft X-rays ranged from 2.33 to 4.37 nm are interested in an application for the X-ray microscopy. In order to investigate the soft X-rays ranged in these wavelengths, we newly constructed a small gas-puff Z-pinch device, and investigated the characteristics of it. The experiments were performed with silicon nitride membranes, which were passed through the soft X-rays ranged in these wavelengths.

I. Introduction

The soft X-rays ranged from 2.33 to 4.37 nm (so-called water window) are interested in an application for the X-ray microscopy[1]. Since the soft X-rays ranged in these wavelengths are not absorbed by oxygen and are absorbed by carbon, those can be used to observe living cells. The X-rays are usually generated with SOR (Synchrotron Orbital Radiation) and laser plasma generation[2], but these methods have problems that those require a large-scale equipment, and those costs are very high. Gas-puff Z-pinch devices are also investigated as the soft X-ray sources of these wavelengths[3], because the devices have simple structures and those costs are relatively low.

In the investigation of the soft X- rays ranged in the water window region, choosing of filters is very important, but it is also very difficult problem. Although thin beryllium foils are usually used as filters in the experiments of Z-pinch plasma, the thin beryllium foils are not able to pass through the X-rays ranged in the water window region. Due to its lightness beryllium is chosen as the filter, but more light or thin material is required in these wavelengths. Silicon nitride membranes have been utilized in study of the X-ray microscopy with laser plasma generation[2]. The membrane is expensive, poor in strength and transparent for visible light, but its transmission rates are several tens of percents in these wavelengths.

In order to investigate the soft X-rays ranged in the water window region, we newly constructed a small gas-puff Z-pinch device, and investigated the characteristics of it. A PIN diode and a grazing incident spectrometer were attached to the device. In front of these measurement tools, the silicon nitride membranes were located as the filters. Since alignment of the grazing incident spectrometer is not completed, spectra have not been obtained. The results of preliminary experiments are presented in this paper.

II. Experimental Setup

Figures 1 show the schematic drawings of the experimental setup. A diode configuration and an external circuit are shown in Fig. 1 (a). The maximum voltage and the maximum stored energy of the device are 30 kV and 5.4 kJ, respectively. In usual

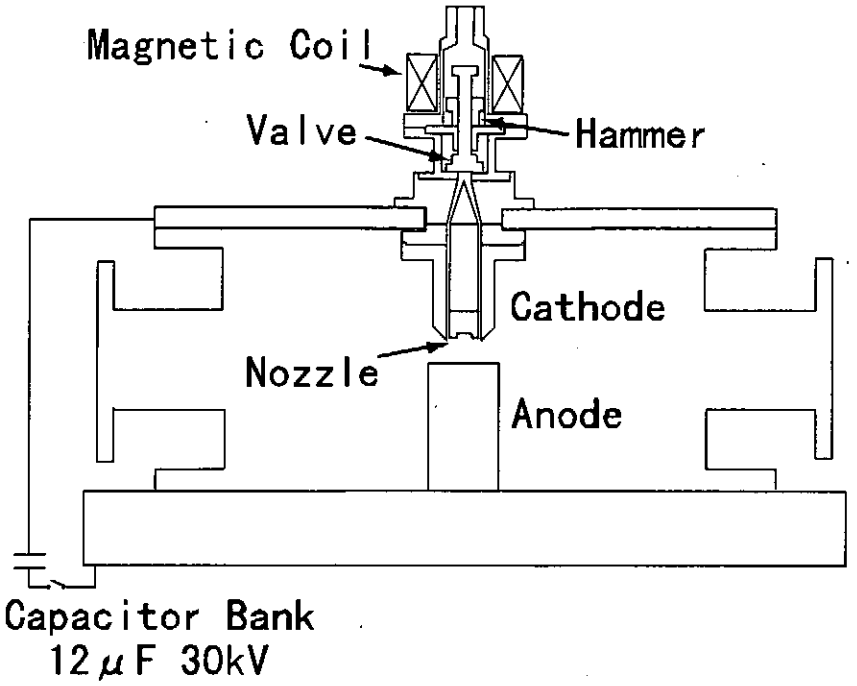

(a)

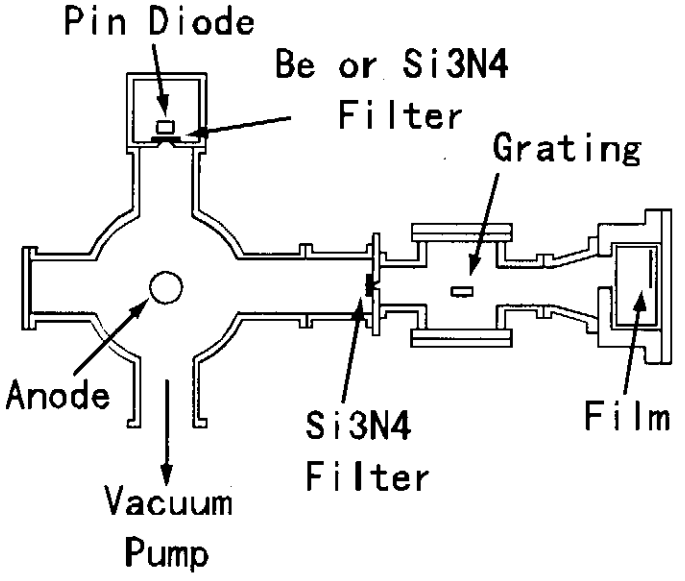

(b)

Fig. 1 The schematic drawings of experimental setup; diode configuration (a), location of measurement tools (b).

experiments, the device is used with the charged voltage of 19 kV, and a current reaches to about 250 kA by 1.4 microseconds from initiation of discharge. Working gas was puffed through a nozzle of which diameter was 20 mm, and a gap length was set at 14 mm. Gases of argon, neon and nitrogen were used as working gases. Argon and neon were used to verify the operation of the device. Nitrogen was used to generate a soft X-rays ranged in the

water window region. From Ref. 4 the radiation generated by nitrogen ranges in the water window region.

In the experiments, a PIN diode and a grazing incident spectrometer were located as shown in Fig. 1 (b). The PIN diode was used to detect the soft X-rays, and appearance of its signal also suggested pinching of the plasma. The beryllium foil of which thickness was 25 micrometers was usually set in front of the PIN diode as a filter. However silicon nitride membranes was required in the case of nitrogen in order to detect the soft X-rays ranged in

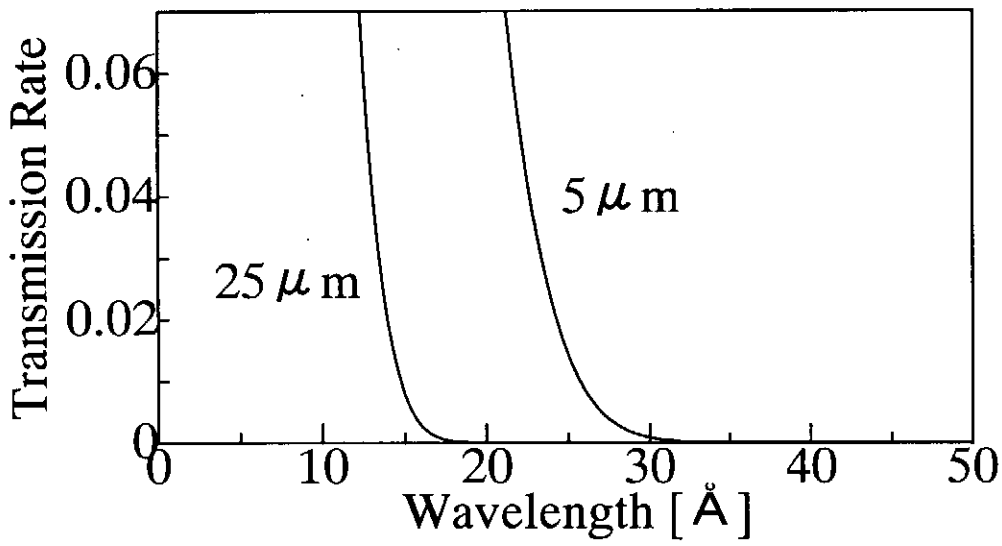

(a)

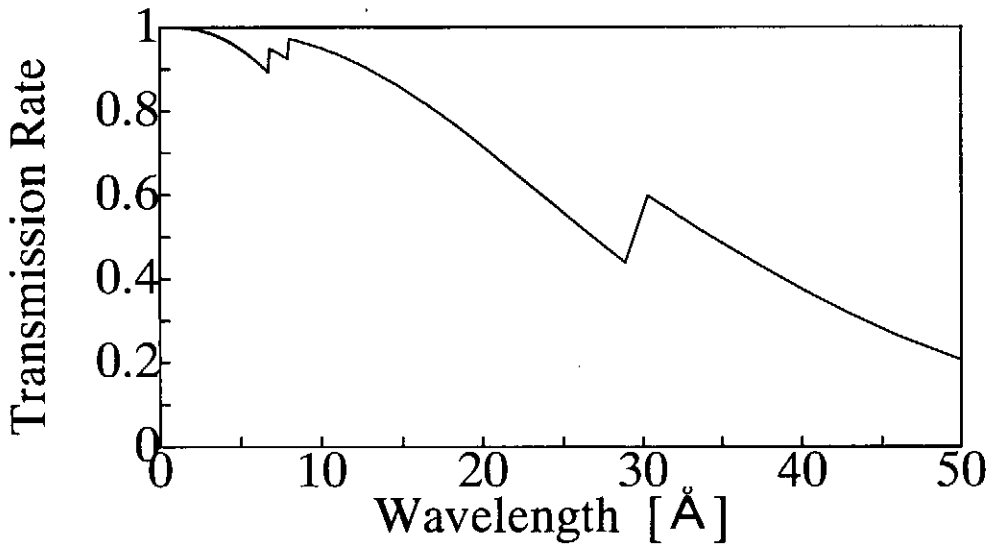

(b)

Fig. 2 Transmission rates in the function of the soft X-rays;
the beryllium foils (a), the silicon nitride membrane (b).

the water window region[2]. The thickness of the silicon nitride membranes was 0.1 micrometers. The membranes were also coated with aluminum of which thickness was 0.05 micrometers to prevent incidence of visible lights. The silicon nitride membrane was made on the part of the silicon substrate, and the geometry of it was a square. The length of a bit of the square was approximately 1 mm. Figures 2 show the transmission rates of the filters for the soft X-rays. As shown in Fig. 2 (a), the soft X-rays ranged in the water window region are not able to pass through the beryllium foil of which thickness is 25 micrometers. In the case of the beryllium foil of which thickness is 5 micrometers, the transmission rates are several percents under 3 nm. Figure 2 (b) shows the transmission rates in the case of the silicon nitride membrane. By using the membrane, the transmission rates of the soft X-rays ranged in the water window region are obtained by several tens of percents. Since the membrane does not have a cut-off for shorter wavelength of the X-rays, measurement with a spectrometer is required to verify generating of the soft X-rays ranged in the water window region.

The grazing incident spectrometer was constructed and adapted to the device. The spectrometer has a grating coated with gold, and it is able to analyze the X-rays of which wavelengths are from 2 nm to 5 nm. The grating had 2400 grooves per millimeter, and the grooves were ruled by a varied space. As a result the grating has a focusing property, and has a flat field at 236 mm from the center of it[5]. The film as the detector is set as shown in Fig. 1 (b).

III. Experimental Result

The waveforms of total currents and the signals of the PIN diode are shown in Figs. 3. The signals shown in Figs. 3 (a), (b) and (c) were obtained by using argon, neon and nitrogen, respectively. In these figures, the upper and the lower traces correspond to the signals of the total currents and the PIN diode, respectively. The maximum values of the total currents are approximately 250 kA, and the dips are shown at the tops of the total currents. The difference by changing working gas was not distinguished in the signals of the total currents. Since the signals of the PIN diode were obtained with the silicon nitride membrane, it is capable that these signals contained the components of the soft X-rays ranged in the water window region. For example the pulse width of the signal shown in Fig. 3 (a) is longer than that obtained with the beryllium foil. This may be caused by the components of the soft X-rays ranged in the water window region; the L shell radiation by argon was detected with the PIN diode by using the silicon nitride membrane. Since the sensitivities of PIN diodes are considerably down at the wavelengths of the water window region[6], comparison of the signals with the beryllium foil and the silicon nitride membrane is difficult. Measurement with X-ray diodes may be required, because the sensitivities of the X-ray diodes are not down at the wavelengths of the water window region.

Since alignment of the grazing incident spectrometer was not completed, the spectra were not obtained. We checked incidence of the soft X-rays into the spectrometer by modifying it into a pinhole camera. The pinhole camera consisted of the silicon nitride membrane and the film shown in Fig. 1 (b), but the positions of the grating and the film were changed. Figure 4 shows a photograph obtained with the pinhole camera. In Fig. 4 the spot-like images are seen along the centerline of the diode, and incidence of the X-rays into the spectrometer was verified. The reason why the spectra were not obtained might be uncompleted alignment of the spectrometer or weak intensities of the soft X-rays. However pinching of the plasma was verified by the spot-like images of the pinhole photograph, the pulsed signals of the PIN diode and the dips of the total currents.

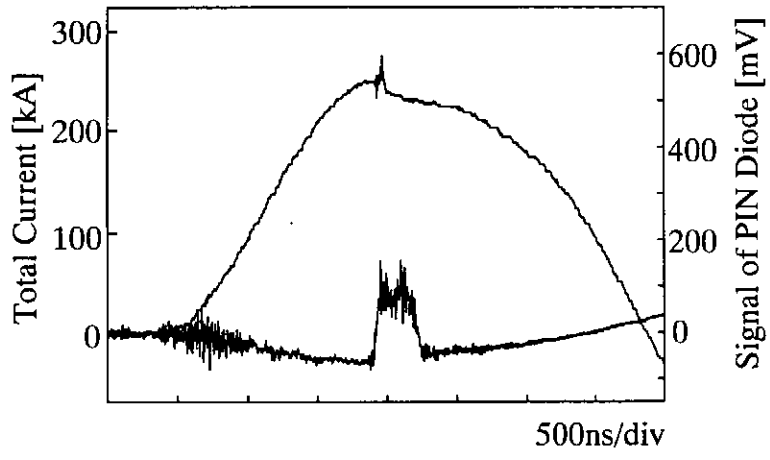

(a)

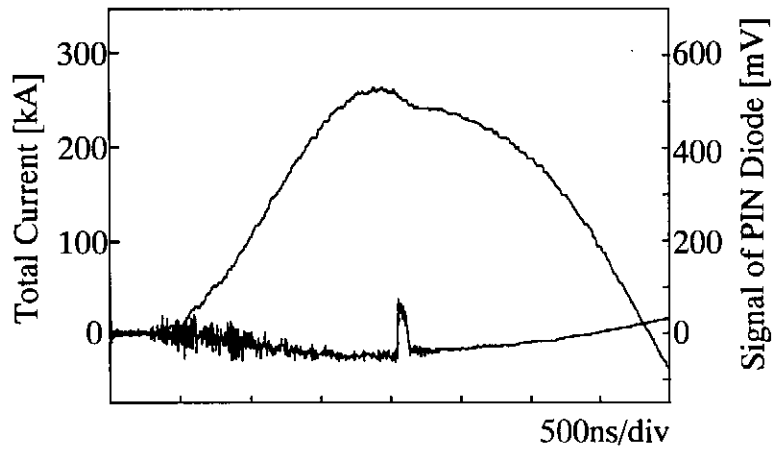

(b)

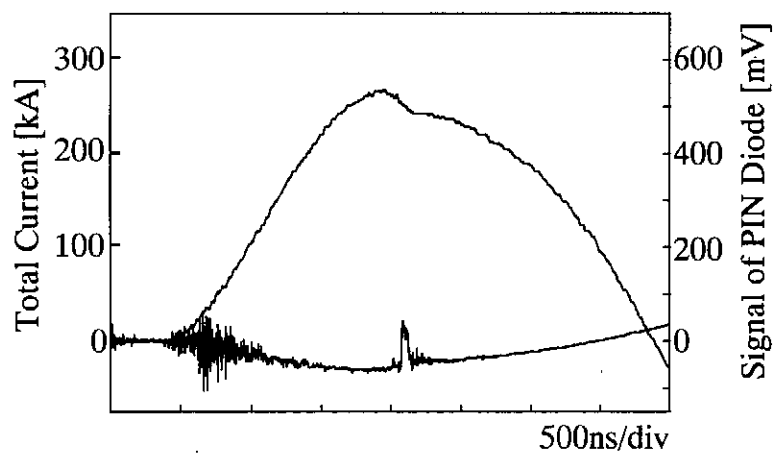

(c)

Fig. 3 The waveforms of the total currents and the PIN diode signals obtained with argon (a), neon (b) and nitrogen (c).

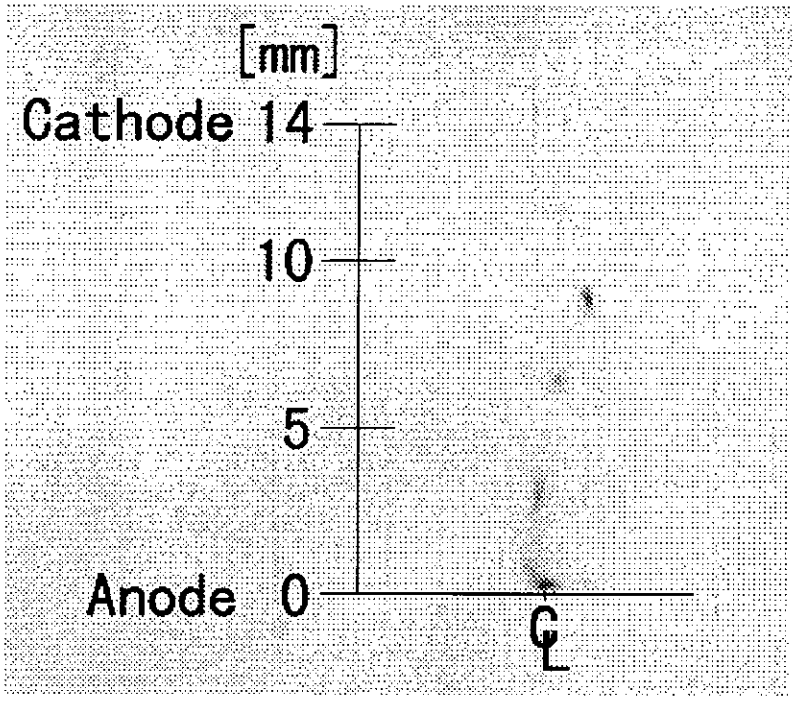

Fig. 4 Pinhole photograph by the soft X-ray

IV. Summary

In order to investigate the soft X-rays ranged in the water window region, we newly constructed a small gas-puff Z-pinch device, and investigated the characteristics of it. The experiments were performed with the silicon nitride membranes, which were passed through the soft X-rays ranged in the water window region. Pinching of the plasma was verified by the spot-like images of the pinhole photograph, the pulsed signals of the PIN diode and the dips of the total currents. Since alignment of the grazing incident spectrometer is not completed, the spectra were not obtained. Alignment and experiments are under going, so the spectra will be obtained in a short time.

References

1) M. Howells, J. Kirz and D. Sayre, Sci. Am., **264** (1991) 42.
2) T. Tomie, H. Shimizu, T. Majima, M. Yamada, T. Kanayama, H. Kondo, M. Yano and M. Ono, SCIENCE, **252** (1991) 691.
3) T. Igusa, K. Takasugi and T. Miyamoto, NIFS-PROC-**39** (1998) 70.
4) A. Krejci, J. Raus, V. Piffl, V. Golubev, Y. Platonov, E. Krousky and O. Renner, IEEE Trans. Plasma Sci., **21** (1993) 584.
5) N. Nakano, H. Kuroda, T. Kita and T. Harada, Appl. Optics, **23** (1984) 2386.
6) R. Spielman, Rev. Sci. Instrum., **66** (1995) 867.

Numerical simulations of dynamic dense sheet Z-pinch

A. Muravich, T. Miyamoto and K. Takasugi

Atomic Energy Research Institute, Nihon University
Kanda-Surugadai, Chiyoda-ku, 101-8308 Tokyo, Japan

Dynamics of a sheet Z-pinch produced between return current plates is studied in the framework of one-fluid MHD model. One-dimensional model of the sheet dynamics is developed. Examples of temporal evolution of the plasma density profiles obtained by direct solution of 2D MHD equations are shown. The shape of dynamic sheet Z-pinch boundary is concave in most part as seen from the plasma. Such a configuration of magnetic field suggests that the sheet Z-pinch is less subjected to destructive influence of interchange MHD instabilities than the Z-pinch with a circular cross-section.

KEYWORDS: Z-pinch, dense plasma, sheet plasma configuration, plasma dynamics

1 Introduction

Z-pinches are widely used as a source of high-temperature, dense plasma in the controlled thermonuclear fusion research [1], the intensive x-ray sources [2] and the production of ultra-high magnetic fields [3]. In most of these applications the stability problem is of great importance. It is established both theoretically and experimentally that magneto-hydrodynamic (MHD) interchange instabilities severely restrict the degree of homogeneity of the radial compression. Recently, dense sheet Z-pinches with a non-circular cross-section were proposed as a way to improve stability of conventional circular Z-pinches [4, 5]. The stationary sheet Z-pinch [5, 6] has a boundary with zero or negative curvature on main (central) part. Such a plasma configuration will be neutral or stable against the interchange instabilities.

In the present paper the dynamics of sheet Z-pinch is considered in the framework of one-fluid MHD. It is shown that the dynamic sheet Z-pinch also has a negative boundary curvature on the central part during almost all the phase of compression, and so gives the possibility to improve stability of the homogeneously contracted plasma in comparison with the Z-pinch of a circular cross-section.

2 Model

We consider the dynamics of a sheet Z-pinch which is produced between two return current conductors (Fig.1). It is assumed that the initial width of the sheet $2a_0$ is much

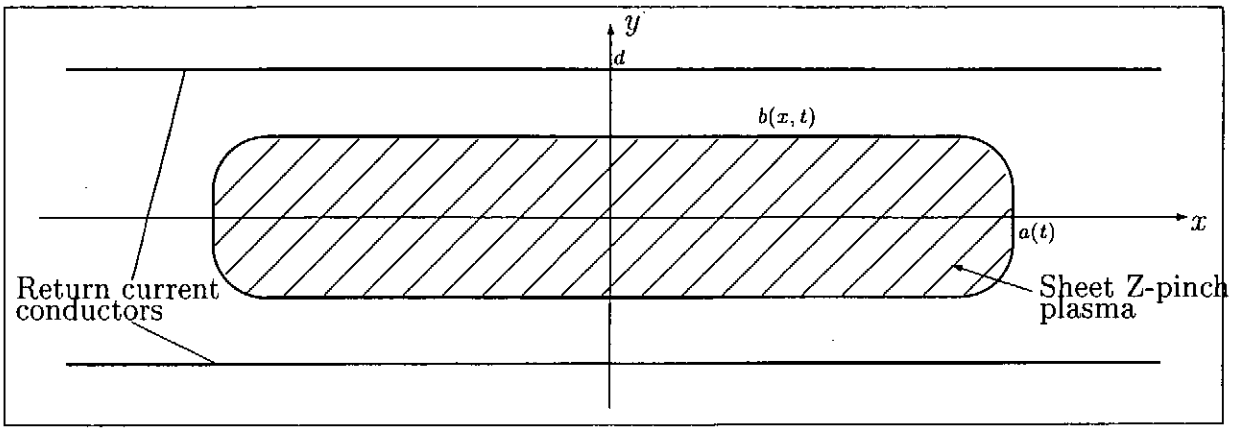

Figure 1: Scheme of sheet z-pinch.

wider than the initial thickness $2b_0$ and that the sheet plasma is initially in a pressure equilibrium state [6] across all the cross-section. The return current plates are assumed as ideal conductors having large width (much wider than $2a_0$), so that the magnetic field does not penetrate into the conductors and the total magnitude of the return current is equal to the total plasma current. The surface current density is determined as

$$I^*(x,t) = \int_{-b(x,t)}^{b(x,t)} j(x,y,t)\mathrm{d}y, \tag{1}$$

where j is the current density directed on the z-axis. The total pinch current is given by

$$I(t) = \int_{-a(t)}^{a(t)} I^*(x,t)\mathrm{d}x. \tag{2}$$

Similarly, the surface density of the sheet Z-pinch is defined as

$$N^*(x,t) = \int_{-b(x,t)}^{b(x,t)} n(x,y,t)\mathrm{d}y, \tag{3}$$

where n is the plasma density. The line density is determined in the same way as for the circular Z-pinches:

$$N = \int_S n(x,y,t)\mathrm{d}x\mathrm{d}y = \int_{-a(t)}^{a(t)} N^*(x,t)\mathrm{d}x. \tag{4}$$

The simulation was provided for the fully ionized deuterium on the base of the system of one-fluid MHD equations:

$$\frac{\partial n}{\partial t} + \mathrm{div}(n\boldsymbol{V}) = 0, \tag{5}$$

$$m_i n\left(\frac{\partial \boldsymbol{V}}{\partial t}+(\boldsymbol{V}\nabla)\boldsymbol{V}\right) = -2k_B\nabla(nT)+\boldsymbol{j}\times\boldsymbol{B}+\mathrm{div}\overline{\Pi}, \quad (6)$$

$$nk_B\left(3\frac{\mathrm{d}T}{\mathrm{d}t}+2T\mathrm{div}\boldsymbol{V}\right) = \mathrm{div}(\kappa\nabla T)+\nu\boldsymbol{j}^2-P_{rad}+\sum_{\alpha,\beta}\overline{\Pi}_{\alpha\beta}\frac{\partial V_\alpha}{\partial x_\beta}, \quad (7)$$

$$\frac{\partial \boldsymbol{A}}{\partial t} = \boldsymbol{V}\times\boldsymbol{B}-\nu\boldsymbol{j}, \quad (8)$$

$$\boldsymbol{B}=\mathrm{rot}\boldsymbol{A} \quad , \quad \boldsymbol{j}=\frac{1}{\mu_0}\mathrm{rot}\boldsymbol{B}.$$

The plasma resistivity across the magnetic field ν is taken following Spitzer [7] as

$$\nu \approx 1.78\frac{\log\Lambda}{m_e}\left(\frac{e}{4\pi\varepsilon_0}\right)^2\left(\frac{m_e}{k_BT}\right)^{3/2}=\nu_0T^{-3/2}. \quad (9)$$

The thermal conductivity κ and viscosity tensor $\overline{\Pi}$ given by Braginskii [8] are used.

Initially the sheet assumed to be in the pressure equilibrium, sustained by the current I_0. It was previously shown [6] that the thickness of such an equilibrium configuration is constant in most sheet part:

$$b \approx 0.75d, \quad |x| \le a.$$

We suppose that the plasma has initially the ionization temperature $T_0 = 13.6\mathrm{eV}$ and separation between the return current conductors $2d = 2\times10^{-3}\mathrm{m}$. Linear current rise is considered:

$$I(t) = I_0 + \dot{I}t \quad (10)$$

Thus, the temporal behaviour of the sheet is determined by the initial maximum plasma density n_0, initial sheet width $2a_0$ and the current time-derivative $\dot{I}$.

3 One-dimensional treatment

3.1 Equations

Simplification of the system of eqs.(5)-(8) is possible if the temperature and current are homogeneous, and if the viscosity and radiation terms are negligible. Then, the local pressure equilibrium in y-direction can be assumed in each cross-section $x = const$:

$$\frac{\partial p}{\partial y}=2k_BT\frac{\partial n}{\partial y}=jB_x\approx\mu_0j^2y. \quad (11)$$

The density distribution can be obtained by integrating eq.(11) with respect to y:

$$n(x,y,t)=n(x,0,t)\left[1-\left(\frac{y}{b(x,t)}\right)^2\right], \quad (12)$$

where

$$n(x,0,t)=\frac{\mu_0b^2(x,t)j^2(t)}{4k_BT(t)}=\frac{\mu_0I^{*2}(x,t)}{16k_BT(t)}. \quad (13)$$

The surface density on the x-axis is related with the plasma density as

$$N^*(x,t) = \int_{-b(x,t)}^{b(x,t)} n(x,y,t)\mathrm{d}y = \frac{4}{3} n(x,0,t) b(x,t). \tag{14}$$

From eqs.(13) and (14) the expression for the sheet half-thickness is given as

$$b(x,t) = \sqrt[3]{\frac{3N^*(x,t)k_B T(t)}{\mu_0 j^2(t)}}. \tag{15}$$

The total pinch current is expressed as

$$I(t) = 4j(t) \int_0^{a(t)} b(x,t)\mathrm{d}x = 4\sqrt[3]{\frac{3k_B T(t) j(t)}{\mu_0}} \int_0^{a(t)} \sqrt[3]{N^*(x,t)}\mathrm{d}x. \tag{16}$$

Denoting

$$\Upsilon(t) = \int_0^{a(t)} \sqrt[3]{N^*(x,t)}\mathrm{d}x, \tag{17}$$

the sheet half-thickness, current density and cross-section square can be expressed in terms of $N^*(x,t)$, $I(t)$ and $T(t)$, respectively, as follows:

$$b(x,t) = \frac{48 k_B T(t) \Upsilon^2(t)}{\mu_0 I^2(t)} \sqrt[3]{N^*(x,t)}, \tag{18}$$

$$j(t) = \frac{\mu_0 I^3(t)}{192 k_B T(t) \Upsilon^3(t)}, \tag{19}$$

$$S(t) = \frac{192 k_B T(t) \Upsilon^3(t)}{\mu_0 I^2(t)}. \tag{20}$$

If the velocity is expressed as:

$$\boldsymbol{V}(x,y,t) = (V_x(x,t), \frac{\partial b(x,t)}{\partial t}\frac{y}{b}, 0),$$

eqs.(5) and (6) can be integrated with respect to y from 0 to $b(x,t)$:

$$\frac{\partial N^*}{\partial t} + \frac{\partial (N^* V_x)}{\partial x} = 0, \tag{21}$$

$$m_i N^* \left(\frac{\partial V_x}{\partial t} + V_x \frac{\partial V_x}{\partial x} \right) = -2k_B T \frac{\partial N^*}{\partial x} - j \int_{-b(x,t)}^{b(x,t)} B_y(x,y,t)\mathrm{d}y. \tag{22}$$

Taking into account that $\partial B_y(x,0,t)/\partial y \equiv 0$, one can approximately write

$$\int_{-b(x,t)}^{b(x,t)} B_y(x,y,t)\mathrm{d}y \approx 2b(x,t) B_y(x,0,t). \tag{23}$$

It was shown [9] that y-component of the magnetic field on the x-axis is:

$$B_y(x,0) = \frac{\mu_0 j}{\pi} \int\limits_{-a}^{a} \arctan\left[\frac{\sin\left(\frac{\pi}{2}\frac{b(|x_0|)}{d}\right)}{\sinh\left(\frac{\pi}{2}\frac{x-x_0}{d}\right)}\right] \mathrm{d}x_0. \tag{24}$$

Therefore, eq.(22) can be rewritten as

$$\frac{\partial V_x}{\partial t} + V_x\frac{\partial V_x}{\partial x} = -\frac{2k_BT}{m_iN^*}\frac{\partial N^*}{\partial x} - \frac{2b\mu_0 j^2}{\pi m_i N^*} \int\limits_{-a(t)}^{a(t)} \arctan\left[\frac{\sin\left(\frac{\pi}{2}\frac{b(|x_0|,t)}{d}\right)}{\sinh\left(\frac{\pi}{2}\frac{x-x_0}{d}\right)}\right] \mathrm{d}x_0. \tag{25}$$

Integration of eq.(7) across all the sheet cross-section gives

$$3Nk_B\frac{\mathrm{d}T}{\mathrm{d}t} + 2k_BT \int\limits_{-a(t)}^{a(t)} N^*\left(\frac{\partial V_x}{\partial x} + \frac{1}{b}\frac{\partial b}{\partial t}\right)\mathrm{d}x = \frac{\nu_0}{T^{3/2}}Sj^2. \tag{26}$$

From eq.(18):

$$\frac{1}{b}\frac{\partial b}{\partial t} = \frac{1}{3N^*}\frac{\partial N^*}{\partial t} + \frac{1}{T}\frac{\mathrm{d}T}{\mathrm{d}t} + \frac{2}{\Upsilon}\frac{\mathrm{d}\Upsilon}{\mathrm{d}t} - \frac{2}{I}\frac{\mathrm{d}I}{\mathrm{d}t} \tag{27}$$

Substituting eqs.(19),(20) and (27) into eq.(26), we obtain the final form of the temperature equation:

$$\frac{\mathrm{d}T}{\mathrm{d}t} + \frac{4T}{5\Upsilon}\frac{\mathrm{d}\Upsilon}{\mathrm{d}t} - \frac{4T}{5I}\frac{\mathrm{d}I}{\mathrm{d}t} + \frac{2T}{5N} \int\limits_{-a(t)}^{a(t)} N^*\frac{\partial V_x}{\partial x}\mathrm{d}x = \frac{\mu_0\nu_0}{960k_B^{3/2}}\frac{I^4}{NT^{5/2}\Upsilon^3}. \tag{28}$$

Thus, eqs.(21), (25) and (28) form a closed set for the variables $N^*(x,t)$, $V_x(x,t)$ and $T(t)$. One can see that solutions of the system are self-similar for the equal parameter $\Gamma = \dot{I}/\sqrt{n_0}$.

3.2 Results

If the parameter Γ (and accordingly, the rate of current rise) is low, the sheet thickness grows initially due to the joule heating. For $\Gamma = \Gamma_{cond}$, thickness expands up to the return current conductors, thus the value Γ_{cond} can be considered as a minimum possible rate of the current rise. From the numerical solution it was obtained that for $a \geq 5$mm

$$\Gamma_{cond} \approx (3.31a + 8.35) \times 10^2 \mathrm{A}\cdot\mathrm{m}^{3/2}/\mathrm{s}, \quad (a \text{ in mm}). \tag{29}$$

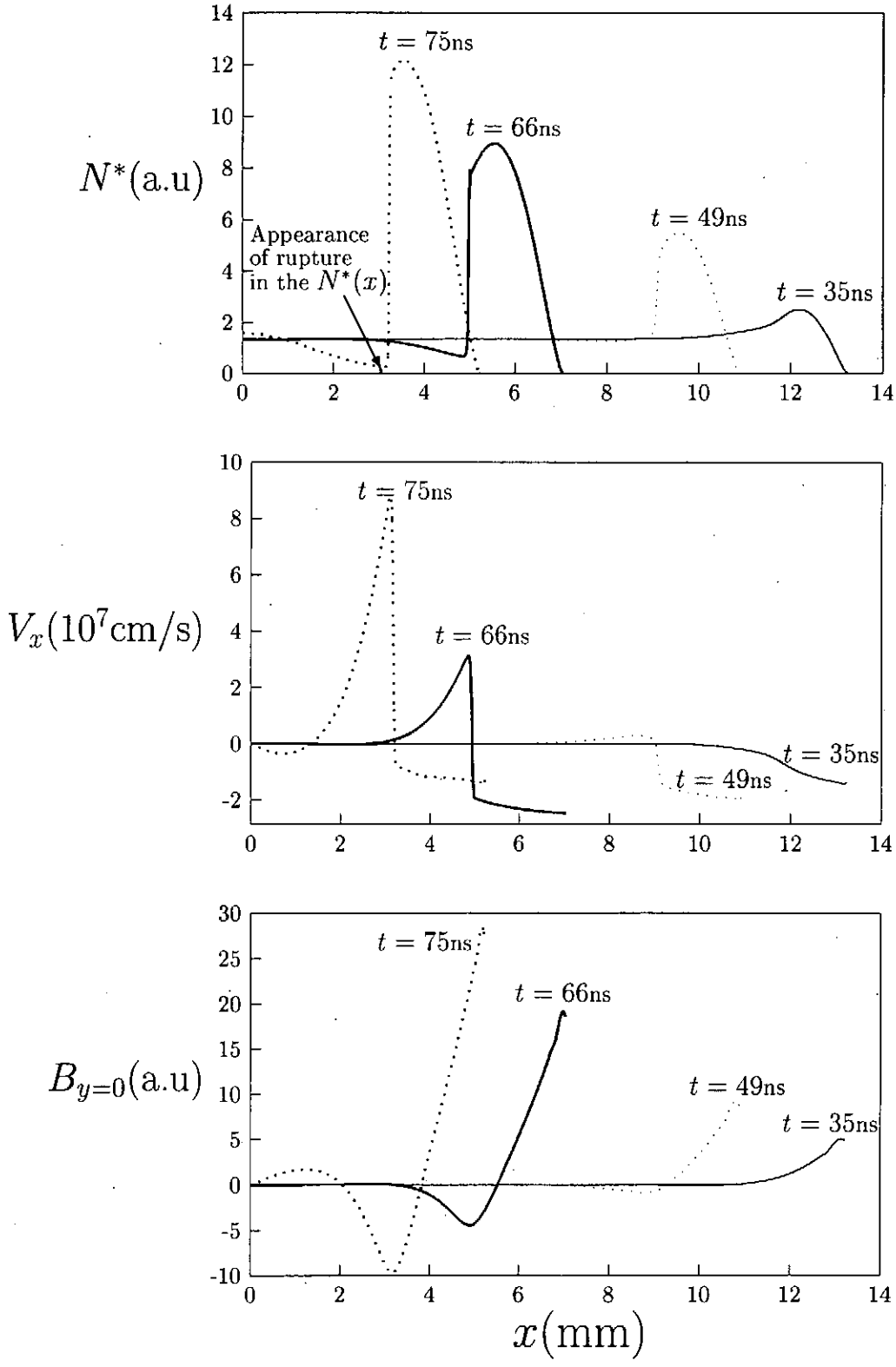

Figure 2: Evolution of the surface density, x-velocity and magnetic field (a_0 = 15mm, $\Gamma = 2.68 \times 10^4 \mathrm{A} \cdot \mathrm{m}^{3/2}$).

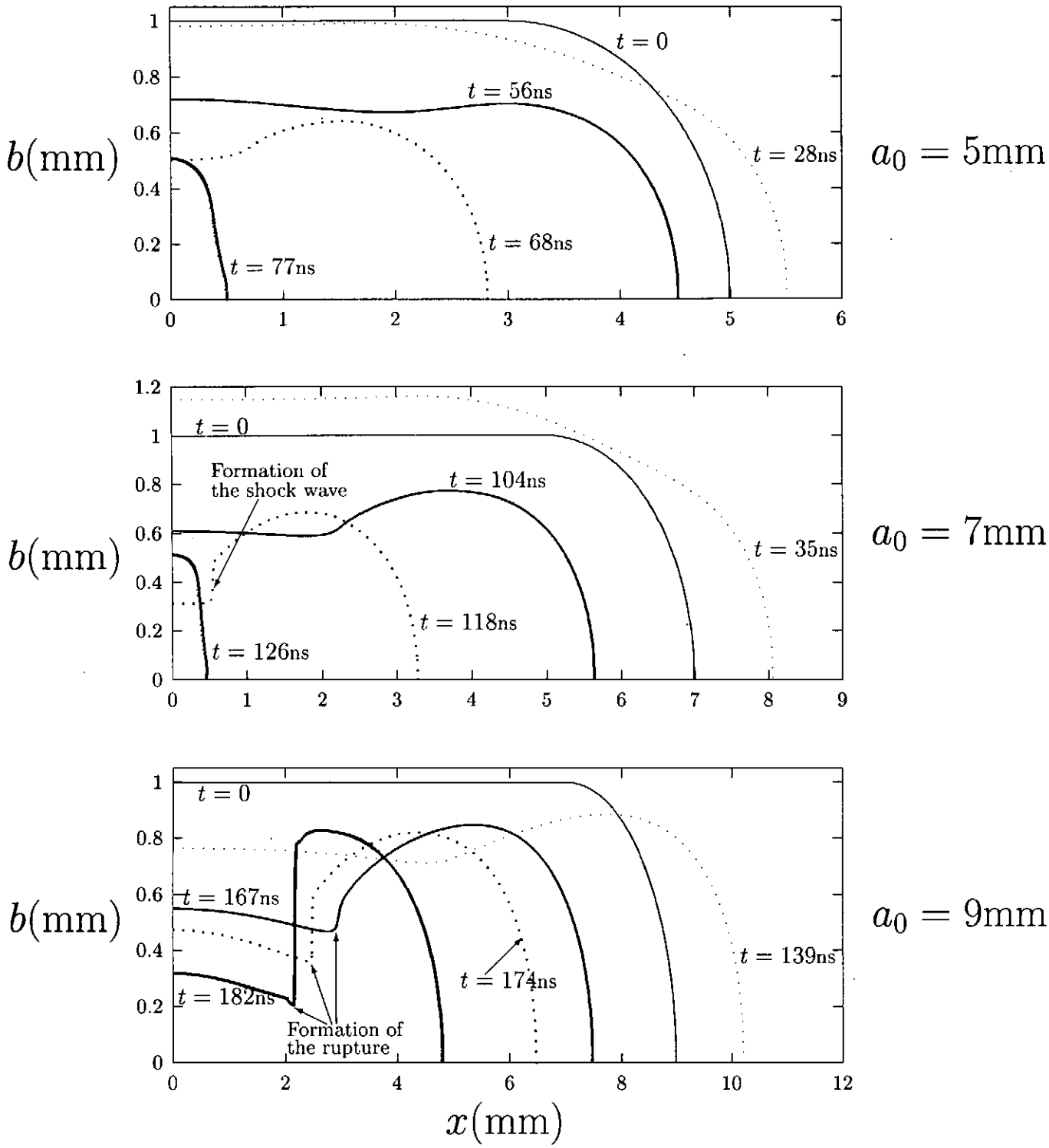

Figure 3: Changes in the sheet dynamics with increasing a_0 ($\Gamma = 1.34 \times 10^4 \mathrm{A} \cdot \mathrm{m}^{3/2}$).

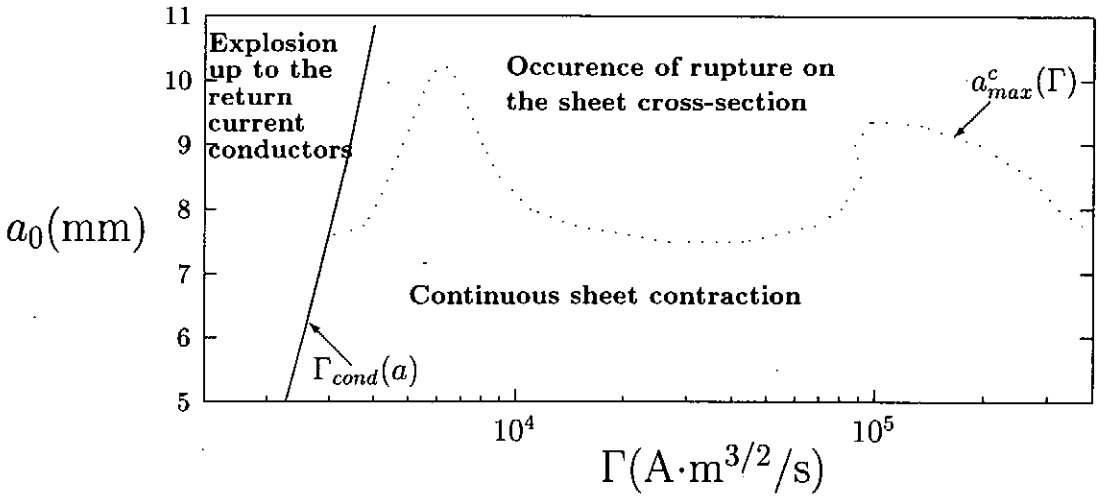

Figure 4: Regions of different sheet compression types.

If the current rise rate exceeds a maximum value, a disruption appears on the sheet cross-section. The following stages of the width dynamics can be distinguished in the case of the disruption occurrence:

1. Appearance of distinction between shapes of the central and end parts.
2. Formation of shock front in the transient layer between the central and end parts.
3. Intensive outflow of plasma from the central part.
4. Appearance of rupture between the central and end parts.

Examples of the surface density, x-velocity and magnetic field distributions that are typical for these four stages are presented in Fig.2 ($a_0 = 15$mm and $\Gamma = 2.68 \times 10^4 \mathrm{A} \cdot \mathrm{m}^{3/2}/\mathrm{s}$). One can see that in the first stage the end part acquires an elliptic shape and begins a snow-plowing motion toward the center. During this stage plasma velocity is rather low and the functions $N^*(x)$ and $V_x(x)$ are continuous. The second stage is characterized by the appearance of discontinuity in the velocity and the surface density distributions. This shape of disruption is common for the hydrodynamic shock waves [10]. In the third stage, the snow-plowing motion results in concentration of significant amount of the pinch plasma in the end parts. The current flowing on the sheet end parts determines a specific configuration of the magnetic field, which becomes negative in the region between the central and the end parts (Fig.2, $t = 71.4$ns). Negative magnetic field accelerates the central part plasma out from the center. Due to this reason the plasma begins to outflow from the central part, as can be seen in the velocity distribution (Fig.2, $t = 71.4$ns). In the typical cases the stages 2 and 3 can be clearly distinguished, but there is no definite criterion for determination of their beginning time. In the fourth stage, the plasma completely outflows from the region between the central and the end parts resulting in the appearance of rupture on the sheet cross-section.

In Fig.3, the temporal sequences of the sheet boundary profiles are shown with increasing a_0 for $\Gamma = 1.4 \times 10^4 \mathrm{A} \cdot \mathrm{m}^{3/2}/\mathrm{s}$. For relatively small initial width ($a_0 = 5$mm), the formation of shock front does not occur during all the compression and the stages 2-4

are absent in the sheet dynamics. At $a_0 = 7$mm stages 2 and 3 appear in the dynamics. If a_0 exceeds some critical value a^c_{max} (approximately 7.85mm for the present Γ), stage 4 occurs at the particular moment. Formation of the rupture can be seen for the case $a_0 = 9$mm.

The dependences $\Gamma_{cond}(a)$ and $a^c_{max}(\Gamma)$ determine the regions with the different types of the sheet dynamics. The mutual position of the regions is shown in Fig.4 in the coordinate system (Γ,a_0). It can be seen that the continuous sheet compression is possible only for

$$a_0 \leq a_{max} \approx 10.2\text{mm}. \tag{30}$$

For $a_0 > 10.2$mm, the disruption of the sheet cross-section occurs at any Γ. If $a_0 \geq 7.4$mm, the continuous compression occurs in a wide range of Γ.

4 Two-dimensional treatment

In order to check the accuracy of the developed one-dimensional model, the numerical solution of the system of eqs.(5)-(8) was provided including viscosity effects. In spite of the complicated 2D structure of the shock wave, the results of *§3.2* are sufficient to describe the behavior of high-dense (and accordingly non-viscous) sheet. Initial maximum plasma density n_0 exerts great influence upon the sheet dynamics. Particularly, the maximum possible sheet half-width a_{max} rises with decreasing n_0 and can reach about 40mm for $n_0 \approx 10^{21}\text{m}^{-3}$, that is 4 times larger than given by eq.(30). For the comparatively low current rise the sheet contraction is quasi-stationary and the thickness does not change significantly during the width contraction. Temporal sequences of two-dimensional density profiles that appear under such a contraction are shown in the Figs.5-6 for the sheet Z-pinches with $a_0 = 5$mm and $a_0 = 20$mm, respectively. For $a_0 = 5$mm, the half-thickness of the sheet on the y-axis $b(0,t)$ does not become smaller than 0.8. In spite of the clear distinction between comparatively low-dense "central part" and high-dense "end parts" that appears during compression of the sheet with $a_0 = 20$mm, half-thickness of the "central part" does not become smaller than 0.65. Increasing of Γ at a given a_0 results in greater initial thickness contraction and more clear difference between "central" and "end" parts (Figs.7-8).

In Figs.5-8, it can be seen that the shape of the shock front is not sharp (as follows from one-dimensional analysis, Figs.2-3) but has smooth or barbell-like structure both for small and large Γ. In the main (central) part of such a configuration curvature of the plasma boundary (and accordingly, curvature of the magnetic field lines) is negative with respect to the plasma. This property makes central part stable against interchange MHD instabilities [10]. A circular Z-pinch is strongly subjected to the influence of this kind of instabilities, because the magnetic field lines of circular Z-pinch are convex as seen from the plasma. Thus one can conclude that the contraction of a sheet Z-pinch is more homogeneous and stable process than that of a circular Z-pinch.

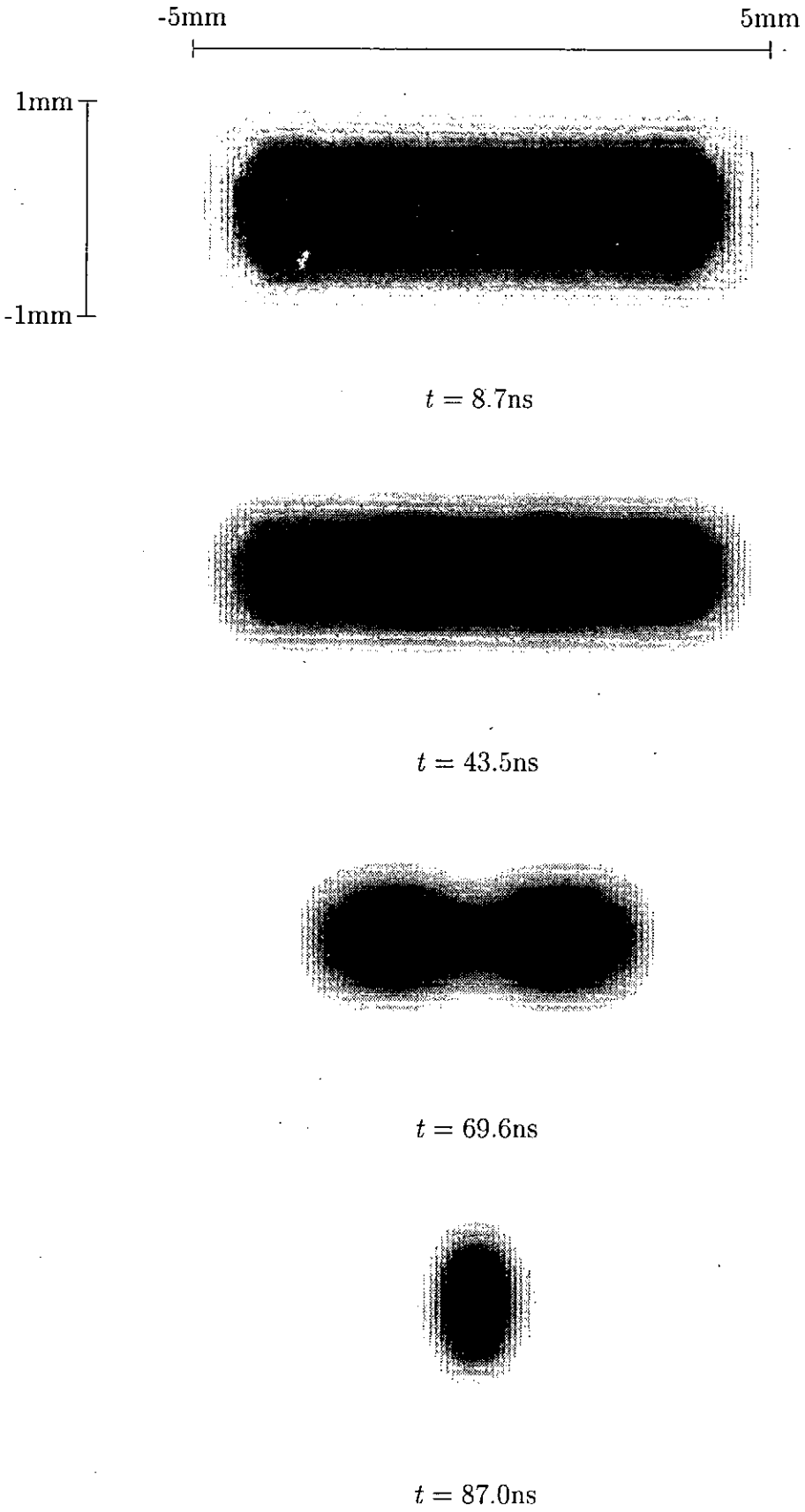

Figure 5: Example of quasi-stationary sheet Z-pinch contraction ($n_0 = 10^{23}\mathrm{m}^{-3}$, $a_0 = 5.0 \times 10^{-3}\mathrm{m}$, $\mathrm{d}I/\mathrm{d}t = 5.6 \times 10^{11}\mathrm{A/s}$)

$t = 69.6$ns

$t = 243.6$ns

$t = 313.2$ns

$t = 339.3$ns

Figure 6: Example of quasi-stationary sheet Z-pinch contraction ($n_0 = 10^{23}\mathrm{m}^{-3}$, $a_0 = 2.0 \times 10^{-2}\mathrm{m}$, $\mathrm{d}I/\mathrm{d}t = 9.0 \times 10^{11}\mathrm{A/s}$)

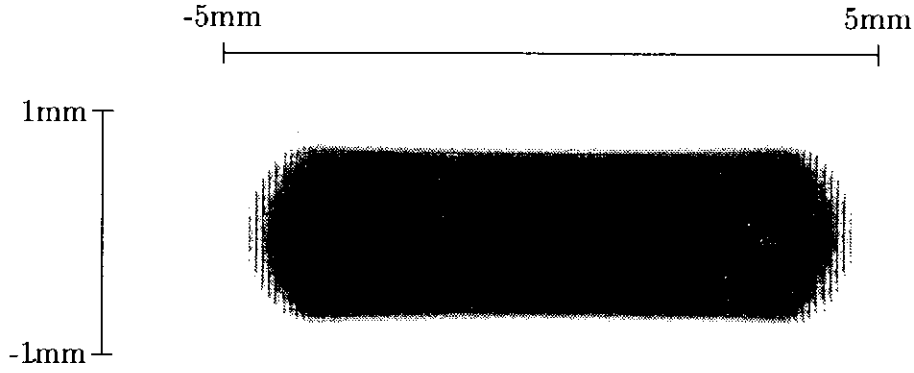

$\tilde{t} = 5.2\text{ns}$

$\tilde{t} = 10.4\text{ns}$

$\tilde{t} = 19.1\text{ns}$

$\tilde{t} = 24.4\text{ns}$

Figure 7: Example of "fast" sheet Z-pinch contraction ($n_0 = 10^{23}\text{m}^{-3}$, $a_0 = 5.0 \times 10^{-3}\text{m}$, $\mathrm{d}I/\mathrm{d}t = 7.4 \times 10^{12}\text{A/s}$)

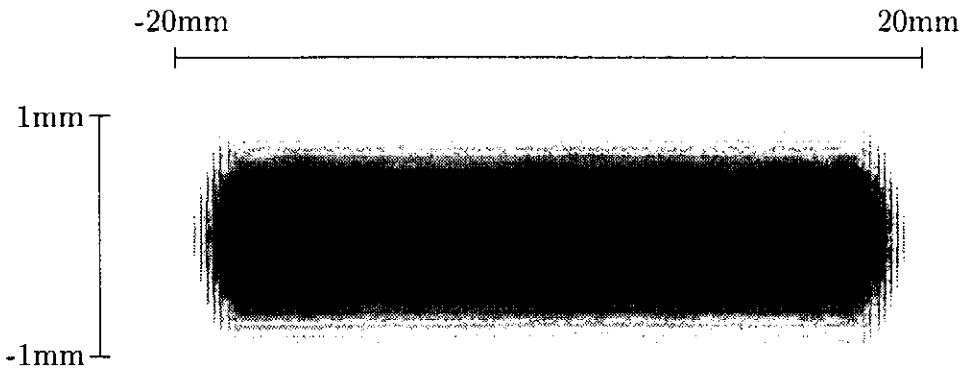

$t = 17.4$ns

$t = 69.6$ns

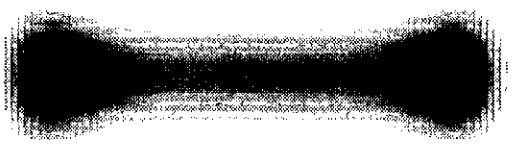

$t = 104.4$ns

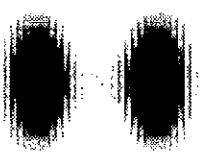

$t = 130.5$ns

Figure 8: Example of "fast" sheet Z-pinch contraction ($n_0 = 10^{23}\mathrm{m}^{-3}$, $a_0 = 2.0 \times 10^{-2}\mathrm{m}$, $\mathrm{d}I/\mathrm{d}t = 2.5 \times 10^{12}\mathrm{A/s}$)

5 Conclusions

1. In order to prevent the initial expansion of the sheet thickness up to the return current conductors, the parameter $\Gamma = \dot{I}/\sqrt{n_0}$ must be greater than $\Gamma_{cond} \approx (3.31a + 8.35) \times 10^2 \mathrm{A} \cdot \mathrm{m}^{3/2}/\mathrm{s}$.

2. If the non-viscous sheet half-width exceeds the critical value $a^c_{max}(\Gamma)$, a disruption appears on the sheet cross-section during compression. Maximum $a^c_{max} \approx 10.2\mathrm{mm}$ is reached at $\Gamma \approx 3.29 \times 10^3 \mathrm{A} \cdot \mathrm{m}^{3/2}/\mathrm{s}$.

3. Viscous effects provide a possibility to increase a^c_{max} by several times in comparison with the high-dense case. The sheet contraction without disruption of the cross-section is possible for $a_0 \leq 40\mathrm{mm}$ at $n_0 = 10^{23}\mathrm{m}^{-3}$.

4. At the "central" part of transient sheet Z-pinch, the magnetic field lines are concave as seen from the plasma (Figs.5-8). This makes dynamic sheet Z-pinch stable against interchange instabilities in this part.

References

[1] J. D. Sethian et al.: Phys. Rev. Lett. **59** (1987) 892
D. W. Scudder et al.: AIP Conf. Proc. **299** (1994) 503

[2] R. B. Spielman et al.: Appl. Phys. Lett. **47** (1985) 229
S. Maxon et al.: J. Appl. Phys. **57** (1985) 971

[3] S. A. Sorokin and S. A. Chaikovsky: AIP Conf. Proc. **299** (1994) 83

[4] T. Miyamoto: AIP Conf. Proc. **409** (1997) 401

[5] T. Miyamoto: J. Phys. Soc. Japan **68** (1999) 1238

[6] A. Muravich: J. Phys. Soc. Japan **68** (1999) 1452

[7] L. Spitzer, Jr: Physics of Fully Ionized Gases (Interscience, New York, 1962)

[8] S. I. Braginskii: in Plasma Physics and the Problem of Controlled Thermonuclear Reactions **1** (Pergamon Press, New York, 1959) 205

[9] A. Muravich: preprint of Atomic Energy Research Institute, Nihon University, NUP-A-99-18 (1999)

[10] Ya. B. Zel'dovich and Yu. P. Raizer: Physics of Shock Waves and High-Temperature Hydrodynamics Phenomena (Academic Press, New York, 1967)

[11] B. B. Kadomtsev: in Reviews on Plasma Physics **2** (Consultants Bureau, New York, 1966) 153

X-ray Imaging using a Concave X-ray Mirror

Keiichi Takasugi, Takashi Yoshida,[+]
and Tetsu Miyamoto

Atomic Energy Research Institute, Nihon University
[+]College of Science and Technology, Nihon University

Abstract

X-ray mirror optics for x-ray imaging was discussed. Basic relation for x-ray imaging using a concave x-ray mirror was derived. The focal point was found to stick to a spherical surface. Wavelength of x-ray was shown to be selected by adjusting the size of the mirror.

I. Introduction

X-ray optics components around the water window (23 - 44 Å) have wide range of applications especially in medical and biological fields. Glass capillary converter[1,2] and x-ray multilayer mirror[3,4] are those kinds. Recently the x-ray multilayer mirror for near normal incidence at shorter wavelength became available commercially. It has applied for x-ray telescopes of x-ray microscopes. These can also be applied as powerful imaging tools for the investigation of hot spot formation in z-pinch plasmas.[5]

In this report we will discuss about the basic formula for x-ray mirror optics and the application for imaging device.

II. Mirror Optics

The reflection of x-ray on the multilayer mirror is based on the Bragg relation. The primary reflection occurs at

$$2d\cos\phi = \lambda, \tag{1}$$

where d is the layer spacing, ϕ is the incident and also reflection angle relative to the normal, and λ is the wavelength of x-ray. This means that the angle ϕ is fixed if the wavelength λ is fixed.

Figure 1 shows the schematic diagram of the x-ray mirror optics. The circle centered at the point O shows the spherical surface of the x-ray mirror. The actual x-ray mirror occupies some part of the surface. The curvature of the mirror or the radius of sphere is R.

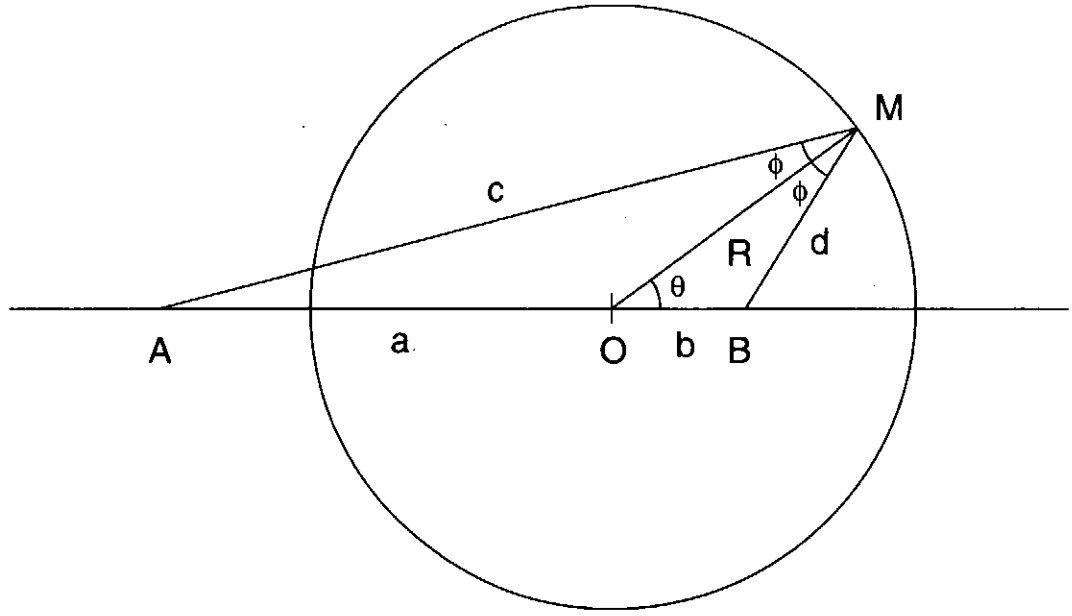

Figure 1: Schematic diagram of the mirror optics.

The position of the x-ray source is A. The distance AO is a. The x-ray started at the point A is reflected at the point M with the angle ϕ, then comes to the point B on the axis. The distance BO is b. As the reflection is cylindrically symmetric, the point B is the focal point. The distance b is expressed as

$$b = \frac{aR}{R + 2a\cos\theta}, \tag{2}$$

where the angle θ is $\angle$MOB.

The mirror angle θ is better expressed in terms of the reflection angle ϕ,

$$\cos\theta = \frac{-R\sin^2\phi + \cos\phi\sqrt{a^2 - R^2\sin^2\phi}}{a}, \tag{3}$$

then

$$b = \frac{aR}{R(1 - 2\sin^2\phi) + 2\cos\phi\sqrt{a^2 - R^2\sin^2\phi}}. \tag{4}$$

This equation is the basis for the x-ray mirror imaging.

Figure 2 shows the normalized focal point b as a function of the source point a for fixed reflection angle ϕ. Except at the small $a/R(< 0.7)$ the focal point b does not shift so much. The size ratio of the image to the object is simply b/a.

III. Stretch of Image

From the eq.(4) we can calculate rate of change of parameters. The change of the focal point b with a is

$$\delta b = \frac{\partial b}{\partial a}\delta a,$$

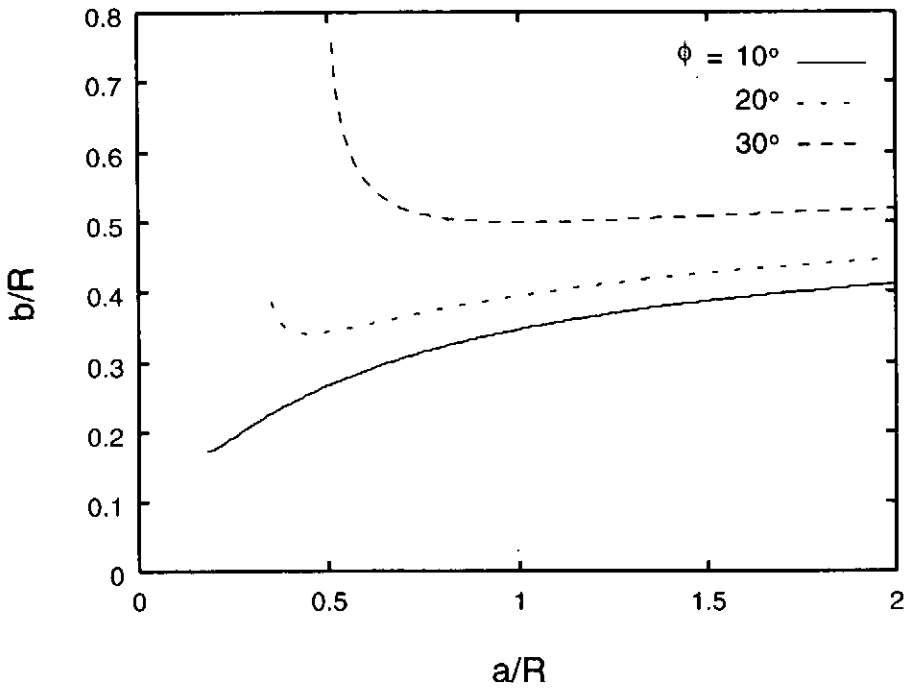

Figure 2: Focal point b as a function of a.

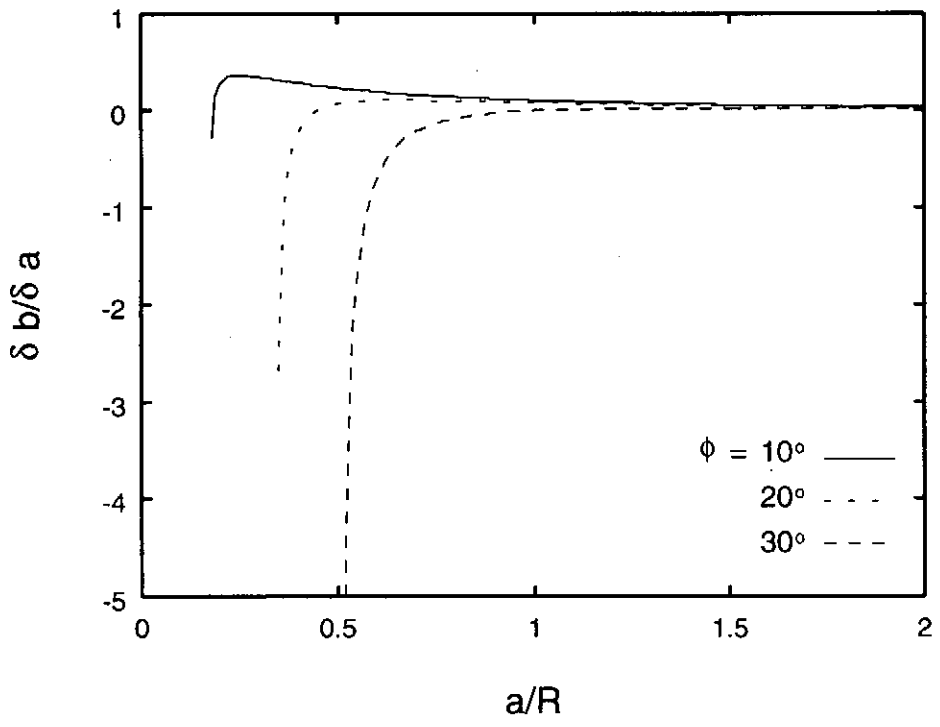

Figure 3: The rate of change of the position b with a.

where

$$\frac{\partial b}{\partial a} = \frac{-2a^2 R\cos\phi}{\sqrt{a^2 - R^2\sin^2\phi}\left(R - 2R\sin^2\phi + 2\cos\phi\sqrt{a^2 - R^2\sin^2\phi}\right)^2} + \frac{R}{R - 2R\sin^2\phi + 2\cos\phi\sqrt{a^2 - R^2\sin^2\phi}}. \quad (5)$$

From this relation we can estimate the radial stretch of the image. Figure 3 shows the rate of change of the focal point b with a. The change $\partial b/\partial a \ll 1$ is at $a/R > 0.7$. This means that the focal point sticks to a spherical surface with radius b, even if the x-ray source is thick.

IV. Wavelength Selection

Next we consider about the shift of image with the angle ϕ. The relation

$$-2d\sin\phi\delta\phi = \delta\lambda \quad (6)$$

indicates that the change in the angle ϕ corresponds to the change in wavelength λ.

Similar to the previous results, the change of the point b with the incident angle ϕ is

$$\delta b = \frac{\partial b}{\partial\phi}\delta\phi = -\sin\phi\frac{\partial b}{\partial\cos\phi}\delta\phi,$$

where

$$\frac{\partial b}{\partial\cos\phi} = \frac{-2aR\left(2R\cos\phi + \dfrac{R^2\cos^2\phi}{\sqrt{a^2 - R^2\sin^2\phi}} + \sqrt{a^2 - R^2\sin^2\phi}\right)}{\left(R - 2R\sin^2\phi + 2\cos\phi\sqrt{a^2 - R^2\sin^2\phi}\right)^2}. \quad (7)$$

And the change of the angle θ with ϕ is

$$\delta\theta = \frac{\partial\theta}{\partial\phi}\delta\phi = \frac{\sin\phi}{\sin\theta}\frac{\partial\cos\theta}{\partial\cos\phi}\delta\phi,$$

where

$$\frac{\partial\cos\theta}{\partial\cos\phi} = \frac{2R\cos\phi + \dfrac{R^2\cos^2\phi}{\sqrt{a^2 - R^2\sin^2\phi}} + \sqrt{a^2 - R^2\sin^2\phi}}{a}. \quad (8)$$

Figure 4 shows the rate of change of the focal point b with the incident angle ϕ. This is usually small for near normal reflection ($\phi < 1$), however, the magnitude of the change $\delta\phi$ is essential. So if $\delta\phi \ll 1$ stands, $\delta b \ll R$.

Figure 5 shows the rate of change of the mirror angle θ with the angle ϕ. This is not negligible for most regions.

The actual mirror does not cover whole sphere but has a small radius r compared to the curvature R. If the change of the anle $\delta\theta$ becomes sufficiently large, the reflection point will

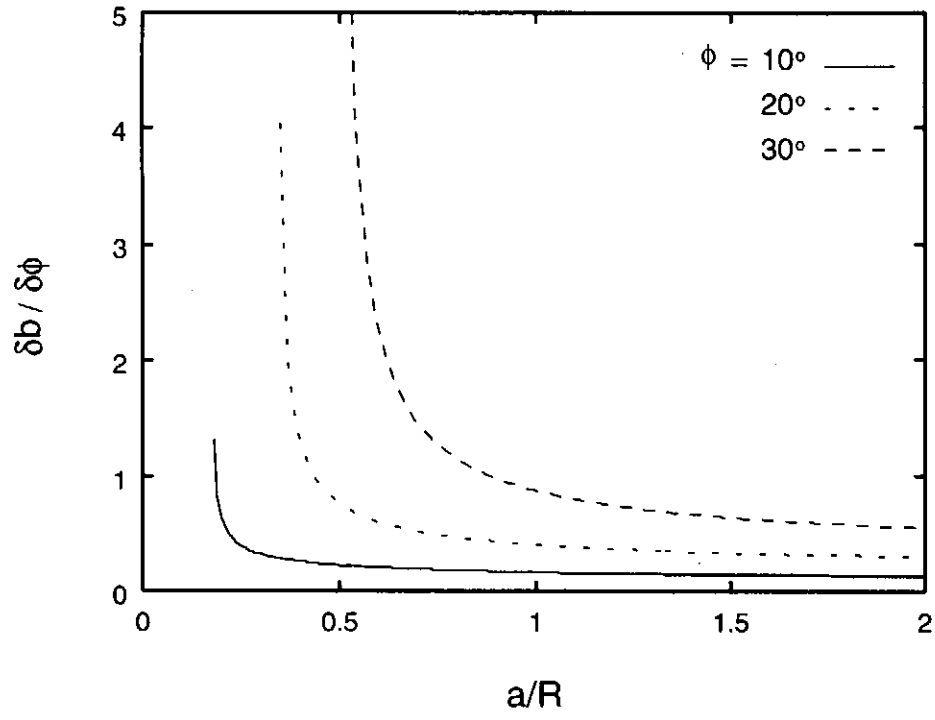

Figure 4: The rate of change of the position b with ϕ.

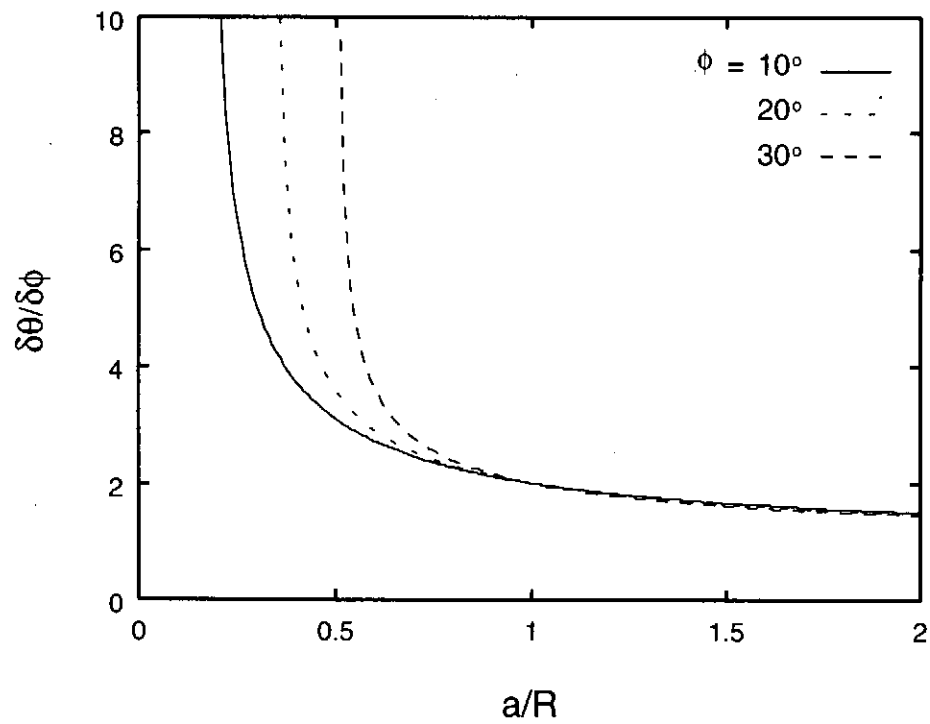

Figure 5: The rate of change of the angle θ with ϕ.

get out of the mirror.

$$\begin{aligned} \delta\lambda &= 2d\sin\phi\frac{\partial\phi}{\partial\theta}\delta\theta \\ &< 2d\sin\phi\frac{\partial\phi}{\partial\theta}\frac{r}{R}. \end{aligned} \tag{9}$$

This condition limits the reflection band of wavelength $\delta\lambda$. We can enhance the wavelength resolution by choosing the spread of the mirror angle $\delta\theta$, or even we can choose only one line spectrum for imaging.

V. Summary

X-ray mirror optics for x-ray imaging was discussed. Basic relation for x-ray imaging using a concave x-ray mirror has derived. The focal point do not shift so much by changing the position of the x-ray source. This means that the focal point sticks to a spherical surface. The stretch of the image and the resolution of wavelength were also discussed. Wavelength of x-ray can be selected by adjusting the mirror location and size. We can choose only one line spectrum for imaging if we use a sufficiently small x-ray mirror.

References

[1] V.L. Kantsyrev, N.R. Mingaliev, O.G. Petrukhin, S.A. Pikuz, V.M. Romanova, T.A. Shelkovenko, A.S. Shlyaptseva and A.Y. Faenov: Tech. Phys. Lett. **19**, 205 (1993).
[2] V. Kantsyrev and R. Bruch: Rev. Sci. Instrum. **69**, 770 (1997).
[3] A.V. Vinogradov and B.Y. Zeldovich: Appl. Optics **16**, 89 (1977).
[4] I.V. Kozhevnikov and A.V. Vinogradov: Physica Scripta **T17**, 137 (1987).
[5] V.L. Kantsyrev, K. Takasugi, K. Tatsumi, T. Miyamoto and A.S. Shlyaptseva: Proc. 1996 Int. Conf. Plasma Physics Vol. 2, 1106 (1997).

X-ray device for 0.7-200 keV based on Johansson quartz crystals on optical contact and Cauchois crystals

E.O.Baronova, M.M.Stepanenko, N.Pereira,*
*A.Muravich**, K.Takasugi** and T.Miyamoto***
RRC Kurchatov Institute, Moscow, Russia
**Ecopulse, Washington, USA、 **Nihon University, Tokyo, Japan*

The X-ray spectrograph that is used simultaneously in Cauchois transmission and Johansson reflection schemes was manufactured and applied to plasma diagnostics.

1. Introduction.

Focusing x-ray spectrographs of Johann/Johansson reflection geometry and of Cauchois transmission geometry use different type of dispersive elements, so called x-ray crystals. Partially, Johann type device uses crystals with x-ray reflecting planes parallel to optical and mechanical crystal surface. Cauchois type device uses crystals with reflecting planes perpendicular to optical crystal surface. Johann/Johansson spectrograph is mainly applied for enough soft x-ray region, E<8keV, and its metal chamber should be often pumped. Cauchois spectrograph is employed to measure E>8keV and do not need pumping thanks to high penetration of analysed x-rays in air. Mentioned facts give rise to principally different design of reflection and transmission devices.

The present paper describes combined x-ray spectrograph, designed to operate both in reflection (Johann/Johansson) and transmission (Cauchois) geometry. For both regimes one metal chamber is used. Exclusively wide energy range 0.7-200 keV is achieved in comparison with existing prototypes.

Spherical Johansson quartz crystals on optical contact and mica crystals of Johann type on glue are employed in reflection scheme. Special cylindrical quartz dispersive element was manufactured for the first time to be used simultaneously in Cauchois and Johansson optical schemes. A whole series of properties of this combined device are presented. We discuss the results and what they imply to plasma diagnostics. Spectra are shown, taken from a gas puff z-pinch machine. Similar spectrometers can be used for investigation of various kind of laboratory plasmas, providing data on electron and ion temperature, electron density, ionization equilibrium, electron velocity distribution function, electromagnetic fields [1-4]

2. Operation of device in Johansson geometry.

Figure1 shows operation of device in traditional Johansson optical scheme. In our case radius of reflected planes $2R$=500 mm, where R is the radius of Rowland circle. The crystal surface

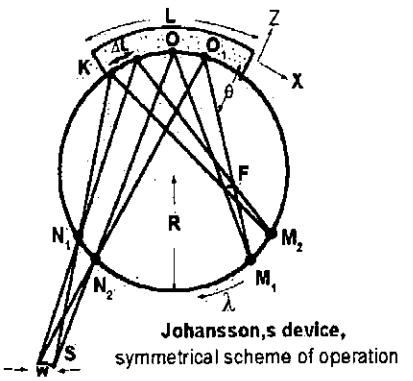

Fig.1.

lies on Rowland circle. X-ray source S can be of point type or extended one (w).

Spectra are obtained in meridional direction. Rays are reflected from crystal planes (points O, O_1), and are focused on Rowland circle at the place corresponding to Bragg,s law (points M_1).

Focal distance F_m for spherical mirror in meridional direction is:

$$F_m=(R_{cr}/2)\sin\theta \qquad (1)$$

Position F of the wavelength λ, corresponding to Bragg angle θ, is determined by relation:

$$F=R_{cr}\sin\theta \qquad (2)$$

Where R_{cr}=500 mm-radius of crystal, and F is the distance from the center of crystal to the focusing point on Rowland circle. Width of lines slightly depends on source size for Johann device, and does not depend on source size at all for Johansson one.

Image of X-ray source in different wavelength is available (if crystal is spherical, toroidal) in sagittal direction, where focal distance for wavelength λ can be found:

$$F_s=R_{cr}/2\sin\theta \qquad (3)$$

If θ~90 degrees (x-ray microscope situation) $F_m \sim F_s$, and spherical aberrations, which in some cases influence spectral resolution, are minimal.

X-ray source can be situated on Rowland circle, outside and inside it. Registered wavelength range depends on plasma to crystal distance and size of crystal in the following way:

$$\Delta\lambda=(2dL/\ell)\sin^2\theta \qquad (4)$$

where L is the length of crystal, ℓ -the length from plasma to crystal, θ-Bragg angle, 2d-intermidiate plane crystal distance.

In our device the novelty is the using of spherical Johansson crystals connected with substrates by intermolecular forces. In this case there is no any layer of uncertain thickness between crystal and substrate, and resolution is expected to be better than otherwise can be obtained. We use different cuts of quartz crystal and mica crystals. Wavelength range, available with different crystals are presented below for grazing angle range 20-80 degrees providing by our device.

Table 1. Wavelength range in A for grazing angles 20-80 degrees,
Corresponding energy range for 10(-1)0 crystal is:
first order of reflection 2.91 A-8.381 1.48 keV- 4.26 keV
second order of reflection 1.455A-4.190A 2.96 keV- 8.52 keV
third order of reflection 0.97A-2.794A 4.44 keV- 12.8 keV

quartz cut index,	d,A	1 order	11 order	111 order
10(-1)0	4.255	2.92-8.38	1.46-4.19	0.97-2.79
10(-1)1	3.343	2.28-6.58	1.14-3.29	0.76-2.19
11(-2)0	2.457	1.68-4.84	1.34-2.42	0.56-1.61
12(-3)0	1.608	1.10-3.16	0.55-1.58	0.37-1.05
13(-4)0	1.180	0.81-2.32	0.40-1.16	0.27-0.77
14(-5)0	0.928	0.63-1.83	0.31-0.92	0.21-0.61
0001	1.80	1.23-3.55	0.61-1.77	0.41-1.18
30(-3)1	1.372	0.94-2.70	0.47-1.35	0.31-0.9

We also use spherical Johann mica crystals with $2d$=19.98 A on glue. We measure soft x-rays up to E~0.65 keV (λ~19.3 A) with mica crystals at maximal grazing angle 75-80 degrees.

To use high orders of reflection it is necessary to get knowledge on reflection coefficients for these orders. We analysed relative reflection coefficients of spherical Johansson crystal with $2d$=8.51 A in second (garzing angle 32 degrees) and third (54 degrees) orders of reflection, using x-ray tube with Cr anode. Results of those measurements are shown on Fig. 2 . The conclusion is that our crystal reflection coefficient in third order of reflection is 5 times less than in second order.

Due to experimental data for 10(-1)0 cut, taken from optical plant (Alexandrov town, Moscow region), reflection coefficients at θ~45 degrees are:
first order 1.6 10-5
second order 1.13 10-5 ;
third order 0.16 10-5

Our experimental data are in reasonable agreement with those, taken from optical plant.

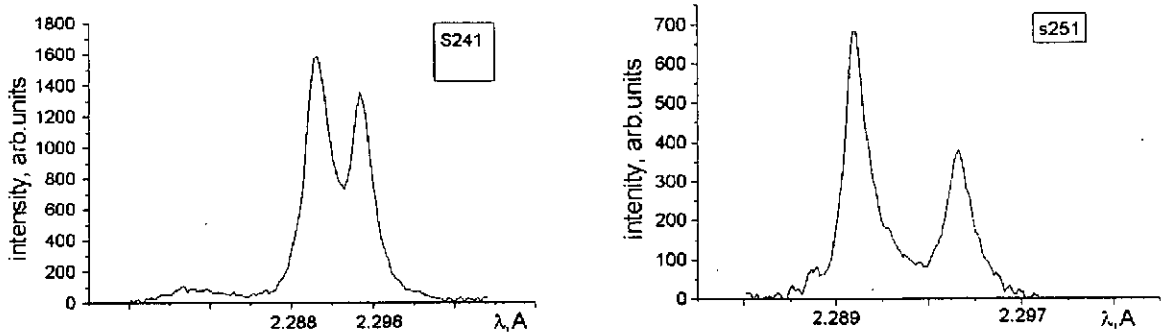

Fig. 2. Cr K-alpha lines reflected from 10(-1)0 in second (s241) and third (s251) orders.

Additional possibility is to use inclined cuts B, i.e. to measure spectra in so called non-symmetrical schemes. Spectral lines, reflected from inclined crystal planes B are focused at the same Rowland circle, as Protopopov showed it in [5]. φ is the angle between inclined cut B and main cut A, or optical crystal surface. Focal distance in meridional direction for nonsymmetrical schemes is determined:

$$F_m=(\sin^2\theta-\sin^2\varphi)/\sin\theta\cos\varphi. \qquad (5)$$

Focal distance in sagittal direction for nonsymmetrical case is :

$$Fs=(Rcr)/2\sin\theta\cos\varphi \qquad (6)$$

X-rays are reflected from given inclined cut B at Bragg angle, $2d\sin\theta=\lambda$, where θ is Bragg angle with inclined cut B. But now grazing angle with crystal surface is $(\theta+\varphi)$, reflected angle with crystal surface is $(\theta-\varphi)$. Directions to x-ray source and detector are mutually replaced, so that if detector is on Rowland circle at $(\theta+\varphi)$ direction, than x-ray source should be at $(\theta-\varphi)$ direction.

For example, let us consider crystal with mechanical crystal surface parallel to 10(-1)0 cut. Figure3 shows K-alpha lines of Cr reflected from inclined 30(-3)1 cut in 10(-1)0 crystal before chemical polishing and after it. φ=14.7 degrees, $(\varphi+\theta)$=71.3 degrees, $(\theta-\varphi)$=41.9 degrees. Reflection coefficient for Cr lines from 30(-3)1 inclined cut is compared with reflection coefficient for Cr lines in second order from 10(-1)0 cut. In general, for every crystal made in parallel to main

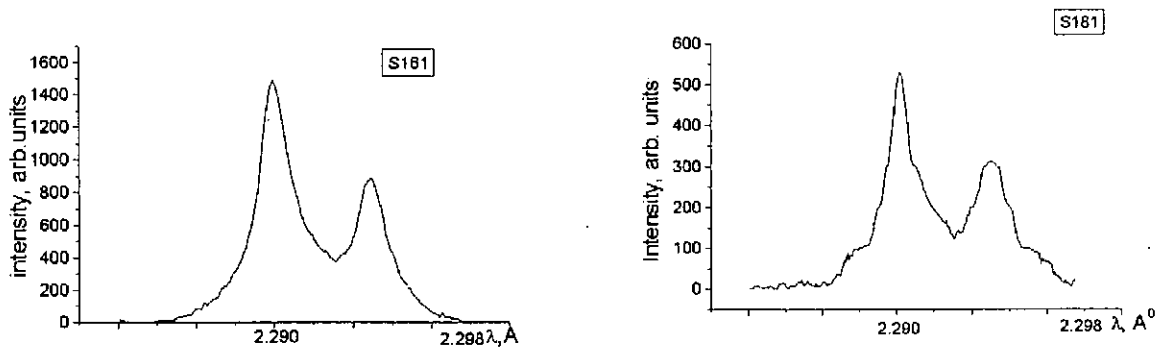

Fig.3. Cr K-alpha lines, reflected from 30(-3)1 inclined cut before polishing (s161) and after it (s181)

cut A, there are several inclined cuts B with various φ, which have appropriate reflection coefficients and can be used in x-ray measurements.

We investigated several inclined cuts close to 10(-1)0 crystal cut. We have shown that crystal made mechanically parallel to 10(-1)0 orientation has relatively high reflection coefficients and spectral resolutions of the following cuts: 10(-1)0, 20(-2)0, 30(-3)0, 13(-4)0,14(-5)0,30(-3)1, which can be successfully applied in plasma diagnostics. The plot is given in Fig.4 for some possibilities of 10(-1)0 Johansson crystal. Plot is useful to make choice what crystal cut to use for registration of necessary wavelength.

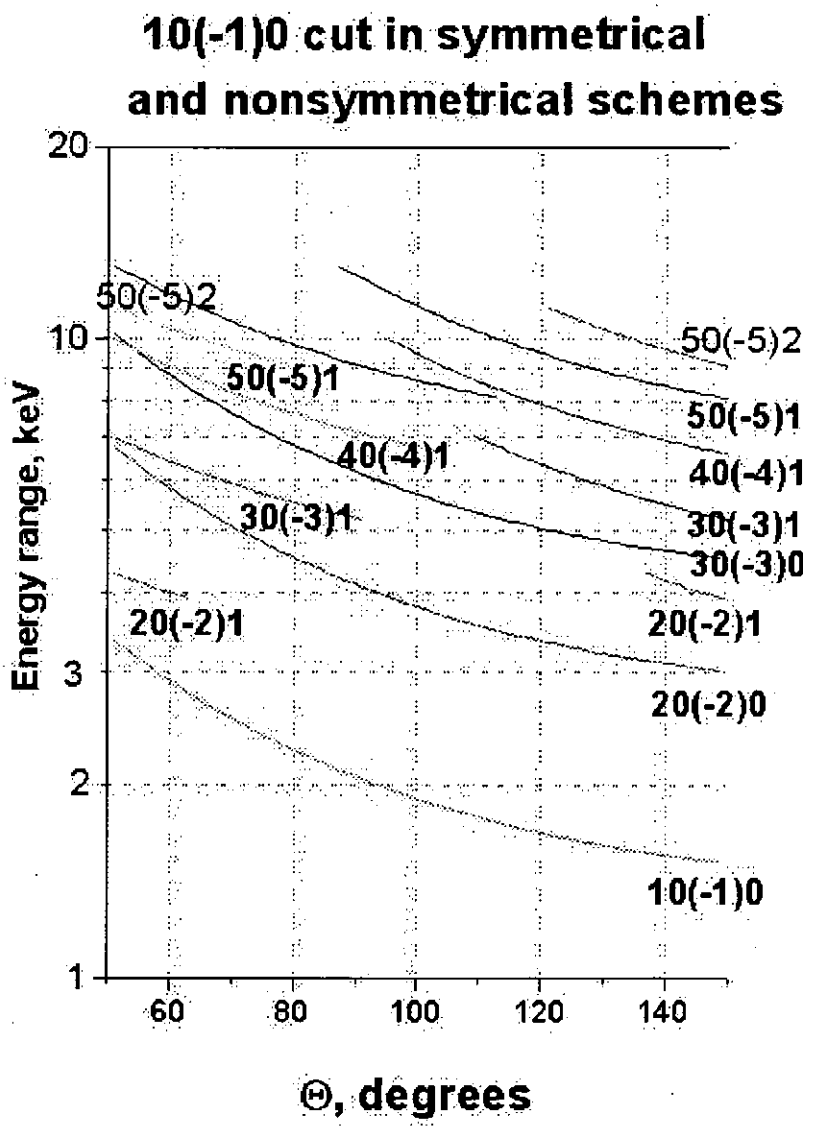

Figure 4. Plot for energy versus angle Θ for 10(-1)0 crystal and geometry of our device. Θ is angle between grazing and reflected rays with wavelength λ.

Practical knowledge of different reflection planes of given crystal is important for the next reasons:

to make right interpretation of complete spectra,
to provide incident on detector angle more close to 90 degrees to avoid defocusing of x-ray lines,
to reflect given lines from different reflection planes to check measurements,
to enlarge energy range of device with given crystal.

3. Operation of device with combined crystal both in Cauchios and Johansson geometries.

Figure 5 presents an optical scheme of Cauchois device, widely used for study x-rays E>8keV. Several cuts of quartz are usually employed in transmission schemes, such as 13(-4)0, 30(-3)1, 50(-5)1, etc.. Reflected planes B of cylindrically bent crystal are perpendicular to mechanical and optical crystal surface. For our device curvature radius of reflected planes is 500 mm, thickness of crystal is 350-400 microns.

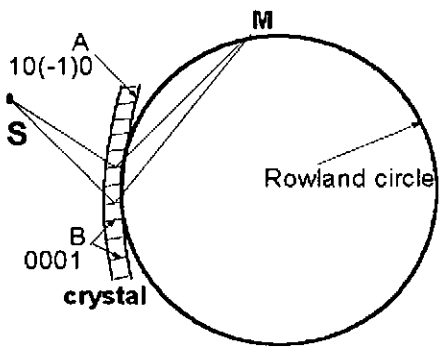

Fig.5. Optical scheme of Cauchois device

X-rays penetrate through crystal, and are reflected from x-ray planes B. Bragg's law is more convenient to use in the form:

$$E=12.4/2d\sin\theta, \qquad (7)$$

where E-energy is in keV, d in angstroms, and θ is Bragg angle.

Registered energy range depends on the source to crystal distance, length and thickness of crystal. Width of lines is influenced by crystal thickness. For usual z-pinch geometry, when x-ray source to crystal distance is 0.5-1 m, position of line essentially depends on the position of the source. The using of inclined planes is also possible for transmission geometry, with corresponding focusing of lines, reflected from inclined cuts, on the same Rowland circle.

Cauchois device can be successfully applied for investigation of Bremsstrahlung spectra [6], which provides information on electron velocity distribution function. To study Bremsstrahlung spectra it is necessary to choose crystal without overlapping of the orders, for example 13(-4)0 cut is very suitable for this goal.

We first manufactured unique cylindrical combined quartz crystal, working in both Cauchois and Johansson geometry. The main construction novelty is that all the mechanical surface of crystal lies on the Rowland circle (compare with Fig.5, where crystal contacts with Rowland circle tangentially). In our Cauchois –Johansson device position of the lines does not depend on position of the source. Quartz crystal is made as cylindrical Johansson. Optical and mechanical surface of crystal is parallel to 10(-1)0 quartz crystal planes A. Crystal made in such the way, that additional cuts in reflection regime are: 20(-2)1, 30(-3)1, 40(-4)1, 50(-5)1. Therefore in reflection regime one

can measure 1,5-13,2 keV energy range, see Fig.4. Figure 6a) gives the quality of k-alpha spectra, taken with x-ray tube in reflection from 10(-1)0 cut

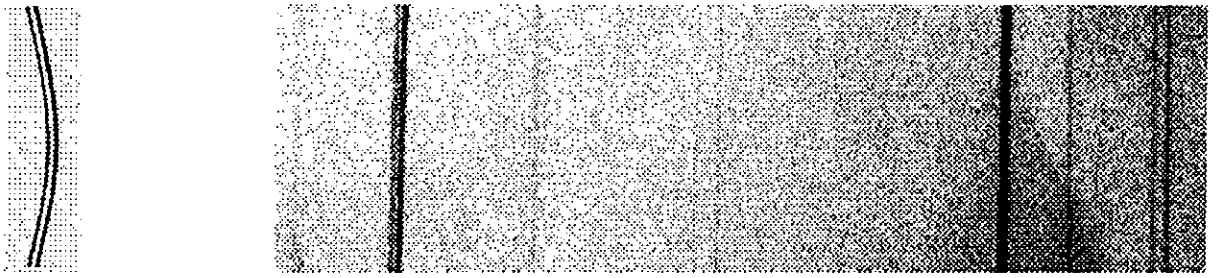

a) b)

Fig.6 Spectra, taken with cylindrical Johansson 10(-1)0 cut (6a) and spectra , taken with series of Cauchois cuts (6b). Spectra are registered with the same combined crystal.

In this 10(-1)0 crystal 0001 is additional cut B, for which φ=90 degrees, $2d$=3.6 A. This cut obviously can be used as main cut for Cauchois scheme. The cuts which are close to 0001 cut and which can also work in Cauchois scheme are : 10(-1)2, 10(-1)3, 10(-1)4, 10(-1)5, 10(-1)6. Therefore in transmission scheme with this combined crystal one can measure 3.2-400 keV energy range. Total energy range, available with this combined crystal in both reflection and transmission schemes is: 1.5-400 keV. We must mention that resolution is not so high in the vicinity 400 keV because of enough small crystal radius, so in practice maximal energy is around 200 keV. Fig 6.b shows spectra taken in Cauchois geometry from x-ray tube with Mo-anode.

Using of such cylindrical combined Cauchois-Johansson crystal in conjunction with spherical Johansson crystals and special design of device chamber provides exclusively wide energy range . Detailed knowledge on inclined cuts is very important for optimal choice of necessary cut in different experimental conditions.

The example: task is to measure E=10 keV at Bragg angle 45 degrees. Such angle is demanded to select one polarisation component of analysed x-rays. Let us consider combined Cauchois Johansson crystal, described above. Obviously, there is no solution in Johansson geometry. The solution is to use 50(-5)2 cut with d=0.812 A in Cauchois scheme.

At the end of the paper we present ArXVI spectra taken from gas puff machine to demonstrate possibilities of device in Johansson geometry with crystal 10(-1)1, which has high reflection coefficient and is recommended when spectra intensity is not enough high.

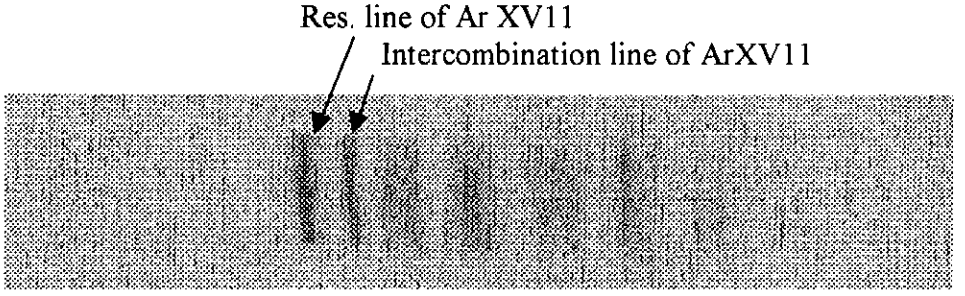

Fig.7. ArXVI spectra, emitted from gas puff machine and registered with 10(-1)1 crystal.

References

1. J.E.Rice,E.S.Marmar, and L.Qu, Nucl.Fusion 37,421,1997.
2. P.Beiersdorfer,S.von Goeler, M.Bitter et all, Rev.Sci.Instrum,60,895,1989.
3. C.DE Michelis and M.Mattiolli, Nucl.Fusion 21,677,1981.
4. Griem H.R., 1997, "Principles of Plasma Spectroscopy",New York.

5. Protopov V.N. Zav.lab,14, no2,196-201,1948.
6. Baronova E.O., Stepanenko M.M., Rantsev-Kartinov V.A.etall, Proc. Beams 98, to be published.

NANOSIZE γ-Al_2O_3 POWDER PRODUCTION BY PULSED WIRE DISCHARGE

T.Suzuki, K.Komson, W.Jiang, K.Yatsui

Extreme Energy Density Research Institute
Nagaoka University of Technology
Niigata 940-2188, Japan

ABSTRACT

Nanosize Al_2O_3 powder was produced by pulsed wire discharge. The discharge was carried out with the peak current of ~10kA, the pulse length of ~20μs, and the pulse energy of ~80J. Nanosize γ-Al_2O_3 powders have been synthesized by pulsed discharge of metal wires in oxygen as an ambient gas. The powder size and its distribution were able to control by the oxygen pressure.

I. Introduction

The particles with the size in the range of 1-100 nm were referred to nano size particle. Though these nano size particles have large specific surface area, its electrical, chemical reactivity, and optical properties are completely different from that of bulk materials. Nano size particles are rapidly absorving the attention of more and more new materials in high technology.

The method of nano size particle production is divided broadly into two categories. The chemical methods represented by sedimentation or pyrolitic decomposition are main methods at present thanks to its high productivity. But there is a difficulty to obtain nano size particle with high purity because of a matter of surface contamination or impurities content. On other hand, laser ablation method has developed recently. It has a strong point as a possibility for the formation of high purity nanosize particle, but it takes much longer time to obtain them and has a matter for high running cost. Each conventional method has a its merits and demerits.

We have put forward pulsed wire discharge to the formation of nano size particle.[1)]

The evaporated metal vapor produced by pulsed wire discharge may react with the ambient gas resulting in ceramic powders. Application of pulsed wire discharge to nanosize powder production is of potential practical use due to the following reasons.

1) The technologies for pulsed high-current generation have been very well established. Many kinds of repetitive pulsed high-current generators are available corrmercia11y.

2) By having the wire resistance higher than the other part of the circuit, one can convert most of the electrical energy to the thermal energy of the wire. In addition, the small cross section of the wire limits the energy loss caused by thermal conduction. Therefore, material heating by pulsed wire discharge may have very high energy-efficiency.

3) Pulsed wire discharge evaporates the entire wire in-stantaneously, which gives rise to a vapor that is more uniform than that evaporated from a solid surface by pulsed laser or particle bean. The vapor uniformity is considered to be very important to the size distribution of the produced powders.

In this paper, we report the effects of experimental conditions for the formation of alumina nano size particles and formation mechanism of nano size powder by measuring plasmas.

II. Experiment

The principals for nano size particle formation by pulsed discharge are illustrated in Fig.1. A pulsed current is driven through a solid wire that is located in an ambient gas [Fig. l(a)]. The current deposits electrical energy in the wire due to its finite resistance. This deposited energy melts, evaporates, and ionizes the wire material resulting in plasma that expands into the ambient gas [Fig.l(b)]. This high temperature plasma gradually cools due to its interaction with the gas, giving rise to a high temperature vapor of the wire material that condenses uniformly in the ambient gas [Fig.1(c)].

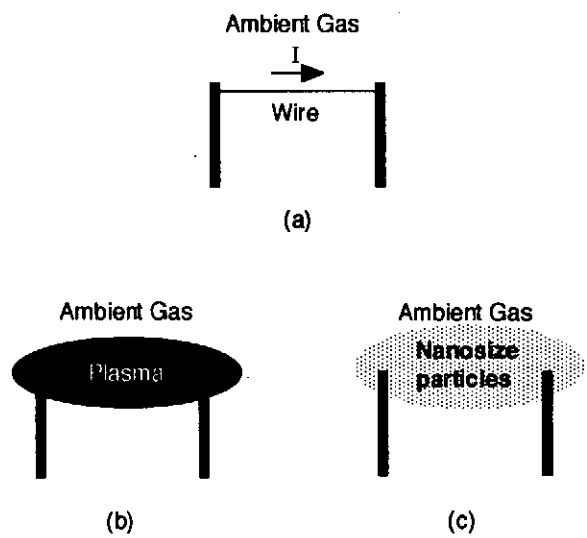

Fig.1 Principle of nanosize powder production by pulsed wire discharge.

Table 1 Experimental conditions.

Wire	Al ϕ0.25x25mm
Ambient gas	O_2 2~600 Torr
Charge voltage	4 kV
Pulse width	10μs
Pulse current	4kA
Capacitance	10μF

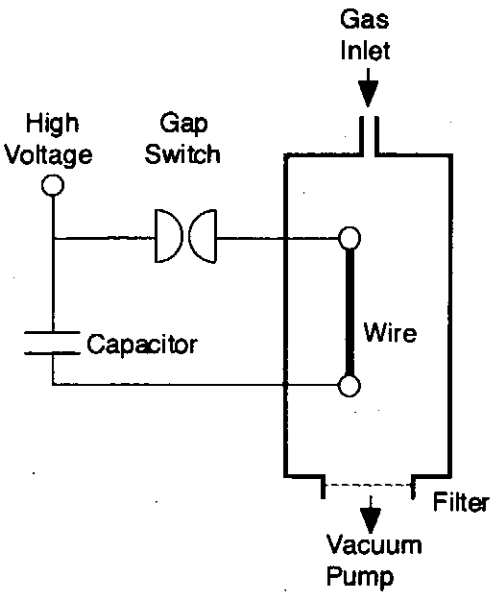

Fig.2 Experimental setup.

Pulsed discharge circuit has used for the plasma generator. Experimental conditions are shown in Table 1. Oxygen pressure has been varied 100-600Torr. Schematic diagram of apparatus ware described in Fig.2. Each Al wire is 0.25mm in diameter and 25mm in length. Wire holders were rotated after one discharge, totally 8 times discharge could be carried out without opening chamber. The energy accumulated in a condenser from the D.C. power supply would be discharged by closing gap switch, electrically charge the Al wire between electrodes and the plasma has been generated.

The particles were collected by the filter connected to the totally pump after firing 8 shots. Gas follow has not carried out.

III. Results and discussions

X-ray diffraction was used for studying the structure of the powders. XRD patterns from the particles formed at the oxygen pressure kept at 10, 60, 400Torr were shown in Fig.3(a)-(c). Totally, six peaks were identified as γ-Al_2O_3. Oxygen pressure with the range of 100-600Torr did not affect to the site of XRD peaks, but higher oxygen pressure enhanced the crystallization as γ-Al_2O_3. Some unidentified peak was observed. They are supposed to be the signal of impurity from electrodes.

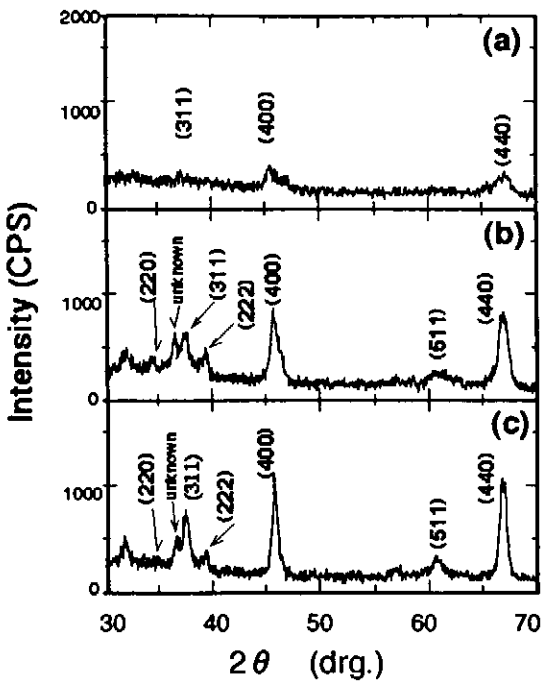

Fig.3 XRD patterns obtained from Al_2O_3 powder obtained at the oxygen pressure of (a)10Torr, (b)60Torr, (c)400Torr.

TEM observation was also carried out. Bright field image (BFI) with selected area diffraction (SAD) of the particle formed at the oxygen pressure of 100 was shown in Fig.4. Totally, seven rings in SAD were identified as γ-Al_2O_3 as same as XRD results. BFI shows that the shapes of all particles were spheres ideally, and their diameter varied in the range of 10-60nm. The distribution of diameter was obtained from the BFI as shown in Fig.5. The average of the powder was approximately 30 at the oxygen pressure of 100Torr. The width of distribution was sharpened at higher pressure.

BET (Brunauer-Emmet-Teller) measurement was carried out for the estimation of specific surface area. Specific surface area and average particle size dependence of the particle with

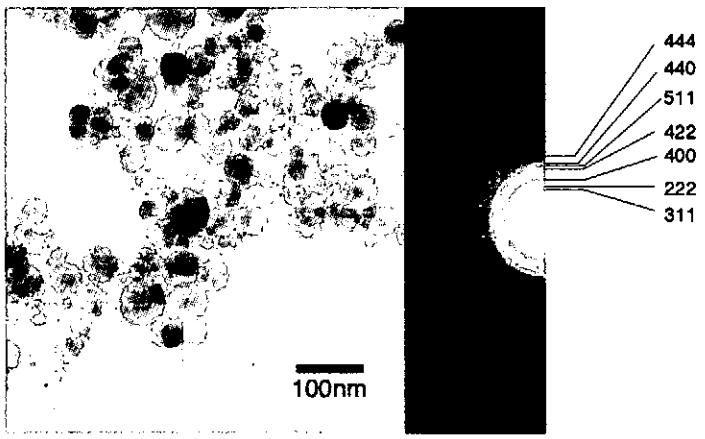

Fig.4 Bright field image and selected area diffraction of Al_2O_3 powder obtained at the oxygen pressure of 100Torr.

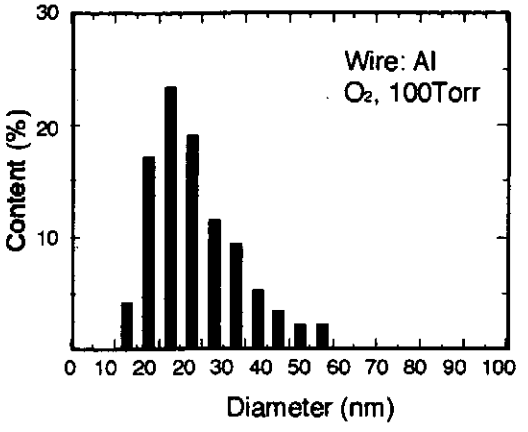

Fig.5 Distribution of average particle size.

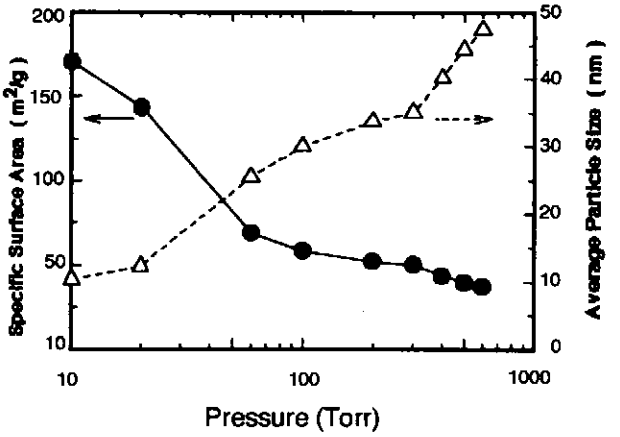

Fig.6 Oxygen dependence on average particle size and specific surface area.

oxygen pressure was shown in Fig.6. Average particle size was by BET (d_{BET}) calculated from specific surface area with following equation.

$$d_{BET} = \frac{6}{S_\rho} \times 10^{-6}$$

where, S was specific surface area (m^2/g) and ρ was density of γ-Al_2O_3 ($3.99g/cm^3$). With decreasing of oxygen pressure, average particle size was decreased; i.e. specific surface area was increased. The value of average particle size at oxygen pressure of 100 and 400Torr was approximately same as the value obtained from BFI.

Flaming picture of expanding plasma was taken for studying the changing in time. Figure 7 shows the expansion of plasma taken from front view at various time and oxygen pressure. Plasma was expanding, and kept over 360μs. At the

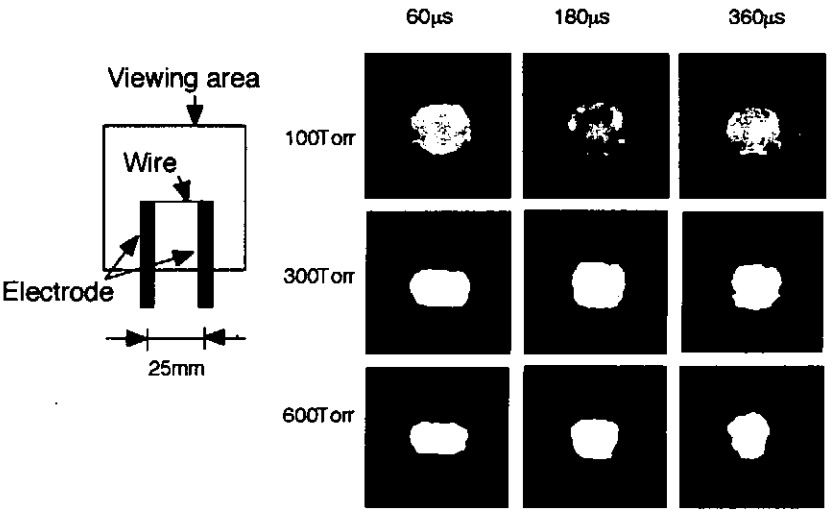

Fig.7 Flaming photograph of plasma.

higher oxygen pressure, the area of expanding plasma was getting small and luminescence was getting strong. The collisions between metal particle and oxygen atoms were occurred frequently. As results, bigger powder was obtained at high oxygen pressure.

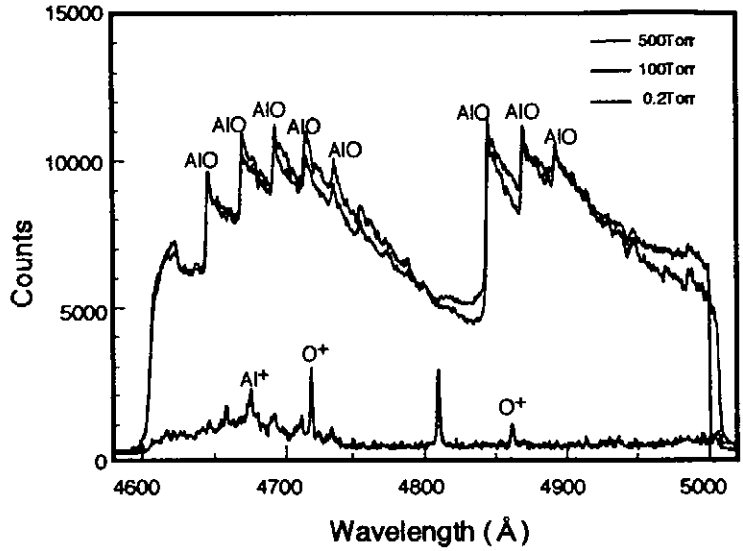

Fig.8 Luminous spectram taken from the plasma.

Luminous spectram taken from the plasma formed at oxygen pressure of 0.2, 100, and 500Torr are shown in Fig.8. At oxygen pressure of 0.2Torr, only spectra caused by aluminum ion and oxygen ion were observed. At higher oxygen pressure, AlO peak was observed. In case of making metal oxide powder by pulse wire discharge, it was considered that Al atoms were already combined with oxygen atoms at the plasma state.

Reference

1) W. Jiang, and Y. Yatsui, "Pulsed Wire Discharge for Nanosize Powder Synthesis", IEEE Transaction on Plasma Science, VOL 26, 1498-1501 (1998).

FABRICATION OF GAS SELECTIVE FILTER USING ULTRA FINE POWDER

Y. Kinemuchi, T. Suzuki, W. Jiang and K. Yatsui

Extreme Energy Density Research Institute, Nagaoka University of Technology, Nagaoka, Niigata, 940-2188, Japan

ABSTRACT

Gas selective filter has been successfully fabricated by collecting ultra fine powders on heated porous substrate. Since powders are very small, the powders float in the chamber like aerosol. Evacuation through the porous substrate resulted in accumulation of the powders on the substrate. Since gas tends to permeate large pore prior to small pore, the powder is accumulated from large pore. The powders were sintered on the heated substrate, resulted in porous membrane. Gas separation experiments showed that the ratio of gas permeation values was nearly similar to the square root of the ratio of the molecular masses of each gas. Therefore, Knudsen diffusion took place in the filter, which enables to separate gases having different molecular mass

I. Introduction

Because of environmental concern, filtration technology using membrane is focused on as low cost process. Organic filter have been adopted in various applications. However, applicable temperature is limited below 200℃. In contrast with organic filter, ceramic filter is enable to operate up to 1,000℃. Further, ceramic filter has superior chemical resistance. Owing these advantage, there are applications such as micro-filtration (10 nm < pore size < 10 μ m), ultra-filtration(pore size < 10 nm), filtration of molten metal, gas separation under high temperature, and particle removal from exhausted gas of diesel engine.

Most commercial ceramic filter is produced by the powder metallurgy process. The permeability of them is low due to low porosity and long permeate pass. In order to increase permeability, high porosity filter is fabricated using whisker network.[1] However, this method has practical limitation for the small pore size. Another method is to fabricate asymmetric filter.[2-4] Asymmetric filter consists of several layers with different pore sizes. Permeability increases by thinning the layer with small pore size. Coating by Sol gel method or CVD are proposed. Problems of the process are crack generation in Sol gel method and process cost of CVD.

To solve the problem, new method using ultra fine powder (UFP) is proposed in the

present paper. UFP is small particle less than 100 nm, and float in gas. Using the characteristics of UFP, fabrication of gas selective filter was attempted.

II. Experimental

Fabrication process of gas selective filter consists of two processes. One is fabrication of UFP and the other is sintering of UFP on a porous substrate. UFP was fabricated by means of pulsed wire discharge. Experimental arrangement is shown in Fig. 1. In pulsed wire discharge, high density plasma is produced with applied pulsed current (10 μ s, 10^6 A/cm^2) to the wire. Gas surrounding plasma condenses plasma into UFP. When the gas is reactive to the plasma, compounds such as oxide is formed. In the present study, pulsed current was applied to aluminum wire (diameter: 0.25 mm, length: 25 mm). Atmosphere was 40 Torr of oxygen. Applied energy was 80 J, which was charged in the condenser with 10 μ F of capacitance. Thus, the energy density in the wire was 670 kJ/mol that is twice the sublimation energy of aluminum. Formed UFP was collected on porous aluminum substrate by evacuation. The substrate was heated up to sintering temperature before evacuation. Sintering was carried out at 500, 600 and 700 ℃ for 30 min.

The size of UFP was estimated basing upon specific surface area measured by using BET. Since shape of the UFP fabricated by present method is sphere, the size is given by $6/(S\rho)$ where S is specific surface area and ρ is density. In order to clarify phase stability of UFP at sintering temperature, sintered UFP was investigated by using XRD. The surface of filter was observed by using SEM. Gas permeation was measured for H_2, O_2 and CO_2 in order to confirm permselectivity.

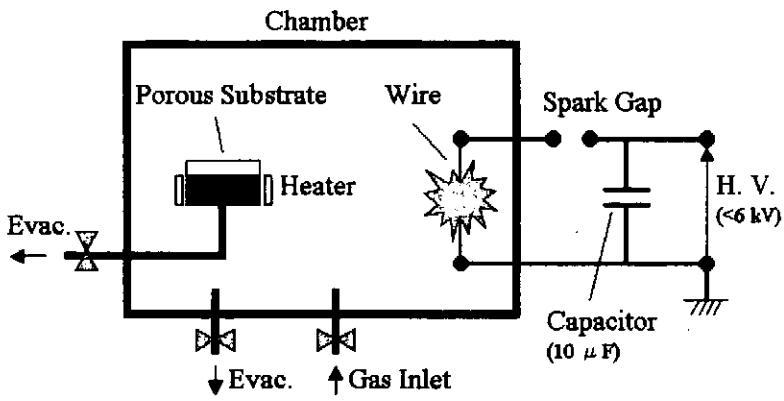

Fig. 1 Schematic illustration of experimental set up. Pulsed current applying to the wire results in formation of plasma that condensed by gas in chamber. The condensed plasma forms UFP that accumulates on the heated porous substrate by evacuation.

Table I Specific surface area of UFP and average particle size converted from specific surface area.

Specific surface area (m^2/g)	Average particle size (nm)
91±9	23±2

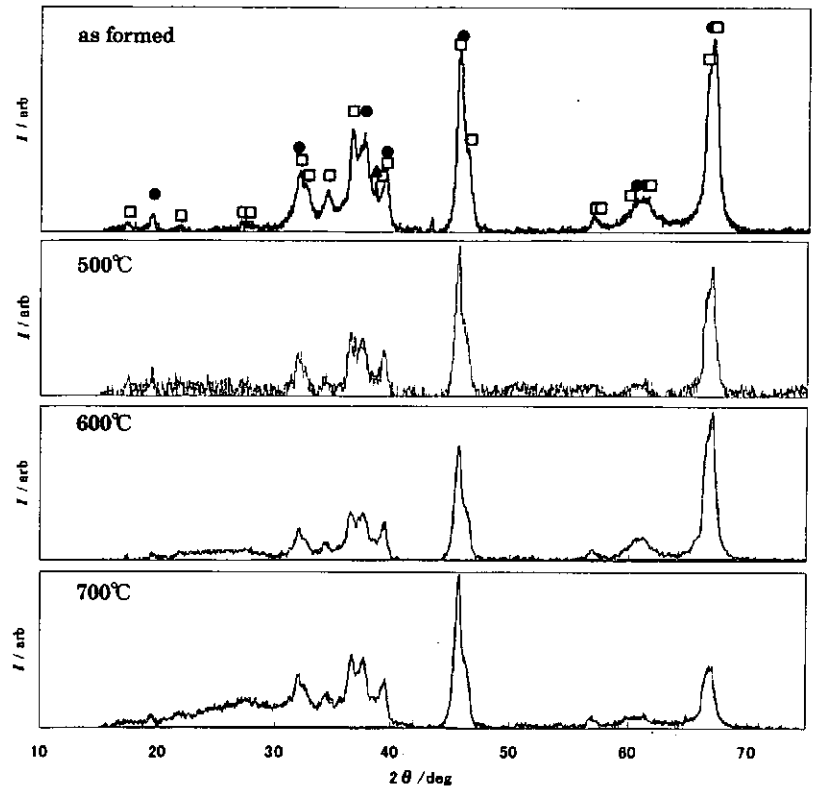

Fig. 2 X-ray diffraction pattern of as formed and sintered UFP. The marks of ●, □ and ▲ indicate γ -Al_2O_3, δ -Al_2O_3 and Al, respectively.

III. Results

The average particle size of UFP was about 20 nm as shown in Table I. Major constitution phases before and after sintering were γ - and δ - Al_2O_3 as shown in Fig. 2. Aluminum was also detected as minor phase. Phase transformation from δ to α was not observed below 700℃. Surface of filter is shown in Fig. 3. As a comparison, surface of substrate is also shown. The size of particle was larger than the average particle size measured by BET. This is due to sintering of UFP because the particle size became larger as increasing sintering temperature. Distance between particles decreased as increasing the temperature. Permeate is shown in Fig. 4 as a function of sintering temperature. Lines indicate permeability of substrate. Permeate decreased after forming UFP filtering layer. Decreased amount was large for light gas. Figure 5 shows permselectivity for H_2/CH_4 and H_2/O_2 as a function of sintering temperature. The permselectivity increased as increasing sintering temperature.

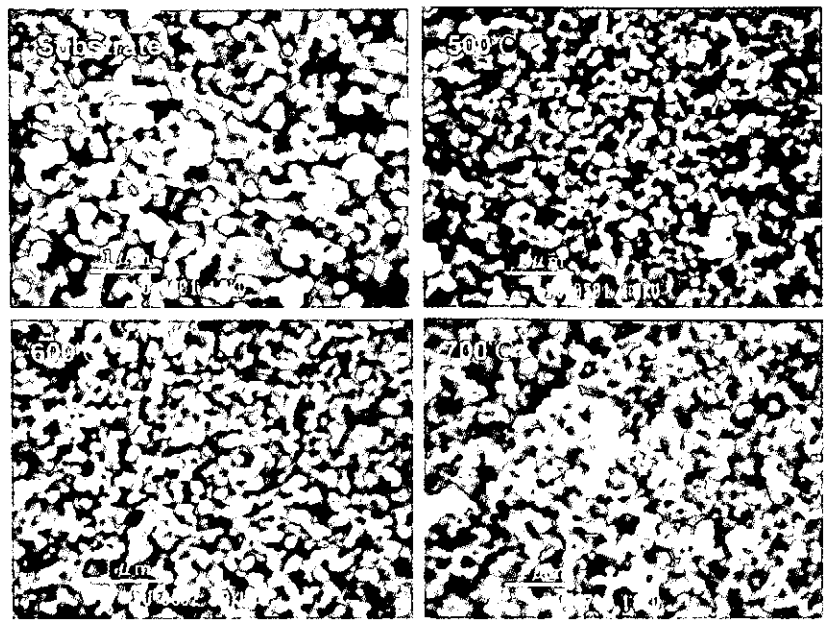

Fig. 3 SEM photograph of surfaces of substrate and filters.

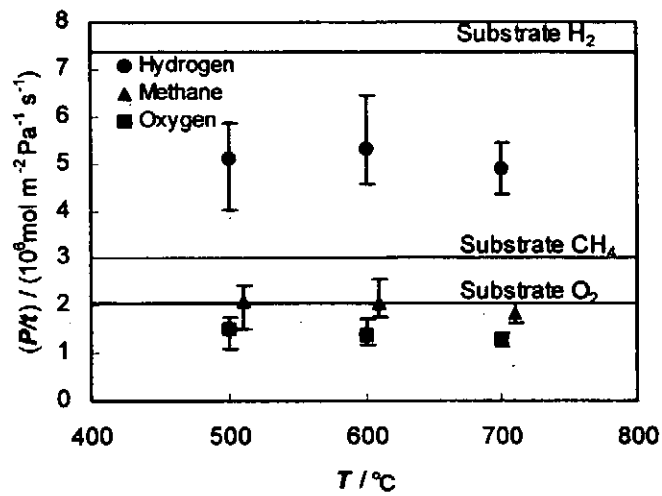

Fig. 4 Permeate (P/t) as a function of sintering temperature (T).

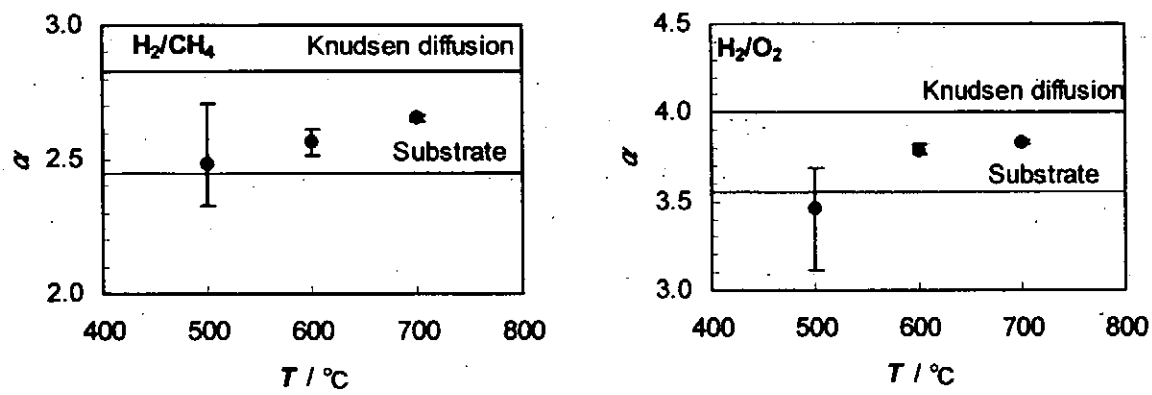

Fig. 5 Permselectivity (α) for H_2/CH_4 and H_2/O_2 as a function of sintering temperature (T).

IV. Discussions

The flow rate of gas through filter (q) depends on permeability (P), pressure difference (p_h - p_l) and the thickness of filter (t). The relation between the parameters is expressed as:

$$q = P\frac{p_h - p_l}{t} \tag{1}$$

It is practical to use filter with high flow rate among filters having same ability. In this sense, thickness has to be thinner as much as possible, according to Eq.(1). Asymmetric filter is produced for this purpose as mentioned in introduction. To increase permeability is also effective to increase the flow rate. Often, permeate (P/t) is used to evaluate gas flow for asymmetric filter.

Fabricated filters consisted of porous substrate and sintered UFP layer. Permeate of them was about 70 % of that of substrate. This is same order of permeate reported by others.[5,6]

Gas separation is possible by using difference of flow rate. When pore radius (r) is larger than five times as long as mean free path (λ), gas flow is governed by Poiseille flow. Under atmospheric conditions, λ of oxygen is about 60 nm. Therefore, Poiseille flow occurs in the filter with 300 nm of pore radius for oxygen. Poiseille flow is expressed by the following equation.

$$q = \frac{r^4\varepsilon(P_h + P_l)}{8\eta RT}\frac{P_h - P_l}{t} \qquad \left(\frac{r}{\lambda} > 5\right) \tag{2}$$

Here, ε indicates porosity, η viscosity, R gas constant and T temperature. Since each gas has different viscosity, it is possible to separate gases in this flow. Viscosity of H_2, CH_4 and O_2 are 8.8, 11.0, 20.4 Pa·s, respectively. Permselectivity using Poiselille flow becomes 2.3 and 1.25 for H_2/O_2 and H_2/CH_4, respectively. When the pore radius is smaller than the mean free path, flow of gas follows Knudsen flow that is expressed as following.

$$q = \frac{4}{3}r\varepsilon\left(\frac{2}{\pi MRT}\right)^{\frac{1}{2}}\frac{P_h - P_l}{t} \qquad \left(\frac{r}{\lambda} < 1\right) \tag{3}$$

Here, M is molecular mass. Equation 3 indicates the gas separation using the difference of molecular mass. Permselectivity using Knudsen flow is 4.0 and 2.8 for H_2/O_2 and H_2/CH_4, respectively. Within the intermediate range ($1<(r/\lambda)<5$), both Poiselille and Knudsen flows occur. Permselectivity in this range takes the value between Poiselille and Knudsen.

As increasing sintering temperature, permselectivity increased from that of substrate to that of Knudsen. Because permselectivity of substrate was higher than that of Poiseille, pore radius is smaller than 300 nm. Enhancement in permselectivity as increasing sintering

temperature indicates decrease in pore radius. Pore radius depends on packing of powder and shrinkage of powders. Packing is mainly influenced by pressure. High pressure leads dense packing. Since pressure condition during UFP collection was the same in the experiments, decrease in pore radius was caused by shrinkage of powder as seen in Fig. 3.

Porous substrate was sintered at 1300℃, which results in no shrinkage of porous substrate during formation of UFP layer. The mismatch of shrinkage between substrate and UFP layer normally causes crack in UFP layer. The generated crack may erase in present process, because sintering and powder collection are carried out simultaneously. Gas passes through fast along crack. Due to the gas flow, UFP is gathered and sintered on the crack. This is the main reason to succeed the fabrication of gas selective filter.

V. Conclusions

Fabrication of gas selective filter was attempted using alumina-UFP fabricated by pulsed wire discharge. Permselectivity of the filter was evaluated by measuring permeate of H_2, CH_4 and O_2 gas. Followings are concluded.

1. Gas selective filter has been successfully fabricated by collecting and sintering of UFP on porous substrate.
2. The gas diffusion through the filter follows Knudsen diffusion. As increasing sintering temperature, permselectivity is closed to the theoretical value, which is a result of shrinkage of powders.

References

1) C. Kawai and A. Yamakawa, "Network Formation of Si_3N_4 Whiskers for the Preparation of Membrane Filters", J. Mater. Sci. Lett., **17**, 873-875(1998).

2) T. Yoshida, I. Mukouzawa, Open for Japanese Patent, H6-73557(1994).

3) C. Kawai, A. Yamakawa, Open for Japanese Patent, H6-239674(1994).

4) K. Torii, T. Iwasaki, Y. Onodera, H. Hayashi, Japanese Patent, No.2125054.

5) S. Vercauteren, K. Keizer, E. F. Vansant, J.Luyten and R. Leysen, "Porous Ceramic Membranes: Preparation, Transport Properties and Applications", J. Porous Mater., **5**, 241-258(1998).

6) J. C. D. Da Costa, G. Q. Lu, H. Y. Zhu and V. Rudolph, "Novel Composite Membranes for Gas Separation Preparation and Performance", J. Porous Mater., **6**, 143-151(1999).

CHARACTERISTICS OF (Cr, Al) N THIN FILMS PREPARED BY PULSED LASER DEPOSITION

M. Hirai, Y. Ueno, Y. Kinemuchi, T. Suzuki, W. Jiang, C. Grigoriu, and K. Yatsui

Extreme Energy Density Research Institute, Nagaoka University of Technology, Nagaoka, Niigata 940 – 2188, Japan

ABSTRACT

Chromium aluminum nitride ((Cr, Al) N) thin films have been successfully prepared by pulsed laser deposition (PLD). The (Cr, Al) N film, which is hard and resistant against wear and oxidation, is one of the most promising pseudobinary nitrides for applications in the protective coatings. These films were synthesized by depositing chromium and aluminum metal vapors in nitrogen. Experiments were carried out by changing the surface area ratio of the target (Al/(Cr+Al)) from 0 to 100 %. From the results of energy dispersive X-ray spectroscopy (EDS) and Rutherford back-scattering spectroscopy (RBS), we have found that the metal content ratio of the films agreed well with the surface area ratio of the target. The film hardness showed the maximum value (HV ~ 2700) at the AlN content ratio of 75 at. %, being in a reasonable agreement with the theoretical prediction. Phase transition from B1 (NaCl) structure to B4 (wurtzite) structure occurred at the AlN content ratio of 75 ~ 80 at. %. The hardness of (Cr, Al) N films has been found to be much stronger than that of CrN.

I Introduction

Chromium nitride (CrN) coatings are being applied for various metal forming operations, for plastic manufacturing, for cutting copper alloys as well as for machinery elements[1~3]. Presently, titanium nitride (TiN) coatings are used most widely in industry[4, 5]. CrN is characterized by a slightly lower hardness than TiN but shows a significant higher oxidation temperature[3].

The film of (Cr, Al) N solid solution is obtained to dissolve aluminum nitride (AlN) in CrN. AlN has attracted considerable attention in the past owing to its high thermal conductivity, chemical stability and hardness[6]. These characteristics are required to improve the wear resistance of coating material. By adding AlN to CrN, both hardness and oxidation resistance can be significantly improved compared with pure CrN[3]. In addition, AlN has the largest solubility into CrN among various transition nitrides with B1 structure[7~9].

In the present, (Cr, Al) N films have been synthesized by the PLD method. Different techniques have been reported for depositing (Cr, Al) N films, including cathodic vacuum arc evaporation, magnetron and rf-assisted magnetron sputtering[3, 7~9]. Considering the lifetime, a coating film is required to be thick enough. The PLD method, where high deposition rate and low temperature deposition are available, is suitable to prepare a coating film.

It was the aim of this investigation to identify the extent of solid solution of (Cr, Al) N film prepared by PLD method, by the determination of the physical properties for these films.

II Experimental setup

Figure 1 shows the schematic diagram of the experimental apparatus. The films were deposited by the irradiation of a Nd:YAG (355 nm) laser beam onto the target. The laser was electro-optically Q switched by a Pockels cell to produce intense pulses of short duration (~ 7 ns) by the repetition rate of 10 Hz. A laser beam was concentrated by lens, and the energy density was adjusted to 2 J/cm^2 on the target. As a target, we used 99.9 % chromium and 99.5 % aluminum plate.

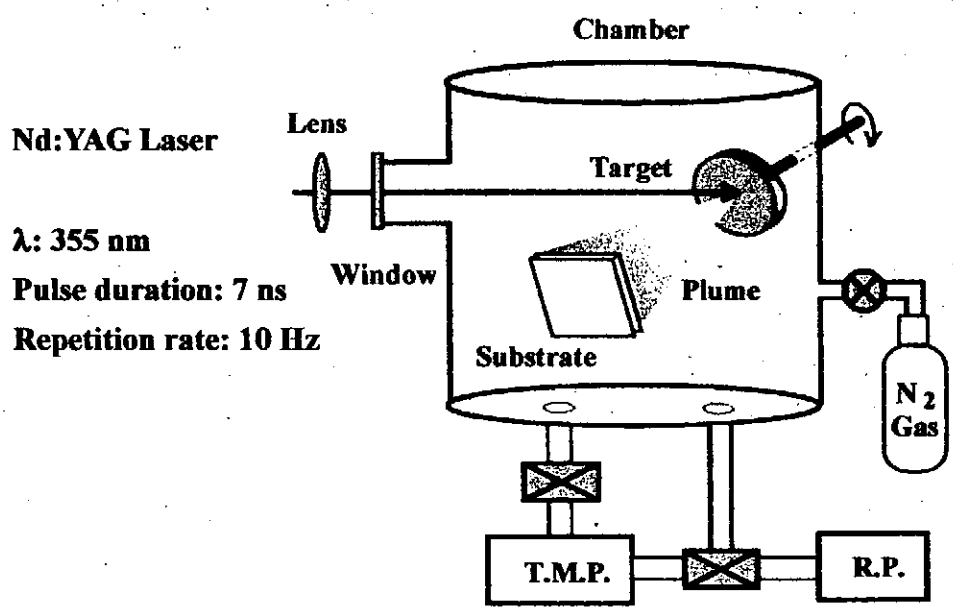

Fig. 1 Experimental setup.

The variation of Cr/Al content was obtained by changing the irradiated area of Cr and Al plate. The chamber was evacuated to 3×10^{-6} Torr with a rotary pump and a turbo molecular pump. The experiments were carried out at a nitrogen pressure of 50 mTorr. A single-crystal (100) oriented silicon substrate was placed at the distance of 40 mm from the target. Using a heater and a thermocouple, the substrate temperature was controlled. Typical experimental conditions are shown in Table 1.

Table 1 Experimental conditions.

Fluence	2 J / cm^2
Target	Cr, Al
Substrate	Si (100)
Distance (d_{TS})	40 mm
Substrate temperature	400 °C
Nitrogen pressure	50 mTorr
Surface area ratio of target (Al/(Al + Cr))	0, 25, 50, 75, 100 %

The elemental composition of the films was measured by EDS and RBS. Surface morphology has been evaluated by scanning electron microscope (SEM). Crystalline phases of the films were identified by X-ray diffraction (XRD) using CuKα radiation at the operating conditions of 40 kV and 30 mA. Infrared spectrometer was used to obtain the IR absorption characteristics of the films. The hardness of the films was measured by Vickers indenter. The film thickness was measured by using a surface profiler.

Ⅲ Results and discussion

Figure 2 shows the metal content ratio of the films as a function of the surface area ratio of the target. The composition ratio of the films can be seen to be coinciding well with the surface area ratio of the target by PLD method. Thus, it is possible to control the composition ratio of the film.

Figure 3 shows SEM image of (Cr, Al) N film at the AlN content of 50 at. %. Although there were some droplets on the film, the exfoliation of the film could not be found. Vapor produced by pulsed laser ablation of the target is usually found to contain atoms, ions, molecules, clusters, and particles.

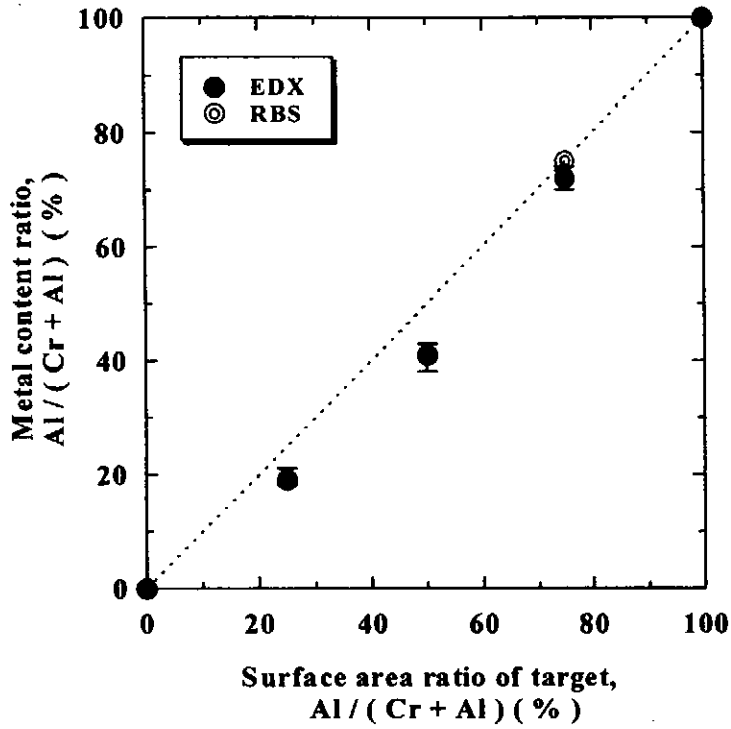

Fig.2 Metal content ratio of film as a function of surface area ratio of target.

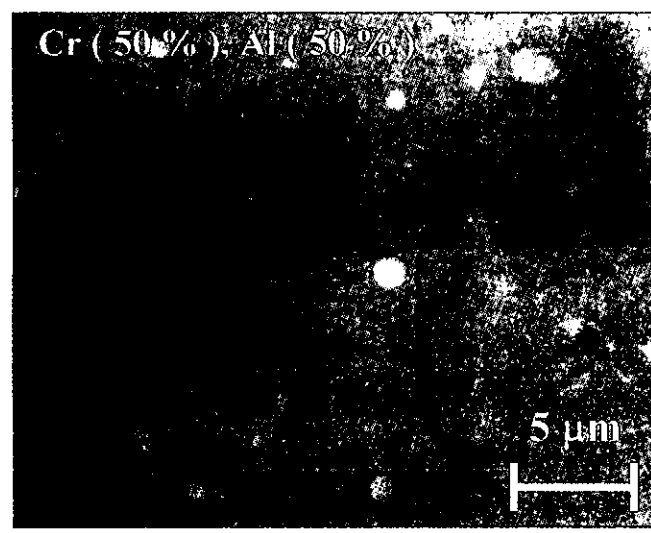

Fig.3 SEM image of (Cr, Al) N film.

Liquid particle deposited on the film is called droplet, which will form defects in the film. The presence of the droplets is one of the problems of the PLD method, and the diameter of big one was reported to be several ten μm[10, 11]. As a consequence, the lifetime of the coating material should be lowered at the poor roughness. In this case, there were a few droplets on the film, the diameter of which was less than 1 μm. The film surface in the absence of the droplets was found to be very smooth.

Figure 4 shows XRD pattern of (Cr, Al) N films. The film with AlN content of 0 at. % appeared a diffraction peak near 44°. Cubic CrN and hexagonal Cr_2N are known in the bulk chromium-nitrogen equilibrium system[12]. This film was considered to consist mainly of CrN and Cr_2N. With increasing AlN content, the peak near 44° is seen to shift to high angle side. It seems to be due to the fact that chromium atoms in the CrN lattice were replaced by aluminum atoms with smaller atomic radius. (Cr, Al) N film is known to be substitutional solid solution. The film with AlN content of 100 at. % wasn't crystallized.

Figure 5 shows the lattice constant as a function of metal content ratio. The dotted line indicates the lattice constant of CrN (JCPDS)[13]. The lattice constant with AlN content of 0 at. % was a little bit bigger than JCPDS data. It seems to be due to the influence of internal stress in the film. As the AlN content in (Cr, Al) N film increased, the lattice constant decreased from 4.19 Å to 4.08 Å.

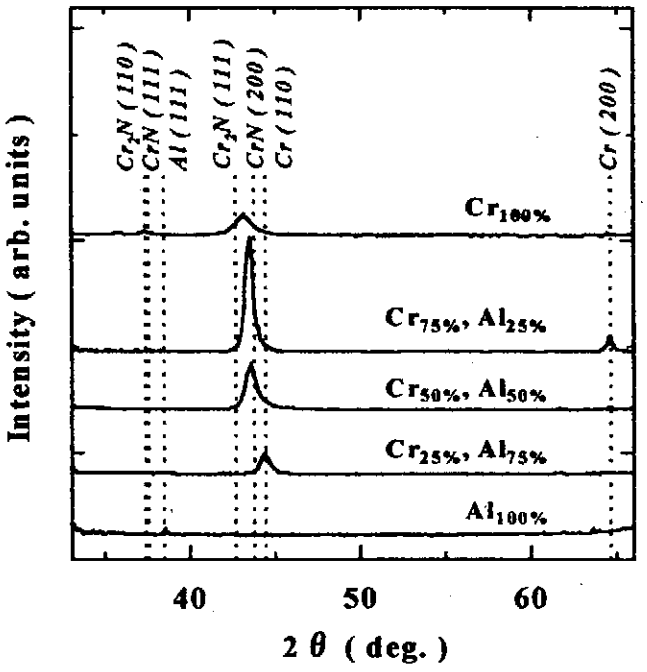

Fig. 4 XRD pattern of (Cr, Al) N films.

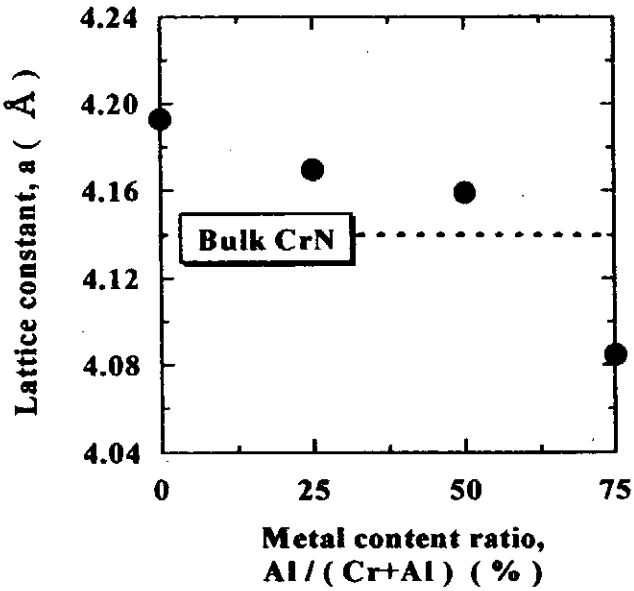

Fig. 5 Lattice constant as a function of metal content ratio.

Figure 6 shows FT-IR spectra of (Cr, Al) N films. Characteristics of IR absorption were determined from 1400 to 400 cm^{-1}. These spectra were obtained by the subtraction of Si (100) substrate background. The thickness of each film was about 800 nm. The RBS measurement has shown the compound of the oxygen of ~10 at. % in the film. Absorption attributable to the vibration of Cr-O and Al-O bonds has been known to appear peak at near 410 and 460 cm^{-1}, [14] but the absorption of these bond wasn't confirmed. The strong absorptions centered around 560 and 730 cm^{-1} are attributed to the vibration of Cr-N and Al-N bond respectively[14]. The absorption near 500 cm^{-1} is due to (Cr, Al) N, and this type of absorption decreased with increasing AlN content. It has been indicated from chemical bond that (Cr, Al) N films are B1 structure up to the AlN content of 75 at. %.

Figure 7 shows Vickers hardness as a function of metal content ratio. The hardness was determined with the critical load of 5 gf. The indenter penetrated about 200 nm into the film. The number of measurements was 7 times, and the hardness was evaluated to take out the minimum and maximum values. The film hardness increased monotonically with the increase in AlN content, but decreased rapidly above ~75 at. %. The maximum hardness of (Cr, Al) N film was obtained HV~2700 at the AlN content ratio of 75 at. %, which is much higher than that of CrN ~2300, seems to be due to solid solution hardening that restricts the movement of dislocation. Phase transition from B1 to B4 structure has been reported to occur at the AlN content ratio of 70 ~ 80 at. %. Thus, the hardness of (Cr, Al) N film thus observed has been revealed the film become the hardest near the solubility limit.

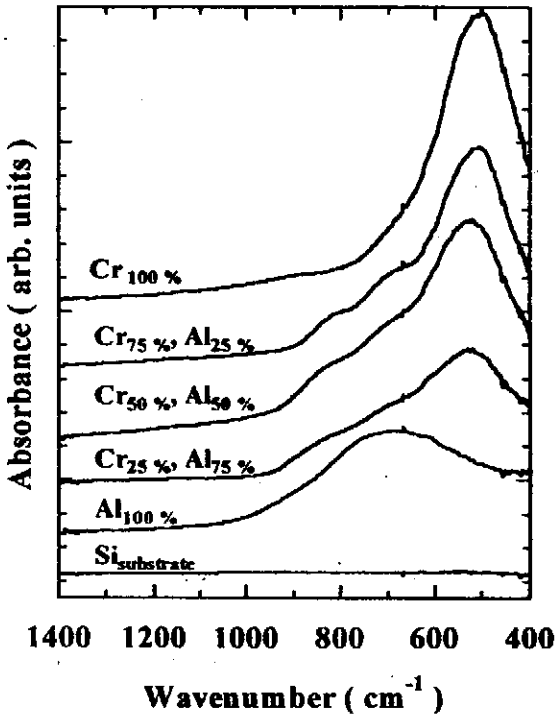

Fig. 6 FT-IR spectra of (Cr, Al) N films.

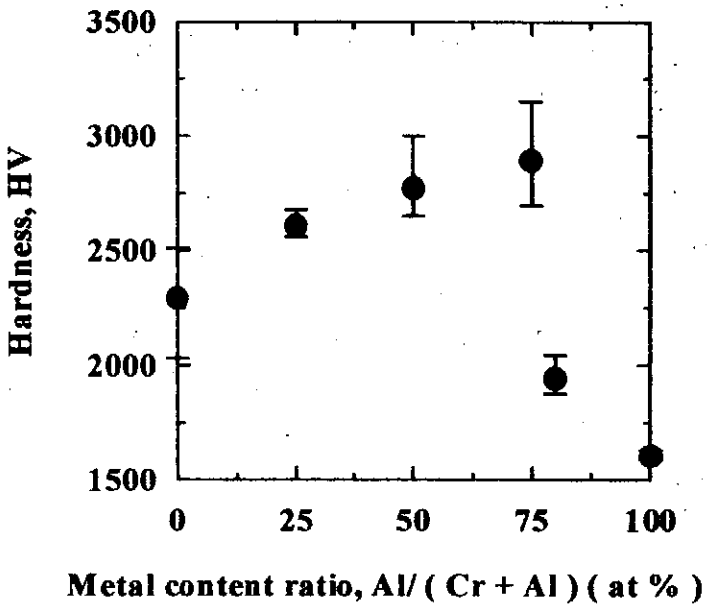

Fig. 7 Vickers hardness as a function of metal content ratio.

Ⅳ Conclusions

From these experimental results, we have obtained the following conclusions:

1) (Cr, Al) N films have been successfully prepared from metal targets by PLD method.
2) The hardness of (Cr, Al) N film increased monotonically with increasing AlN content up to ~75 at. %, above which it decreased rapidly.
3) The solubility limit of AlN in CrN is about 75 at. %, being in a reasonable agreement with the theoretical estimate.

References

1) T. Kacsich, M. Neubauer, U. Geyer, K. Baumann and F. Rose : J. Phys. D: Appl. Phys., **28** (1995) 424.
2) Y. Tsuchiya, K. Kosuge, Y. Ikeda, T. Shigematsu, S. Yamaguchi and N. Nakayama : Material Transactions, TIM, **37** (1996) 121.
3) J. Vetter, E. Lugscheider and S. S. Guerreiro : Surface and Coating Technology, **98** (1998) 1233.
4) J. C. S. Kools, C. J. C. M. Nillesen, S. H. Brongersma, E. van de Riet and J. Dielman : J. Vac. Sci. Technol., **A10** (1992) 1809.
5) I. N. Mihailescu, N. Chitica, L. C. Nistor, M. Popescu, V. S. Teodorescu and I. Ursu : J. Appl. Phys., **74** (1993) 5781.
6) S. Kumar and T. L. Tansley : Jpn. J. Appl. Phys., **34** (1995) 4154.
7) Y. Makino : Materials Science and Engineering, **A 192 / 193** (1995) 77.
8) A. Sugishima, H. Kajioka and Y. Makino : Surface and Coating Technology, **97** (1997) 590.
9) Y. Makino and K. Nogi : Surface and Coating Technology, **98** (1998) 1008.
10) E. van de Riet, C. J. C. M. Nillesen and J. Dieleman : J. Appl. Phys., **74** (1993) 2008.
11) D. Feiler, R. S. Williams, A.A. Talin, H. Yoon : J. of Crystal Growth, **171** (1997) 12.
12) ASM International : Binary alloy phase diagrams (1990) CD-ROM .
13) Pinsker, Ambrosimova and Kristallografiya : Sov. Phys. Crystallogr., **3** (1958) 285.
14) R.A. Nyquist and R. O. Kagel : " Infrared spectra of inorganic compounds ", (Academic Press, 1971), pp114-216.

PRODUCTION OF A NANOCRYSTALLINE AND AUSTENITIC PHASE ON A HIGH-SPEED TOOL STEEL SURFACE BY THE IRRADIATION OF INTENSE PULSED ION BEAM

Hiroshi Akamatsu, Yoshisuke Tanihara, Tsutomu Ikeda*, Kingo Azuma, Etsuo Fujiwara, and Mitsuyasu Yatsuzuka

Himeji Institute of Technology, 2167 Shosha, Himeji, Hyogo 671-2201, Japan
*Ion Engineering Research Institute Corporation, 2-8-1 Tsudayamate, Hirakata, Osaka 573-0123, Japan

ABSTRACT

A hydrogen-intense pulsed ion beam with the ion energy of 180 keV, ion beam current density of 500 A/cm^2 and pulse duration (F.W.H.M.) of 65 ns was irradiated on a high-speed tool steel (SKH51), resulting in production of an austenitic phase composed of nanometer-sized polycrystals on the target surface. The average grain size in the austenitic phase was 40 nm. The treated depth was observed to be approximately 7 μm from the surface, and the second phase carbides were removed from the treated region.

1. Introduction

Intense pulsed ion beams (IPIBs) provide a new technology for metal surface modification.[1-14] The IPIBs with high energy and short pulse duration enable to modify a metallic material by a rapid melting and cooling treatment. In the scheme, the typical cooling rate is estimated to be 10^7-10^9 °C/s,[14] resulting in formation of non-equilibrium microstructures such as amorphous,[5-7] nanocrystalline[8,9,11] or metastable phases with improved mechanical and chemical properties.

Tool steels are composed of a martensitic structure in low temperature. The martensitic structure is transformed into an austenitic structure in high temperature above a transfer temperature. The austenitic structure is usually unstable in low temperature. However, if the austenite is so rapidly cooled that the transformation from the austenite to the martensite is prevented, the resolidification of the austenitic phase is realized in low temperature. Besides, the rapid melting and cooling treatment by irradiation of IPIBs enables to produce the austenitic structure in the only surface layer of the martensitic sample. In this paper, production of an austenitic structure composed of nanometer-sized polycrystals on a high-speed tool steel surface by IPIB irradiations is successfully demonstrated.

2. Experimental

A hydrogen-IPIB was generated by an inverse pinch ion diode (IPD)[15] using the pulsed power machine "HARIMA-II" (maximum output voltage: 400 kV, output impedance: 3 Ω, pulse duration: 50 ns). Figure 1 shows a scheme of the IPD and a target. The IPD consists of a cylindrical cathode with the diameter of 18 mm and a flat ring anode with the diameter of 50 mm, where the gap length between the

anode and the cathode is 4.75 mm. An acrylic of 2 mm in thickness is attached on the anode surface as an ion source. As the IPIB was focused by the electrostatic field in the IPD region, a target was located at the focal point of the IPIB (135 mm from the anode surface).[14, 15] Figure 2 shows the typical waveforms of (a) diode voltage and (b) ion current density measured at the focal point. As shown in Fig. 2(a) and (b), the average diode voltage is 180 kV, the maximum ion current density is 500 A/cm^2 and the pulse duration (F.W.H.M.) is 65 ns. The fluense is estimated to be approximately 5 J/cm^2. A high-speed tool steel (SKH51) sample was polished with the emery paper of #1000 before IPIB-irradiation.

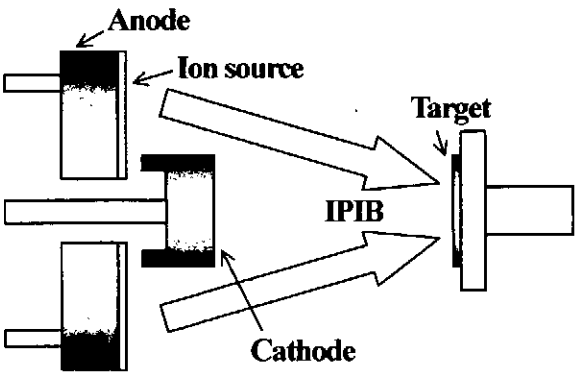

Fig. 1. Scheme of an inverse pinch ion diode and a target.

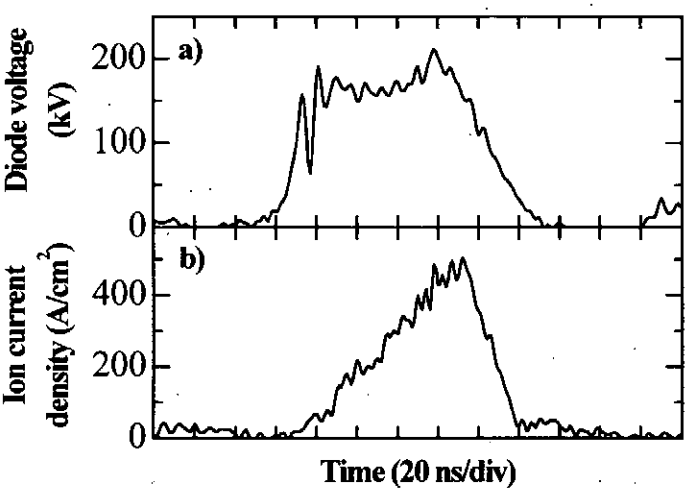

Fig. 2. Typical waveforms of a) diode voltage and b) ion current density measured at the focal point of the IPIB.

The crystalline grains of the untreated and the treated SKH51s were observed by an optical microscope and a transmission electron microscope (TEM), respectively. Structural analysis of the untreated and the treated SKH51s was performed by the glancing angle X-ray diffraction (GAXRD) using CuKa radiation (V=40 kV, I=200 mA). Variation in temperature of the IPIB-irradiated SKH51 was estimated by the numerical calculation of a differential equation for thermal conduction.

3. Results

3.1. Nanocrystallizaion

Figure 3 shows the optical micrograph of the untreated SKH51 surface. The sample was etched by the solution composed of hydrochloric acid, ethyl alcohol, copper(α) sulfate and water. In Fig. 3, the grain size is approximately 7 μm. White spots of approximately 1 μm in diameter are the second phase carbides (Fe_6C, Cr_6C and VC). Figure 4 shows a TEM micrograph of the SKH51 treated by 1 pulse irradiation. In Fig. 4, the average grain size is 240 nm. Figure 5 shows a TEM micrograph of the SKH51 treated by 10 pulses irradiation. In Fig. 5, the grains under 100 nm in diameter are observed, and the average grain size is 40 nm. These results show that the grain size of matrix is decreased to 1/170 by repeated irradiations of the IPIB.

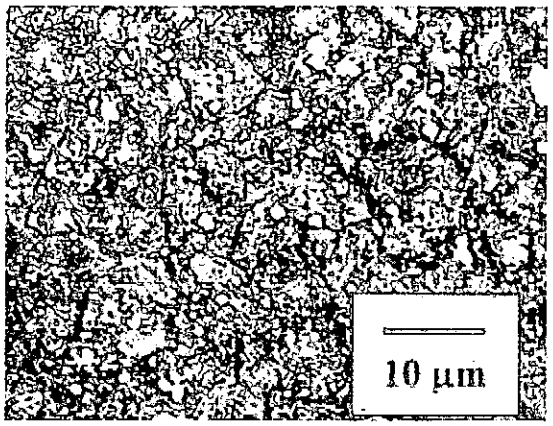

Fig. 3. Optical microscope photograph of the untreated SKH51.

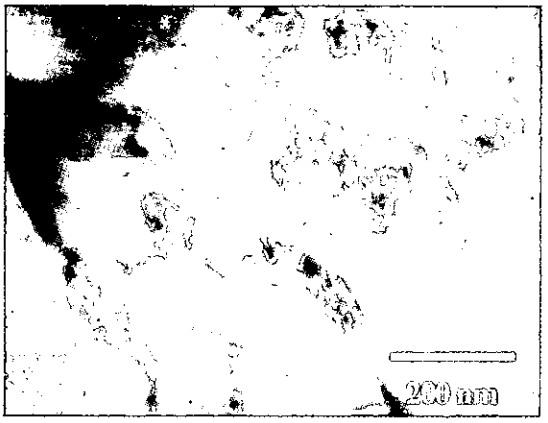

Fig. 4. TEM micrograph of the SKH51 treated by 1 pulse irradiation.

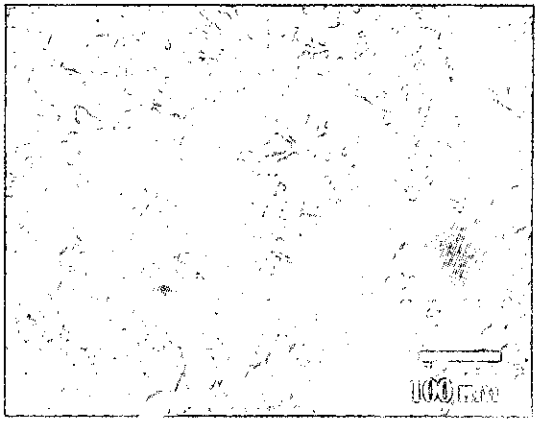

Fig. 5. TEM micrograph of the SKH51 treated by 10 pulses irradiation.

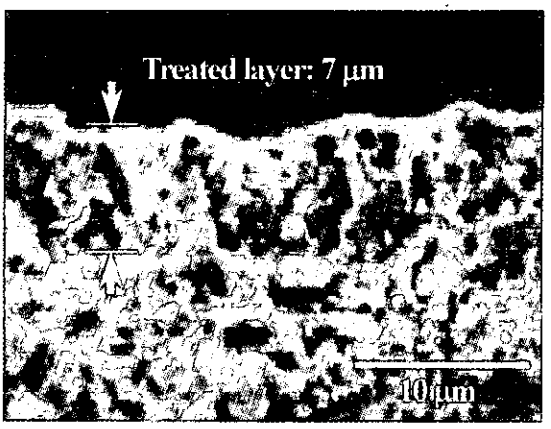

Fig. 6. Cross sectional view of the SKH51 treated by 10 pulses irradiation.

Figure 6 shows a cross sectional view of the SKH51 sample treated by 10 pulses irradiation. As shown in Fig. 6, the surface region within approximately 7 μm is treated by IPIB-irradiation.

3.2. Formation of an austenitic phase

Figure 7 shows the GAXRD profiles of (a) the untreated SKH51 and (b) the treated ones by 1, 5, and 10 pulses, where the incident angle of the X-ray was 1° corresponding to the maximum diffraction depth of 0.17 μm from the surface. As shown in Fig. 7(a), the diffraction peaks of untreated SKH51 have the martensitic structure, α-Fe(110), at $2\theta = 44.4°$ and the second phase carbides (Fe_6C, Cr_6C and VC). On the other hand, the second phase carbides disappear in the GAXRD profiles of the treated SKH51 samples as shown in Fig. 7(b). After 1 pulse irradiation, the SKH51 sample has the mixed phase of martensite and austenite, γ-Fe. The intensity of the γ-Fe(111) peak is lower than that of α-Fe(110) peak. In the GAXRD profile of the SKH51 treated by 5 pulses irradiation, the intensity of γ-Fe(111) is comparable with that of α-Fe(110). The austenitic structure becomes more dominant by repeated irradiations of the IPIB. After 10 pulses irradiation, the only austenitic structure is observed in the GAXRD profile of the SKH51.

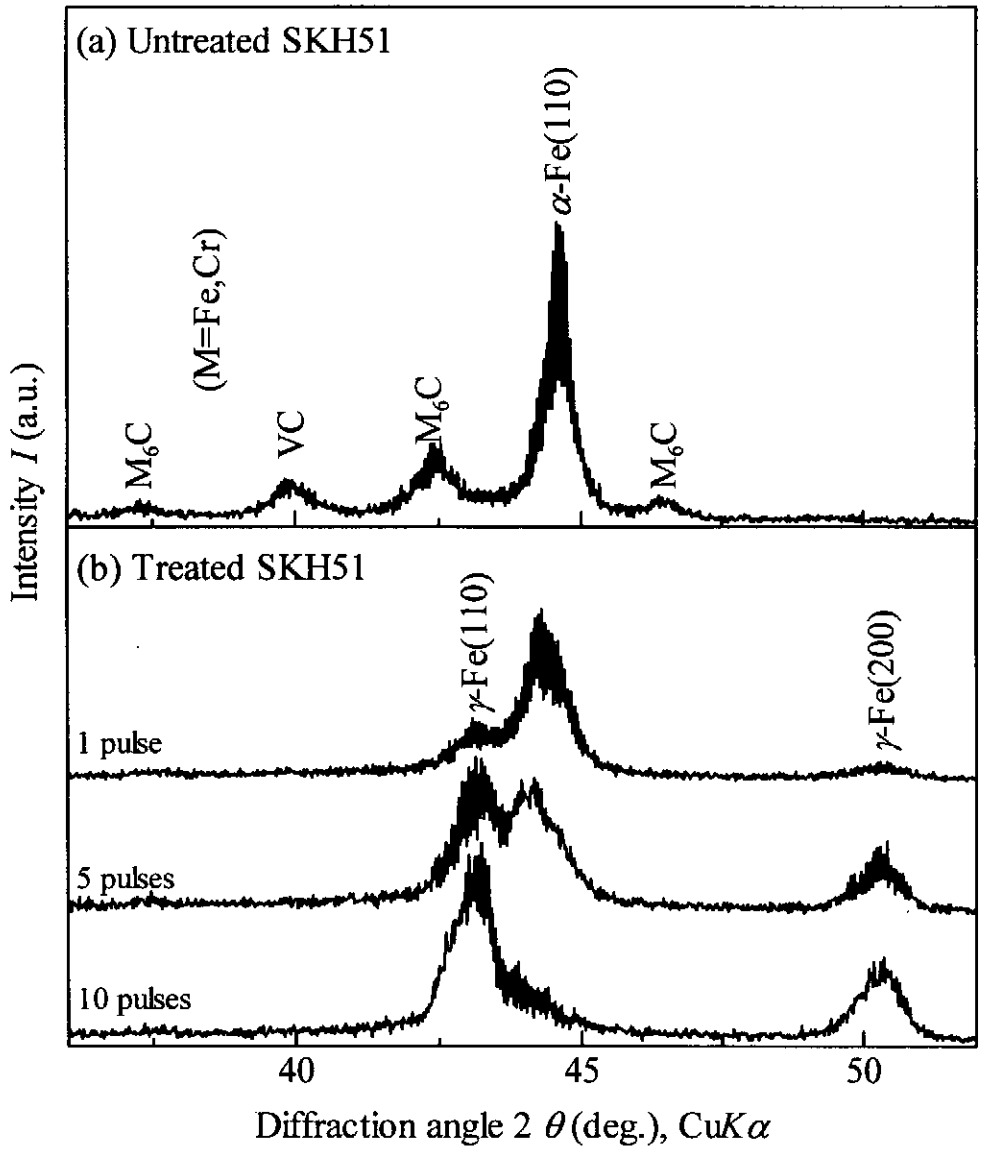

Fig. 7. GAXRD profiles of the untreated SKH51 and the treated SKH51 samples.

4. Discussion

We will calculate time evolution of target temperature by the IPIB-irradiation. Since the beam area is larger than the target area in the present experiment, the beam density irradiated on the target is considered to be uniform. Then the target temperature can be estimated by the differential equation for thermal conduction as follows:

$$\rho c \frac{\partial T(z,t)}{\partial t} = \lambda \frac{\partial^2 T(z,t)}{\partial z^2} + A(z,t), \qquad \cdots 1)$$

where T, z, t, ρ, c, and λ are the temperature, distance from the target surface, time, density, heat capacity and thermal conductivity, respectively. A is the energy per unit time per unit volume of a heat source, and can be written as follows:

$$A(z,t) = E(z)J_{ib}(t), \qquad \cdots 2)$$

where E is the energy deposited by ion beam and J_{ib} is the ion current density.

Equation 1) was numerically solved by the finite difference method with the initial condition

$$T(z,0) = T_0, \qquad \cdots 3)$$

and the boundary condition

$$-\lambda \frac{\partial T(0,t)}{\partial z}\bigg|_{z=0,z=l} = 0. \qquad \cdots 4)$$

T_0 is the initial temperature of the material, and l is the thickness of the material. The material parameters of SKH51 (ρ=8.513 g/cm^3, c=0.757 J/g/℃, λ=0.258 W/cm/℃, and T_0=20 ℃, l=0.1 mm) were used for the calculation. J_{ib} was given by Fig. 2b) and E is determined from TRIM code simulation.[16] Figure 8 shows the time evolution of surface temperature of IPIB-irradiated SKH51, where the effect of the latent heat for fusion (267 J/g) and vaporization (6285J/g) was also considered in calculation. As shown in Fig. 8, the temperature of the surface region within 2 μm exceeds the melting point (1235 ℃), and top surface region within 1 μm is heated to the boiling point (2750 ℃). After the IPIB is turned off, the temperature is rapidly decreased. The cooling rate from the melting point to the crystallization temperature assumed to be 1/2 of the melting point in Kelvin is estimated to be dT/dt = 2.7x10^7 ℃/s. This rapid cooling leads to production of nanocrystalline phase shown in Fig. 5. In addition, the formation of the austenitic structure is ascribed to the rapid cooling rate.

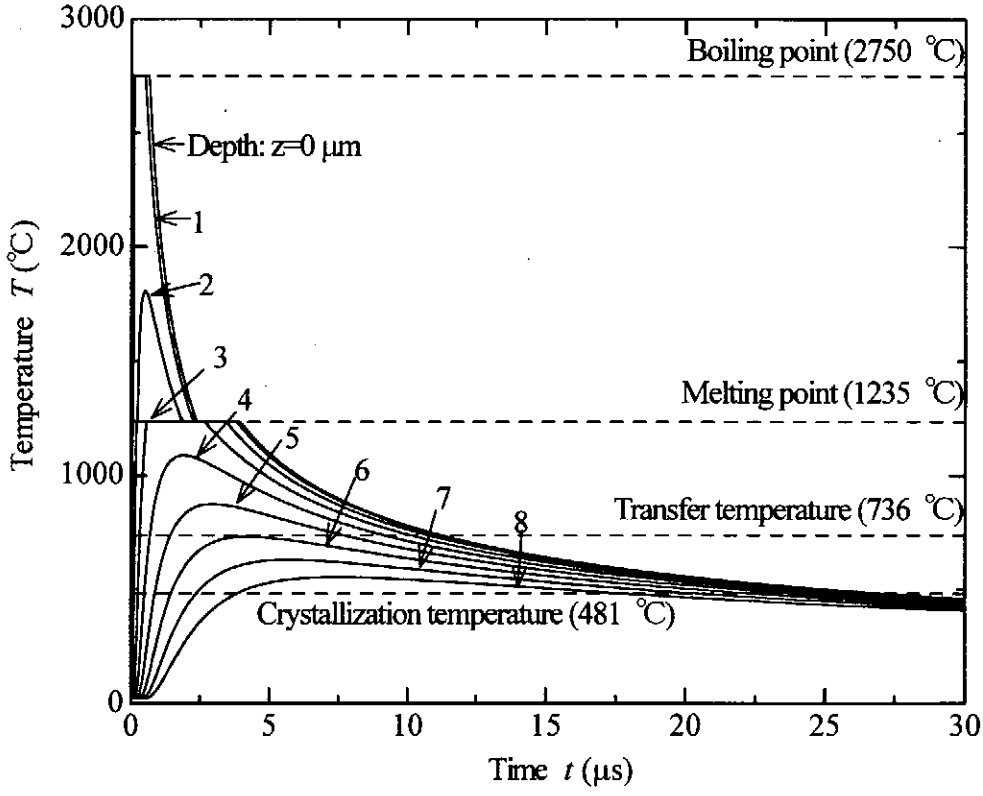

Fig. 8. Time evolution of surface temperature by an IPIB irradiation

Since the temperature of the surface region within 5 μm, as shown in Fig. 8, exceeds the transfer temperature (736 ℃), the structure in the surface layer of 5 μm in depth is able to be transformed into the austenitic structure. This result is in good agreement with the SEM observation in Fig. 6.

5. Summery

A high-speed tool steel was treated by the irradiation of a hydrogen-IPIB. After 10 pulses irradiation, an austenitic structure of nanometer-sized polycrystals was formed in the target surface of approximately 7 μm in depth. The average grain size of the austenite was 40 nm. The second phase carbides were dispersed from the treated layer.

References

1) R. W. Stinnett, R.G. Buchheit, F. A. Greulich, C.R. Hills, A. C. Kilgo, D.C. McIntyre, J. B. Greenly, M. O. Thompson, G. P. Johnston, and D. J. Rej, Mat. Res. Soc. Symp. Proc (1994) Vol. 316, pp. 521-532.
2) G. E. Remnev and V. A. Shulov, Laser & Particle Beams, **11**, 707-731 (1994).
3) E. L. Neau, IEEE Trans. Plasma Sci., **22**, 2-10 (1994).
4) R. W. Stinnett, D. C. McIntyre, R. G. Buchheit, E. L. Neau, John B. Greenly, Michael O. Thompson, G. P. Johnston, and D. J. Rej, Proc. 10th Int. Conf. on High Power Particle Beams (San Diego, 1995) Vol. 1, pp. 215-221.
5) M. Yatsuzuka, Y. Yamasaki, H. Uchida, and Y. Hashimoto, Appl. Phys. Lett., **67**, 206-207 (1995).
6) M. Yatsuzuka, T. Yamasaki, Y. Hashimoto, and H. Uchida, Trans. Inst. Electr. Eng. Jpn., **115A**, 1030-1031 (1995) [in Japanese].
7) M. Yatsuzuka, Y. Hashimoto, T. Yamasaki, and H. Uchida, Jpn. J. Phys., **35**, 1857-1861 (1996).
8) H. A. Davis, G. E. Remnev, R. W. Stinnett, and K. Yatsui, MRS Bulletin, **21**, 58-62 (1996).
9) M. Yatsuzuka, Y. Hashimoto, T. Yamasaki, and H. Uchida, Proc. 1st Int. Sym. Applied Plasma Sci. (Los Angeles, 1997), pp.165-171.
10) Y. Hashimoto, M. Yatsuzuka, S. Ishizaki, and M. Yatsuzuka, Appl. Plasma Sci. **5**, 84-89 (1997) [in Japanese].
11) D. J. Rej, H. A. Davis, J. C. Olson, G. E. Remnev, A. N. Zakoutauv, V. A. Ryzhkov, V. K. Struts, I. F. Isakov, V. A. Shulov, N. A. Nochevnaya, R. W. Stinnett, E. L. Neau, K. Yatsui, and W. Jiang, J. Vac. Sci. Technol., **A15**, 1089-1097 (1997).
12) Y. Hashimoto and M. Yatsuzuka, Appl. Plasma. Sci. **6**, 56-61 (1998) [in Japanese].
13) T. J. Renk, R. G. Buchheit, N. R. Sorensen, D. C. Senft, M. O. Thompson, and K. S. Grabowski, Phys. Plasmas, **5**, 2144-2150 (1998).
14) H. Akamatsu, M. Yatsuzuka, K. Azuma, E. Fujiwara, and Y. Hashimoto, Appl. Plasma Sci. **6**, 3-9 (1998) [in Japanese].
15) Y. Hashimoto, M. Yatsuzuka, and S. Nobuhara, Jpn. J. Appl. Phys. **31** (1992) 1922-1927.
16) J. F. Ziegler, J. P. Biersack, and U. Littmark, The Stopping and Range of Ions in Solids (Pergamon Press, New York, 1985).

PULSED DISCHARGE WITH POWDERS

Y.Kawasaki, H.Ishihara, H.Nozawa, J.Kuroda, S.Ibuka,
Y.S.Liu, K.Yasuoka, and S.Ishii

Department of Electrical and Electronic Engineering
Tokyo Institute of Technology
2-12-1 O-okayama, Meguro-ku, Tokyo 152-8552, Japan

ABSTRACT

Powder is employed instead of gas to generate discharge plasmas. The medium is supplied between discharge electrodes by flying up powder electrostatically which is freely falling down through a glass pipe. The initial stage of breakdown in vacuum was investigated. Breakdown voltage dependence on copper powder shape was measured by using dendritic powder and spherical powder. The breakdown voltage for dendritic powder is lower than that for spherical powder. Discharge phenomena of copper powder in a capillary of dielectric material in vacuum were investigated by optically.

I. Introduction

There are various advantages to use powder instead of gases as a matter for plasma generation. Applications of powder produced plasmas are space physics, high voltage insulation techniques, intense soft X-ray sources by Z-pinch, thin film deposition in material science, dust particle formation in semiconductor manufacturing process, and so on. However, few studies on plasma generation from powder are reported so far. Since powder is not easy to be put into discharge volume as comparing with gases, one has to develop some experimental techniques for handling of powder to investigate physics of powder produced plasmas.

Powder has a variety of shapes. We studied on two types of powder. Microscopic photographs of dendritic powder and spherical powder are shown in Fig.1. Compare to dendritic powder, spherical powder has a uniform size and shape. The dendritic powder has complex structures which influence the discharge characteristics such as edge effect and electric field enhancement. Therefore generalization of the experimental results in powder discharge employing the spherical powder is possible.

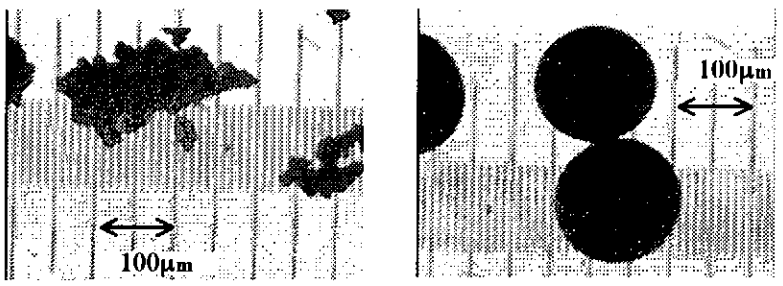

Fig.1 dendritic and spherical powder shape

II. Powder Supply System

We designed and examined two kinds of powder supply systems which have different electrode configurations: a flat-flat type and a flat-slope type, as shown in Fig.2. When DC voltage is applied between electrodes, conductive particle is charged up to Q at the same polarity of the contacting electrode and is accelerated toward the opposite electrode by an electrostatic force. The total charge Q of a particle is written as [1],

$$Q = \frac{2}{3}\pi^3 \varepsilon_0 r^2 E_0 \qquad (1)$$

where r is the particle radius, E_0 the electric field between the charging electrodes, and ε_0 the dielectric constant in vacuum, respectively. The particle executes back-and-forth motions between the electrodes. Some particles will pass through a hole drilled at the center of the bottom electrode. A rubber tube was placed at the center hole for only the accelerated powder by electrostatic force to fall through the center hole. Falling powder goes to discharge region.

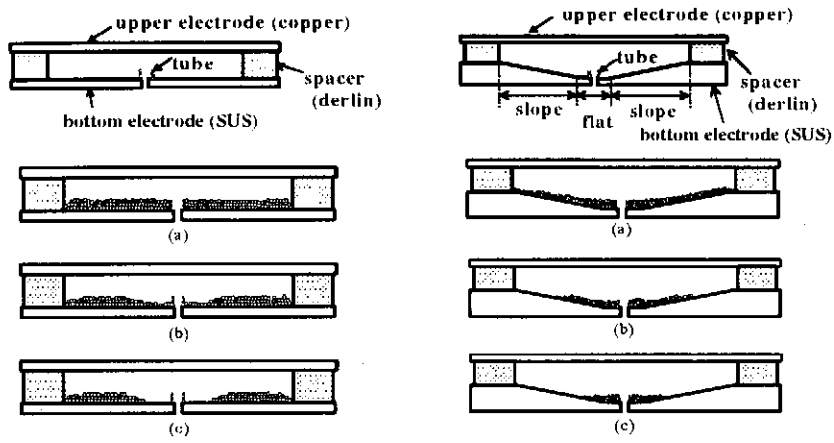

(1) flat-flat electrode type **(2) flat-slope electrode type**

Fig.2 electrode configurations of powder supply system

The supplied powder amount per run between 1st and 10th runs for two types powder supply system are shown in Fig.3. In the case of flat-flat electrode type, the supplied powder amount per run was not the same for each run as shown in Fig.3(1). The result shows that falling powder mostly comes from around the center hole and the amount of powder around the hole decreases as shown in Fig.2(1). Consequently reproducibility of the supplied powder amount per run was not good. To overcome this problem, we designed the flat-slope type electrode in which the bottom electrode has a slope of two degrees as shown in Fig.2(2). In this configuration, powder moves towards the center region along the slope and the amount of powder around the hole was kept to be constant. The amount of powder per run from the supply system for ten runs was almost similar as shown in Fig.3(2) for initial powder amount of 4 g, driving voltage of 6 kV, powder diameter of 75-106 μm. The constant amount of powder per run last for about hundred runs, that does not matter in practical application.

Fig.4 shows a setup of the main discharge electrodes and the powder supply system with the flat-slope electrode type. The powder flow controlled by electrostatic force is freely falling down through a glass pipe to the main discharge region.

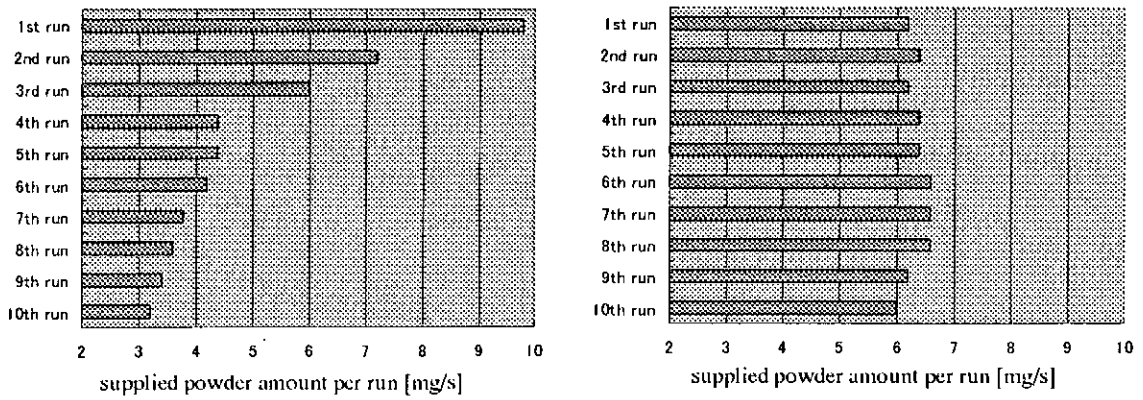

(1) (2)

Fig.3 supplied powder amount of two powder supply systems

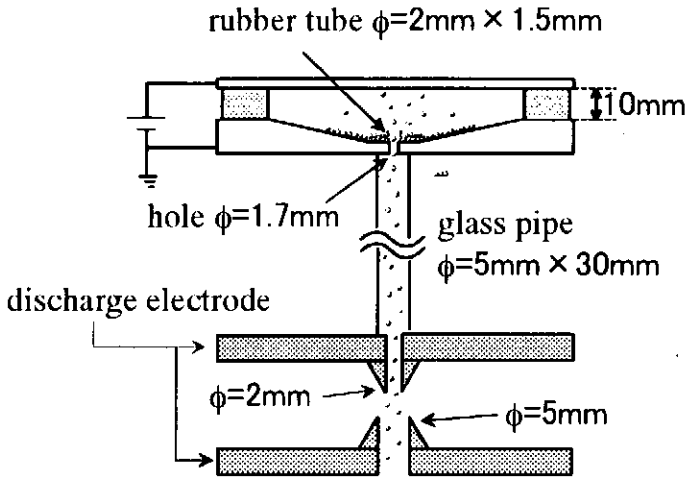

Fig.4 discharge electrode and powder supply system with the flat-slope electrode type

III. Number density measurement

The powder number density was measured by a particle-counting method. When a particle comes into the region illuminated by a He-Ne laser beam, laser intensity is attenuated by the particle. Thus the powder number is counted from the damped light pulse number. Fig.5 shows a experimental setup of the particle-counting method. The He-Ne laser beam is expanded by a beam expander and focused by a convex lens. The light intensity of the laser beam is measured by a photodiode and a oscilloscope.

Since the laser beam is scattered by of the particles, successive spike-like signals corresponding to each particle appear in the photodiode output as shown in Fig.6(a). Fig.6(b)

is the enlargement of the damped light pulse in Fig.6(a). Counting the number of pulses in Fig.6(a), the powder number density $N_{P\text{-}C}$ can be obtained by the relation of,

$$N_{P\text{-}C} = \frac{N_0}{(\phi_1 + 2\phi_2)vl} \tag{2}$$

where N_0 is the number of the pulses for the unite time, ϕ_1 the laser beam diameter, ϕ_2 the particle diameter, l the inner diameter of the glass pipe, and v the particle velocity, respectively.

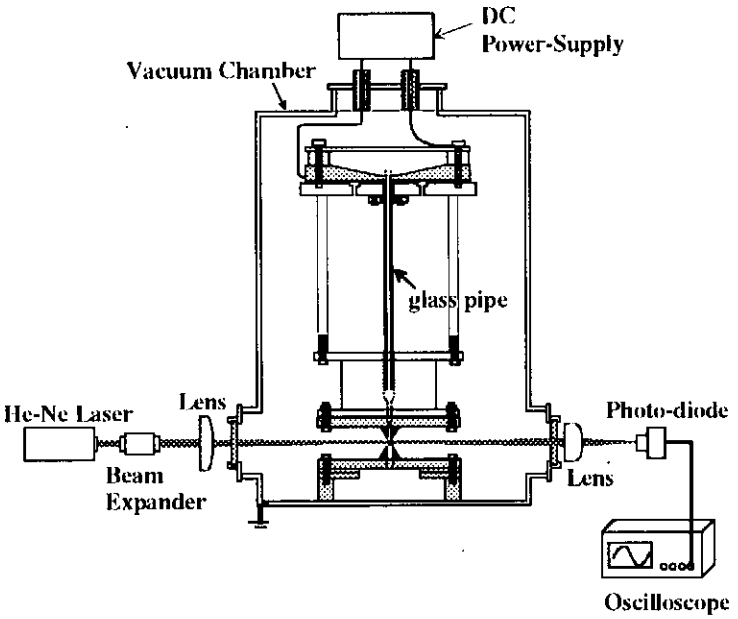

Fig.5 configuration of particle-counting method

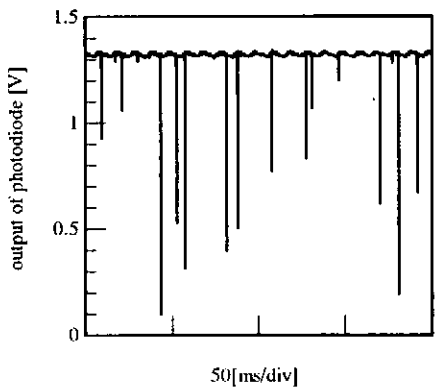

Fig.6(a) output waveform of photodiode by particle-counting method

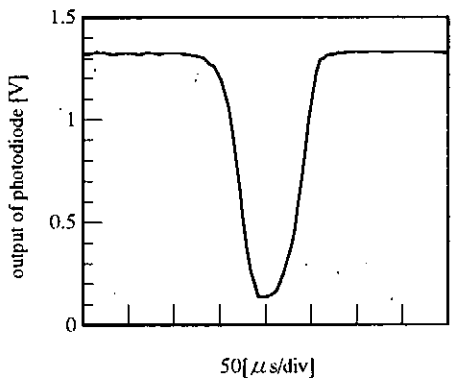

(b) enlargement of a damped light pulse

We have to calibrate the data obtained from the particle-counting method. The total amount of powder can be measured precisely by weighing the powder mass. The powder number densities were calculated from the powder weight measurement [2]. Fig.7 shows the powder number densities obtained from the two measuring methods. Both results agree well. Consequently it is shown that particle-counting method can measure powder number density very precisely.

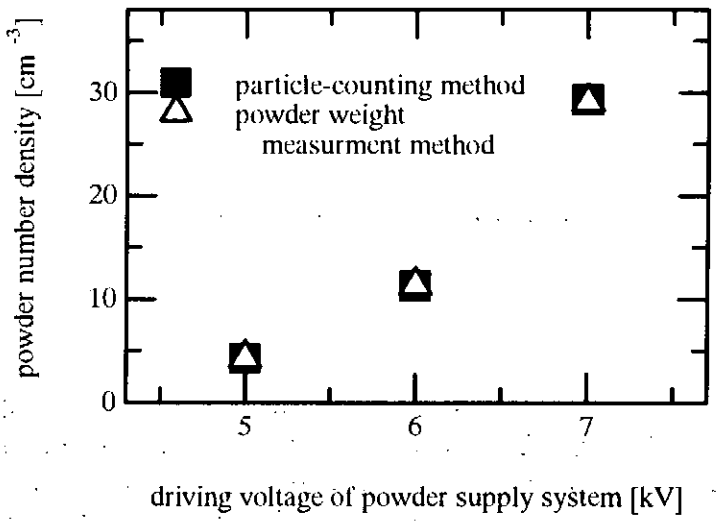

Fig.7 powder number density measurement

IV. Powder Discharge Experiment

(I) Breakdown Voltage Measurement

When the copper powders of dendritic and spherical shapes were employed, the breakdown voltages in the air were measured. The powder diameter was typically 106-150 μm. The gap length between the discharge electrodes was 0.7 mm and 3.0 mm, and the driving voltage was 4 kV and 6 kV. The breakdown voltage with no powder was also measured as reference. The measured results are summarized in Fig.8.

When the dendritic powder is used, the breakdown voltage decreases drastically. On the other hand, the breakdown voltage for spherical powder is almost similar to that for no powder. The low breakdown voltage for the dendritic powder is caused by the local high electric field around the sharp edges of powder as shown in Fig.1.

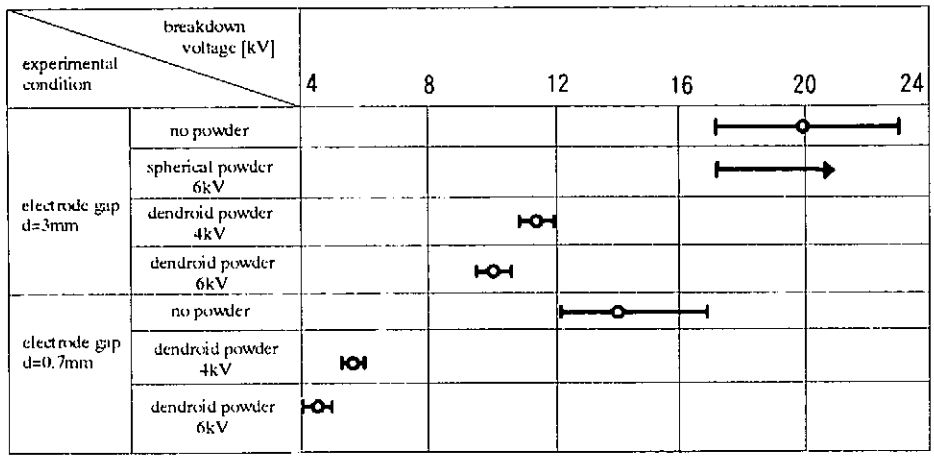

Fig.8 breakdown voltage with powder

(II) Spectroscopic Measurement

Discharge phenomena of copper powder in a capillary of dielectric material in vacuum were investigated by optically. Fig.9 shows an experimental circuit and an electrode configuration. A dielectric material was placed between the main electrodes in order to generate a uniform discharge in the gap. A main capacitor was 1.62 μF charged up to 20 kV. Pressure in the vacuum chamber was kept about 10^{-5} Torr. A third electrode near the cathode was used as a trigger for the main discharge. The trigger is a surface discharge between the cathode and the trigger electrode. When a gap switch is turned on, a vacuum spark like discharge develops. Time integrated spectra from 430 nm to 460 nm is shown in Fig.10. The spectral lines of Cu I, Cu II and Cu III were identified when copper powder was supplied in the discharge volume.

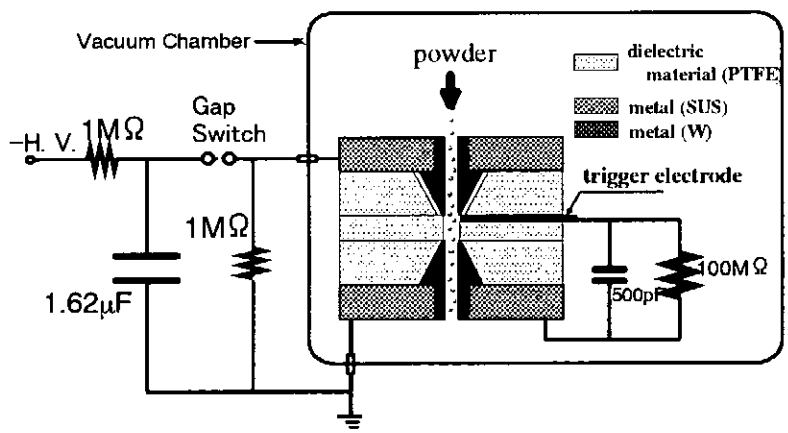

Fig.9 experimental circuit and electrode configuration

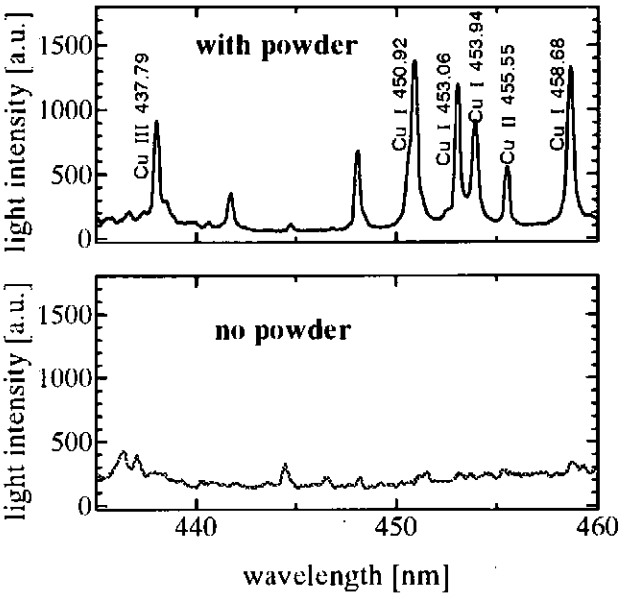

Fig.10 spectral lines of copper powder discharge

V. Conclusion

Employing the powder supply system with the flat-slope electrode type, we can make the amount of powder per run almost similar. The constant amount of powder per run lasts about hundred runs. The powder number density obtained from the particle-counting method agrees well that obtained from the powder weight measurement method. Therefore it is shown that particle-counting method can measure powder number density very precisely. When the dendritic powder is used, the breakdown voltage decreases drastically. On the other hand, the breakdown voltage for spherical powder is almost similar to that for no powder. Discharge phenomena of copper powder in a capillary of dielectric material in vacuum were investigated by optically and the spectral lines of Cu I, Cu II and Cu III were identified.

VI. Reference

1) A.Y.H.Cho, "J. Appl. Phys.", **35** No.9, 2561 (1964).
2) Y.Kawasaki, S.Ishii, "Plasma Science and Technology", IEEJ, EP-99-68 (1999, Japanese).

EXPERIMENT OF FLUE GAS TREATMENT BY PULSE ELECTRON BEAM

R. Kodera, T. Kishi, H. Kawauchi and Y. Nakagawa

Department of Electrical Engineering, Faculty of Engineering, Osaka City University, Osaka 558-8585, JAPAN

ABSTARCT

To develop a new flue gas treatment device by using the pulse electron beam, an experiment of NO_x removal from the atmospheric pressure gas was performed. The pulse electron beam with energy of ≤160keV, beam current of 140A, current density of 2A/cm^2, pulse width of 0.7μs and electron beam power of 12.6J/pulse, or the electron beam with the energy of ≤120keV, 10A, 2.5μs and 2.8J/pulse was injected into the gas cell filled with the atmospheric pressure NO/N_2 or $NO/N_2+O_2(20\%)$ gas. When the electron beam was injected into NO(=200ppm)/N_2 gas, twenty percent of NO was removed by one pulse with the efficiency of 270nmol/J. The efficiency depended on the removal ratio, the volume of the gas cell, initial NO concentration and the electron beam power When the electron beam was injected into the gas mixture of NO(=200ppm)/N_2 with $O_2(20\%)$, the oxidization of NO to NO_2 was highly activated. When the water or NH_3 was added to the gas mixture, NO_x was removed through the process of nitric acid production. The improvement of conversion efficiency from the stored energy in Marx generator to the energy of pulse electron beam up to 48% was obtained.

1. Introduction

The injection of the intense pulse electron beam generated by using the pulse power technology into the flue gas is expected to be a new excellent method for pollutant removal because of its expected some merits compared with the gas discharge or the continuous current, low-density electron beam system [1]-[6]. Extremely high removal efficiency of ~10^4nmol/J(=1eV/molecule) for SO_x was achieved due to the chain reaction induced by the pulse high density electron beam injection[1]. Kinetic analysis of NO_x removal from model gas was calculated and a dose of electron beam per pulse less than 1kGy/pulse has been determined to be optimum for effective radical utilization[3]. Effective decomposition of Freon-12 and removal of NO_x from atmospheric pressure N_2 or oxygen mixed NO/N_2 gas were demonstrated by ourselves[2], [4, 5]. The pulse repetitive short pulse (~3ns) electron beam decomposed the vapor of volatile organic compounds[6].

In this paper, several basic results of removal of NO_x by the pulse high current density electron beam irradiation were described.

2. Experimental

In Fig. 1, the experimental setup for pulse intense electron beam processing of a gas mixture of NO in atmospheric pressure N_2 or O_2 (20%)/N_2 gas is shown. A negative high voltage pulse was applied to the cathode from the Marx generator. Pulse high-energy electron beams were extracted from the electron beam diode in the vacuum of the pressure 1×10^{-5}Torr and injected into the gas cell through the titanium foil of 10 or 20μm thickness. Pulse repetition rate was about one pulse in one min. In most experiment, relatively short pulse electron beam with the pulse width of 0.7μs, maximum energy of 160keV, beam current of 140A, current density of 2A/cm^2 and the electron beam power in single pulse of 12.6J/pulse was injected. In several experiment, relatively long pulse electron beam with the pulse width of 2.5μs, energy of ≤120keV, beam current of 10A, and the electron beam power of 2.8J/pulse were used. A cathode with many needles and a coil with inductance of 50μH inserted in Marx generator were necessary for the long pulse electron beam production. The electron beam power;P_e was measured by two method. One of it was the calorimeter and another was the estimation by $P_e = \int V_e \times I_e \, dt$. Electron energy;$V_e$, of which maximum energy was measured by the attenuation method of electron beam in Al foil, was approximately equal to the measured diode voltage. The electron beam current ;I_e was measured by the Faraday cup. The gas cell with volume of 1.7ℓ (8.8cm inner dia., 27cm long), the gas cell of 6.2ℓ (16cm inner dia., 32cm long) and the gas cell of 25ℓ (31cm inner dia., 30cm long) were used. Mixed gas was prepared introducing several gases into the gas cell measuring partial pressure by the Mercury manometer. The concentration of NO_x(= NO+NO_2) and NO were measured using the NO_x-O_2 gas analyzer (Shimadzu Co.,Ltd., NOA-7000) before and after the beam injection. It was important to measure NO_x concentrations accurately that the NO and NO_2 were uniform in the gas cell. We obtained a flat peak of the signal on the recording paper and a reproducible reading of the indicator by mixing the gas using the gas mixer and waiting for 3min of diffusion time before measurement by NOA-7000.

3. NO_x removal in NO(=200ppm)/N_2 gas

3-1. Typical result

In Fig.2, a typical result of removal of NO_x from NO(=200ppm)/N_2 gas in the gas cell of 1.7ℓ by the relatively short(0.7μs) pulse intense electron beam and simulation result are shown. Change of concentration of NO, NO_2 and NO_x according to increase of the shot number was measured. NO and NO_x in the gas cell decreased from 200ppm to about 100ppm after 2nd shot and less than 10ppm after 8 beam shots. A small amount of NO_2 less than 10ppm was produced at the first and second shot. Due to the reduction by the nitrogen radical produced by pulse electron beam, NO was decomposed in the process $N+NO \rightarrow N_2+O$; $k=3.1\times10^{-11}$. The chemical process was calculated including other process such as $O+NO_2 \rightarrow NO+O_2$; $k=9.7\times10^{-12}$ assuming that nitrogen radical was produced 52ppm($=1.4\times10^{14}$ (molecules/cm^3) per each beam shot. As is obvious from Fig.2, the calculated result approximately agrees with the observed values.

3-2. Comparison of NO_x removal in NO(=200ppm)/N_2 gas under various conditions

In Fig.3, NO_x removal ratio and efficiency depending on the number of electron beam shots for the gas cell with volume of 1.7ℓ and 6.2ℓ were shown. At the same shot number, the removal ratio(76% at 4^{th} shot) was higher for the gas cell of 1.7ℓ compared with that(40% at 4^{th} shot) for the gas cell of 6.2ℓ. However, the removal efficiency of 370nmol/J at the ratio 50% for the large gas cell was larger than that of 250nmol/J for the gas cell of 1.7ℓ. When we used the gas cell with volume of 25ℓ, the efficiency at the removal ratio of 40% increased to 440nmol/J. It seemed that the radial diffusing electron beam and N radicals were effectively utilized for NO_x removal in the large volume gas cell.

The efficiency became low by decreasing the initial concentration of NO from 200 to 55ppm. The efficiency should be low if the initial concentration of NO reduced to the value smaller than the concentration of N radicals. Low efficiency at large removal ratio can be explained by the local deNO_x near the titanium foil caused by the short range of electron beam and slow diffusion time of the gas molecules. When the initial concentration of NO in the gas cell of 6.2ℓ was increased to 2000ppm, the efficiency increased to 580nmol/J at the ratio of 20%.

Separating the distance of gas chamber from the pulsed electron beam diode using drift tube, the energy of the electron beam emitted in gas cell was decreased. The efficiency increased up to 900nmol/J at the removal ratio of 10% according as decrease of the electron beam power in a single shot from 12.6J/pulse to 0.35J/pulse

In the experiment of the relatively long pulse (2.5μs) electron beam, the efficiencies of 420nmol/J, 527nmol/J and 562nmol/J at the ratio of 62%, 32% and 14% were obtained for the electron beam power of 6.8J/pulse, 2.8J/pulse and 0.85J/pulse, respectively. It is anticipated that the optimum value of the efficiency is in the place where electron beam energy per single pulse is low.

It seems that optimum energy efficiency can be achieved at appropriate initial concentrations of NO and the electron beam power in single shot in the large gas cell. The loss of N radicals caused from the radical-radical interaction is small because the reaction rate;k is smaller than that for the reaction of $NO+N \rightarrow N_2+O$.

Simple G-value calculation could not explain these results and the effects of other enhancement of radical production or the chain chemical reaction or the chemical reaction with impurity gas may explain it.

4. NO_x Removal from NO/N_2 gas containing 20% of O_2

In Fig.4, the change of concentration of NO, NO_2, NO_x and removal efficiency after the pulse electron beam irradiation were shown when the water of 2.6% was added to the mixture gas. NO_x decreased with the removal efficiency of 400nmol/J at the removal ratio 40%, which rapidly decreases to 200nmol/J at 50%. By OH radicals produced from water by the electron beam collision, NO_2 was oxidized to HNO_3 and removed from the gas phase.

When the inner wall of gas cell was covered with the wet cloth by using stainless steel

mesh, NO_x slowly decreased in time (40% in 15min) because NO_2 was absorbed to the wet cloth without the electron beam injection. By the pulse electron beam irradiation, NO decreased with the number of pulse and NO_2 remained in a small concentration. It is probable that NO_2 converted to HNO_3 in the gas phase and absorbed by the wet cloth, simultaneously. The total NO_x removal efficiency was 570 and 300nmol/J at the removal ratio of 40 and 84%, respectively.

Change of concentration of NO, NO_2 and NO_x after the pulse electron beam irradiation on the gas mixture containing NH_3 was shown in Fig.5. NH_3 was added in the ratio of NH_3:NO=1:1. After the oxidization of NO to NO_2 was completed at 6^{th} pulse, NO_2 decreased by the electron beam irradiation without water addition. OH and NH_3 radicals can be produced by the electron beam irradiation. These radicals should oxidized NO_2 to HNO_3 and formed the ammonium nitrate;NH_4NO_3. NO_x decreased with constant efficiency of 160nmol/J from the ratio of 36% to 95%.

Some experimental evidences were observed that the removal efficiency depended on the concentration of NO_x, the amount of additional gas and the electron beam power in one shot. It is expected that more higher energy efficiency of deNO_x can be achieved by optimization of these parameters.

5. Improvement of conversion efficiency from the stored energy in Marx generator to the energy of pulse electron beam

The removal efficiency was calculated so far to the electron beam energy injected into the gas cell. The energy efficiency of gas treatment by the pulse electron beam should be estimated to the total energy consumption in the electron beam generator. To improve the conversion efficiency to the electron beam, the electron beam transparency through the anode including the foil in front of the gas cell was increased. The stored energy in Marx generator was decreased to 10.9J at the charged voltage 42.6kV to four 3nF ceramic capacitors. The cathode was modified to generate electron beam when it was operated by such a low power Marx generator. In Fig.6, the diode voltage, diode current, electron beam current, which were measured by the calibrated instruments and the diode impedance were shown. In this case, the energy 9.9J(=91% of the stored energy) was put into the diode and the electron beam with the energy 5.2J(=48% of the stored energy) was produced.

Using this electron beam source, same NO_x removal efficiency for the electron beam energy and about 30 times larger removal efficiency for the stored energy in Marx generator compared with the previous experiment were obtained.

6. Summary

(1)By the injection of the pulse electron beam having pulse width of 0.7μs, kinetic energy of ≤160keV, beam current of 140A, and the beam power of 12.6J/pulse or the pulse electron beam having pulse width of 2.5μs, kinetic energy of ≤120keV, beam current of 10A and the beam power of 2.8J/pulse into the atmospheric pressure NO/N_2 or NO/N_2 containing 20% of

O_2 gas, NO_x was effectively removed through chemical process induced by the electron beam. When it was irradiated on NO(=200ppm)/N_2 gas, NO_x was removed by the reduction with the removal efficiency for the electron beam power of 370nmol/J(=28eV/molecule) at the ratio of 50% in the gas cell of 6.2ℓ.

(2) In NO_x removal from NO(=200ppm)/N_2 gas, the removal efficiency was relatively higher at small removal ratio, large volume of gas cell, dense initial NO concentration and small electron beam power in one pulse.

(3) By the pulse electron beam irradiation on the gas mixture of NO/N_2 containing 20% of O_2, the oxidization of NO to NO_2 was activated with the efficiency of 200nmol/J. By addition of water or NH_3 to the mixture gas, NO_2 was oxidized to HNO_3 by the OH radical produced by the electron beam and removed from gas phase with the efficiency of 400nmol/J at the ratio of 50% for the water addition and the efficiency of 160nmol/J at 95% for NH_3 addition.

(4) The conversion efficiency from the stored energy in Marx generator to the energy of pulse electron beam was improved up to 48%.

References

1) D.L.Kuznetsov, G.A.Mesyats and Yu.N.Novoselov, "Removal of sulfur oxide from stack gas by pulsed electron beams," High Temperature, vol.34, pp. 833-840, 1996.

2) Y.Nakagawa, S.Adachi, A.Kohchi and J.Nagasawa, "Application of pulse high-energy electron beams for decomposition of chlorofluorocarbon in atmospheric-pressure air," Jpn. J. Appl. Phys. vol.34, pp. L793-L796, 1995.

3) B.M.Penetrante,"Removal of NO_x from diesel generator exhaust by pulsed electron beams," in Proc. 11th IEEE Pulsed Power Conference, Baltimore Maryland, June 29-July 2, 1997. (to be published)

4)Y.Nakagawa and H. Kawauchi, "Pulse intense electron beam irradiation on the atmospheric pressure N_2 containing 200ppm of NO," Jpn. J. Appl. Phys. vol.37, pp.5082-5087, 1998.

5) Y.Nakagawa and H. Kawauchi, "Removal of NO_x by pulse intense electron beam" in Proc. 12th Int. Conf. High-Power Particle Beams, Haifa, Israel, June1998, pp.1012-1015.

6) I.E.Filatov and Yu. N. Novoselov, "The removal of volatile organic compounds from air by pulsed electron beams," in Proc. 12th Int. Conf. High-Power Particle Beams, Haifa, Israel, June1998, pp.1020-1022.

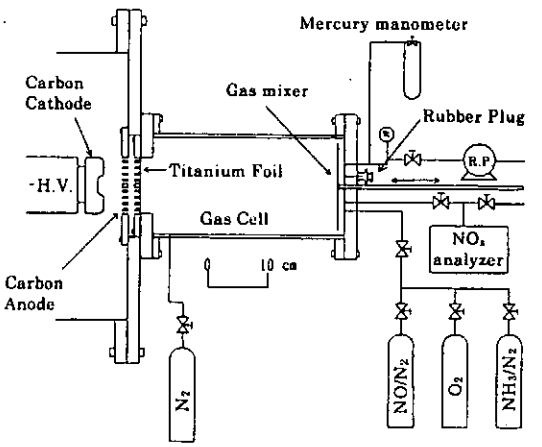

Fig.1. Experimental apparatus.

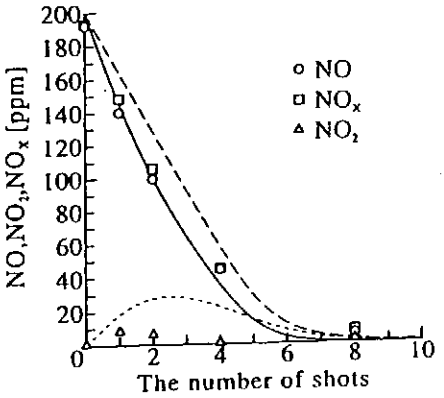

Fig.2.Typical experimental result of the removal of NO_x in N_2 in the gas cell 1.7 ℓ by pulse electron beam irradiation and simulation result of chemical process.

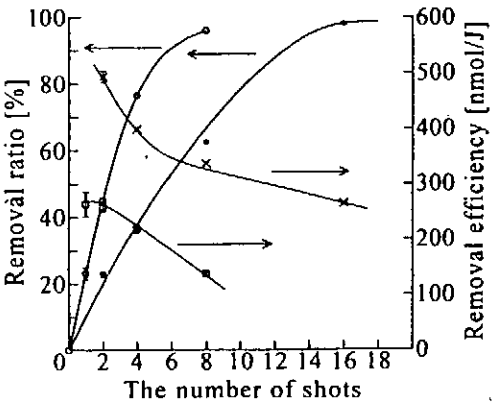

Fig.3. NO_x removal ratio and efficiency depending on the number of electron beam shots for the gas cell of 1.7 l(o, □) and 6.2 l(•, ×).

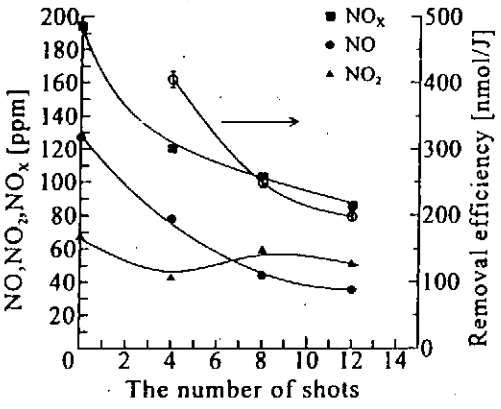

Fig.4. Change of NO, NO_2, NO_x and the efficiency after electron beam irradiation on the oxygen mixed NO/N_2 gas containing 2.6% of water.

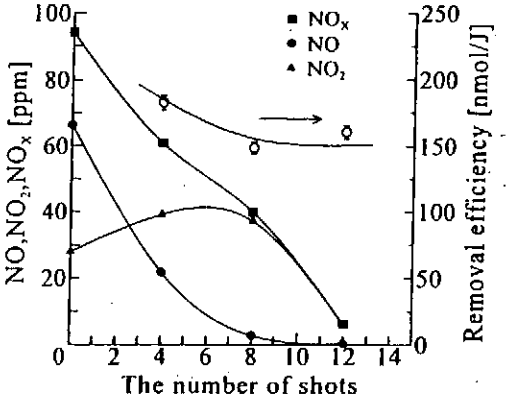

Fig.5. Change of NO, NO_2, NO_x and the efficiency after electron beam irradiation on the NO/N_2 gas containing 20% of O_2. NH_3 was added in the ratio of NH_3:NO=1:1.

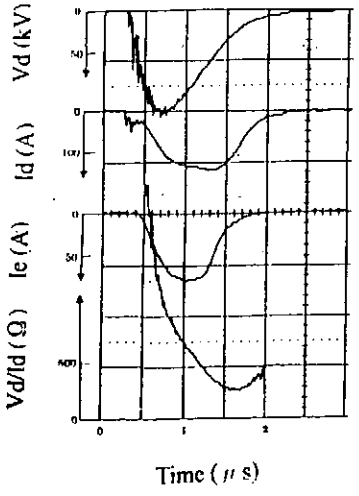

Fig.6. The diode voltage;Vd, current;Id, electron beam current;Ie and the diode impedance;Vd/Id for the improved electron beam diode with low power Marx generator.

NO_X REMOVAL USING PULSED POWER

T. Namihira, S. Tsukamoto, D. Wang, S. Katsuki, R. Hackam, H. Akiyama, Y. Uchida* and M. Koike*

Kumamoto University, 2-39-1 Kurokami, Kumamoto 860-8555, Japan

*Kyushu Electric Power Co., Inc., 2-1-47 Shiobaru, Minami-ku, Fukuoka 815-0032, Japan

ABSTRACT

Pulsed power has been used to remove nitric oxide (NO) in a mixture of nitrogen, oxygen, and water vapor simulating the flue gases from a power station stack. The effect of the pulse width at a fixed applied voltage on NO removal concentration was studied. The dependence of the energy efficiency of the removal of NO at a fixed applied voltage on the pulse width, on the removal ratio of NO and on the discharge current was investigated. This removal energy efficiency increases with decreasing pulse width and decreasing removal ratio of NO.

1. Introduction

The application of pulsed power to the central electrode of a coaxial cylindrical tube containing a gas at atmospheric pressure results in the production of non-thermal plasma. This produces high energy electrons while the ambient temperature of the neutrals and ions remains relatively unchanged thus reducing the energy consumption because most of the energy is utilized to create energetic electrons [1-11]. This was confirmed recently using spectroscopic measurements which showed that for streamer pulses lasting less than 100 ns the gas temperature in atmospheric nitrogen remained in the range 300-350 K [12, 13]. The high energy electrons produce chemical radicals which decompose the pollutant molecules of nitrogen oxides [1, 3, 5, 14-16]. Acid rain is partly produced by emissions of nitrogen oxides of NO and NO_2 originating from fossil burning fuels in thermal power stations, motor vehicles and other industrial processes from steel production and chemical plants [15-20]. The efficient removal of NO_X and other gas pollutants has recently become of worldwide paramount importance. Non-thermal plasmas for removal of NO_X have been produced using an electron beam [2, 14, 20], a dielectric barrier discharge [18, 21] and a pulsed corona discharge [1-11, 22-25] at various energy effectiveness.

In the present work a pulsed corona discharge has been used to obtain a high degree of NO removal efficiency. The effects of the pulse width, the pulse repetition frequency and the discharge current on the percentage removal of NO and its energy efficiency are reported.

2. Experimental set-up and procedure

Fig. 1 shows a schematic diagram of a three-stage Blumlein generator used in the present work. Each stage consisted of two coaxial cables which had a characteristic impedance of 50 Ω (RG-213/U, Mitsubishi Densen, Japan). The length of the coaxial cable defines the pulse width. In this work, the set-up had pulse widths of about 40, 60, 80, 100, and 120 ns and corresponding lengths of coaxial cable of 4, 6, 8, 10, and 12 m. The width of the pulse is defined as the full width at half maximum of the voltage (FWHM). Fig. 2 shows the experimental set-up. The applied voltage from the Blumlein generator to the reactor was measured using a resistive voltage divider which was connected between the central electrode and the ground. The current to the reactor was measured using a Rogowski coil (Pearson current monitor, Model 2878, Pearson Electronics). The energy input to the discharge per pulse was determined from $\int VI\,dt$. V is the voltage across and I is the current through the reactor. The current probe was located on the return current to the ground as shown in Fig.2 when there was no resistance in series with the reactor R=0. When a resistance was placed in series with the low voltage end of the reactor the current probes were placed on the high voltage end of the reactor and on the series resistance R as shown in Fig.2.

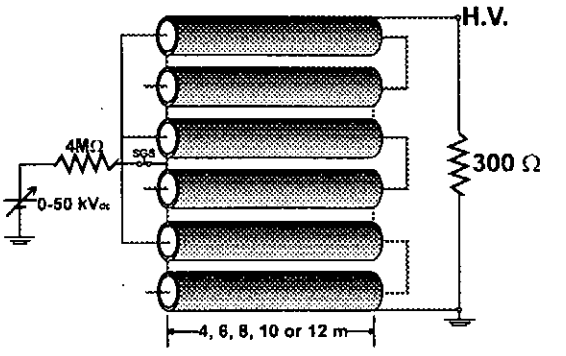

Fig. 1. Three-stage Blumlein generator showing the charging voltage (0-50 kV), the charging resistance (4 MΩ), the spark gap switch (SGS) and the matching output resistance (300 Ω). The cable length varied from 4 to 12 m giving pulse widths of 40, 60, 80, 100 and 120 ns. 300 Ω was removed when coaxial reactor was used.

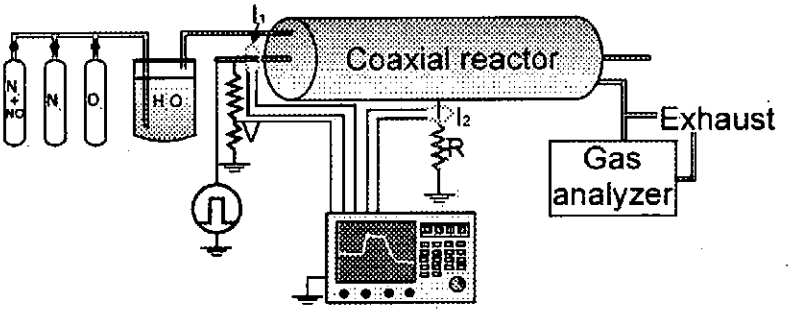

Fig. 2. Experimental set-up for removal of NO using a concentric coaxial electrodes reactor. I_1, current into the reactor; I_2, current in the external resistance R; value of R: 0, 50, 100, 200, 300 Ω. Resistance divider, 1Ω/5kΩ.

Gas cylinders of N_2, N_2 mixed with 0.09 % NO, O_2 and H_2O were used to simulate exhaust gases from a thermal power station. The compositions of the simulated exhaust gases in the admixture were 200 ppm of NO, 5 % O_2, 4 % H_2O and the balance N_2 at 1×10^5 Pa and 298 ± 2 K. Water vapor was attained by allowing the gases to pass through water. The gas flow rate was fixed at 2.0 l/min (reduced to 273 K) at 1.01×10^5 Pa. A coaxial cylindrical reactor having a central rod made of stainless steel, 0.5 mm in diameter placed concentrically in a copper cylinder having 76 mm in internal diameter and a

length of 0.5 m was employed. In the present work, a positive voltage polarity was chosen for the central electrode of the reactor since this was more effective than the negative polarity [1], [6]. A pulse repetition rate of 1 to 13 pulses per second (pps) was used. The concentrations of NO and NO_2 were measured using a gas analyzer (Testo 33, Hodakatest, Japan).

3. Results and Discussion

3.1. Treatment of simulated gases

Fig. 3 shows typical waveforms of the applied voltage (a) to and the discharge current (b) in the coaxial reactor for varying pulse widths. The peak of the voltage was almost the same (49.2 kV ± 0.6 kV) for all pulse widths in the range 40 to 120 ns (Fig. 3a). After the peak the behavior of the pulse for different widths varied due to the varying stored charge with varying capacitance of the Blumlein generator. Fig. 5 shows the input energy to the reactor for different pulse widths and for duration of up to 300 ns when the current decreased to 0 (Fig. 3b). The input energy was calculated from the voltage and the current waveforms shown in Fig. 3. The input energy to the reactor was almost the same (Fig. 4) until the voltage reached its maximum value at about 90 ns (Fig. 3). Thereafter the input energy was different for different pulse widths (Fig. 4). Typically the energy delivered to the reactor after 300 ns of a single pulse having a width of 120 ns was about 0.49 J while that of the 40 ns pulse width was 0.18 J.

Fig. 5 shows the final concentrations of nitric oxide NO_f (a) and NO_2 (b) after applying pulsed powers of different widths and as a function of the repetition rate. NO_f is the final concentration of NO in the mixture after treatment with pulsed power. It will be observed from Fig. 5a that the concentration of NO_f decreased with increasing pulse repetition rate and increasing pulse width from 40 to 120 ns. The concentration of NO_2 increased steadily with increasing pulse rate up to 6 pps and slightly decreased thereafter (Fig. 5b).

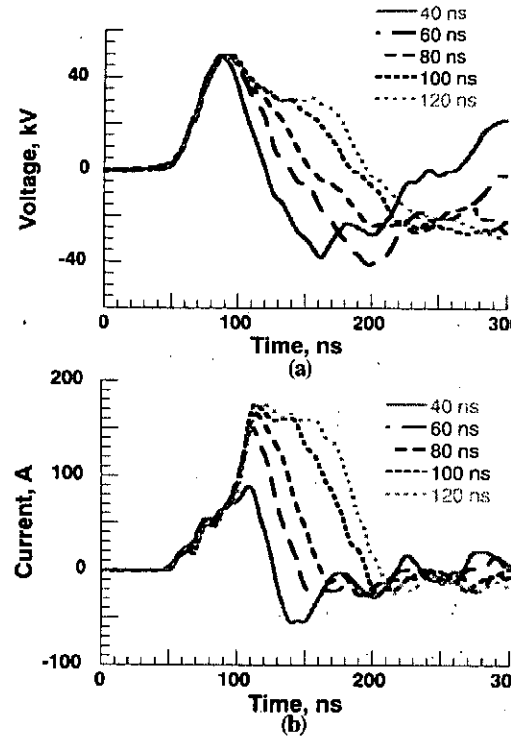

Fig. 3. Applied voltage (a) to and discharge current (b) in the coaxial reactor for varying pulse widths. Conditions: gas pressure, 1.01×10^5 Pa; NO, 200 ppm; O_2, 5 %; H_2O, 4 % and balance N_2; gas flow rate, 2.0 l/min; series resistance with reactor, 0 Ω. Parallel resistance was disconnected.

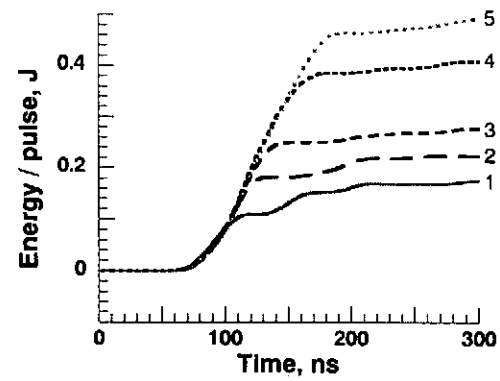

Fig. 4. Input energy to the coaxial reactor per pulse for different pulse widths. Other conditions are as in Fig. 3.

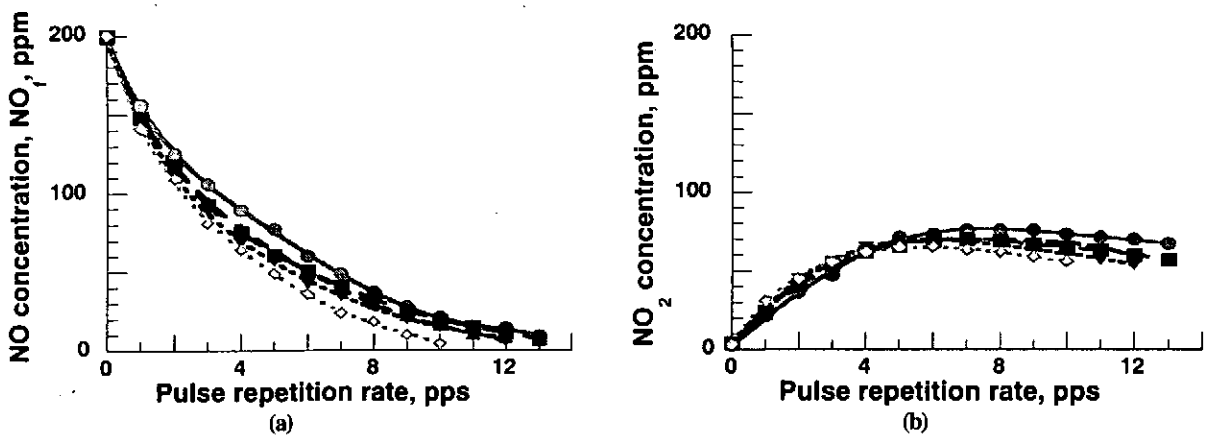

Fig. 5. Final concentrations of nitric oxide NO_f (a) and NO_2 (b) as a function of pulse repetition rate for different pulse widths. Other conditions are as in Fig. 4. ● 40 ns, ■ 60 ns, ◆ 80 ns, ▲ 100 ns, ▼ 120 ns.

3.2. Energy efficiency of NO removal

Fig. 6 shows the dependence of the energy efficiency of the removal of NO from the gas mixture in term of mol/kWh. The percentage of the NO removal ratio NO_R (in %) is,

$$NO_R = \frac{NO_i - NO_f}{NO_i} \times 100 \qquad (1)$$

where NO_i (in ppm) and NO_f (in ppm) are the initial (before treatment) and the final (after treatment) concentrations of NO in the gas mixture, respectively. In the present work NO_i = 200 ppm and the gas flow rate is fixed at 2.0 l/min (reduced to 273 K). The energy efficiency of the removal of NO (NO_E, in mol/kWh) is given by,

$$NO_E = \frac{\frac{2.0\,[l/min]}{22.4\,[l/mol]} \times (NO_i - NO_f) \times 60\,[min/h] \times 10^{-3}}{f \times E} \qquad (2)$$

where f and E are the pulse repetition rate [pulses/s] and the input energy to the reactor per pulse [J/pulse], respectively. Fig. 6 shows the dependence of NO_E on NO_R for different pulse widths in the range 40 to 120 ns while maintaining the same peak pulsed voltage applied to the discharge reactor. It will be observed from Fig. 8 that the energy requirement (mol/kWh) of the NO removal increased, and therefore the removal energy efficiency decreased with increasing NO removal ratio. The successive data in Fig. 6 (from left to right) with increasing NO_R were for pulse repetition rates from 1 to 13 pps. Fig. 6 shows that

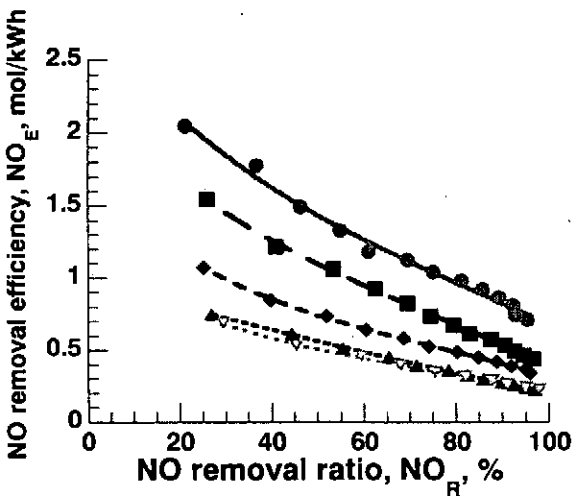

Fig. 8. Dependence of the energy efficiency of the removal of NO (mol/kWh) on the removal ratio of NO_R (Eq. (1)). Other conditions are as in Fig. 4. ● 40 ns, ■ 60 ns, ◆ 80 ns, ▲ 100 ns, ▼ 120 ns.

NO_E was higher for shorter pulse widths at a fixed NO_R. This is because the input energy to the reactor decreased with decreasing pulse width (Fig. 4) while the change in (NO_i - NO_f) (equation 2) was relatively small as can be seen from Fig. 7a, particularly for pulse widths in the range 40 to 100 ns. For the case of 40 ns, typically for NO_R = 70 %, (f = 6 pps), the value of NO_E = 1.12 mol/kWh (33.6 g/kWh) while for NO_R = 23 %, (f = 1 pps), NO_E increased to 2.08 mol/kWh (62.4 g/kWh) (Fig. 6).

The electrical energy requirement for the removal of NO is of a prime importance. The reduction of energy to an acceptable level will ensure a wide acceptance of the application of pulsed power for the removal of the NO pollutant. An attempt is made here to compare our results, wherever possible, with other results. For 90 % removal of NO using 40 ns pulse width and 10 pps, Fig. 8 shows that 0.9 mol/kWh (27.0 g/kWh) was obtained. It was reported in [2] that for 90 % removal of 100 ppm of NO in N_2 it was expended 83.7 J per liter of N_2 using pulsed corona (100 ns) and 14 J/l using electron beam. These correspond to 5.76 g (of NO) /kWh and 34.4 g/kWh, respectively using pulsed corona and electron beam methods. The yield (g/kWh) for the removal of NO using the pulsed corona method from the present study is comparable with that using the electron beam method [2].

3.3. Effect of discharge current on removal of NO_X

A resistance in the range 0 to 300 Ω was connected in series with the coaxial reactor to the ground in order to investigate the effect of the discharge current level on the removal of NO. In this part of the study the currents were measured on the high voltage side at the input to the central wire electrode and in the external resistance (Fig. 2). This was done to mitigate against possible errors which might be present due to parallel capacitance paths between the outer cylinder and the ground when a resistance is connected there. The voltage was measured across both the reactor and the external resistance using the resistance divider (Fig. 2). The voltage across the reactor was calculated by subtracting the voltage drop across the external resistance from the measured voltage between the central electrode and the ground. The energy fed into the corona discharge was calculated using the voltage across and the current flowing into the reactor. Fig. 7 (a) shows that the series resistance has only a small influence on the shape and the peak of the voltage pulse. Fig. 7 (b) shows that the series resistance has, and

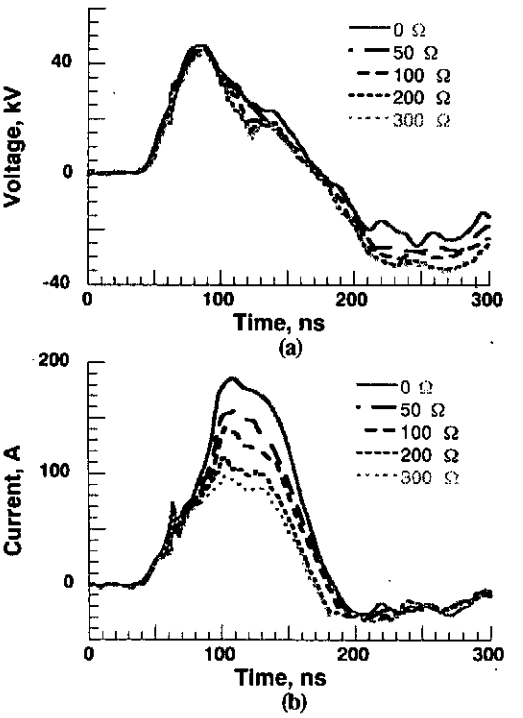

Fig. 7. Dependence of applied voltage (a) and discharge current (b) on series resistance with the coaxial reactor. Nominal pulse width, 100 ns; other conditions are as in Fig. 4. peak currents: 0 Ω (185 A); 50 Ω (156 A); 100 Ω (137 A); 200 Ω (114 A); 300 Ω (98 A).

as expected, a strong influence on the value of the peak current. The peak current typically varied from 185 A with 0 Ω to 98 A with 300 Ω. Fig. 8 shows the input energy to reactor calculated from voltage and current in Fig. 7 for different series resistances. The input energy to the reactor decreased with increasing series resistance. Typically the input energy with 300 Ω in series with the coaxial reactor was about 60 % of that when there was no resistance in series (0.46 J/pulse) while maintaining all other conditions the same.

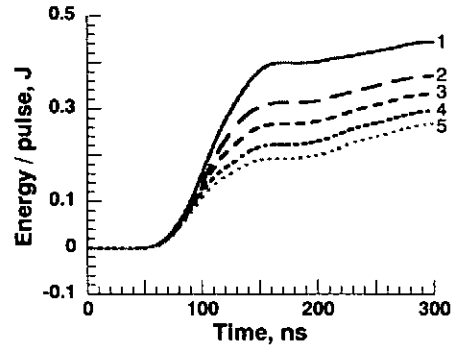

Fig. 8. Input energy to the coaxial reactor per pulse for different series resistances with the coaxial reactor. Nominal pulse width, 100ns; other conditions are as in Fig. 4. curve 1, 0 Ω (185 A); curve 2, 50 Ω (156 A); curve 3, 100 Ω (137 A); curve 4, 200 Ω (114 A); curve 5, 300 Ω (98 A).

Fig. 9 shows the final concentrations of NO_f (a) and NO_2 (b) as a function of the pulse repetition rate for different values of the series resistance. The initial value of NO in the mixture was 200 ppm. It will be observed that more NO was removed with decreasing series resistance for a fixed pulse rate. This was due to the increased current (Fig. 7b) and increased energy (Fig. 8) with decreasing series resistance. The concentration of NO decreased with increasing pulse repetition rate for all series resistance values.

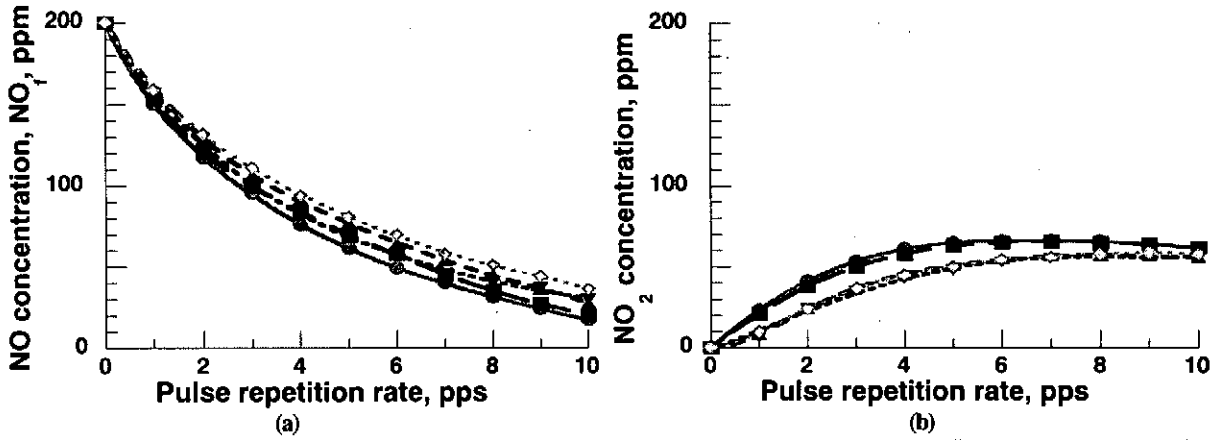

Fig. 9. Final concentrations of nitric oxide, NO_f (a) and NO_2 (b) as a function of the pulse repetition rate for different series resistances (and peak currents) with the coaxial reactor. Nominal pulse width, 100 ns; other conditions are as in Fig. 4. ● 0 Ω (185 A), ■ 50 Ω (156 A), ◆ 100 Ω (137 A), ▲ 200 Ω (114 A), ▼ 300 Ω (98 A).

Fig. 10 shows the energy efficiency of the removal of NO as a function of the removal ratio of NO for different resistance values placed in series with the reactor. It will be observed from Fig. 10 that a higher removal efficiency was obtained at a given removal ratio of NO, with increasing resistance from 0 to 300 Ω and therefore with decreasing discharge current. This is because the energy fed into the discharge decreases with increasing resistance (Fig. 8) while the effect of the latter on the removal of NO is relatively small (Fig.9a) and thus the energy yield (mol/kWh) increases with decreasing current (Fig. 10). It should be mentioned that in calculating the energy efficiency (Fig. 10) only the energy input to the gas mixture was taken into account and that dissipated in the resistance was not considered.

The effect on the removal of NO with changing either the pulse width (Fig. 5a) or the peak current (Fig. 9a) is relatively small. This is because the initial development of the pulse current is practically the same for all pulse widths (Fig. 5a) and pulse currents (Fig. 9a).

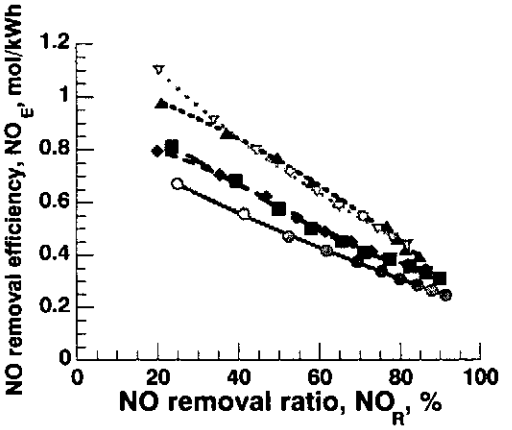

Fig. 10. Dependence of the energy efficiency of the removal of NO (NO_E) on the removal ratio of NO for different discharge currents. Pulse width, 100 ns; other conditions are as in Fig. 4. ● 0 Ω (185 A), ■ 50 Ω (156 A), ◆ 100 Ω (137 A), ▲ 200 Ω (114 A), ▼ 300 Ω (98 A).

4. Conclusions

Pulsed power at short durations (40 to 120 ns) has been used to remove NO in a mixture of N_2, O_2 and H_2O. The following conclusions have been deduced:

1. The energy required to remove NO decreased with decreasing pulse width.
2. The effect on the removal of NO with changing either the pulse width or the peak current is relatively small.
3. The energy removal efficiency of NO using 40 ns duration of pulsed power is comparable to that of the electron beam method.

References

[1] S. Masuda, "Pulse corona induced plasma chemical process: a horizon of new plasma chemical technologies", Pure and Applied Chemistry, vol.60, pp.727-731, 1988.

[2] B.M. Penetrante, M.C. Hsiao, J.N. Bardsley, B.T. Merritt, G.E. Vogtlin, P.H. Wallman, A. Kuthi, C.P. Burkhart and R.J. Bayless, "Electron beam and pulsed corona processing of volatile organic compounds and nitrogen oxides", 10th IEEE International Pulsed Power Conference, Albuquerque, New Mexico USA, pp.144-149, 1995.

[3] H.Akiyama, K. Kawamura, T. Takeshita, S. Katsuki, S. Maeda, S. Tsukamoto and M. Murata, "Removal of NO_X using discharges by pulsed power", 10th IEEE International Pulsed Power Conference, Albuquerque, New Mexico USA, pp.133-137, 1995.

[4] G. Dinelli, L. Civitano and M. Rea, "Industrial experiments on pulse corona simultaneous removal

of NO_X and SO_2 from flue gas", IEEE Transactions on Industry Applications, vol.26, pp.535-541, 1990.
[5] J-S.Chang, P.A. Lawless and T. Yamamoto, "Corona discharge processes", IEEE Transactions on Plasma Science, vol.19, No.6, pp.1152-1166, 1991.
[6] E.J.M. van Heesch, H.W.M. Smulders, S.V.B. van Paasen, P.P.M. Blom, F.M.van Gompel, A.J.P.M. Staring and K.J. Ptasinski, "Pulsed corona for gas and water treatment", 11th IEEE International Pulsed Power Conference, Baltimore, Maryland USA, pp.103-108, 1997.
[7] J.S. Clements, A. Mizuno, W.C. Finney and R.H. Davis, "Combined removal of SO_2, NO_X and fly ash from simulated flue gas using pulsed streamer corona", IEEE Transactions on Industry Applications, vol.25, pp.62-69, 1989.
[8] S. Masuda and H, Nakao, "Control of NO_X by positive and negative pulsed corona discharges", IEEE Transactions on Industry Applications, vol.26, pp.374-383, 1990.
[9] A. Mizuno, K. Shimizu, A.Chakrabarti, L. Dascalescu and S. Furuta, "NO_X removal process using pulsed discharge plasma", IEEE Transactions on Industry Applications, vol.31, pp.957-963, 1995.
[10] H. Akiyama, "Pollution control by pulsed power", Proceedings of 1995 International Power Electronics Conference, Yokohama, Kanagawa Japan, pp.1397-1400, 1995.
[11] H. Akiyama, Y. Nishihashi, S. Tsukamoto, T. Sueda, S. Katsuki, M. Hagler, J.C. Dickens and N. Inoue, "Streamer discharges by pulsed power on a spiral transmission line", 11th IEEE International Pulsed Power Conference, Baltimore, Maryland USA, pp.109-114, 1997.
[12] Y.L.M. Creyghton, E.M. van Veldhuizen and W.R. Rutgers, "Electrical and optical study of pulsed positive corona", in "Non-Thermal Plasma Techniques For Pollution Control", Eds. B.M. Penetrante and S.E. Schultheis, Springer-Verlag, Part A, pp.205-230, 1993.
[13] K. Kawamura, S. Tsukamoto, T. Takashita, S. Katsuki and H. Akiyama, "NO_X removal using inductive pulsed power generator", Transaction on IEEJ, vol.117-A, pp.956-961, 1997. (In Japanese)
[14] B.M. Penetrante, "Removal of NO_X from diesel generator exhaust by pulsed electron beams", 11th IEEE International Pulsed Power conference, Baltimore, Maryland USA, pp.91-96, 1997.
[15] K. Urashima, J-S. Chang, J-Y. Park, D-C. Lee, A. Chakrabarti and T. Ito, "Reduction of NO_X from natural gas combustion flue gases by corona discharge radical injection techniques", IEEE Transactions on Industry Applications, vol.34, pp.934-939, 1998.
[16] B.M. Penetrante, "Pollution control applications of pulsed power technology", 9th IEEE International Pulsed Power Conference, Albuquerque, New Mexico, pp.1-5, 1993.
[17] I. Gallimberti, "Impulse corona simulation for flue gas treatment", Pure and Applied Chemistry, vol.60, pp.663-674, 1988.
[18] K. Urashima, J-S. Chang and T. Ito, "Reduction of NO_X from combustion flue gases by superimposed barrier discharge plasma reactors", IEEE Transaction on Industry Applications, vol.33, pp.879-886, 1997.
[19] D. Bhasavanich, S. Ashby, C. Deeney and L. Schlitt, "Flue gas irradiation using pulsed corona and

pulsed electron beam technology", 9th IEEE International Pulsed Power Conference, Albuquerque, New Mexico USA, pp.441-444, 1993.
[20] J-S. Chang, P.C. Looy, K. Nagai, T. Yoshioka, S. Aoki and A. Maezawa, "Preliminary pilot plant tests of a corona discharge-electron beam hybrid combustion flue gas cleaning system", IEEE Transactions on Industry Applications, vol.32, pp.131-137, 1996.
[21] L. Rosocha, G.K. Anderson, L.A. Bechtold, J.J. Coogan, H.G. Heck, M. Kang, W.H. McCulla, R.A. Tennant and P.J. Wantuck, "Treatment of hazardous organic wastes using silent discharge plasmas", in "Non-Thermal Plasma Techniques For Pollution Control", Eds. B.M. Penetrante and S.E. Schultheis, Part B, Springer-Verlag, pp.281-308, 1993.
[22] S. Tsukamoto, T, Namihira, D. Wang, S. Katsuki, H. Akiyama, E. Nakashima, A. Sato, Y. Uchida and M. Koike, "NO_X and SO_2 removal by pulsed power at a thermal power plant", 12th IEEE International Pulsed Power Conference, Monterey, California USA, pp.1330-1333, 1999.
[23] S. Masuda and H. Nakao, "Control of NO_X by positive and Negative pulse corona discharges", IEEE Transactions on Industry Applications, vol.26, No.2, pp.374-383, 1990.
[24] S. Tsukamoto, T, Namihira, D. Wang, S. Katsuki, H. Akiyama, E. Nakashima, A. Sato, Y. Uchida and M. Koike, "Pollution control of actual flue gas using pulsed power at a thermal power plant", Transaction on IEEJ, vol.119-A, pp.984-989, 1999. (In Japanease)
[25] T. Namihira, D, Wang, S. Tsukamoto, S. Katsuki and H. Akiyama, "Effect of gas composition for NO_X removal using pulsed power", Transaction on IEEJ, vol.119-A, pp.1190-1195, 1999. (In Japanease)

CALCULATION ON COOLING RATE OF AN INTENSE PULSED ION BEAM IRRADIATED METAL SURFACE

Yoshiyuki Hashimoto and Mitsuyasu Yatsuzuka*

Department of Electronic Engineering, Kobe City College of Technology,
8-3 Gakuen-Higashimachi Nishiku, Kobe, Hyogo 651-2194

*Department of Electrical Engineering, Himeji Institute of Technology,
2167 Shosha, Himeji, Hyogo 671-2201

ABSTRATC

We calculated a temperature rise of the target caused by an intense pulsed ion beam irradiation. When a proton beam with energy of 100 keV, current density of 100 A/cm^2, and pulse width of 50 nsec are irradiated to a pure titanium target, the temperature of surface region within about 0.5 μm is increased above the target melting point. The maximum cooling rate is reached to 3 x 10^{11} K/sec. This cooling rate is 10^3~10^5 times larger than a cooling rate obtained by the other method for production of non-equilibrium microstructures.

§1. Introduction

The intense pulsed ion beam (IPIB) irradiation of target results in rapid heating of the target surface above its melting point. After the beam is turned off, the heated region is immediately cooled by thermal conduction at a fast cooling rate typical of 10^6-10^9 K/sec. Such a rapid cooling of the heated region produces non-equilibrium microstructures such as amorphous and nanostructured layer. We have succeeded in production of nanostructured crystallites on a pure titanium surface and an amorphous layer on a nickel alloy by an IPIB irradiation.[1-4] Measurement of the cooling rate that is most important parameter for production of non-equilibrium microstructures is impossible. In this paper, we describe on the numerical calculation of temperature rise of the target caused by IPIB irradiation.

§2. Calculation Model

When intense pulsed ion beams (IPIB) are irradiated to the target metal, ions in the IPIB lose kinetic energy and stop in the target. The ion's energy loss that is converted into heat

energy will rise the temperature of the target. The temperature rise $T_0(z)$ is expressed as follows,

$$T_0(z) = \frac{e \times E_L(z) \times N}{c\rho} - H(T) \ [\mathrm{K/cm^3}], \tag{1}$$

where N is the number of incident ions, c [J/g/K] is the specific heat of the target, ρ [g/cm^3] is the density of the target, and $H(T)$ is corrective term for latent heat of the target. E_L [eV/cm/ions] that changed with ion beam energy is energy loss of ions in the target.

Assuming an ideal rectangular beam with a constant current I [A] and a pulse width τ [sec], N becomes the following equation.

$$N = \frac{I \times \tau}{e} \tag{2}$$

If equation (1) is rearranged using equation (2), it becomes the following equation.

$$T_0(z) = \frac{I \times \tau \times E_L(z)}{c\rho} - H(T) \ [\mathrm{K/cm^3}] \tag{3}$$

Next, we consider as thermal diffusion of the target. If it is assumed that the beam is uniformly irradiated to the target, the thermal diffusion in the target is expressed one-dimensional equation as follows,

$$\frac{\partial T(z,t)}{\partial t} = \chi \frac{\partial^2 T(z,t)}{\partial z^2} - H(T) \tag{4}$$

where $T(z, t)$ [K] is the temperature, z [cm] is the depth, and χ [cm^2/sec]is the thermal

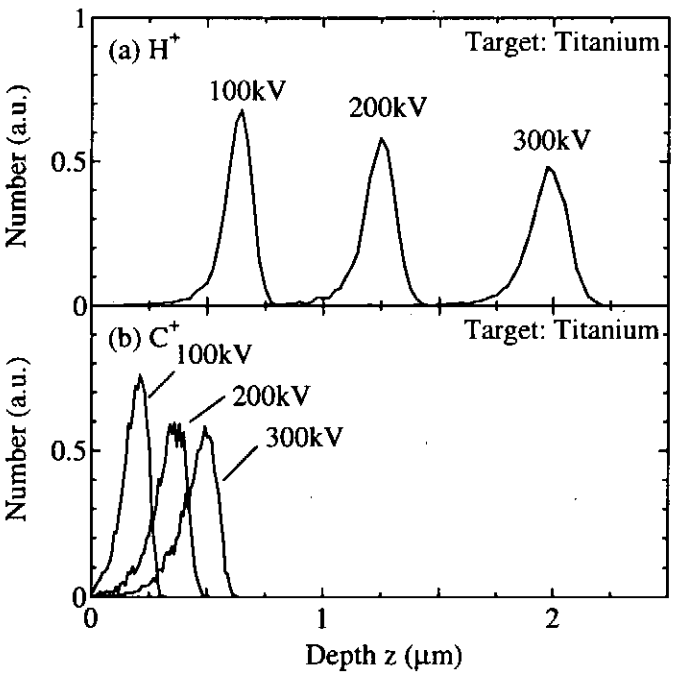

Fig.1 The normalized ion distribution in a titanium target.

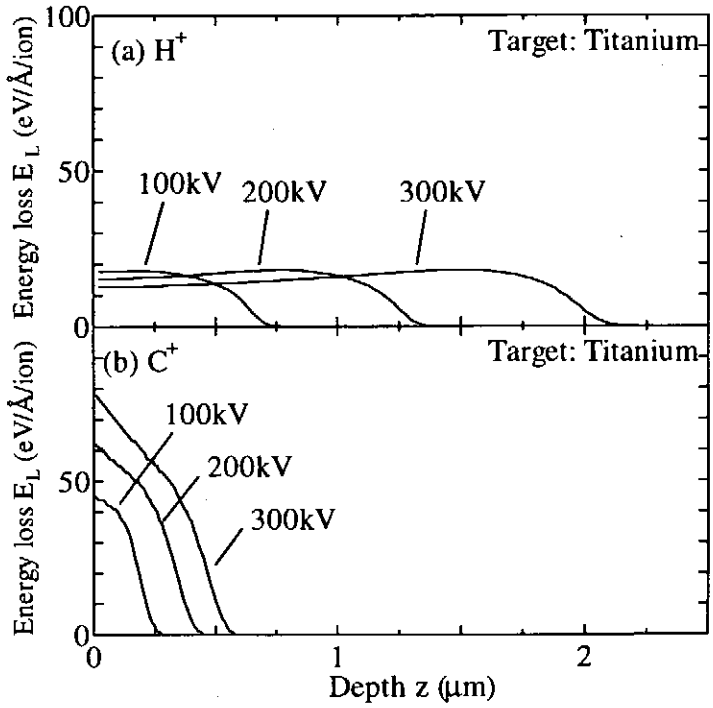

Fig.2 The energy loss as a function of depth for various ion energy.

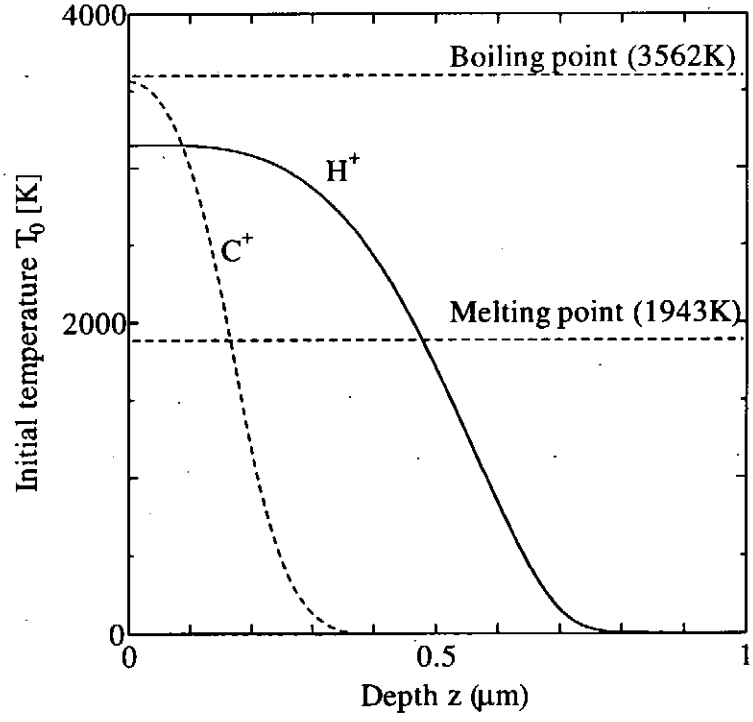

Fig.3 The initial temperature rise of the titanium target.

diffusivity. To estimate the change of the target temperature with time and depth, we solve equation (4) by using the finite difference method. If the thermal diffusion length during the IPIB irradiation is very shorter than ion range, the initial values of the target temperature gives $T_0(z)$ in equation (3).

§3. Calculation Results

3.1 Energy loss of ions in the target

The normalized ion distribution in a titanium target is shown in Fig.1 for various values of the ion energy, where (a) and (b) are in the case of H^+ and C^+ irradiation, respectively. When the ion energy is increased, the depth at the peak of the ion distribution becomes deeper. The depths at the peak of H^+ distribution are 0.62 μm for 100 keV, 1.21 μm for 200 keV, and 1.92 μm for 300 keV, respectively. In the case of C^+, the depths at the peak of the distribution are 0.18 μm for 100 keV, 0.32 μm for 200 keV, and 0.45 μm for 300 keV, respectively.

Figure 2 (a) and (b) show the energy loss of H^+ and C^+ for various values of the ion energy. From Fig.2, it is found that C^+ lose energy at near surface compared with H^+. The peak of the energy loss of H^+ and C^+ for 100 keV are 18 eV/Å/ion and 45 eV/Å/ion, respectively. Hence, in the case of C^+, the target temperature is increased at near surface.

3.2 Temperature rise and thermal diffusion of the target

The initial distribution of the target temperature was obtained from equation (3) by substituting the results of energy loss as shown in Fig.1. Figure 3 shows the initial temperature of the titanium target after irradiation of the IPIB with the energy of 100 keV, current density of 100 A/cm^2 and pulse width 50 nsec. In Fig.3, the region heated by H^+ IPIB is larger than that heated by C^+ IPIB.

We estimated the change of target temperature with time and depth from equation (4). Figure 4 shows the temperature of the titanium target as a function of time for various depths, where (a) and (b) indicate in the case of H^+ and C^+ IPIB irradiation, respectively. As seen in Fig.4, the temperature of surface region within about 0.5 μm in H^+ IPIB and 0.3 μm in C^+ IPIB is increased above the target melting point. The maximum temperature rise in C^+ IPIB reaches the boiling point of the target. However, since the latent heat for evaporation of the target is very large, the temperature of the target can't exceed its boiling point in this calculation condition.

3.3 Cooling rate of the target surface

We estimated the cooling rate from the change of the temperature shown in Fig.4. The cooling rate was defined as followed,

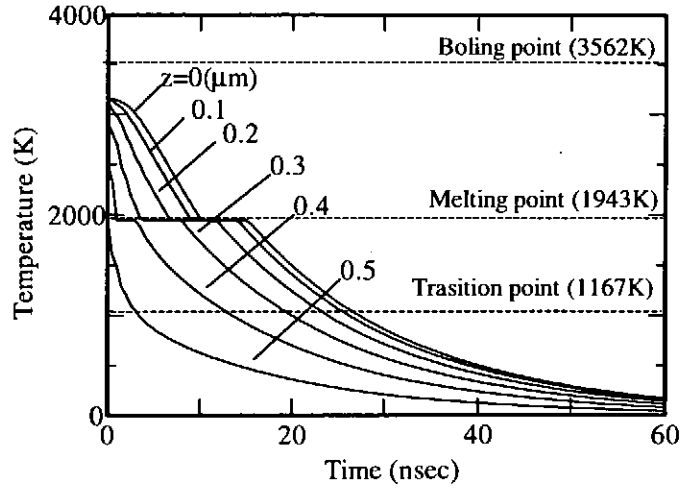

(a) H^+ IPIB with 100 keV, 100A/cm^2 and 50 nsec

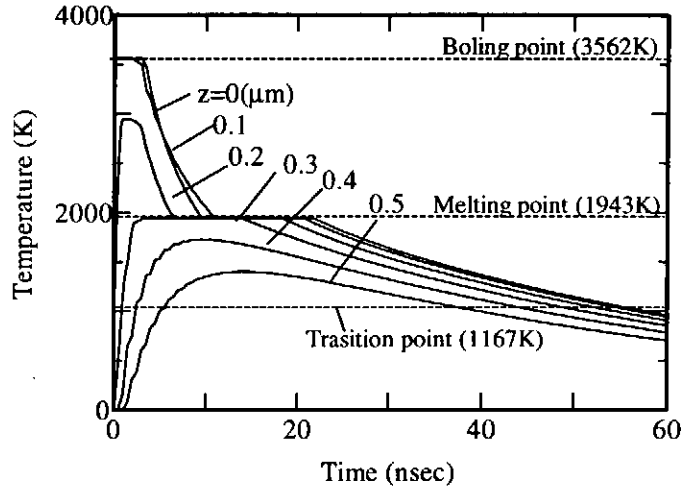

(b) C^+ IPIB with 100 keV, 100A/cm^2 and 50 nsec

Fig.4 The change of target temperature with time and depth.

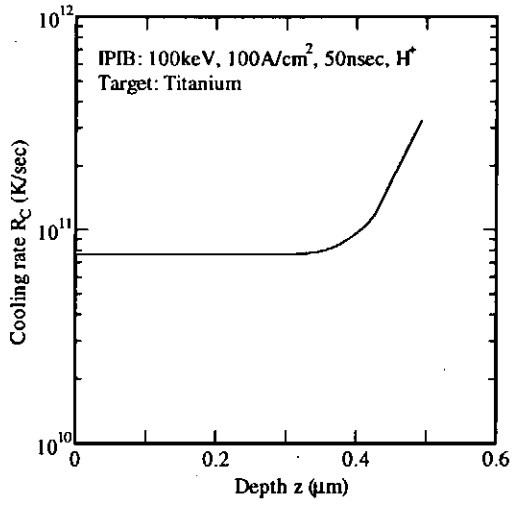

Fig.5 The cooling rate as a function of the target depth.

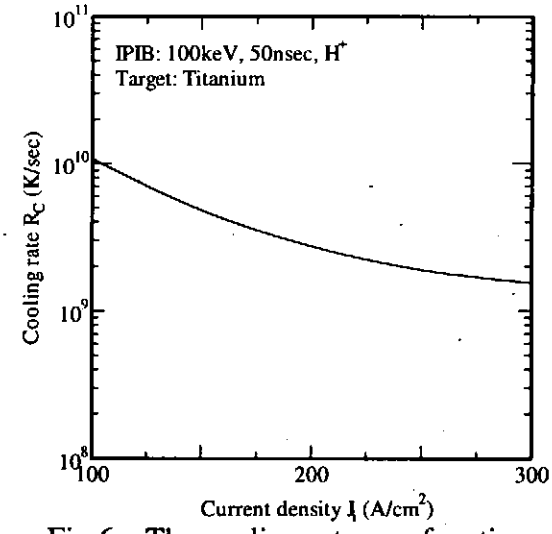

Fig.6 The cooling rate as a function of beam current density.

$$R_C = \frac{T_M - T_T}{\Delta t} \text{ [K/sec]} \quad (5)$$

where T_M and T_T are the melting point and the transition point of the target, respectively. Δt is time for decreasing the target temperature from T_M to T_T. Figure 5 shows the cooling rate as a function of the target depth when the IPIB with H^+, 100 keV, 100 A/cm^2, and 50 nsec was irradiated the titanium target. In the near surface region within about 0.3 μm, the cooling rate of 7.8 x 10^{10} K/sec is constant. The cooling rate increase with the depth in 0.3~0.5 μm region. Large temperature gradients at the deep region of the target lead to increasing the cooling rate. The maximum cooling rate is 3 x 10^{11} K/sec at 0.5 μm. This cooling rate is 10^3~10^5 times larger than a cooling rate obtained by the other method for production of non-equilibrium microstructures. The region above 0.5 μm isn't melted by the IPIB irradiation.

Figure 6 shows the cooling rate as a function of beam current density, where the IPIB is H^+, 100 keV, 50 nsec and the target is titanium. The cooling rate decreases with increasing the current density of the IPIB in this calculation condition. This result indicates an excess energy of the IPIB prevent rapid cooling of the target. However, the target melting by the IPIB irradiation is necessary for material processing.

§4. Summary

We calculated a temperature rise of the target caused by an intense pulsed ion beam irradiation numerically. When a proton beam with energy of 100 keV, current density of 100 A/cm^2, and pulse width of 50 nsec are irradiated to a pure titanium target, the temperature of surface region within about 0.5 μm is increased above the target melting point. The cooling rate is constant in the near surface region within about 0.3 μm. The maximum cooling rate is reached to 3 x 10^{11} K/sec. This cooling rate is 10^3~10^5 times larger than a cooling rate obtained by the other method. The cooling rate decreases with increasing the current density of the IPIB in this calculation condition.

Acknowledgment

The Muramoto Research Grant supported a part of this work.

References

1) M. Yatsuzuka, et.al: Appl. Phys. Lett., **6**, 206-207 (1995).
2) M. Yatsuzuka, et.al: Jpn. J. Appl. Phys.; **35**, 1857-1861(1996).
3) Y. Hashimoto, et.al: Proc. of 11th Int Conf. on High Power Particle Beams, Praque, 848-851(1996).
4) Y. Hashimoto, et.al: Proc. 1996 Int. Conf. on Plasma Physics, Nagoya, 1406-1409(1996).

RADIATION INHOMOGENEITY SMOOTHING IN A VALLEY FORMED BY ION BEAM DEPOSITION IN ICF FUEL PELLET

J. Sasaki, T. Nakamura, T. Nagai, K. Fujita, T. Kikuchi and S. Kawata

Department of Electrical and Electronics Engineering, Utsunomiya University, Utsunomiya 321-8585, Japan. kawata@cc.utsunomiya-u.ac.jp

ABSTRACT

We study the beam non-uniformity smoothing effect of the radiation transport in the density valley formed by an ion-beam deposition in an ion-beam inertial confinement fusion pellet by numerical simulations. The simulation results show that the radiation energy is confined in the density valley, and the beam non-uniformity can be smoothed out by the radiation transport along the density valley.

I. Introduction

In inertial confinement fusion(ICF), one of the most important issues is to find a way to implode a fuel pellet in a spherically symmetrical manner. In this paper, we studied a radiation-smoothing effect on an implosion symmetry under a non-uniform acceleration. In an ion beam pellet implosion, ion beams may introduce an implosion non-uniformity. The non-uniformity introduces the non-uniform implosion and degrades the fusion energy output. Even in a direct-driven reactor-size pellet, the radiation smoothing is important. In addition, an ion deposition layer is rather thick in ion-beam ICF. It may be several hundred μm, although it depends on particle energy and material. A pressure peak appears in a rather deep part of a deposition layer. Therefore, a density valley is formed in the beam-energy absorber. This density valley has a role of the radiation confinement and we can also expect the smoothing of the beam non-uniformity in this valley.

In this paper the radiation non-uniformity smoothing effect is studied by the computer simulation. It confirms that a density valley is formed by the ion beam deposition and the initial non-uniformity can be smoothed by the radiation transport in the density valley.

II. Simulation model

In order to study the non-uniformity smoothing effect of the radiation transport on an ion-beam pellet implosion, we employed a two-dimensional (r, θ) Lagrangian hydrodynamic code. The physical model employed in this paper is based on a two-temperature (plasma and radiation temperatures) fluid model.

An ion-beam ICF pellet employed in this paper is presented in Fig. 1, and consisted of three layers of Pb, Al, and DT. The DT fuel contained is 4mg, and the total masses of D and T are equal. The inner radius of the pellet is 3mm. The initial state of Pb, Al and DT are in solid. An ion (Pb)-beam energy driver parameter in this paper is presented in Fig. 2. The total Pb-ion-beam input energy is 7MJ. The ion-beam pulse duration is 34ns. The beam power pulse shape is shown in Fig.2. The ion-beam deposition energy is computed by solving the equations for ion stopping power including the plasma effect. In this paper, a Pb beam ion

impinges the pellet surface with an incident angle, and the incident angle distribution is uniform between the normal and the maximum incident angle(see Fig.1b).

The non-uniformity is introduced by changing the ion-beam number density as follows:

$$n = n\_0\ (1.0+\delta[cos(m\theta)])$$

where δ is the amplitude of the non-uniformity and m is the mode number. In this paper, the mode number is 2 in the simulation.

III. Non-uniformity smoothing effect of radiation transport

Figure 3 presents the density profile in space. The beam non-uniformity is 2.5% and the maximum incident angle is 30 degree. The beam non-uniformity introduces the implosion non-uniformity. The low-density part exists in the Al layer. This is called the density valley in this paper and the beam non-uniformity is smoothed by the radiation transport along the density valley.

Figure 4(a) presents the density and the radiation temperature profiles as a function of radius at 30 nsec; a solid line shows the density profiles and a dotted line shows the radiation temperature. It is shown that the density valley is formed and the radiation is confined in the valley. Figure 4(b) presents the peak radiation temperature profiles in the Al layer at 34.1*nsec* as a function of θ; a solid line shows a result in which a radiation transport is included normally and a dotted line shows one including a radiation transport only in the radius direction. The beam non-uniformity can be smoothed out by the radiation transport from 2.5% to 2.1%.

Figure 5 presents the fusion output energy as a function of the Pb beam non-uniformity; a solid line shows a result in which a radiation transport is included normally and a dotted line shows one including a radiation transport only in the radius direction. The beam non-uniformity can be smoothed well, and that the maximum tolerable beam non-unformity is 2.5% in this study. Table 1 also shows the simulation results, the fusion output energy, ρR, the maximum ion temperature and the implosion efficiency, which supports the result shown in Fig. 5.

These simulation results for a pellet implosion demonstrate that the radiation transport may smooth out the non-uniformity in the density valley even in the direct-driven ICF pellet.

IV. Density valley formation

In the previous section, it was found out that the Pb beam non-uniformity can be smoothed in the density valley. The simulation study also shows that the density valley structure is controlled by changing the beam maximum incident angle.

Figure 6 presents the density profiles as a function of radius at about 25 nsec, 30 nsec and 35 nsec. Figure 7 presents the radiation temperature profiles as a function of radius at about 25 nsec, 30 nsec and 35 nsec. The density valley shape changes slightly, when the maximum beam incident angle becomes changes. Table 2 shows that the fusion energy output, ρR and the maximum ion temperature are kept large enough to extract the sufficient fusion energy

output, when the maximum incident angle does not become too large (<35 degree). The implosion efficiency becomes lower, when the maximum incident angle becomes too large (>35 degree). When the maximum Pb ion impinging angle becomes large, the temperature and pressure peaks move outward (see Fig.7), and therefore the larger mass should be imploded. Consequently the implosion efficiency becomes lower with the increase in the Pb incident angle. Consequently, the beam non-uniformity can be smoothed out along the density valley by the radiation transport, when the maximum incident angle is kept small enough.

V. Conclusions

In this paper, we studied the radiation smoothing effects on a pellet implosion by computer simulations. We also studied that the density valley structure is influenced by changing the beam maximum incident angle. The first result obtained is that the beam non-uniformity can be smoothed out by the radiation transport along the density valley. In a direct-driven Pb-ion-beam ICF pellet, the temperature of the ablation part is about several hundred eV and the density is rather high. In the density valley in the energy absorber, the radiation is confined and plays a roll to smooth out the beam non-uniformity. We also found that the density valley structure is influenced by changing the beam maximum incident angle; the implosion efficiency is also influenced by changing the valley structure. The simulation results present in this paper that the beam non-uniformity can be smoothed out along the density valley by the radiation transport, when the maximum incident angle is kept small enough.

References

1) M.H. Emery, et al., Phys. Rev. Lett. **48**, 253 (1982).
2) S. Kawata and K. Niu, J. Phys. Soc. Jpn., **53**, 3416 (1984).
3) M. Tabak and D. Callahan-Miller, Phys. Plasmas, **5**, 1895 (1998).
4) M. Tabak, D. Callahan-Miller, D.D.M. Ho and G.B. Zimmerman, , Nucl. Fusion, **38**, 509 (1998).
5) S. Kawata, T. Sato, T. Teramoto, E. Bandoh, Y. Masubuchi and I. Takahashi, Laser and Particle Beams, **11**, 757 (1993).
6) N. A. Tahir, , K.A. Long, E. W. Laing, J. Appl. Phys. **60**, 898 (1986).
7) S. Kawata, and H. Nakashima, Laser and Particle Beams, **10**, 479 (1992).
8) S. Kawata, Laser and Particle Beams, **13**, 383 (1995).

TABLE 1. The non-uniformity smoothing effect of the radiation transport. When the radiation transport is included normally, the beam non-uniformity can be smoothed well, and the maximum tolerable beam nonunformity is 2.7%.

Radiation	Nonuniformity [%]	OutPut Ene. [MJ]	ρ R [g/cm^2]	Ti max. [kev]	Imp.Eff. [%]
	0	297.1	0.62	24.8	1.04
ON	0.5	297.2	0.62	25.7	1.03
	1.0	306.3	0.66	26.0	1.01
	1.5	293.5	0.69	25.5	1.06
	2.0	247.3	0.76	25.3	1.05
	2.5	172.3	0.77	24.4	1.05
	2.7	101.7	0.82	16.7	1.05
	3.0	10.44	0.88	6.31	1.04
OFF	0.5	296.8	0.61	25.7	1.03
	1.0	305.7	0.66	25.5	1.01
	1.5	284.2	0.68	25.2	1.06
	2.0	234.9	0.75	24.7	1.05
	2.5	102.4	0.75	23.4	1.05
	2.7	10.86	0.79	6.70	1.05
	3.0	3.410	0.49	3.39	1.04

TABLE 2. Simulation results by changing the beam maximum incident angle. The maximum beam incident angle should be kept small, in order to obtain a sufficient fusion energy output.

Max incident Angle[degree]	OutPut Ene.[MJ]	ρ R [g/cm^2]	Ti max [kev]	Imp.Eff. [%]	void closing Time[nsec]
0	279	0.99	28.8	1.08	38.5
5	292	1.0	28.8	1.08	38.7
15	284	0.95	28.3	1.10	38.8
25	258	0.92	26.8	1.08	39.2
35	227	0.60	21.9	1.05	39.5
40	7.54	0.67	3.25	1.03	39.7

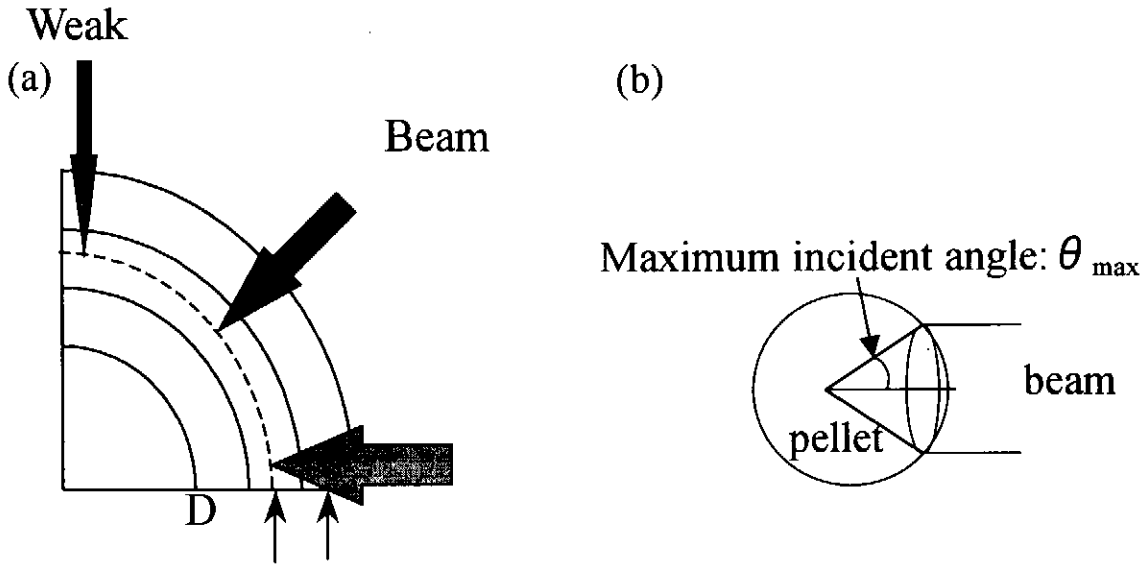

FIGURE 1. (a)The fuel pellet structure employed in the simulation in this paper. The Pb ion-beam impinges the fuel pellet and deposits its energy mainly in Al. The Pb layer behaves as a tamper and the Al layer as a beam energy absorber. The inner part of Al behaves as a pusher. (b)An ion-beam has the incident angle θ, and the distribution of beam incident angle is uniform between the normal (0 degree) and the maximum incident angle θ_{max}.

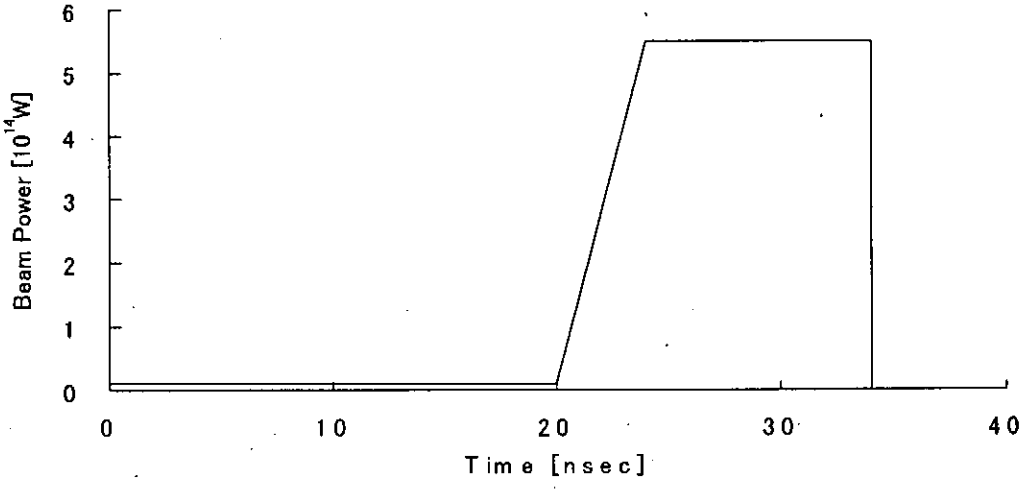

FIGURE 2. A Pb ion-beam energy driver parameter. The total Pb-beam input energy is 7MJ. The Pb-beam pulse duration is 34ns. The particle energy is 10GeV.

(a)30.0nsec

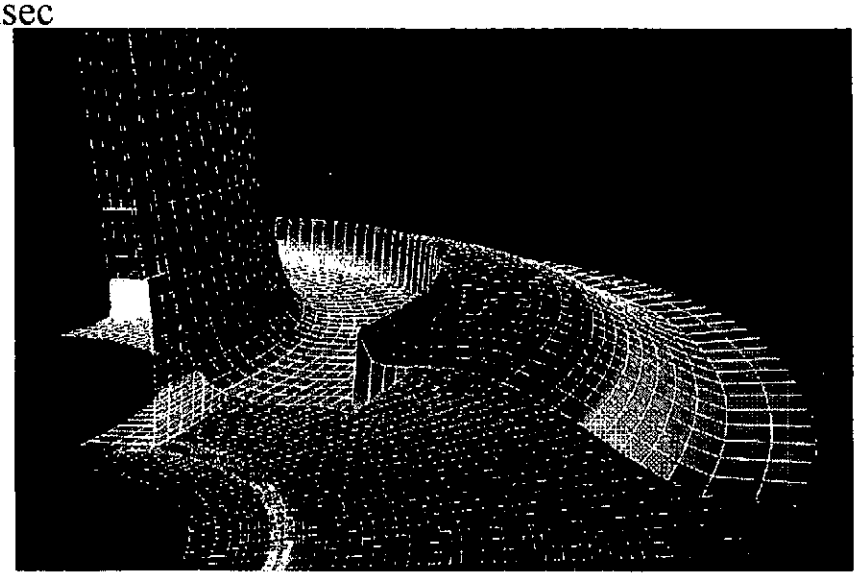

(b) 40.7nsec

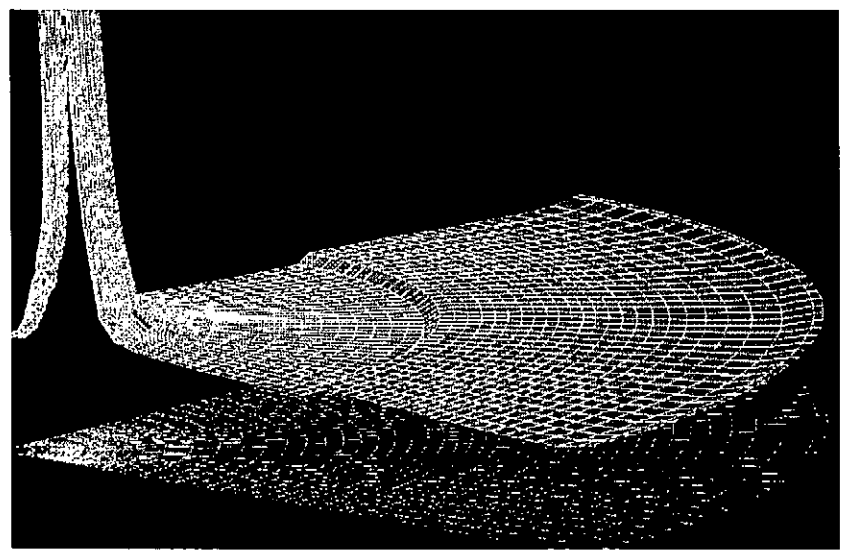

FIGURE 3. Density profiles in space at the 2.5% beam non-uniformity, and the maximum beam incident angle is 30 degree. The beam non-uniformity introduces the non-uniform implosion.

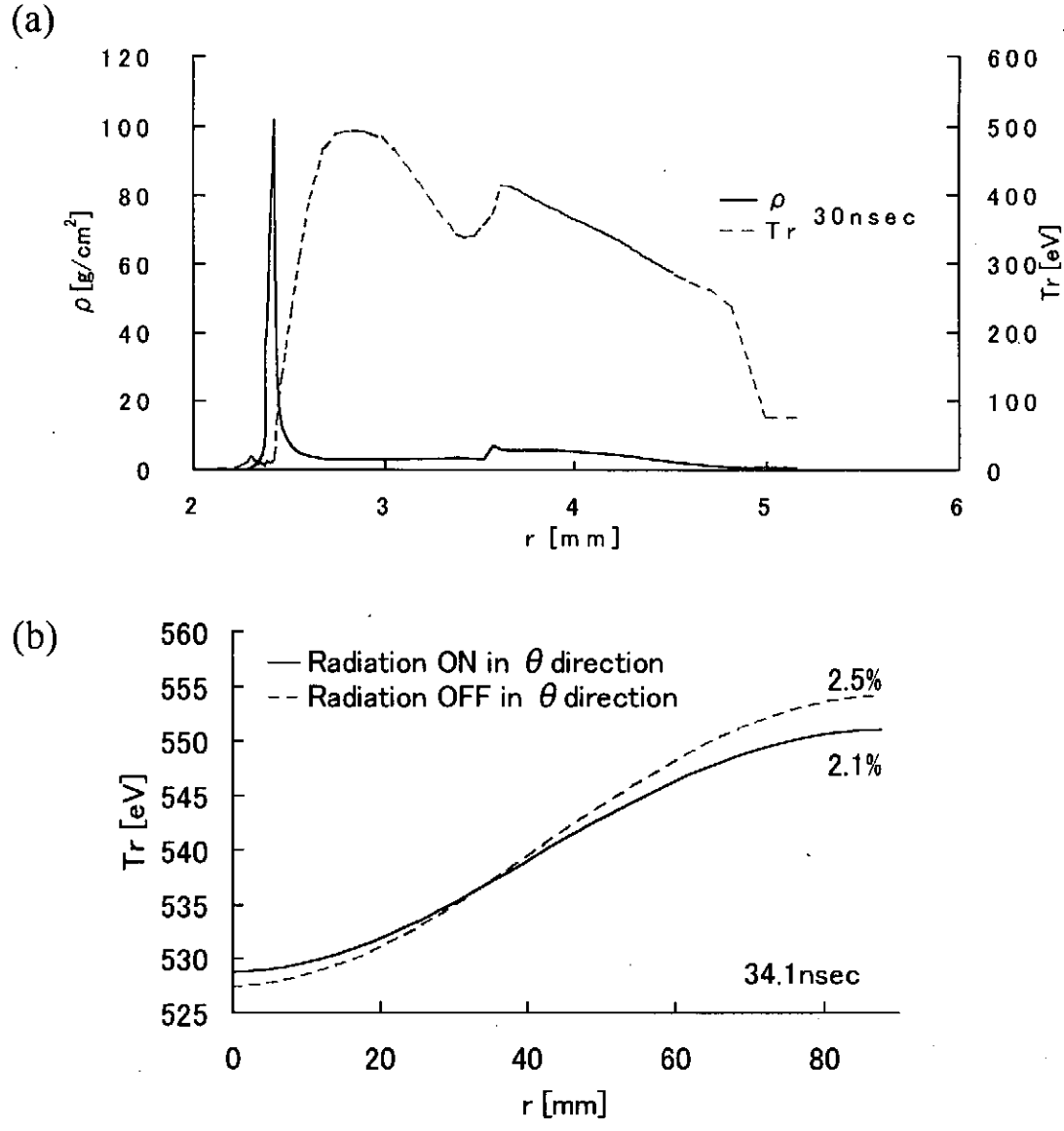

FIGURE 4. (a)The density and the radiation temperature profiles as a function of radius at 30 nsec. The density valley is formed and the radiation is confined in the valley. (b)The peak radiation temperature profiles as a function of θ in the Al layer at 34.1nsec. The beam non-uniformity can be smoothed out by the radiation transport from 2.5% to 2.1%.

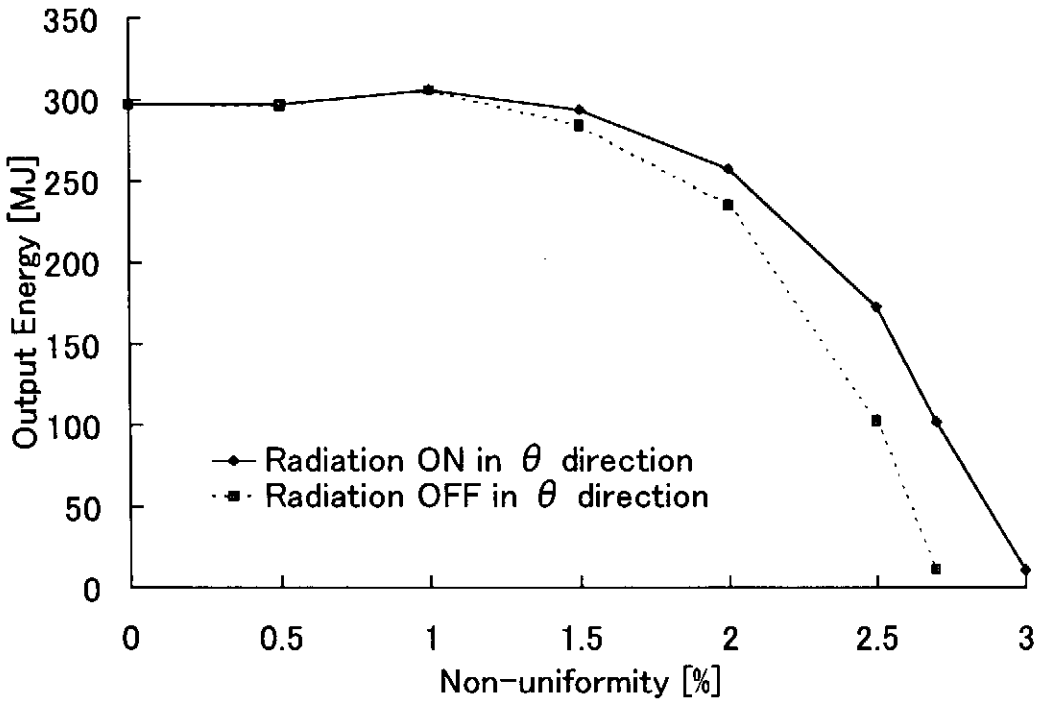

FIGURE 5. The fusion output energy as a function of the beam non-uniformity. The beam non-uniformity can be smoothed well, and the maximum tolerable beam non-unformity is 2.7% in this simulations.

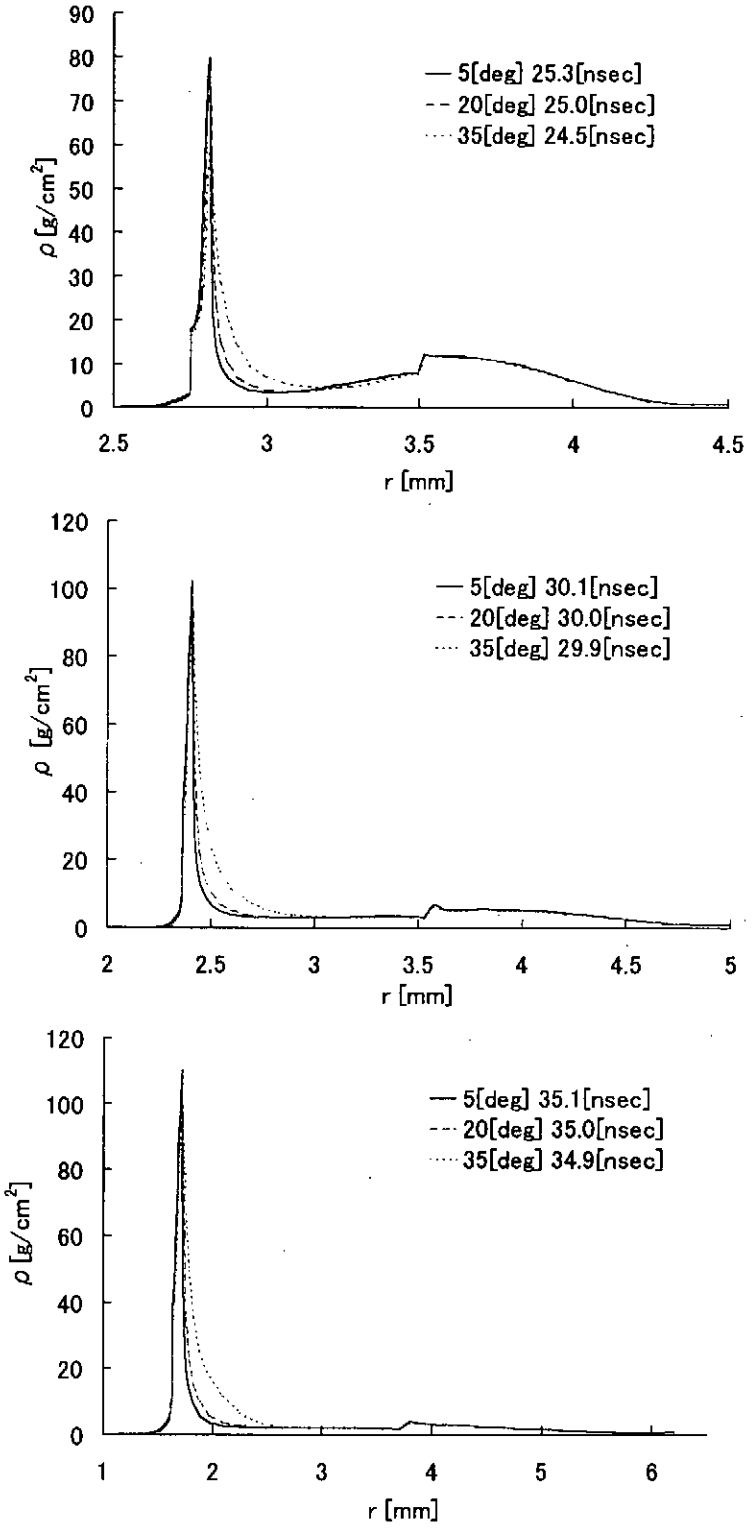

FIGURE 6. The density profiles as a function of radius at about 25 nsec, 30 nsec and 35 nsec.

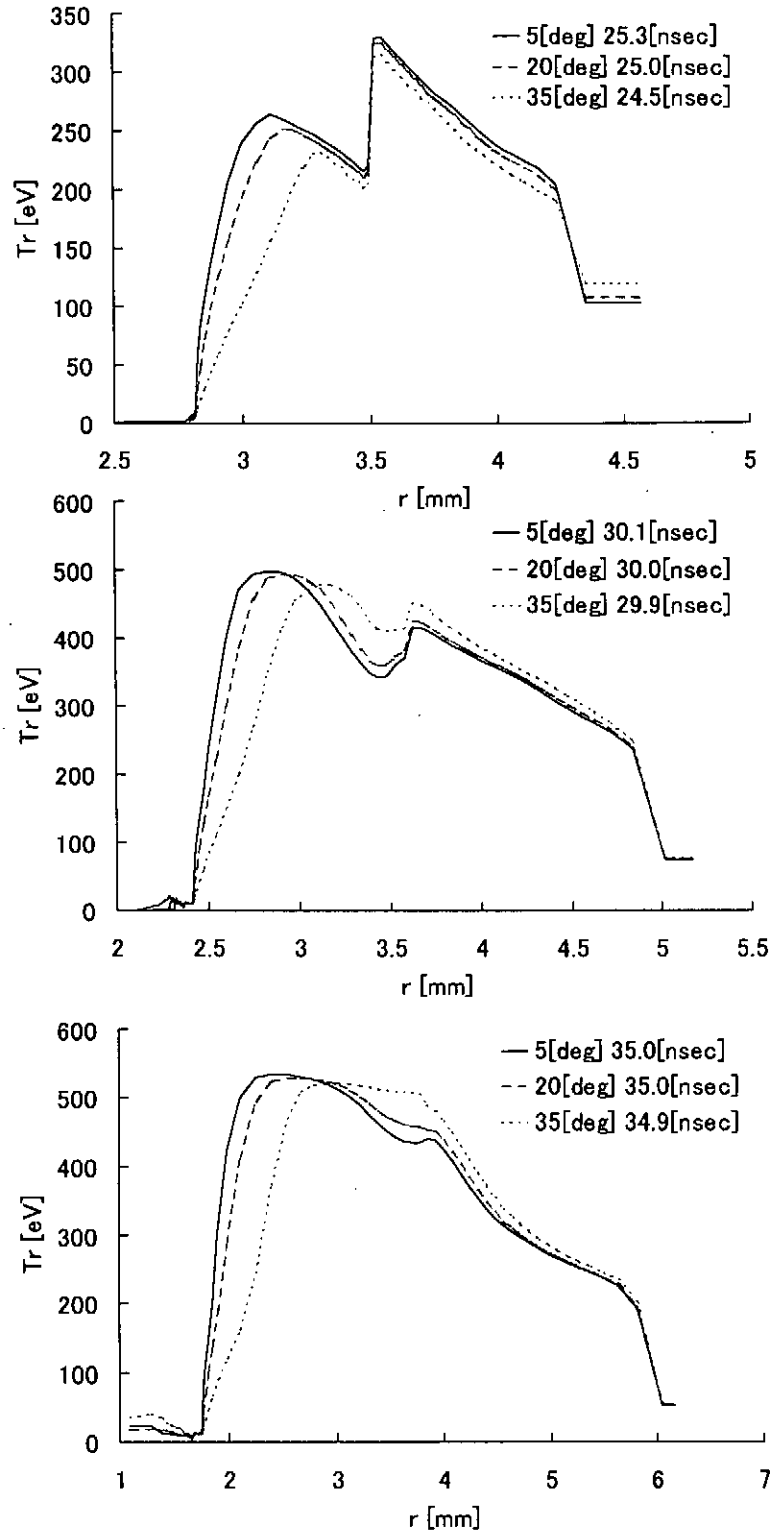

FIGURE 7. The radiation temperature profiles as a function of radius. The radiation temperature peak moves outward, when the maximum incident angle becomes large.

GENERATION OF HIGH CURRENT PULSED HEAVY ION BEAMS USING BI-DIRECTIONAL PULSES

K. Masugata, K. Kinbara, T. Atsumura, Y. Kawahara, K. Takao,
I. Kitamura, T. Takahashi and K. Yatsui*

Faculty of Eng., Toyama University, Toyama 930-8555, Japan
**Nagaoka University of Technology, Nagaoka, Niigata 940-2188, Japan*

ABSTRACT

Intense pulsed heavy ion beams (PHIB) of carbon, nitrogen, aluminum, etc., have a wide area of applications including nuclear fusion, materials science, etc. To produce a pure PHIB a new type of pulsed power ion accelerator is proposed. The accelerator consists of two acceleration gaps (an ion source gap and a post acceleration gap) and a drift tube and a bi-directional pulse is used to accelerate the ions. The concept of the accelerator is described with the principle to remove impurities. In addition, two types of pulse forming lines are proposed to produce bi-directional pulses for the accelerator. In the experiment, the bi-directional pulse of negative and positive pulse of duration 50 ns each is successfully produced by the proposed pulse forming lines.

I. Introduction

Intense pulsed heavy ion beams (such as carbon, nitrogen aluminum, etc.) have a wide area of applications including nuclear fusion, materials science, etc. Those ion beams can easily be generated in pulsed power ion diodes, however the purity of the beam is usually very poor and many kinds of ions are produced in the same time. For example, an ion beam produced by a point pinch ion diode was found to contain protons, multiply ionized carbons, organic ions etc [1]. In the usual DC ion accelerators a magnetic mass analyzer is used to remove impunities, however, in the pulsed ion beam the mass analyzer will not work due to the following reasons;

1) Charge and current of the PIB are highly neutralized by the commoving electrons.
2) PIB have a large divergence angle (usually more than several degree).

Hence the remove of impurities from the PIB by the mass analyzer is considered to be impossible and the application of the PIB has been limited due to the poor purity.

To improve the purity of the PIB a new type of pulsed power PIB accelerator is proposed[2,3], where a bi-directional pulse is used to accelerate the PIB. In the paper the principle of the accelerator is described. In addition, two types of pulse forming lines proposed to produce bi-directional pulses are described with the experimental results of the production of bi-directional pulses by the lines proposed.

2. Principle

Figure 1 shows the conceptual drawing of the PIB accelerator (ion diode) proposed. A conventional pulsed ion diode is also shown for comparison. The proposed ion diode shown in Fig.1 (a) consists of a grounded ion source, a drift tube and a grounded cathode. In the diode, bi-directional pulse (V_1) is applied to the drift tube and by the negative voltage of V_1, ion beam is accelerated towered the drift tube. When the top of the ion beam reaches the 2nd gap, the pulse is reversed and the positive voltage is applied to the drift tube, which again accelerates the ion beam in the 2nd gap.

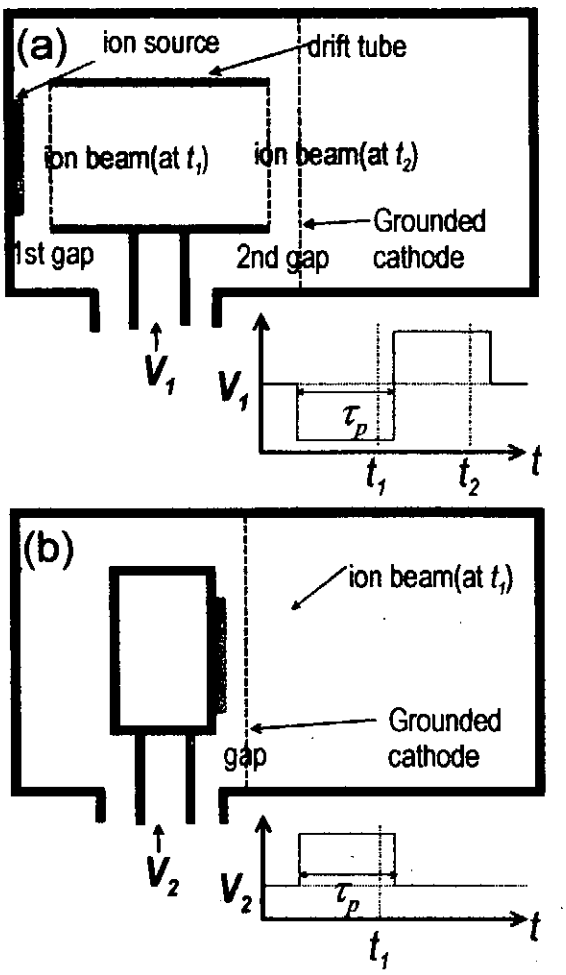

Fig.1 (a) Conceptual of the proposed PIB accelerator. (b) Conventional ion diode.

As seen in Fig.1 (b), in the conventional PIB diode, ion source is placed on the anode where a high voltage positive pulse is applied. In contrast, in the proposed ion diode, ion source is placed on the grounded anode, which extremely enhance the accessibility to the anode. This is favorable especially for the active ion sources[4,5] where discharge power supplies or gas-puff valves are placed on the anode. In addition, ion beam is accelerated in two gaps and the beam energy is enhanced in the proposed accelerator.

Here considering the acceleration of C^+ ions and a contamination of H^+ ions also exist in the ion source. In the case ions of C^+ and H^+ are accelerated in the first gap toward

the drift tube when negative voltage is applied to the drift tube (see Fig.2). In Fig.2 C^+ and H^+ beams are schematically described. As seen in the figure, due to the deference of the velocity the length of the beams is much longer for H^+. Here assuming that the length of the drift tube is designed to be same as the length of C^+ beam of duration τ_p at acceleration voltage V_p. It is calculated to be 0.24 m when V_p = 1 MV, τ_p = 50 ns. When carbon beam of length 0.24 m is in the drift tube ($t = t_1$) the voltage is reversed and positive voltage is applied to the drift tube, which accelerate the carbon beam in the 2nd gap. Since length of H^+ beam at V_p = 1 MV, τ_p = 50 ns is 0.83 m, more than 70 % of H^+ beam has passed the second gap at t_1. Hence 70 % of H^+ will not be accelerated in the 2nd gap (70 % of H^+ is removed).

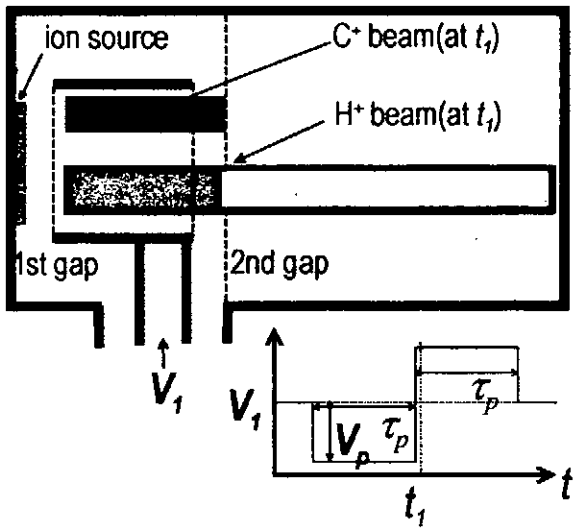

Fig.2. The principle of the removal of impurity ions of H^+ in the C^+ accelerator.

Figure 3 schematically shows the beam current waveforms after passing the 2nd gap (J_c and J_i describe the beam current of C^+ and H^+ ions, respectively). For Fig.3 (a) a usual bi-directional pulse is used and in Fig.3 (b) specially shaped pulse is used where the voltage is zero for duration of τ_z before the positive pulse. As seen in Fig. 3 (a), proton beam is only observed in the front of the pulse with short duration of τ_z. After the short pulse H^+ will not observed in the beam. Figure 3 (b) shows that if we use a specially shaped bi-directional pulse H^+ will be perfectly removed.

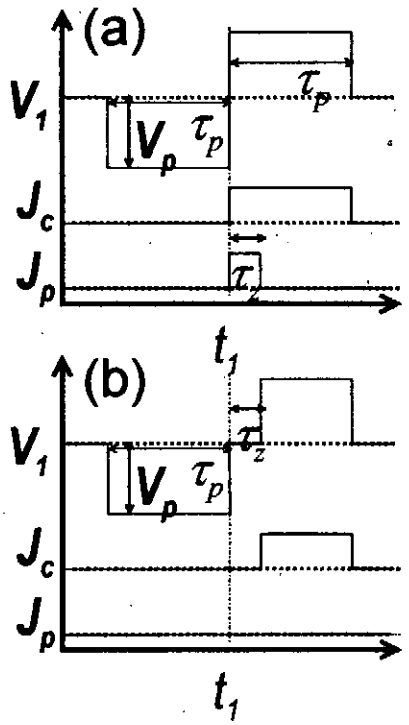

Fig.3 Beam current waveforms of the ion current after passing the 2nd gap

3. Ion diode experiment

As the first step of the development of intense pulsed heavy ion beams we are evaluating the conventional pulsed power ion diode. Magnetically insulated ion diode under construction in our laboratory. Figure 4 shows the schematic of the ion diode. The diode is B_r type magnetically insulated ion diode, which is constructed of a stainless steel cathode, aluminum anode and a pair of magnetic coils installed on the cathode. The cathode is constructed of a pair of coaxial, blade like cylinders of diameter 50 mm and 90 mm. The magnetic coils are powered by a capacitor bank of 6 kV, 4.5 kJ. The diode is powered by a specially designed fast charging Blumlein pulse forming line of output voltage 600 kV, current 24 kA, and a duration 60 ns.

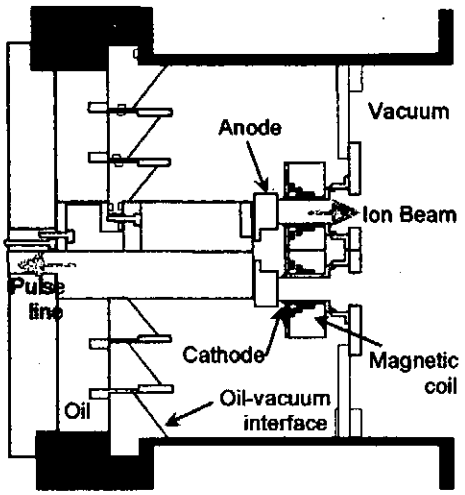

Fig.4 Br type magnetically insulated ion diode.

4. Pulse forming lines for bi-directional pulse generation

Figure 5 shows the pulse forming lines (PFL's) proposed to generate bi-directional pulses. Two types of PFL's are proposed, i.e., single coaxial type and double coaxial type. For single coaxial type (Fig. 5 (a)), a reversing switch (SW_1) and an output switch (SW_2) are used with single coaxial transmission line of length L_S. The electrical length of the line (single way transit time, L_S/v, v is the transmission velocity of the electrical signal on the line) is designed to be same as τ_p. In the operation the center conductor of the line is

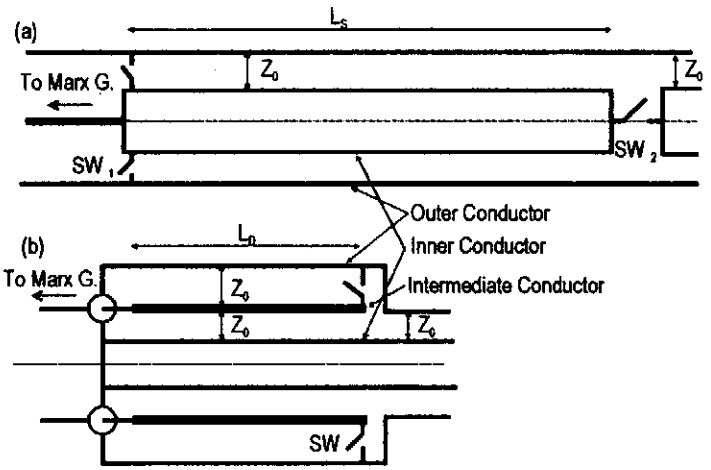

Fig.5 Pulse forming lines proposed to generate bi-directional pulse. (a) Single coaxial type. (b) Double coaxial type.

charged negatively by a high voltage power source such as the Marx generator. When charging is finished, two switches are triggered simultaneously and produce a bi-directional pulse. The feature of the line is as follows; it is simple and by changing the trigger timing of two switches the ratio of the duration of negative and positive pulses can be adjusted.

Figure 5 (b) shows the double coaxial type PFL. The PFL is the application of the pulse line cavity used in the air core type liner induction accelerators[6-8]. The line consists of a double coaxial line and a switch. The switch is placed between the outer conductor and the intermediate conductor. The electrical length of the line is designed to be $\tau_p/2$, hence the length of the line is half of the single coaxial type. In the operation, intermediate conductor is charged positively by a high voltage source and after the charging the switch is triggered. The feature of the line is as follows; the length of the line is short and since single switch is used, power loss in the switch is reduced.

Figure 6 shows the experimental circuit to simulate the double coaxial type PFL. The circuit consists of two coaxial cables (which act as transmission lines between outer-intermediate conductor and intermediate-inner conductor of the double coaxial PFL), a discharge gap switch and a dummy load. The coaxial cables used are 5D2V type ($Z = 50\ \Omega$) and the length are 5 m each, which gives a single way transit time of 25 ns. Hence the circuit is expected to produce bi-directional pulses of $\tau_p = 50$ ns and impedance 50 Ω. The coaxial lines are DC charged by a high voltage power supply.

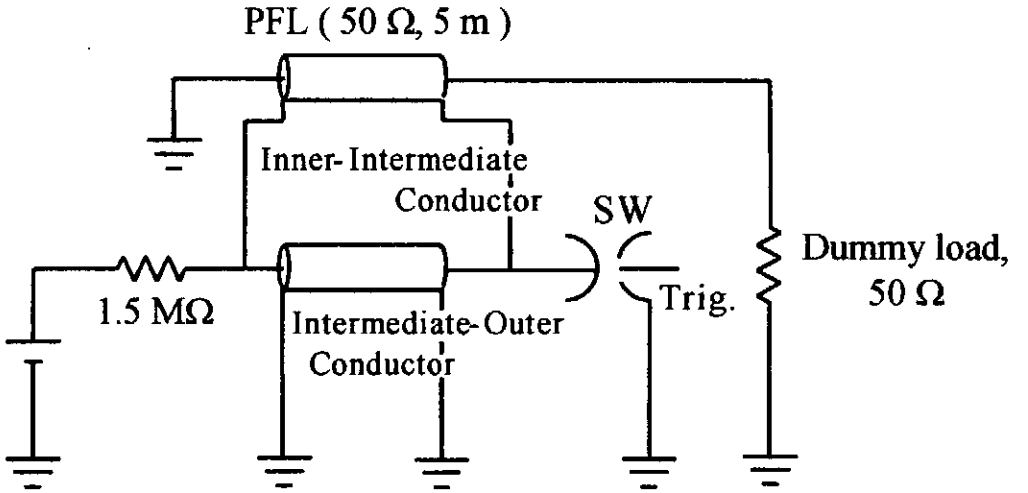

Fig. 6 Experimental circuit to simulate the double coaxial type PFL.

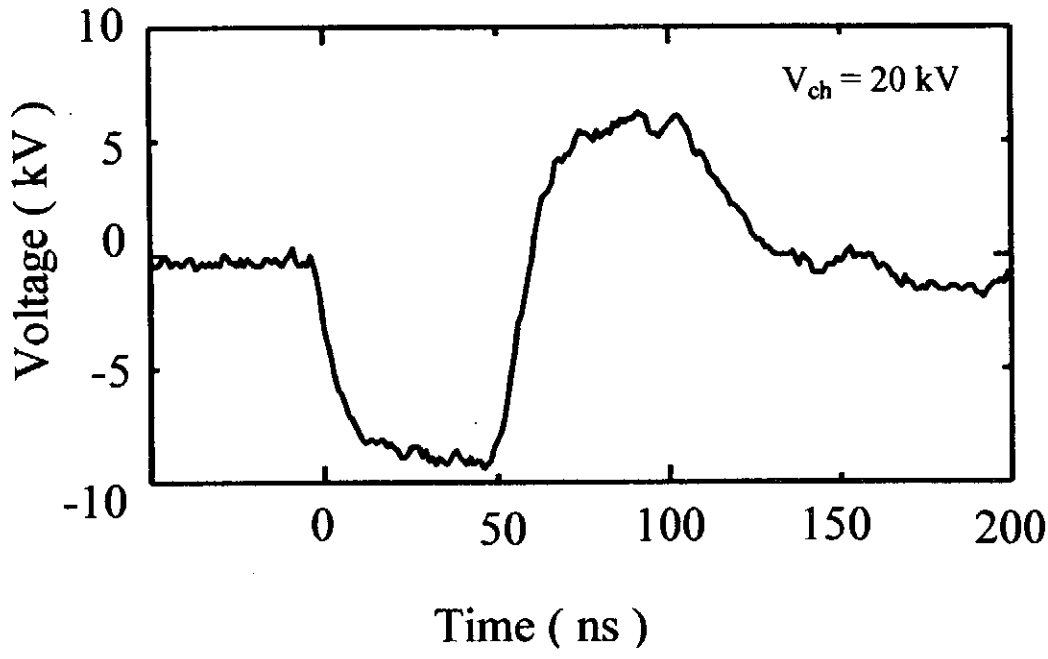

Fig. 7 shows typical waveform of the output voltage.

Figure 7 shows typical waveform of the output voltage. As seen in the figure, bi-directional pulse is successfully obtained. In the first pulse (negative pulse) peak voltage of –9.4 kV is obtained with sharp rise of rise time around 15 ns. In contrast the voltage of second pulse is less than 6.3 kV and the waveform tend to become dull. The reduction of the voltage in the 2nd pulse seems to be due to the resistance of the discharge gap switch.

5. Conclusion

Intense pulsed heavy ion beams (PHIB) of carbon, nitrogen, aluminum, etc., have a wide area of applications including nuclear fusion, materials science, etc. To produce a pure PHIB a new type of pulsed power ion accelerator is proposed. The accelerator consists of two acceleration gaps (an ion source gap and a post acceleration gap) and a drift tube and a bi-directional pulse is used to accelerate the ions. The concept of the accelerator is described with the principle to remove impurities. In addition, two types of pulse forming lines are proposed to produce bi-directional pulses for the accelerator. In the experiment, the bi-directional pulse of negative and positive pulse of duration 50 ns each is successfully produced by the proposed pulse forming lines.

Reference

1) K. Masugata, H. Okuda, K. Yatsui and T. Tazima, "Diagnosis of high-brightness ion beams produced in point pinch diodes", J. Appl. Phys. 80(9) pp. 4813-4818 (1996)
2) K. Masugata, "High current pulsed ion beam accelerators using bi-directional pulses" Nuclear Instruments & Methods in Physics Research, Section **A 411** pp.205-209 (1998)
3) K. Masugata T. Atsumura, I. Kitamura, and T. Takahashi "Electrostatic multi-stage accelerators for high current pulsed ion beam" Research Report, NIFS-PROC-42 (National Institute for Fusion Science, Nagoya, Japan) pp.56-63 (1999)
4) S. Humphries, Jr., R.J.M. Anderson, J. R. Freeman, and L. Greenly, Rev. Sci. Instrum. 52, (1981) 162.
5) H. J. Bluhm, P. J. W.Hoppe, H. P. Laqua, and D. Rusch, Proc. IEEE 80, (1992) 995.
6) A. I. Pavlovskii, V. S. Bosamykin, G. D. Kuleshov, . I. Gerasimov, V. A. Tananakin and A. P. Klement'ev, Sov. Phys. Dokl., 20 (1975) 441.
7) I. Smith, Rev. Sci. Instrum 50 (1979) 714.
8) J. Ohmura, M. Ozawa, A. Okino, J-H. Park, K-C. Ko and E. Hotta, "Bidirectional Pulse Generator System for Linear Induction Accelerator", Proc. of 12th Int. Conf. on High-Power Particle Beams (BEAMS'98) (1998)

DEVELOPMENT OF HIGHLY REPETITIVE PULSED POWER SYSTEM USING AN AIR CORE TRANSFORMER

K. Takao, K. Masugata and K. Yatsui*

Faculty of Engineering, Toyama University, 3190, Gofuku, Toyama 930-8555, Japan.
** Nagaoka University of Technology, 1603-1, Nagaoka Niigata 940-2188, Japan*

ABSTRACT

A new type of multi-pulse generator is proposed for the generation of high power pulses with extremely short pulse repetition interval. In this system, an air-core step-up transformer is used with a magnetic switch. The pulse forming line is charged on a double resonance mode. Numerical simulations of the system have shown that 600 kV, 56 ns duration pulses, matched to a 20 Ω impedance can be produced with a minimum pulse separation of 2.7 μs. To demonstrate the production of double pulses experimentally, the small system was constructed. The system is constructed of two first stage capacitors (150 nF each), an air-core step-up transformer of turn ratio 1:15, magnetic switch using cobalt based material, a second stage capacitor of 1.6 nF and a load of 80 Ω. Double pulses of duration 100 ns, peak voltage 85 kV (1st pulse) and 90 kV (2nd pulse) are successfully generated with interval of 3.75 μs when initial charging voltage of the first stage capacitors were 14 kV (for 1st pulse) and 17 kV (for 2nd pulse).

I. Introduction

A multi-pulse generator, which generates two or three independently controlled pulses with a short pulse repetition interval (T_d) of less than 100 μs, is useful in the development of pulsed power technology. For example, the generator is used to study the recovery process of the electron or ion beam diode, decay processes of high-density plasma channel in a dense gas. Two pulse generators were developed successfully using two independent pulse-forming lines (PFL) [1), 2)]. On the other hand, two pulses separated by T_d about 40μs were generated using a single PFL, where a magnetic pulse compression circuit is used with a pulse transformer [3)]. In the system, it is necessary to reset the ferromagnetic cores within T_d, hence, the repetition interval is limited by the reset time. Recently, we have proposed a new type of multi-pulse generator [4),5)], where an air-core step-up transformer [6), 7)] is used with a magnetic switch. In the system, reset less operation of the magnetic switch is possible [8)], hence we expect to generate pulses with extremely short pulse repetition interval. In the numerical simulations of the system, we have shown that 600 kV, 56 ns duration pulses, matched to a 20 Ω impedance can be produced with a minimum pulse interval of 2.7 μs [4)].

In this study, we have successfully demonstrate the production of double pulses with $T_d \leqq$ 3.75 μs.

II. System description

An equivalent circuit of the double pulse system is shown in Fig.1. The system is constructed of two first stage capacitors of 150 nF each (C_{01}, C_{02}), triggertron type discharge switches (GS_1, GS_2), inductors (L_1, L_2), an air core step-up transformer of turn ratio 1:15, a magnetic switch (MS), a second stage capacitor of 1.6 nF (C_2) and a dummy load of 80 Ω.

By the sequential closing of GS_1 and GS_2, two independent pulses are produced. The second pulse from C_{02} is transported via GS_2, L_2, C_{01}, GS_1, L_1, if GS_1 is closed.

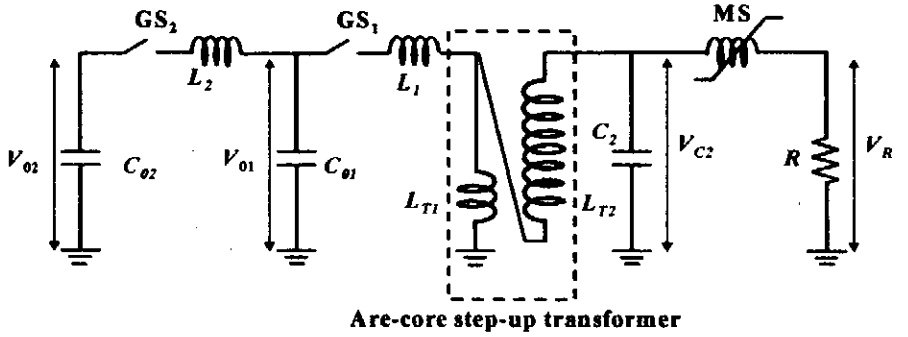

Figure 1. Equivalent circuit of the system.

An air-core spiral strip winding type transformer is utilized as the transformer. The transformer has a single turn primary surrounding a 15-turn secondary winding. The active width of both windings is 150mm. Two layers of 0.25mm thick polyester film provide the turn to turn insulation between the 0.25mm thick copper turns. The width of the polyester insulation is 200mm which leaves a 25mm margin on both sides of the copper winding. The secondary winding is wound on an acrylic pipe of outer diameter 330mm and thickness 10mm. Inductance of the primary winding (L_{T1}), secondary winding (L_{T2}) and mutual inductance (M) are estimated by the LC oscillation frequencies. To tune the effective coupling coefficient of the transformer (k_{eff}) to be 0.6, a tuning inductor (L_1) of 0.37 μH is installed in the primary circuit. Here, the k_{eff} is defined by

$$k_{eff} = \frac{M}{\sqrt{(L_1 + L_{T1}) \cdot L_{T2}}}. \qquad (1)$$

In this case, the double resonance condition

$$(L_1 + L_{T1}) \cdot C_{01} = L_{T2} \cdot C_2. \qquad (2)$$

is satisfied when C_{01}=150nF and C_2=1.6nF. For the case, the voltage gain (α) is given by

$$\alpha = \sqrt{\frac{L_{T2}}{L_1 + L_{T1}}} = \sqrt{\frac{C_{01}}{C_2}} . \qquad (3)$$

and the voltage gain of 9.6 is expected.

The parameters of the transformer are listed in Table.1.

The magnetic switch (MS) is used as an output switch of C_2. In the double resonance mode, the charging voltage of the C_2 (V_{C2}) is given by Eq. (4) when circuit resistance is neglected:

$$V_{C2}(t) = \frac{\alpha \cdot V_{C01}}{2}\left(\cos\frac{\omega t}{\sqrt{1-k_{eff}}} - \cos\frac{\omega t}{\sqrt{1+k_{eff}}}\right). \qquad (4)$$

Here V_{C01} is charging voltage of C_{01}, ω is resonant frequency given by $\omega = \{(L_1 + L_{T1}) \cdot C_{01}\}^{-1/2} = (L_{T2} \cdot C_2)^{-1/2}$.

Figure 2 shows the ideal waveform of V_{C2} and the B-H loop of the MS in the double resonance mode. As seen in Fig.3 (a), peak voltage of V_{C2} is appeared after voltage reverse, and both $V \cdot t$ value $V \cdot t_1$ and $V \cdot t_2$ are equal. As seen in Fig.3 (b), the MS is magnetized as a → b → c → d. Therefore, the magnetic state of the MS begins and ends at the same position in the B-H loop. As a result, it is not necessary to reset before the next operation. In this mode, the $V \cdot t$ value ($\Delta B \cdot S \cdot N$) of the MS have to satisfy the following relationship:

$$\Delta B \cdot S \cdot N > \int_{t_0}^{t_1} V_{C2}(t) \cdot dt . \qquad (5)$$

Here, ΔB is the magnetic flux swing, S is the cross-sectional area and N is the number of turns of the MS.

In Eq. (5), t_1 is time of the voltage reverse of V_{C2} and from Eq. (4), t_1 is given by Eq. (6).

$$t_1 = \frac{2.65}{\omega} \qquad (6)$$

From Eq. (6), we get $t_1 = 0.95\mu s$.

Table 1. Parameter of the air-core step-up transformer.

Width of windings	150 mm
Primary winding	1
Secondary winding	15
Primary inductance (L_{T1})	0.49 μH
Secondary inductance (L_{T2})	80 μH
Mutual inductance (M)	5 μH
Coupling coefficient (k)	0.8
Tuning inductance (L_1)	0.37 μH

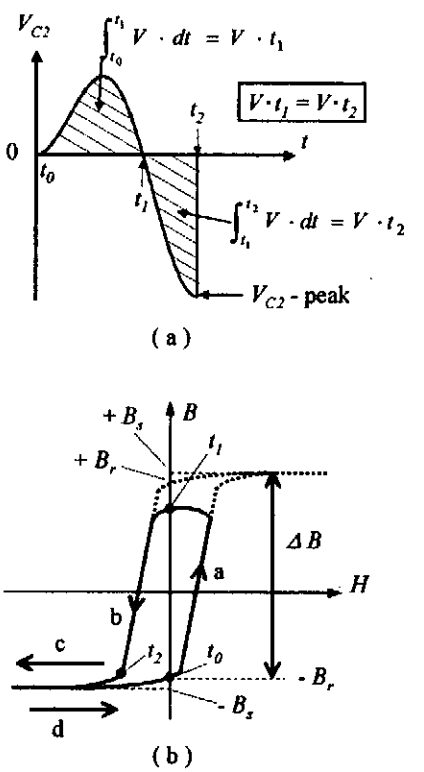

Figure 2. Charging voltage waveform and the B–H loop in double resonance mode.

We designed the maximum switching voltage of the MS take about 100kV. From Eq. (4) - (6), the MS must have the $V \cdot t$ value more than 0.03Vs in this case.

The MS is constructed of 14 stack of racetrack type cobalt-based amorphous metallic cores (AC30, TDK Electronics Ltd.), which has ΔB = 1.63 T. A 3-turn aluminum plate is used as a winding of the MS. The measured value of the residual inductance is 0.8μH. The MS has the $V \cdot t$ value of 0.04Vs and the MS can be used up to the maximum charging voltage of 136kV. The parameter of the MS is listed in Table.2.

Coupling inductor (L_2) is installed between C_{01} and C_{02} and the inductance is tuned 0.55 μH to obtain a maximum energy transfer from C_{02} to C_2.

Table 2. Parameter of the MS.

Magnetic material	Cobalt based amorphous
Number of core section	14
Magnetic cross section : S	0.00806 m^2
Flux swing : ΔB	1.63 T
Core volume : V	0.00356 m^3
Number of switch turns : N	3
Winding inductance : L_w	0.8 μH
$\Delta B \cdot S \cdot N$	0.04 Vs

The system is operated on the following sequence;

1. Before the operation C_{01}, C_{02} are charged to V_{01}, V_{02} respectively, and MS is reset to $-B_r$.
2. At first, GS_1 is triggered and the charge of C_{01} is transferred to the C_2 via the transformer.
3. After the interval GS_2 is triggered. In the moment, GS_1 must be kept closed to transfer the charge of C_{02}.

Since the reset of the MS is not necessary in the system, production of double pulses with extremely short pulse interval is expected.

III. Experimental result and discussion

A. Single pulse operation

The system has been tested at first on the single pulse operation. Figure 3 shows typical waveforms obtained for the conditions listed in Table.3. As seen in Fig.3 (a), C_2 is charged to -120 kV at t = 1.4 μs and -110 kV at t = 1.7 μs in the 1st and 2nd pulse respectively. Here, the voltage decreases and the charging time increases in the 2nd pulse due to the off resonance of the circuit. $V \cdot t$ values evaluated by integrating V_{C2} during the charging phase are 0.035 Vs and 0.036 Vs in the 1st and 2nd pulse respectively, which are about 90 % of the ΔBSN value of the MS. Figure 3 (b) shows the output pulse applied to the dummy load of R = 80 Ω and peak voltage (V_R) of -105 kV and -95 kV are obtained with durations 100 ns (FWHM) in the 1st and 2nd pulse respectively. The voltage decreases and the time delay increases in the 2nd pulse due to the reduction of V_{C2} and the elongation of charging time of C_2 in the 2nd pulse. The pre-pulse voltages in V_R of + 5 kV (5 % of the main pulse) are observed in both pulses.

Table 3. The operation conditions in the single pulse operation.

	V_{01}	V_{02}	GS_1	GS_2
1st pulse	17 kV	0	Closed at t = 0	Open
2nd pulse	0	17 kV	short	Closed at t = 0

The output pulse energies (E_R) are evaluated to be 9.7 J and 7.8 J in the 1st and 2nd pulses shown in Fig.3.

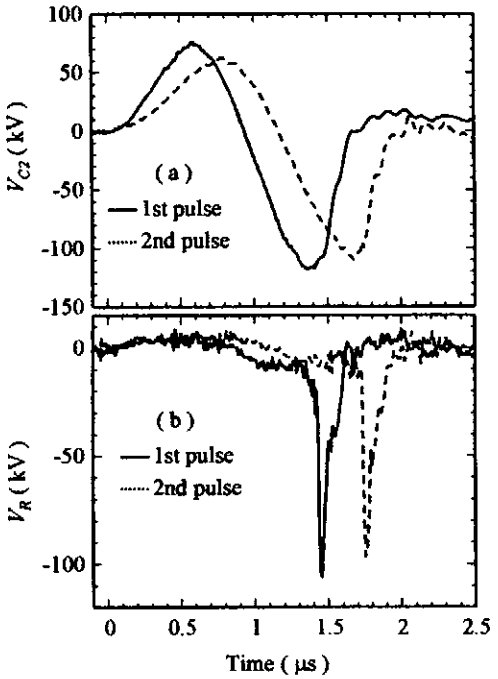

Figure 3. Results of the single pulse operation when $V_{01} = V_{02} = 17$ kV.

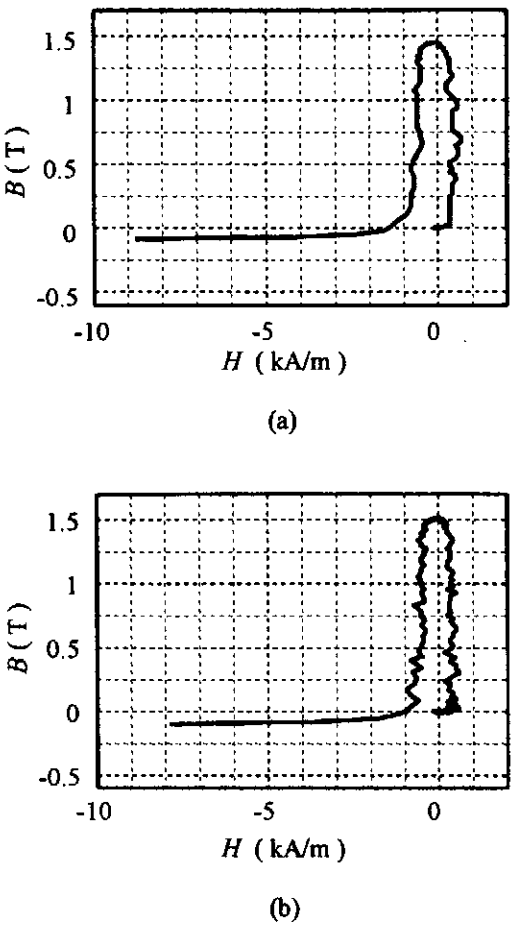

Figure 4. *B-H* loops of the magnetic switch. (a) 1st pulse. (b) 2nd pulse.

Figure 4 shows typical *B-H* loops of the MS in (a) the 1st pulse and (b) the 2nd pulse. As seen in the figure, MS is successfully magnetized in the 1st and 2nd pulses. Maximum magnetic flux swings were 1.47 T and 1.5 T at the 1st and 2nd pulses, respectively. The relative permeability of the MS in saturation were evaluated to be 2.

B. Double pulse operation

In the double pulse operation, charging voltages of C_{01} and C_{02} are adjusted to obtain a same output voltage. Fig.5 shows typical waveforms obtained at $V_{01} = 14$ kV, $V_{02} = 17$ kV and trigger delay time between GS_1 and GS_2 is 3.5 μs.

As seen in the figure, the 1st pulse of $V_{C2} = -95$ kV, $V_R = -85$ kV and the 2nd pulse of $V_{C2} = -105$ kV, $V_R = -90$ kV are successfully produced with $T_d = 3.75$ μs. The E_R for the 1st and 2nd pulse are evaluated to be 6.3 J and 6.6 J respectively. The voltage and the output energy of the 2nd pulse decrease about 10% and 20% respectively as compared with the single pulse operation. This is due to the ohmic loss in GS_1.

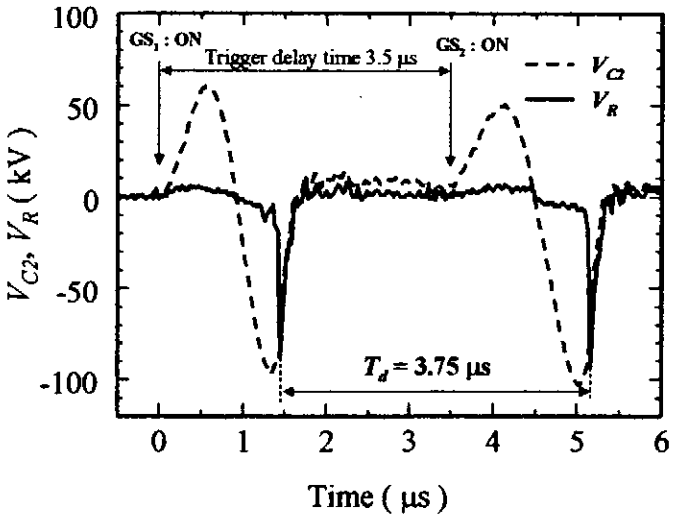

Figure 5. Results of the double pulse operation when V_{01} = 14 kV, V_{02} = 17 kV.

IV. Summary

A new type of multi-pulse generator is proposed for the generation of high power pulses with extremely short pulse repetition interval. To demonstrate the production of double pulses experimentally, the small system was constructed. Double pulses of duration 100 ns, peak voltage 85 kV (1st pulse) and 90 kV (2nd pulse) are successfully generated with interval of 3.75 μs when initial charging voltage of the first stage capacitors were 14 kV (for 1st pulse) and 17 kV (for 2nd pulse).

References

1) F.M. Bieniosek, J. Honing, and E.A. Theby, "MEDEA-II two-pulse generator development," Rev. Sci. instrum. 61 1713 (1990)
2) R.C. Noggle, R.J. Adler, K.J.Hendricks, "A reliable dual Blumlein device," Rev. Sci. Instrum. 60 3540 (1989)
3) K. Masugata, H. Maekawa and K. Yatsui, "Double pulse generation using a single pulse forming line system," The Trans. of IEE of Japan 118-B 261 (1998)
4) K. Masugata, "A pulsed power system for generating multiple high voltage pulses with a short pulse repetition interval," Rev. Sci. Instrum. 69 591 (1998)
5) K. Takao, K. Masugata, K.Yatsui, "GENERATION OF MULTIPLE PULSES WITH EXTREMELY SHORT PULSE REPETITION INTERVAL," Proc.12th IEEE Pulsed Power Conf. PA104 (1999)
6) G.J Rohwein, "A THREE MEGAVOLT TRANSFORMER FOR PFL CHARGING," IEEE Trans. On Nuclear Science, NS-26 4211 (1979)
7) D. Finkelstain, P. Goldbelg and J. Shuchatowitx, "High Voltage Impulse system," Rev. Sci. Instrum. **37** 159 (1966)
8) H.C. Kirbie, G.Y. Otani and G.M. Hughrs, "A MAGNETICALLY SWITCHED TRIGGER SOURCE FOR FXR," Proc.6th IEEE Pulsed Power Conf. 171 (1987)

SHOCK WAVE DEVELOPMENTS FROM PULSED HIGH-CURRENT DISCHARGE

K. Takaki, Y. Chida, and T. Fujiwara

Department of Electrical and Electronic Engineering, Iwate University, Ueda 4-3-5, Morioka 020-8551, Japan

ABSTRACT

Interferometer measurements are extremely informative in shock wave studies allowing direct evaluations of the gas density. The primary goal of the work presented is to build a laser interferometer that meets the requirements of the highest possible simplicity, economy, convenience, and ease of construction. In our experiments, we used a low average power (10 mW) He-Ne laser without complication, expense, and environmental section. The He-Ne laser interferometer with the Michelson arrangement was used to measure the line-averaged gas densities of shock waves. Temporal and spatial measurements of the density were performed for shock wave developments from high-current pulse discharges. The shock wave propagates in the radial direction of the discharge channel with supersonic speed. The shock velocity, however, decreased from 2 to 0.5 km/s with the distance of the shock propagation. The width of the high density region, that is in the vicinity of the shock front was compressed from 3.5 mm to 1.8 mm according to the time variation of the discharge current.

I. INTRODUCTION

The interferometry method has been widely used for measurements of various physical and mechanical parameters in experiments, and allows the measurement of distances comparable with those of a laser beam wavelength.[1] High resolution is provided by the high coherence and low divergence of the laser radiation that makes fine measurements of distance and velocities possible.

Laser interferometry is a well-known method of shock wave diagnostics, allowing direct measurements of gas densities.[2,3] The method is based on the fact that the gas index of refraction is proportional to the density of neutral particles in shock waves. The variation in the index of refraction is similar to the change in the path length of the scan laser beams, resulting in a phase shift which can be determined by the fringe amplitude of combined scan and reference beams. The phase shift ϕ in any refractive medium is expressed by the following formula:

$$\phi = \frac{2\pi}{\lambda} \int_0^L (n-1) dL , \qquad (1)$$

where λ, n, and L are the wavelength of laser light, the index of refraction, and the length of the beam path in the refractive medium. The refraction index n_ρ of neutral gas for high-frequency electromagnetic waves is mostly determined by the gas density

$$n_\rho = 1 + \beta \frac{\rho}{\rho_s} , \qquad (2)$$

where β, ρ and ρ_s are the dimensionless constant, the gas density, and the standard gas density,

respectively. The neutral particles produce a positive phase shift because the effective index of refraction is more than 1.

Short-time scale shock waves play a key role in some applications, such as laser triggered gap switch, demolition of materials, and laser triggered lightning.[2-4] The shock wave propagating duration is usually between 100 ns and 1 ms, which makes it possible to use an interferometer without a precise arm length stabilization, since the vibration of the optical elements of the interferometer has a characteristic time of 1-20 ms.[5]

The development of the shock wave from a spark discharge has been measured by an image-converter camera and a two-color Mach-Zehnder interferometer.[2] Moreover, Loeb *et. al.* have reported that the velocity of the shock wave from the discharge changes from 0.4 to 1.1 km/s using the beam attenuation by the density gradient of the shock wave.[6] In this article an easy to use and very flexible laser interferometer is constructed and used in the measurements of the shock wave developments from high-current pulse discharges.

II. INTERFEROMRTER SETUP

The schematic of the interferometer is shown in Fig. 1. A beam splitter divides the laser beam (10 mW, 0.7 mm in diameter) into reference and scan beams, where the latter passes twice through the shock wave. Both beams recombine at the beam splitter and travel a 1.5 m distance to the beam registration system based on a photodiode. A narrow bandpass filter (10 nm full width at half maximum) was used to avoid false signals due to the discharge luminosity. A Si PIN photodiode (Hamamatsu S3399) with sensitivity equal to 0.4 A/W for the He-Ne laser wavelength was used in the high load resistance (1 kΩ) system used for registration. The signal from the photodiode was recorded with an 1 GS/s TDS 540C digital oscilloscope.

The recorded signals are analyzed as follows. In our experimental condition, the fringe shift $\Delta\Phi$ is more than π and gives the following formula for the density evaluation:

$$\frac{\Delta\rho}{\rho_s} = \frac{\Delta\phi}{2\pi\beta}\left(\frac{\lambda}{L}\right), \tag{3}$$

where $\Delta\rho$ is the change in gas density. The dimensionless constant β is 0.000297 for nitrogen gas. Therefore, a positive fringe shift means an increase of gas density, and a negative shift means a decrease of gas density. The fringe shift $\Delta\Phi$ is obtained by analysis of the recorded signal with the formula

$$I^2 = I_1^2 + I_2^2 + 2I_1 I_2 \cos\Delta\phi, \tag{4}$$

where I is the interference beam intensity (the recorded signal), and I_1 *and* I_2 are the reference and scene beams intensity, respectively.

Figure 2 shows a schematic diagram of the shock wave generation system used in the experiment. A capacitor with normal voltage of 60 kV and capacitance of 1.89 μF is charged slowly up to high voltage. The stainless steel electrodes of hemispherical shape with radius of 1.58 cm are mounted inside a housing where the nitrogen gas pressure can be changed to the required value. Carborundum resistors were used to obtain a unipolar critically damped or overdamped pulse. The current is returned to ground through 12 stainless steel rods 1.0 cm in diameter. The discharge current is measured by a Pearson current transformer (model 4997) and the digital oscilloscope TDS 540C.

The photodiode signal of the shock wave measurement and the current waveform of the pulse

discharge are shown in Fig. 3. Knowing the amplitude of the signal before a shock wave front arrival, makes it easy to determine the initial phase necessary for the correct calculation of the gas density in the shock wave. It should be noted that the signal induced by shock waves can be both positive and negative over the initial signal level. The polarity of the signal depends on the initial phase and the sign of its derivative prior to a shock arrival.[5] In our experiments, we had approximately 50% recorded in each polarity, proving the absence of any false signal in the system.

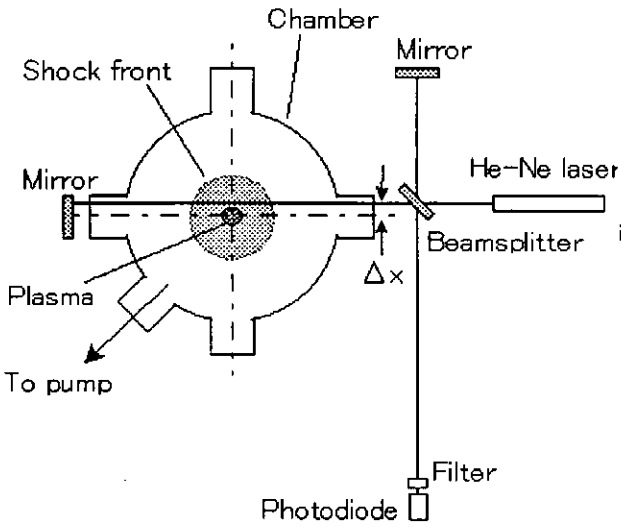

Fig. 1. The diagram of the interferometer setup.

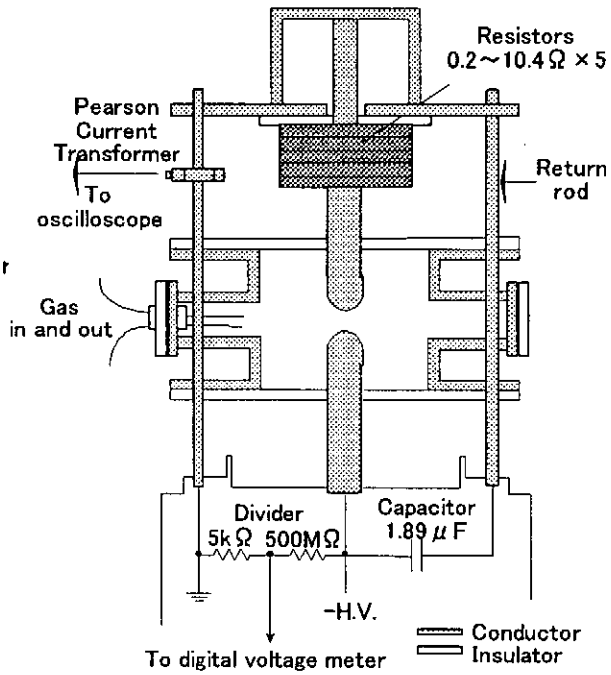

Fig. 2. The schematic of the experimental apparatus.

III. SHOCK PROPAGATION MEASUREMENTS

When the discharge occurs, joule heat is released in the arc channel. It leads to an increase in the gas pressure and a thickening of the channel. The thickened channel acts like a piston on the remaining gas and the expansion takes place with supersonic speed. As a result a shock wave is generated in the gas and is propagated in the radial direction.[7] In Fig. 3, the fringe shift appears after 10 μs from the discharge start (shown by arrow ①). The horizontal axis indicates the time when the shock wave arrives at the 1.5 cm distance from discharge channel center. The propagation velocities of the shock wave from high-current pulse discharge were measured using a He-Ne interferometer. The waveforms of the discharge current and the photodiode signals at the different scene beam positions ΔX are shown in Fig. 4. The nitrogen gas pressure and the gap length were 100 mTorr and 1.0 cm, respectively. Under the experimental condition, the maximum discharge current reaches almost 4.5 kA with rise time of 1 μs. The arrows show the time when the shock front arrives at the scan beam positions. The times are 3, 5, 10 and 17 μs for the

distance of 0.5, 1.0, 1.5, and 2.0 cm from the channel to the beam, respectively.

The time dependences of the shock front velocity and the shock column radius are shown in Fig. 5. The shock front velocity is calculated by differentiating the approximate function of the shock column radius with respect to the time. The sound velocity of nitrogen is 334 m/s in standard state (1 atm, 0 °C). The shock column generated by the pulse discharge expands and its radius r can be approximately expressed as

$$r = K \cdot t^{0.59} \quad (5)$$

where K and t are the constant and the time, respectively. The cylindrical shock wave produced by instantaneous energy release expands as $r = K \cdot t^{1/2}$.[8] Under our experimental condition, the pulse width of the discharge current was 2.26 μ s full width at half maximum. The value gives a difference between the above formulas with respect to the radius.[9] The velocity of the shock wave propagation v decreases with the distance as $v \propto r^{-0.7}$. If the energy is liberated instantaneously, the velocity can be obtained from the equation $r = K \cdot t^{1/2}$, and is expressed as $v \propto t^{-1}$.[10]

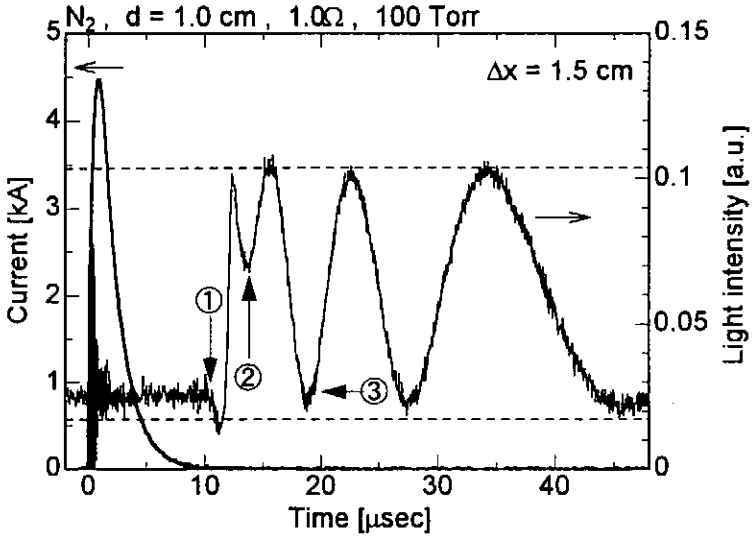

Fig. 3. Pulse discharge current and photodiode signal waveforms for shock wave. The laser beam is 1.5 cm from the center of discharge channel. Dotted line shows the amplitude of mechanical fringe shift.

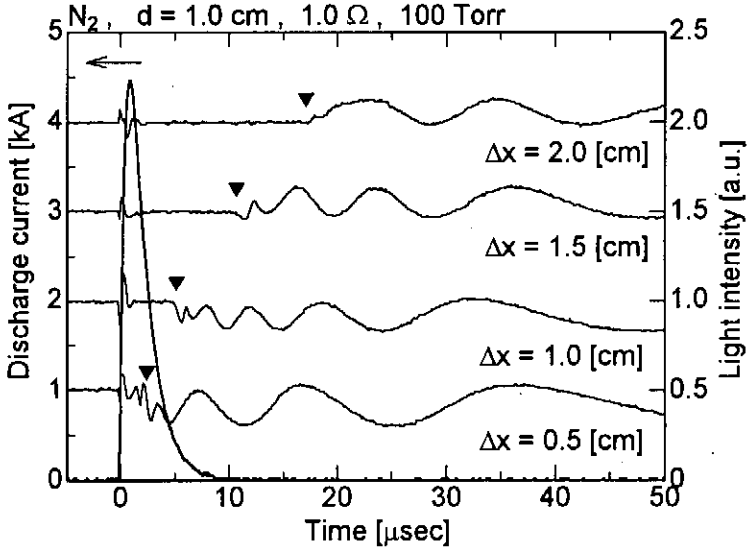

Fig. 4. Photodiode signal waveforms for various distances from discharge channel axis to the beam.

IV. GAS DENSITY MEASUREMENTS

With cylindrical shock waves produced by instantaneous energy release, the density of the gas in the vicinity of the shock front is much higher than in the gas at rest. On the contrary the gas density in the core is very low, and the major part of the mass of the moving gas is displaced from

it.[7,10] Therefore, the fringe shift $\Delta\Phi$ by the shock front arrival seems to be a positive, owing to the positive $\Delta\rho$, which is the change of gas density from the gas at rest. In Fig. 3, the fringe shift occurred at 10 μs and increased with time. However, the phase inversion is confirmed at the point shown by arrow ② in Fig. 3, and this indicates that the fringe shift decreases with time after that. The arrow ③ shows the moment in time when $\Delta\Phi$ become zero again. The sign of the gas density change $\Delta\rho$ is expressed as follows:

~①: $\Delta\rho = 0$, $d\Delta\rho/dt = 0$,

①~②: $\Delta\rho > 0$, $d\Delta\rho/dt > 0$,

②~③: $\Delta\rho > 0$, $d\Delta\rho/dt < 0$,

③~ : $\Delta\rho < 0$, $d\Delta\rho/dt < 0$.

The time dependence of the line averaged gas densities at various positions, which are measured with the interferometer, are shown in Fig. 6. The gas pressure of 100 Torr indicates the density of 3.54×10^{18} cm^{-3} in standard temperature gas at rest. The gas density in the vicinity of the shock front increases by propagating from Δx = 1 cm to 1.5 cm, and decreases by propagating from Δx = 1.5 cm to 2.0 cm. After the shock front passes through, the density decreases to a lower value than in the gas at rest.

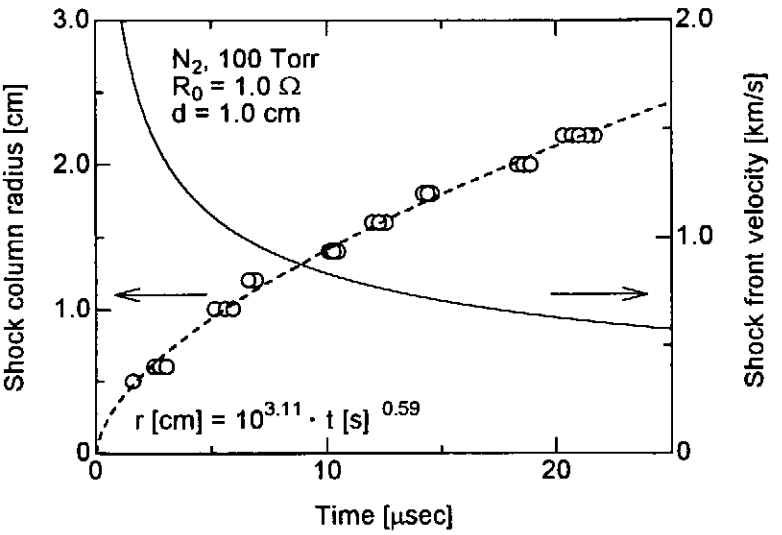

Fig. 5. Shock propagation and velocity versus time from a beginning of discharge.

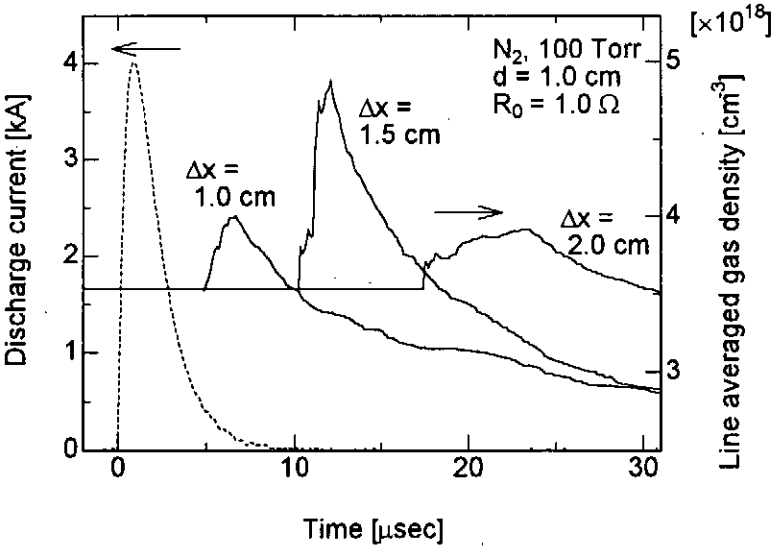

Fig. 6. Time dependency of line-averaged gas density (solid) of shock wave from pulse discharge at various positions, and current waveform (dotted) of pulse discharge.

The width of the shock front, which is defined as the region of higher gas density than that of the gas at rest, is shown in Fig. 7. The gas pressure is 30 Torr. The shock front width take the minimum value at the shock radius of 1.4 cm: this value is the propagation distance at 10 μs,

when the discharge current decreases to zero. This indicates that the shock front is compressed, while the discharge current is flowing and it begins to disperse when the discharge ends.

ACKNOWLEDGMENTS

The authors would like to thank Professor H. Akiyam of Kumamoto University and Professor K. Yukimura of Doshisha University for their valuable discussions. The authors would also like to thanks S. Kato of Iwate University for his technical assistance and support.

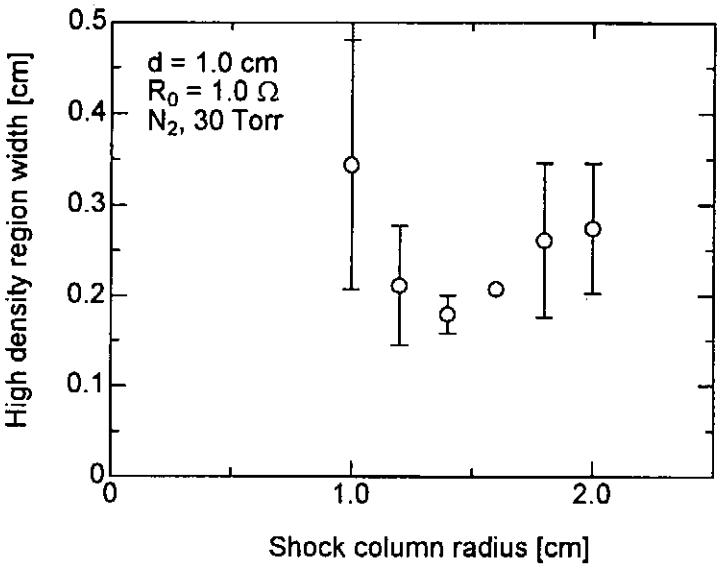

Fig. 7. Width of high density region in the vicinity of shock front vs. shock column radius.

REFERENCES

1 C.M. Vest, Holographic Interferometry (Wiley, New York, 1979) 502.

2 W.D. Kimura, M.J. Kushner, E.A. Crawford, and S.R. Byron, IEEE Trans. Plasma Sci. **PS-14**, 246 (1986).

3 C. Honda, M. Nakazawa, T. Takuma, K. Uchino, K. Muraoka, F. Kinoshita, O. Katahira, and M. Akazaki, in Proceedings of the 8th International Symposium on High Voltage Engineering 1993, Yokohama, Vol. 3, p. 289.

4 I.V. Lisitsyn, T. Muraki, and H. Akiyama, Appl. Phys. Lett. **70**, 1676 (1997).

5 I.V. Lisitsyn, S. Kohno, T. Kawauchi, T. Sueda, S. Katsuki, and H. Akiyama, Jap. J. Appl. Phys. **36**, 6986 (1997).

6 A. Loeb, M. Loebenstein, A. Ludmirsky, S. Eliezer, S. Maman, and Y. Gazit, J. Appl. Phys. **57**, 2501 (1985)

7 S.I. Braginskii, Soviet Physics JETP **34**, 1068 (1958).

8 J.M. Meek and J.D. Craggs, Electrical Breakdown of Gases (Wiley, New York, 1979) 802.

9 R.A. Freeman and J.D. Craggs, Brit. J. Appl. Phys. **2**, 421 (1969).

10 Shao-Chi Lin, J. Appl. Phys. **25(1)**, 54 (1954).

INTENSE-HEAVY-ION-BEAM TRANSPORT AND HIGH EFFICIENCY POWER GENERATION SYSTEM FOR INERTIAL CONFINEMENT FUSION

Takashi Kikuchi, *Shigeo Kawata, and Nob. Harada

Department of Electrical Engineering, Nagaoka University of Technology, 1603-1 Kamitomioka, Nagaoka, 940-2188, Japan

**Department of Electrical and Electronics Engineering, Utsunomiya University, 7-1-2 Yohtoh, Utsunomiya, 321-8585, Japan*

ABSTRACT

We investigate an intense-heavy-ion-beam transport using an insulator beam guide and a high efficiency power generation system using a magnetohydrodynamic (MHD) power generation for inertial confinement fusion (ICF) power generation system by numerical simulation. An efficient beam-transport method must be established for realization of ICF using charged-particle beams. For this purpose, we have proposed an insulator beam guide. An intense ion beam generates a plasma on the surface of it. Electrons are extracted from the plasma, and the space charge of the beam is effectively neutralized. It is confirmed that the ion beam is efficiently transported through the insulator beam guide. We propose to use closed cycle MHD (CCMHD) generator, which is driven by a non-equilibrium ionized gas, in order to recover ICF output energy efficiently. It has been found that using a CCMHD generator, total plant efficiency of an ICF power generation system increases with an enhancement of power generation efficiency. Total plant efficiency of 60% has been successfully achieved, which is much higher than that of conventional steam turbine system. Further, this enhancement must reduce the requirements such as pellet gain and so on, for ICF technologies.

I. Introduction

A heavy ion beam may be one of promising energy-driver candidates for an inertial confinement fusion (ICF).[1] An intense-heavy-ion beam ($\geqq$kA) is required for ICF implosion. However, it is difficult to transport such an intense ion beam in vacuum. Because the beam diverges due to the space charge effect of itself. In our previous papers,[2-4] we proposed a

transport system using an insulator beam guide, and reported that electron, proton and Cs ion beams are effectively transported through the insulator beam guide. In this study, we apply the above insulator beam guide system to an intense-Pb-ion-beam transport, which may be a candidate in heavy ion ICF. We study the intense-Pb-ion-beam transport by using a numerical simulation. The simulation results present that the intense-Pb-ion beam can also be efficiently transported by using the simple insulator beam guide system.

One of the problems to realize a nuclear fusion power plant is the economic performance. In a commercial fusion power plant, it is predicted that the total capital cost and the cost of electricity becomes high. In order to reduce their costs, the power generation efficiency and the total plant efficiency must be increased. From the viewpoint of thermodynamics, if the operating temperature of a power conversion cycle becomes high, the cycle efficiency also becomes high. Consequently, the temperature of the thermal output from a fusion reactor should be as high as possible, for example, Cascade ICF reactor design.[5] When the thermal output with high temperature (about 2000~2400K) can be extracted from the fusion reactor, neither a gas turbine Brayton cycle nor a steam turbine Rankine cycle can be used because of the mechanical and material restrictions. A magnetohydrodynamic (MHD) generator, however, can still be available even such high temperature conditions.[6-8] In this study, we investigate on a high efficiency gas-cooled ICF power generation system using a non-equilibrium closed cycle MHD (CCMHD) generator. We proposed a high efficiency ICF reactor models yielding high temperature thermal energy, and examined the efficiency of the ICF+MHD power generation system. As a result, we can expect that the total plant efficiency of the ICF power generation system can be reached 60%.

II. Intense-heavy-ion-beam transport through the insulator beam guide

The physical mechanism for the beam transport through the insulator beam guide is as follows: the intense heavy ion beam creates a local electric field on the insulator inner surface, the local electric field induces the local discharges, and the plasma is produced on the insulator inner surface. Then electrons are extracted from the plasma which is generated on the inner surface of the insulator beam guide, because of the beam net charge. The electrons follow up the heavy ion beam, and the beam charge is effectively neutralized by them. Therefore, the heavy ion beam propagates efficiently through the insulator beam guide. On the contrary to an intense proton beam,[3] the Pb ion beam does not form a clear virtual anode, so that we do not need an initially prefilled plasma gas in the beam transport region.[4] Therefore, in the case of the intense-heavy-ion-beam transport, a simple beam-transport system can be established by using the insulator beam guide without a prefilled gas.

As can be seen from Fig.1, our simulation model is as follows: we assume that the phenomenon concerned is cylindrically symmetric. In this study, we carry out a

particle-in-cell (PIC) simulation. The PIC code used is a 2.5-dimensional one. The field components (E_r, E_z, B_θ), and the particle position and velocity (r, z, v_r, v_θ, v_z) are solved using the Maxwell equations and the relativistic equation of motion.

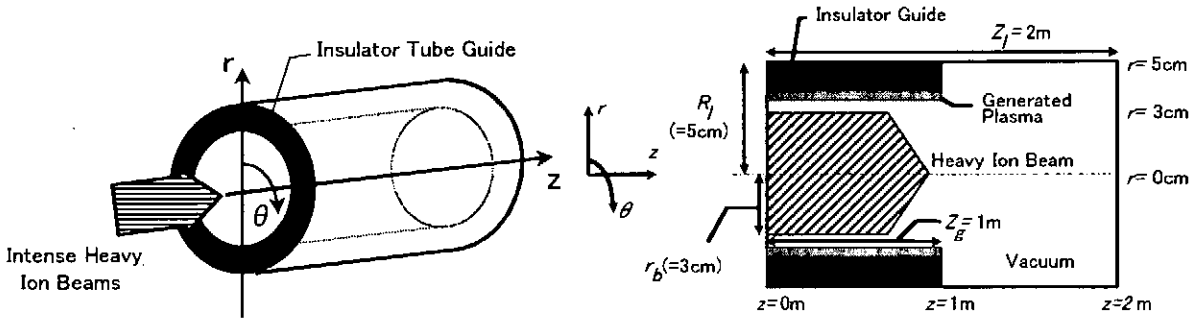

(a) outline figure (b) calculation model

Fig.1 (a) A system for intense-heavy-ion-beam transport through an insulator beam guide and (b) simulation model.

The Pb-ion-beam-parameter values are as follows: the input Pb ion beam waveform is shown in Fig.2; the maximum current is 10kA, the particle energy is 4GeV, the pulse width is 10ns and the rise and fall time is 2ns. The initial beam radius is 3cm. The average longitudinal speed v_{z0} of the beam ions injected is determined by the waveform shown in Fig.2, and the beam temperature is 0.1eV; v_{z0} is $0.2c$ at z=0. Here c is the speed of light in vacuum. At the entrance of the insulator beam guide system, that is, z=0, the beam ions enter uniformly, and the transport area is in vacuum. The Pb ions of the beam are singly charged. The computation area is $0 \leqq z \leqq Z_l$ (= 2m) and $0 \leqq r \leqq R_l$ (= 5cm) (see Fig.1(b)), and the inner radius of the insulator guide is 3.25cm (see Fig.1(b)). The center line of r=0 is the cylindrical axis, at which the cylindrically-symmetric boundary condition is imposed. The other three outer boundaries are conductors. The relative permittivity of the insulator beam guide is 5. In our simulation, a local plasma is generated on the insulator guide surface, when the magnitude of the electric field exceeds the threshold for the local discharge. The threshold is 10^7V/m in this study.

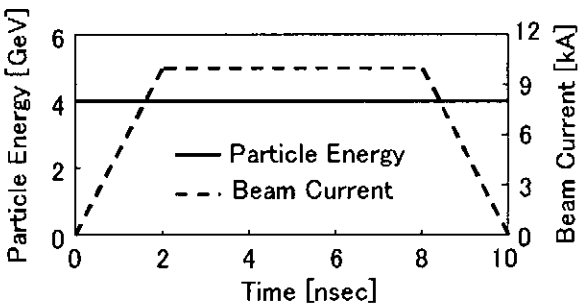

Fig.2 Input Pb ion beam waveform: the maximum current is 10kA, the maximum particle energy is 4GeV, the pulse width is 10ns, and the rise and fall time is 2ns.

At first, we simulate the Pb ion beam propagation in vacuum without the insulator beam guide. The particle maps of the Pb beam are shown in Fig.3. In this case, the beam radius tends to expand gradually and reaches up to the wall. Figures 4 and 5 present the particle maps of the Pb beam ions and the electrons emitted from the insulator guide surface through the insulator beam guide. The electrons extracted from the plasma which is generated on the insulator inner surface move along with the Pb ion beam. The electrons effectively neutralize the space charge of the ion beam, and suppress the radial expansion of the beam.

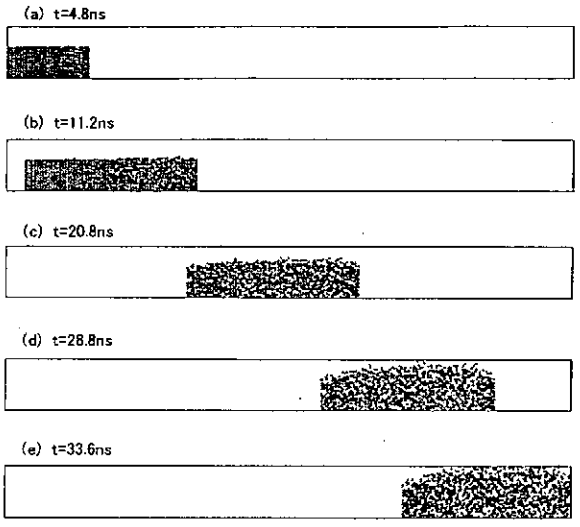

Fig.3 Particle maps for the Pb ion beam without the insulator guide: (a) at t=4.8ns, (b) at t=11.2ns, (c) at t=20.8ns, (d) at t=28.8ns and (e) at t=33.6ns. The beam radius becomes large due to the self space charge.

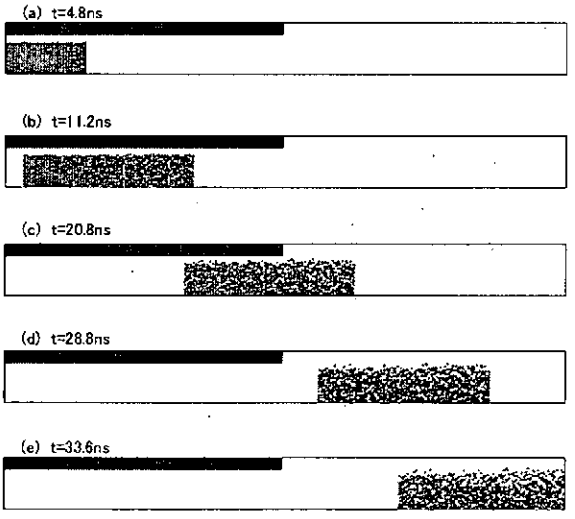

Fig.4 Particle maps for the Pb ion beam through the insulator beam guide: (a) at t=4.8ns, (b) at t=11.2ns, (c) at t=20.8ns, (d) at t=28.8ns and (e) at t=33.6ns. The beam charge is neutralized well by the emitted electrons, and the beam expansion is suppressed.

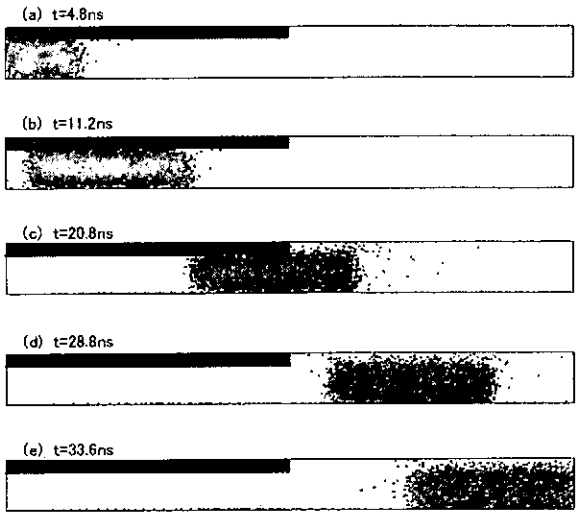

Fig.5 Particle maps for the electrons emitted from the insulator beam guide in the case of Pb ion beam transport through the insulator guide: (a) at t=4.8ns, (b) at t=11.2 ns, (c) at t=20.8ns, (d) at t=28.8ns and (e) at t=33.6ns. The electrons follow the Pb ion beam well.

III. High efficiency ICF power plant using CCMHD power generation system

We also study a highly efficient electrical power conversion system using an MHD generator for an ICF reactor. In the case of deuterium and tritium fusion reactions, the neutron gets about 70% of total ICF output energy, and residual 30% of it is carried by the X-ray and the target debris. The neutron energy is absorbed in a blanket of the reactor, and the non-neutron energy from the ICF target is absorbed in a first wall (FW). Figure 6 presents the cross sectional image of the ICF reactor. The FW is made of graphite, and can endure high temperature ($\geqq$2000K). On the other hand, the blanket is made of Li compound, such as $LiAlO_2$ and LiO_2, because the blanket must generate tritium of the fusion fuel. Therefore, the

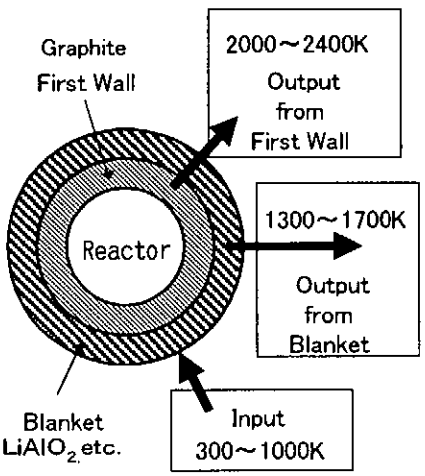

Fig.6 Input and output helium gas temperature at ICF reactor model. The first wall of the reactor is graphite, and the blanket is Li compound. Intermediate temperature (1300~1700K) is from the blanket, and high temperature (2000~2400K) helium is from the first wall.

blanket cannot operate at higher temperatures.[5)]

From the above reasons, intermediate temperature (≧1300K) helium gas is extracted from the blanket in the fusion reactor, and high temperature (≧2000K) helium can be extracted from the FW. We propose that a plant model is shown in Fig.7. In the case of the present model, the intermediate temperature helium extracted from the blanket is reheated in the FW up to 2000K. Heated helium can drive a non-equilibrium CCMHD generator, where electrical power can be extracted efficiently from the thermal energy. We apply a single CCMHD power generation system to this ICF power plant.[6)]

In the system analysis, assumed parameters are as follows: the blanket gain is 1.1. The pellet gain is about 66.2, which was given by the energy driver input energy of 6.5MJ and the ICF output energy of 430MJ.[1)] From the temperature limit of the blanket, operating temperature in the blanket is decided lower than 1800K. Energy driver efficiency is 30% by using heavy ion beam.[1)] The MHD generator has the enthalpy extraction ratio of 34%, the isentropic efficiency of 85%, and the thermal loss of 0.5%. Adiabatic efficiency of a compressor is 85%, and the unit number of the compressor is 4. Supposing a commercial scale power plant, the net electrical output power from the ICF power plant is 1000MWe. As a result, it is found that this power plant has the power generation efficiency of 65.6%, and the total plant efficiency of 61.0%. These values of efficiency are much higher than that of nuclear power plants using a conventional steam turbine system.

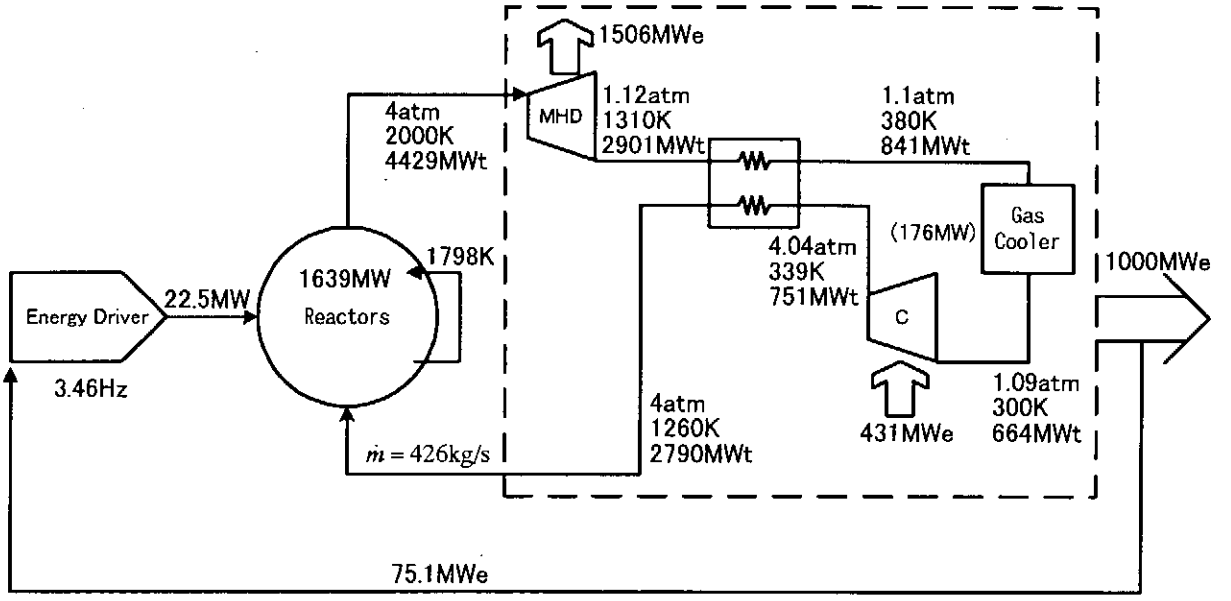

Fig.7 A high efficiency ICF power plant model using a single MHD power generation system. The blanket gain is 1.1, and the pellet gain is about 66.2. From the temperature limit of the blanket, operating temperature in the blanket is decided lower than 1800K. Energy driver efficiency is 30% by using heavy ion beam. The MHD generator has the enthalpy extraction ratio of 34%, the isentropic efficiency of 85%, and the thermal loss of 0.5%. Adiabatic efficiency of a compressor is 85%, the unit number of compressor is 4. The net electrical output power from this plant is 1000MWe. In this case, the power plant has power generation efficiency of 65.6%, and the total plant efficiency of 61.0%.

Further, it is found that loads for the fusion technologies could also be decreased with the increase of the power generation efficiency. The required pellet gain G can be calculated by

$$G = \frac{1}{(\eta_e - \eta_p) M_b \eta_d}, \quad (1)$$

where η_e is the power generation efficiency, η_p is the total plant efficiency, M_b is the blanket gain, η_d is the energy driver-efficiency. The energy driver efficiency is expected ordinarily 10% in laser and 30% in ion beam,[1] respectively. Figure 8 presents the required pellet gains estimated by Eq.(1). In the ICF power plant using the conventional steam turbine system, which is the power generation efficiency range of around 40% and the total plant efficiency range of around 34%, the required pellet gain is ordinarily 150 for laser and 50 for heavy ion beam as a driver. If the power generation efficiency is 65%, the total plant efficiency is 40%, the blanket gain is 1.1 and the energy driver efficiency is 30%, the required pellet gain can be much reduced as only 12 from Eq.(1). Although, there are many subjects to be studied for realization of ICF power plant, such as final focusing of energy driver beam, non-uniform radiation to ICF target pellet, large total input energy, etc.,[9] the significant enhancement of the power generation efficiency must reduce the above problems of ICF technologies.

IV. Summary

In this work, we studied the intense Pb ion beam transport through an insulator beam guide and a high efficiency power generation system using an MHD power generation for ICF reactor. In the intense Pb ion beam transport, electrons were emitted from the plasma which was generated on the insulator inner surface. The electrons moved with the heavy ion beam,

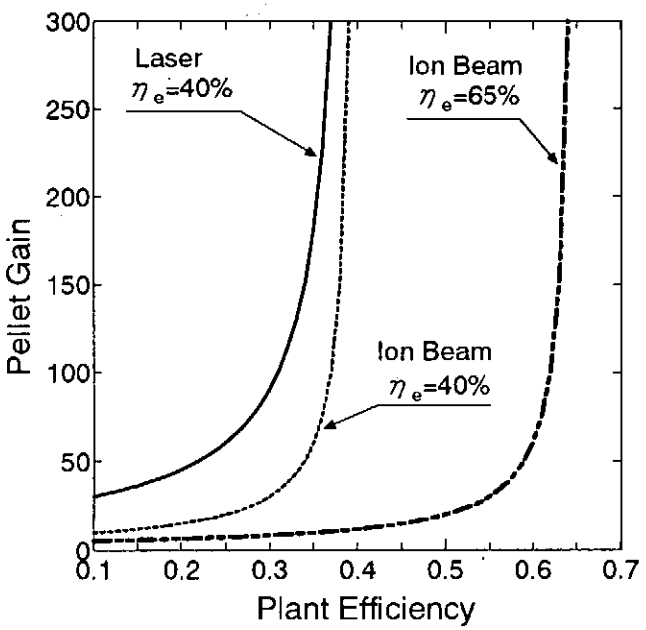

Fig.8 A relation between a required pellet gain and a plant efficiency in power generation efficiency of 40% and 65% as laser or ion beam energy driver.

and the beam charge was neutralized effectively by the electrons. Consequently, the heavy ion beam propagated efficiently through the insulator beam guide. In the high temperature gas-cooled ICF reactor, the power generation efficiency was increased by using the CCMHD power generation system. The total plant efficiency of the ICF power generation system increased with the enhancement of the power generation efficiency. In the proposed system, the total plant efficiency of ICF power plant could be reached 60%. Further, we can expect that the enhancement must reduce the requirements for ICF technologies.

References

1) M. Tabak, and D. Callahan-Miller, "Design of a Distributed Radiator Target for Inertial Fusion Driven from Two Sides with Heavy Ion Beams", Phys. of Plasmas, Vol.5, No.5, pp.1895-1900 (1998).
2) S. Kawata, S. Kato, S. Hanamori, S. Nishiyama, K. Naito, and M. Hakoda, "Effect of Plasma Generation at Insulator Surface on Transport of Intense Electron Beam through an Insulator Beam Guide", Jpn. J. Appl. Phys. Vol.35, pp.L1127-L1129 (1996).
3) S. Hanamori, S. Kawata, S. Kato, T. Kikuchi, A. Fujita, Y. Chiba, and T. Hikita, "Intense-Proton-Beam Transport through an Insulator Beam Guide", Jpn. J. Appl. Phys. Vol.37, pp.L471-L474 (1998).
4) T. Kikuchi, S. Kawata, S. Kato, S. Hanamori, and M. Yazawa, "Intense-Heavy-Ion-Beam Transport Through an Insulator Beam Guide", Jpn. J. Appl. Phys., Vol.38, pp.L270-L272 (1999).
5) R. F. Bourque, "Power Conversion Options for the Cascade ICF Power Reactor", Fusion Technology, Vol.15, pp.1270-1274 (1989).
6) S. Kabashima, "Advanced Researches of Closed Cycle MHD Power Generation in Tokyo Institute of Technology Fuji-1 Experiments and Numerical Simulations", Proc. of the 33rd Intersociety Eng. Conf. on Energy Conversion (Colorado Springs, 1998), 158.
7) N. Harada, "Cooperative Program on Utilization of He/Xe Medium for an MHD Conversion", Proc. of the 33rd Intersociety Eng. Conf. on Energy Conversion (Colorado Springs, 1998), 377.
8) M. Ishikawa, Y. Inui, J. Umoto, and K. Yoshikawa, "Preliminary analysis of MHD-Brayton cycle applied to fusion reactors (CFAR)", Fusion Eng. and Design, Vol.29, pp.57-63 (1995).
9) K. Fujita, T. Kikuchi, D. Takahashi, M. Yazawa, and S. Kawata, "Inhomogeneity Smoothing Using Density Valley Formed by Ion Beam Deposition in ICF Fuel Pellet", Proc. of Space Charge Dominated Beam Phys. for Heavy Ion Fusion (Saitama, 1998), pp.108-119.

CHARACTERISTICS OF HIGH CURRENT INDUNCTIVE VOLTAGE ADDER ASO-X

Y. Teramoto, S. Kohno, I. V. Lisitsyn, S. Katsuki, and H. Akiyama

Department of Electrical and Computer Engineering, Kumamoto University,
2-39-1 Kurokami, Kumamoto 860-8555, Japan

ABSTRACT

The pulsed power generator ASO-X is a 3-stage inductive voltage adder at Kumamoto University, where it is used for POS and Z-pinch experiments. Because of its simple coaxial geometry, ASO-X can generate a current of 400 kA and a voltage of 180 kV with the current rise time of 1.33 μs. ASO-X uses a plasma opening switch (POS) to sharpen the current rise time. With optimum conditions, POS on ASO-X can make the rise time of load current faster than that of generator current by a factor of 30. In addition, it was found that POS opening impedance and current rise rate can be improved by modifying the direction of plasma flow of injected plasma.

1. Introduction

Some kind of pulsed power applications such as Z-pinches require a large current with short rise time. In the large pulsed power facilities, several MARX capacitor banks are used as a primary energy storage. However, because of its large capacitance and inductance, secondary water capacitors, which are charged by high voltage from primary MARXs, are necessary for pulse compression. Then the shortened pulse is transferred through the MITLs to the vacuum load. In such a capacitive energy storage system, whole generator-load system configuration must be complicated and the sections between each component must be well-insulated to avoid the breakdown by the high voltage. One candidate is the use of inductive voltage adder and inductive energy storage system. ASO-X is a 3-stage inductive voltage adder, which provide a current of 400 kA with the rise time of 1.33 μs. ASO-X has a simple coaxial configuration and is directly connected to the vacuum load. In addition, ASO-X uses inductive energy storage for shortening the rise time of the load current by POS. The POS on ASO-X has eight cable plasma guns as a plasma source to achieve over 1 μs conduction time. In this paper, characteristics and configuration of ASO-X are described. Also improvement of POS operation by modifying the plasma flow is described.

2. ASO-X generator

Fig. 1 shows the configuration of ASO-X. ASO-X has three stages connected in series for voltage multiplication. Each stage has a magnetic core, two field-distortion spark gap switches and two capacitors of 3.2 μF each. Since ASO-X is high current pulsed power generator, the magnetic core must be the one designed for use in high current generators. Otherwise saturation occurs and then current cannot flow into the load. In ASO-X, HITACH METALS Ltd. FINEMET^{TM} FT-1H cores are used. FINEMET^{TM} has suitable properties for pulsed power use, which are high saturation flux density, high permeability, low losses, and is fast enough to be used in pulsed power generators. The core cross-section of 300 cm^2 provides magnetic flux swing high enough to avoid the core saturation. Current and energy loss is negligibly low. Over 90% of the current is transferred into secondary winding. Two capacitors of 3.2 μF each are connected to the winding of the core through the field-distortion spark gap switches. Fig. 2 shows configuration of the switch. It consists of epoxy insulators, silver-tungsten trigger electrode, and silver-tungsten main electrode. In order to decrease the triggering time, distance between the main and the trigger electrodes is set to 2.4 mm. Also the switch is filled with SF_6 gas at optimum pressure for the charging voltage. The switches are enclosed in the grounded vessel which is filled with SF_6. Since all the switches must be triggered simultaneously, another spark gap switch is used to trigger the main switches. Actually, at the optimum gas pressure, the measured jitter of all six gap switches is less than 130 ns. When the capacitors are charged to its nominal voltage 60 kV, load voltage, load current, rise time of load current and stored energy are 180 kV, 400 kA, 1.33 μs and 34.5 kJ, respectively. Though two capacitors are connected in parallel, each stage has two additional ports to connect the capacitors. It leads to increase in load current. Also increase of the number of stages leads to further multiplication of load voltage. The design of

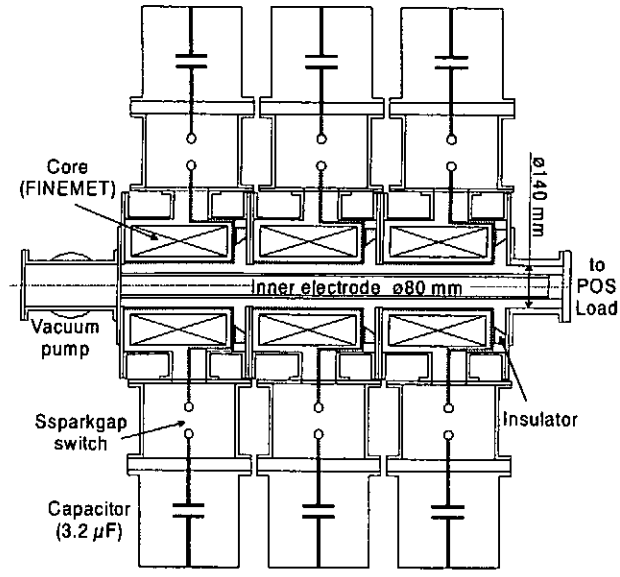

Fig. 1. Configuration of ASO-X generator.

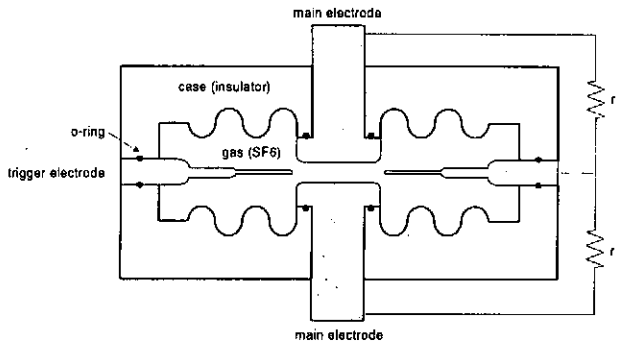

Fig. 2. Configuration of field-distortion spark gap switch in ASO-X generator.

inductive voltage adders is flexible and allows straightforward ways to increase both voltage and current.

This kind of inductive voltage adder has suitable properties for high current pulsed power generator compared with conventional generators in which capacitive energy storage is used. ASO-X has coaxial electrode configuration (140 mm of outer diameter and 80 mm of inner diameter) and is directly connected to the vacuum load without any kind of secondary storage capacitor and high voltage insulation interface. Also, since outer electrode is always grounded, insulation against the breakdown to the other equipments or ground is not necessary. They result in low inductance generator, then, high energy and fast generator.

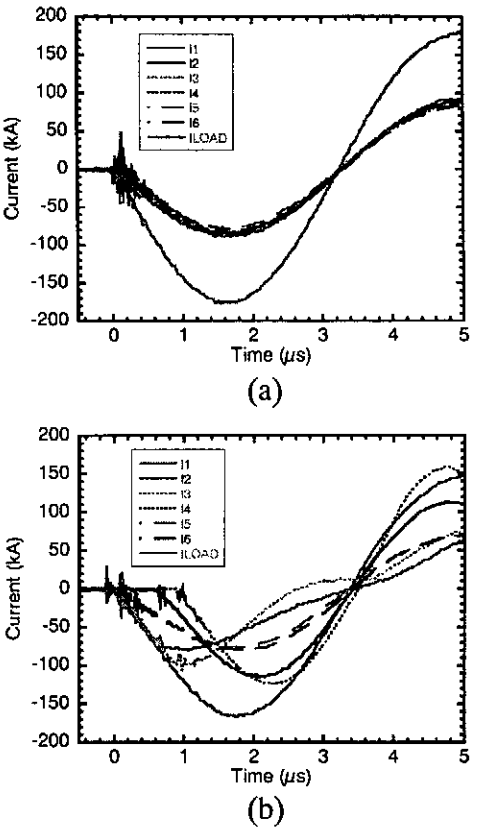

Fig. 3. Typical waveforms of ASO-X shot when all the switches are triggered simultaneously (a) and when the switches have jitters (b).

Fig. 3 shows typical waveforms of ASO-X shots. Charging voltage was 30 kV and short-circuit load was used. Fig. 3(a) shows the currents when all the switches were triggered completely at the same time. Each capacitor provides 90 kA and the current into the load is 180 kA since two capacitors are connected in parallel. On the other hand, Fig. 3(b) shows the worst case of ASO-X shot. In this case, two switches (#2 and #4) in the first and second stages were delayed. Though load current during first quarter period is not different from Fig. 3(a), the currents flowing through the switches #1 and #3, which are connected in parallel to the delayed switches, are doubled. Then, after the delayed switches are triggered, currents through the switch #1 and #3 decrease. Currents through the delayed switches are also higher than usual shot. This unstable switch behavior results in damage of the switch insulators, which would lead to decrease of lifetime of the switches. However, unstable switch behavior can be avoided by adjusting the switches and filling SF_6 gas at optimum pressure.

3. Plasma opening switch

ASO-X is also inductive energy storage system with plasma opening switch (POS). Fig. 4 shows POS-load configuration on ASO-X. POS on ASO-X has coaxial geometry which has inner cathode of 80 mm in diameter and outer grounded anode of 140 mm in diameter. Diameter of the cathode can be changed for the various experiments. Plasma source is eight

coaxial cable plasma guns which are mounted on the outer anode and equally spaced by 45°. Plasma guns are made of standard high voltage coaxial cable and the nozzles. When high voltage is applied to the gun, flashover occurs on the dielectric surface of the cable. The ablated plasma, which mainly consists of hydrogen and carbon, is injected by Lorentz force through the nozzle. The nozzles have a hole of 3 mm in diameter to inject plasma. Usually plasma is injected perpendicularly to the inner cathode from outer anode. However the nozzles can be replaced with different kind of nozzles, which enable various direction of plasma injection flow. Each two of eight guns are driven by single capacitor of 0.7 μF and current flowing through each gun is 8 kA when capacitors are charged to 25 kV. Since single spark gap switch is used, all guns are discharged simultaneously. For the POS experiment, inductive short-circuit load is used as shown in Fig. 4. Two vessels are connected as a grounded anode and each vessel has inductance of 70 nH. The length of the load chamber is 435 mm and its inductance is 140 nH. Inner and outer electrodes are connected with a copper plate. Fig. 5 shows typical waveforms of upstream (generator) and downstream (load) current of POS shot. During approximately 1 μs POS conducts all current from generator then immediately interrupts and transfers the current to the load in typically less than 50 ns. Load current becomes 30 times faster than generator current and also voltage applied to the load is amplified. This fast current is very attractive for Z-pinches to avoid RT instability.

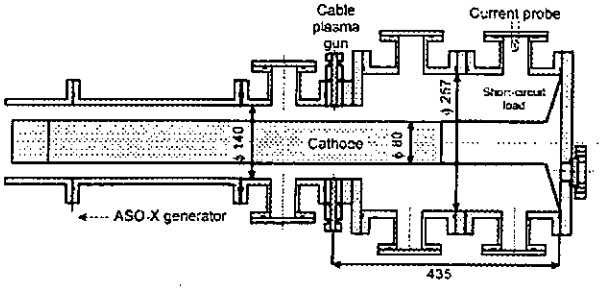

Fig. 4. POS-load configuration on ASO-X.

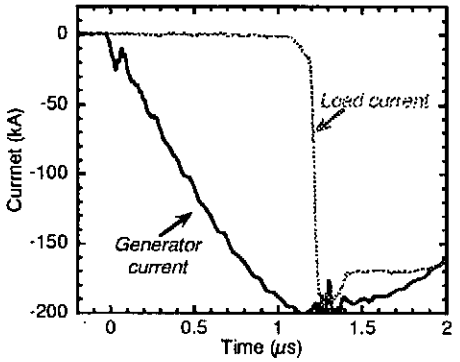

Fig. 5. Typical waveforms of upstream (generator) and downstream (load) current.

4. Improved operation of plasma opening switch

Usually POS plasma is injected perpendicularly to the cathode by external plasma source as well as in ASO-X POS. However, plasma guns in ASO-X have injection nozzles to change the direction of plasma flow. In this study, the effect of plasma flow on POS characteristics is investigated.

4.1. Experimental setup

The experiments were carried out with standard POS experimental setup as shown in

Fig. 4 except guns' nozzles. Fig. 6(a) shows the cross section of the conventional cable gun used in our experiment before modifications. The center electrode of the plasma gun is a copper wire 2.9 mm in diameter and is covered by a polyethylene insulator with an outer diameter of 9.7 mm (a standard Mitsubishi 10D-2V coaxial cable). The brass nozzle has a hole 3mm in diameter and a cone shape at the side of the injection.

The modified plasma gun nozzle is shown in Fig. 6(b). The plasma flow produced by this gun is not strictly radial, but it is slanted in an angle of 30 degrees. The total number of experimental runs using the modified guns is three with plasma flow slanted upstream (U), downstream (D) the load and with azimuthally inclined (A) plasma flow. These three arrangements are schematically shown in Fig. 7. The results of these experimental runs are compared with the case of conventional radial plasma flow (R) using the nozzle shown in Fig. 6(a).

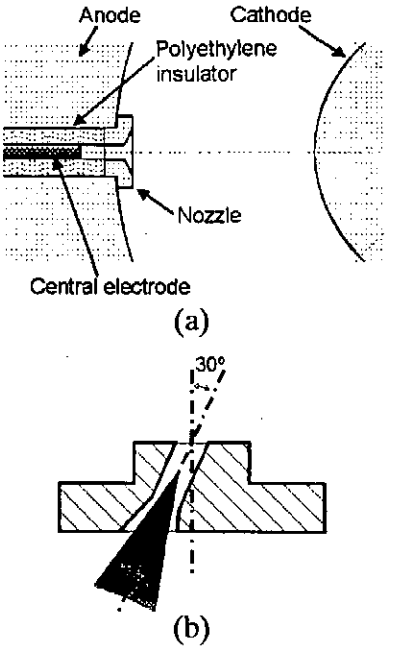

Fig. 6. Cross section of the conventional cable plasma gun (a) and a modified plasma gun nozzle (b).

The POS upstream (generator) and downstream (load) currents are measured by self-integrating Rogowski coil at the output end of the ASO-X and B-dot probe with external integrating circuit, respectively. Signals from five-turn, 3 mm-diameter, externally calibrated B-dot are integrated by an RC (50 kΩ, 100 pF) circuit at the oscilloscope input. The signals are recorded by a 1.5 GHz, 8 GSa/s Hewlett Packard HP54845A digital oscilloscope. The POS conduction time is varied by changing the time delay between triggering the plasma guns and the firing of the main generator. To control the time delay, a Stanford Research DG-535 delay/pulse generator is used. The charging voltage of the generator and the maximum POS current were 30 kV and 200 kA, respectively. The charging voltage of the plasma source capacitor bank was 25 kV. The time delay was varied between 1 and 6 μs providing the conduction phase duration between 200 and 1500 ns, although the quarter period of the current oscillation is 1400 ns. Four subsequent experimental runs were carried out with four different plasma flow directions: U, D, A and R (Fig. 7), respectively. Each run consisted of approximately 40 shots with various time delays.

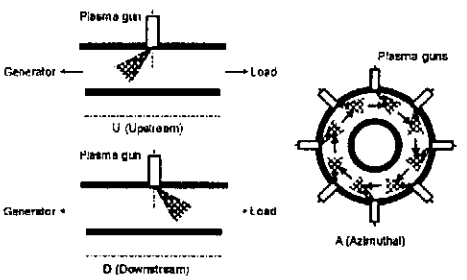

Fig. 7. Schematics of plasma injection. Upstream (U), Downstream (D) – side views and azimuthally inclined (A) – front view.

4.2. Experimental result

The dependence of the duration of the POS conduction phase on Δt is shown in Fig. 8 for all four runs. As is shown in previous detailed plasma density measurements, for Δt between 1 and 6 μs, the plasma density rises monotonously and it is nearly proportional to the time delay. To achieve a similar conduction time, the lowest time delay is necessary for the conventional radial plasma flow because of the absence of flow re-direction by modified nozzles and of the shortest effective path for plasma to flow a nozzle to the inner cathode. Therefore this case cannot be directly compared with other cases with slanted plasma flow. Among three cases with slanted plasma flow, the shortest time delay is required for the case U then A then D. In other words, in order to obtain a similar conduction time, the highest plasma density is required in case U.

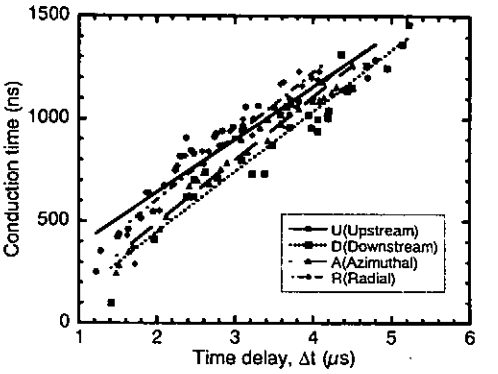

Fig. 8. POS conduction time versus Δt.

The results of the measurements of the maximum load current time derivative dI_L/dt during the POS opening versus conduction time are shown in Fig. 9(a) for the conduction time less than 1 μs. Each point corresponds to a single shot; best-fit curves show a linear increase of dI_L/dt. The time derivative of the load current is proportional to the POS voltage, assuming the load inductance is independent on the conduction time and the direction of the plasma injection, which is true if axial plasma displacement is small compared with the length of the coaxial line downstream of the POS. This is proven by the interferometer measurements of the plasma displacement from its initial position showed that it is negligibly small. This is usual for a low self-magnetic field, low A-K gap POS. It is seen in Fig. 9(a) that the highest dI_L/dt (and voltage) correspond to the case D. A and R cases are similar in the dI_L/dt amplitudes and the case U is the worst. If the conduction time of the POS exceeds 1 μs, dI_L/dt in the cases D,A and R is similar and

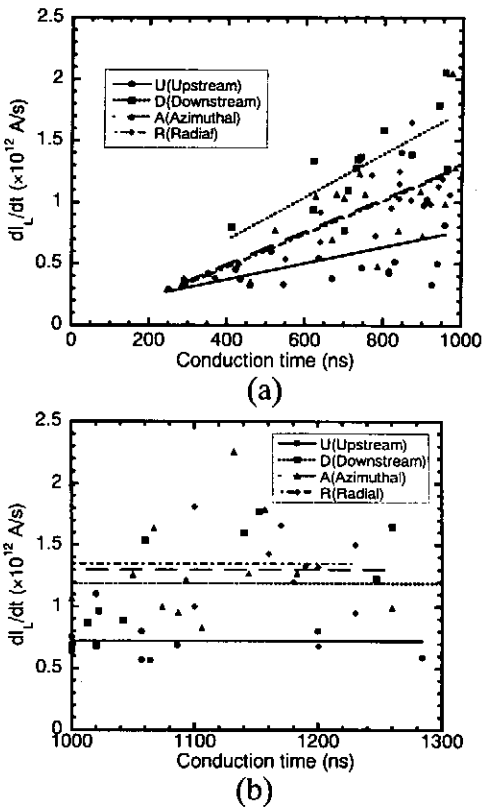

Fig. 9. Maximum load current time derivative dI_L/dt during the POS opening versus conduction time less than 1 μs (a) and higher than 1 μs (b).

weakly dependent on the conduction time, but dI_L/dt in the case U is still the lowest (Fig. 9(b)).

The POS shunt impedance is calculated using a conventional formula:

$$Z_{POS} = \frac{V_{POS}}{I_{POS}} = \frac{L_{LOAD}\dfrac{dI_L}{dt}}{I_G - I_L},$$

where IL and IG are the load and generator currents, respectively. The shunt impedance is a very important switch parameter, indicating the energy loss during a POS opening. The impedance calculated for the shots in all tested geometries are shown in Fig. 10. As well as the load current derivative, the maximum POS shunt impedance was obtained for the case of downstream plasma injection.

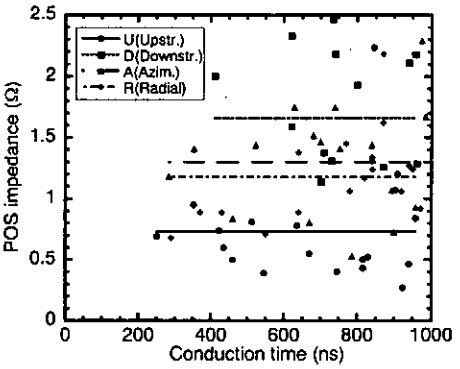

Fig. 10. POS shunt impedance versus conduction time.

4.3. Discussions

The obtained dependencies can be explained in the frame of the snowplow POS model. The snowplow model of the plasma displacement in a microsecond POS assumes weak magnetic field penetration into the bulk plasma [1]. This model well describes existing POS scalings [2] in a wide range of switch parameters. The special importance of the model is in long-conduction-time switches. The plasma ahead of the current-conducting layer is displaced due to the pressure gradient at the magnetic piston. The validity of the snowplow model is proven by adequate dependence of the POS conduction current versus plasma density in various long-duration POS experiments.

For analysis, let us make the assumptions standard for the snowplow model[1]. The plasma develops a thin current-carrying channel and the plasma pressure is negligible. The onset of switch opening corresponds to the time when the current-carrying channel arrives at the load end of the switch plasma. Specializing to a plasma current linearly increasing in time, the snowplow model yields the following relationship between the current, conduction time, POS length and plasma density [1-2],

$$\frac{IT}{rl} \propto \sqrt{n}\,.$$

Here, I is the peak conduction current, T is the conduction time, r is the radius of the POS cathode, l is the length of switch and n is the plasma density.

A cable plasma gun produces a cone-shaped plasma flow with an average angle of approximately 90 degrees [3]. In this arrangement, the length of plasma l is proportional to the distance from the gun nozzle. The current-conducting layer is not strictly radial during the conduction phase. It follows the upstream plasma surface initially, and then its development is

dependent on the plasma density distribution. Assuming the interelectrode distance is much less than the cathode radius r, the current-conducting layer arrives simultaneously to the load end of the plasma cone (Fig. 11) if the product

$$l\sqrt{n} = \text{const},$$

at any distance from a gun nozzle. This condition yields the following expression for the line-integrated (along the axial line of symmetry) plasma density distribution versus the distance from the gun nozzle in the radial direction:

$$n \propto \frac{1}{l^2} \propto \frac{1}{L^2} \quad \therefore l \propto L;$$

$$nl(L) \propto \frac{1}{L}.$$

Here L is the distance from the gun nozzle. This scaling is very close to the dependence obtained in the experiment (Fig. 12). For this measured density distribution, the current-conducting layer can be represented by a straight line in the POS cross section along the line of symmetry. The channel moves from the generator end to the load end of the plasma cone and its motion can be represented as rotation around the nozzle of a gun.

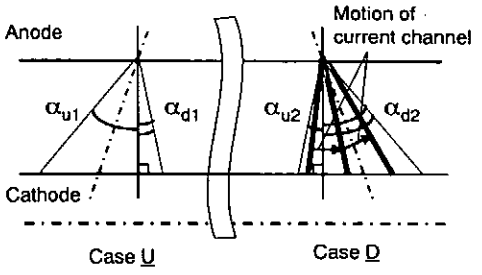

Fig. 11. Plasma flow arrangements for cases U and D with upstream and downstream angles and a snowplow motion scheme.

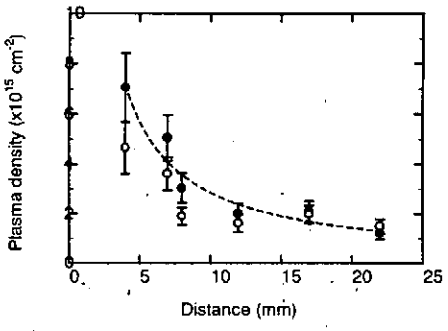

Fig. 12. Line-integrated plasma density versus distance from the gun nozzle at 3 μs (white dots) and 4 μs (black dots).

The opening of the POS takes place due to the radial motion of the plasma, resulting in the formation of a vacuum gap. After this gap is formed, the load current is rapidly switched to a downstream load. The acceleration of the plasma by the current conducting layer ends at this time and the plasma moves only by inertia. Therefore, the radial velocity of the plasma at the end of the conduction phase determines the opening rate and, as a result, electrical characteristics of a POS such as voltage and impedance.

Knowing the duration of the conduction phase, length of the switch, plasma fill geometry and assuming the picture of the snowplow motion (for example, as it is shown in Fig. 11) we can estimate the radial velocity of the plasma at the end of the conduction phase. According to our model, the motion of the current-conducting layer is the rotation around anchored top end. This is motion with constant acceleration foe the linear current increase through the POS plasma in the snowplow approach. The rotation velocity ω at the end of the conduction phase with the duration T is $\omega=2\alpha/T$, where $\alpha=\alpha_{u1}+\alpha_{d1}=\alpha_{u2}+\alpha_{d2}$ is the angle of

the plasma cone. This velocity is equal for both arrangements shown in Fig. 11. However, different initial angles between downstream ends of the plasma cones and the radial line (α_{d1} and α_{d2}, respectively) result in different values of the redial velocities when the current-conducting layer reaches the downstream plasma end.

The radial velocities at each distance L from the gun nozzle for U (v_{r1}) and D (v_{r2}) cases can be expressed as

$$v_{r1} = L\omega\sin(\alpha_{d1}),$$
$$v_{r2} = L\omega\sin(\alpha_{d2}).$$

For a larger angle α_{d2} corresponds to the case D, the radial velocity is evidently higher. Substituting L=3 cm, α=90º and T=1 μs, the radial velocity for U and D cases are 2.439×10^6 cm/s and 9.104×10^6 cm/s, respectively. This must result in a faster and better opening with a higher load current rise rate and higher POS impedance compared with case U. A 3.73-fold difference in the calculated radial velocities yields two times higher POS voltage. The intermediate case of the radial plasma flow will yield an intermediate value of the plasma radial velocity at the end of the conduction phase and moderate values for switch parameters as it is seen in the experiment.

Further development of the vacuum gap essential for the POS opening is faster for case D, since the plasma has higher radial velocity at the end of the snowplow conduction process. This results in a lower conduction time for the same plasma parameters in case D. This is also in good agreement with experimental data.

The absence of the positive effect at the conduction times longer than 1 μs is probably due to the influence of the secondary plasmas from the electrodes, which perturb the initial plasmas density distribution. The large effect of electrode plasma to POS characteristics is well documented. The measurements showed a significant increase of the plasma density near the cathode at the time delays over 4μs. This is especially important if the interelectrode distance is small.

There are also other processes that may occur. For example, the formation of a vacuum gap may take place at different radial locations for different directions of the plasma flow. Also, the snowplow motion in the downstream direction may result in additional plasma compression in case U.

5. Conclusion

ASO-X generator with POS has good characteristics providing fast and large load current. Characteristics of POS such as POS voltage and shunt impedance can be improved by modifying the plasma flow.

References

[1] W. Rix, D. Parks, J. Shannon, J. Thompson, and E. Waisman, IEEE Trans. Plasma Sci., **19**, 400 (1991)

[2] W. Rix, P. Coleman, J. R. Thompson, D. Husovsky, P. Melcher, and R. J. Commisso, IEEE Trans. Plasma Sci., **25**, 169 (1997)

[3] S. Kohno, Y. Teramoto, I. V. Lisitsyn, S. Katsuki, and H. Akiyama, IEEE Trans. Plasma Sci., **27**, 778 (1999)

CHARACTERISTICS OF MULTICHANNEL ARC GAP

S.Furuya, Y.Watanabe, T.Yoshikawa, S.Takano and J.Irisawa

Nagaoka University of Technology, Nagaoka, 940-2188, JAPAN

ABSTRACT

The characteristics of multichannel arc gap are investigated experimentally. The gap comprises 12 steel needle electrodes and a brass rod electrode. In the first case, the characteristics of multichannel arc gap are tested in the atmosphere of mixed gas including oxygen. It is found that with a little addition of oxygen the number of arc channels for mixed gas becomes similar to that for pure oxygen. In the second case, the effect of curvature of needle electrodes is examined. As a result, the number of channels is independent of the curvuture, therefore, it is considered that electrodes with large curvature are useful for long life time.

1. Introduction

A multichannel arc gap is a switch which produces a large number of arc channels in parallel. Compared to a single gap, a multichannel arc gap has lower switching inductance and electrode erosion rate, which is superior in fast rise time and long life time. A multichannel arc gap is frequently used as a pulsed power switch, however, its characteristics have hardly been investigated, particularly in the voltage range of less than 40kV.

Therefore, we have been examining the characteristics of multichannel arc gap[1]-[3]. The gap comprises 12 steel needle electrodes and a brass rod electrode. Voltage pulses which have high dV/dt are necessary to generate a large number of arc channels simultaneously[4]. A non-linear coaxial line of ferrite sharpener has been used to produce voltage pulses which have high dV/dt of 12kV/ns and peak voltage of 45kV[1]. In this report, we will describe the experimental results as follows. In the first case, the characteristics of multichannel arc gap are tested in the atmosphere of mixed gas including oxygen. In the second case, the effect of curvature of needle electrodes is examined.

In Sec.2, the experimental setup of multichannel arc gap is described. In Sec.3, the experimental results of multichannel arc gap in the atmosphere of mixed gas including oxygen are presented. In Sec.4, the effect of curvature of needle electrodes is described. Finally, the results of this report are summarized in Sec.5.

2. Experimental setup

Voltage pulses which have high dV/dt are produced by ferrite sharpener. Fig.1 shows the structure of the ferrite sharpener which is non-linear coaxial line. A peace of ferrite bead is TDK-HF70BB 2.5×5×0.8mm. The principle of the sharpener is illustrated in Fig.2. The input voltage pulse which has low dV/dt is steepened at the end of the sharpener by its non-linear effect. Typical output waveform of open-ended ferrite sharpener is shown in Fig.3. The rise time and the peak voltage of the pulse are 2.4ns and 45kV, respectively, and high dV/dt of 12kV/ns is achieved. Voltages are measured by Tektronix high voltage probe: P6015A and Hewlett Packard digital oscilloscope: HP54510A.

Fig.4 shows the geometry of multichannel arc gap. The gap comprises 12 steel needle electrodes and a brass rod of 18mm diameter. The rod electrode is grounded and positive or negative voltage pulse is applied to the needle electrodes. The apparatus allows the gap length to be varied. The gap is contained in the chamber, the kinds and the pressure of inter-gap gas are changeable. The number of arc channels is detected by Sony CCD video camera: CCD-TR650. Fifty shots at each experimental conditions are performed and the data of the number of arc channels is handled by taking the mean.

3. Characteristics for mixed gas including oxygen

Initial electrons in the gap largely affect the characteristics of multichannel arc gap. As oxygen is an electronegative gas, electron is likely to attach it. In order to verify this effect for multichannel operation, we carried out the experiments for mixed gas including oxygen. Fig.5(a) shows the result for different mixture ratio of oxygen and argon, and (b) for oxygen and helium. The gap length is 1mm and positive high voltage pulses are applied to the needle electrodes. In both cases, with a little addition of oxygen the characteristic of the number of channels becomes similar to that for pure oxygen. It is not clear that the results are related to attachment of electron to oxygen, which is an electronegative gas.

4. Effect of curvature of needle electrodes

In order to clarify the effect of curvature of needle electrodes, the characteristics of multichannel arc gap are examined with different curvature of needle electrodes. Fig.6 shows the tip of needle electrodes. We prepared five kinds, sharp and diameter of 2, 3, 4, 5mm, of electrodes. Fig.7 shows the result. The gap length is 1mm and positive high voltage pulses are applied to the needle electrodes. Dry air is used as inter-gap gas. The result apparently shows that the number of channels is independent of the curvature of needle electrodes, therefore, it is considered that electrodes with large curvature are useful for long life time.

5. Conclusion

The characteristics of multichannel arc gap are investigated experimentally. The gap comprises 12 steel needle electrodes and a brass rod electrode. In the first case, the characteristics of multichannel arc gap are tested in the atmosphere of mixed gas including oxygen. It is found that with a little addition of oxygen the number of arc channels for mixed gas becomes similar to that for pure oxygen. In the second case, the effect of curvature of needle electrodes is examined. As a result, the number of channels is independent of the curvuture, therefore, it is considered that electrodes with large curvature are useful for long life time.

Reference

(1) S.Takano et. al., NIFS-PROC-26(1996)115
(2) J.Ohrui et. al., NIFS-PROC-36(1997)1
(3) S.Furuya et. al., NIFS-PROC-39(1998)11
(4) G.R.Neil and R.S.Post, Rev. Sci. Instrum., 49(1978)401

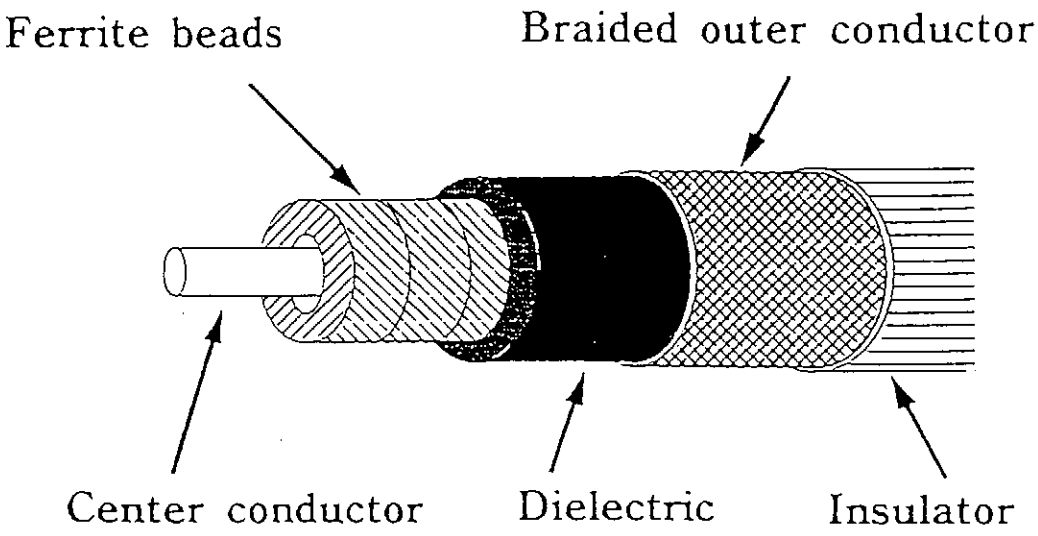

Fig.1 Structure of ferrite sharpener

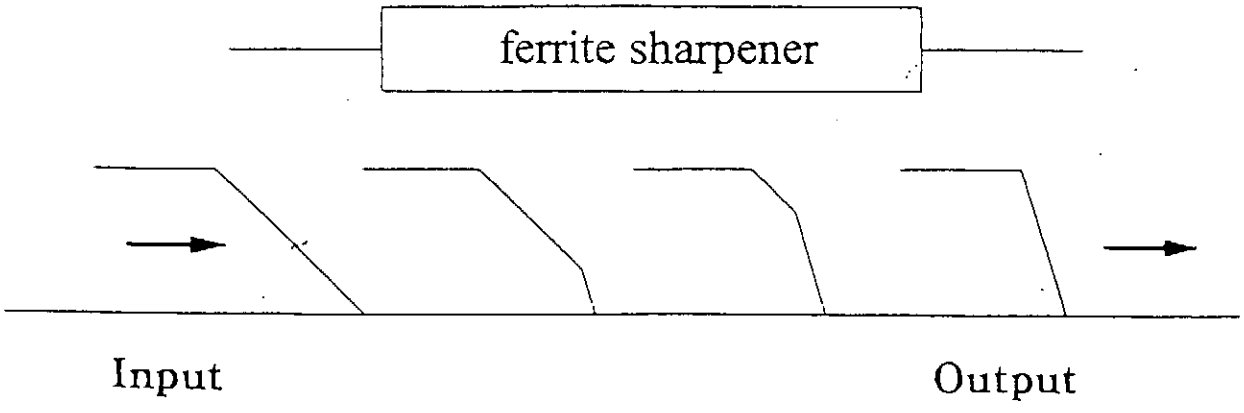

Fig.2 Principle of ferrite sharpener

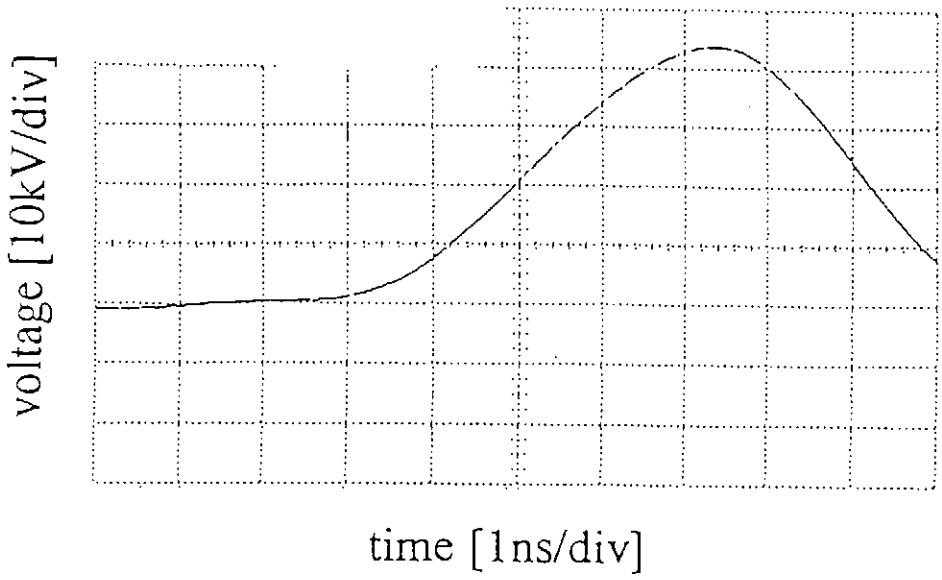

Fig.3 Output waveform of open-ended ferrite sharpener

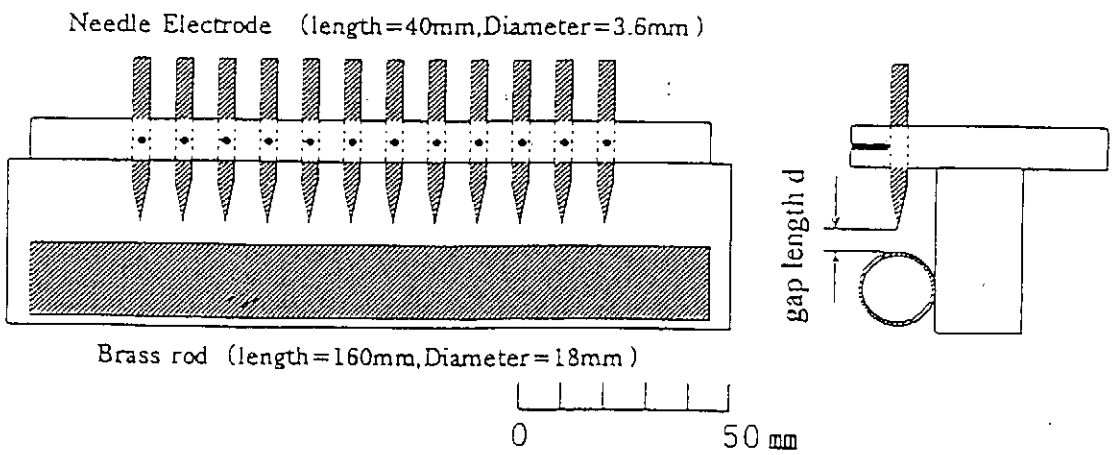

Fig.4 Geometry of mutichannel arc gap

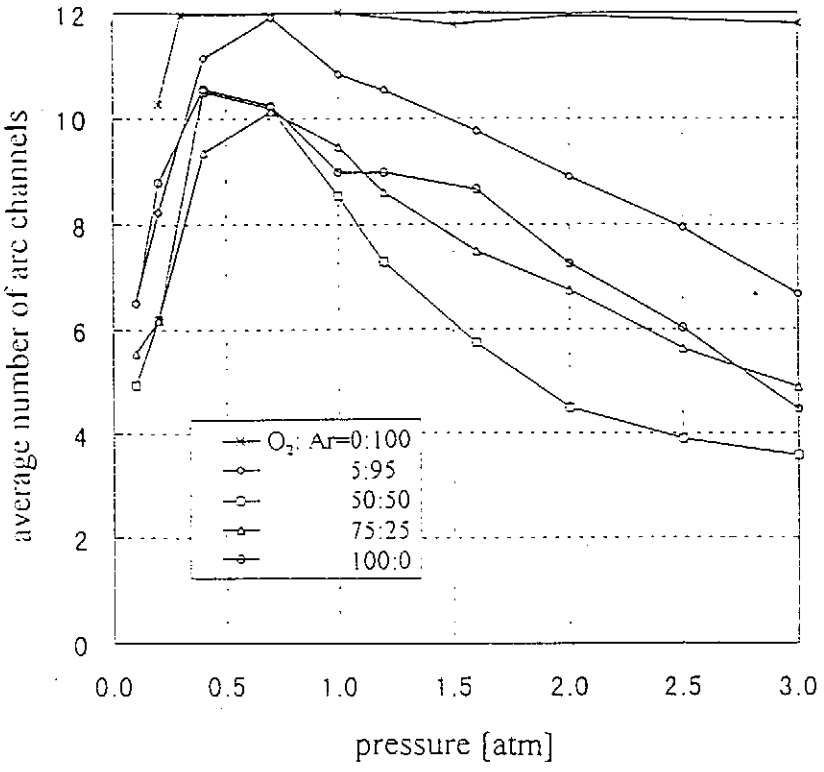

(a) mixed gas of oxygen and argon

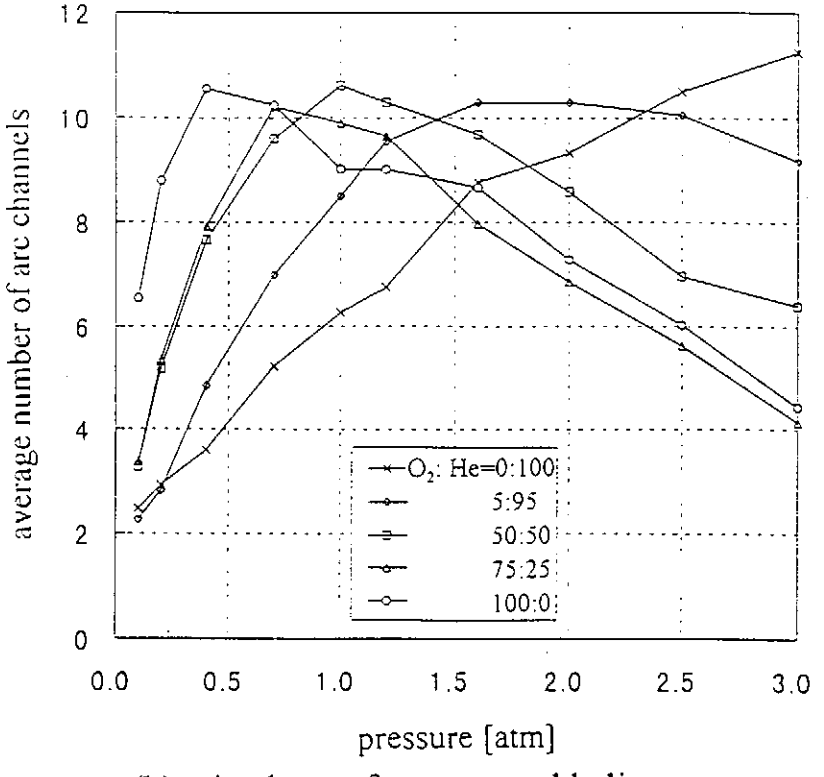

(b) mixed gas of oxygen and helium

Fig.5 Relations between average number of arc channels and gas pressure for mixed gas including oxygen

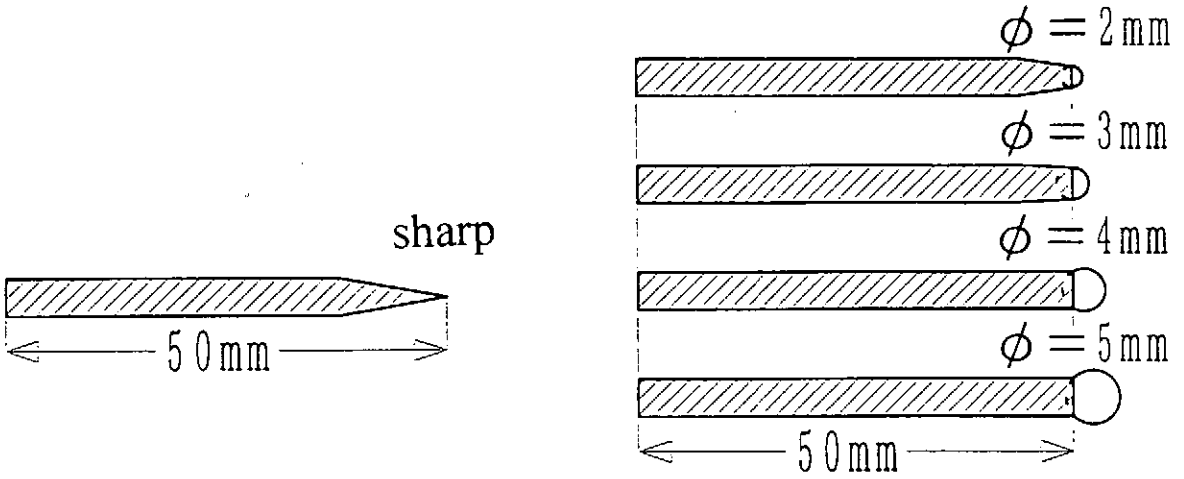

Fig.6 Tip of needle electrodes

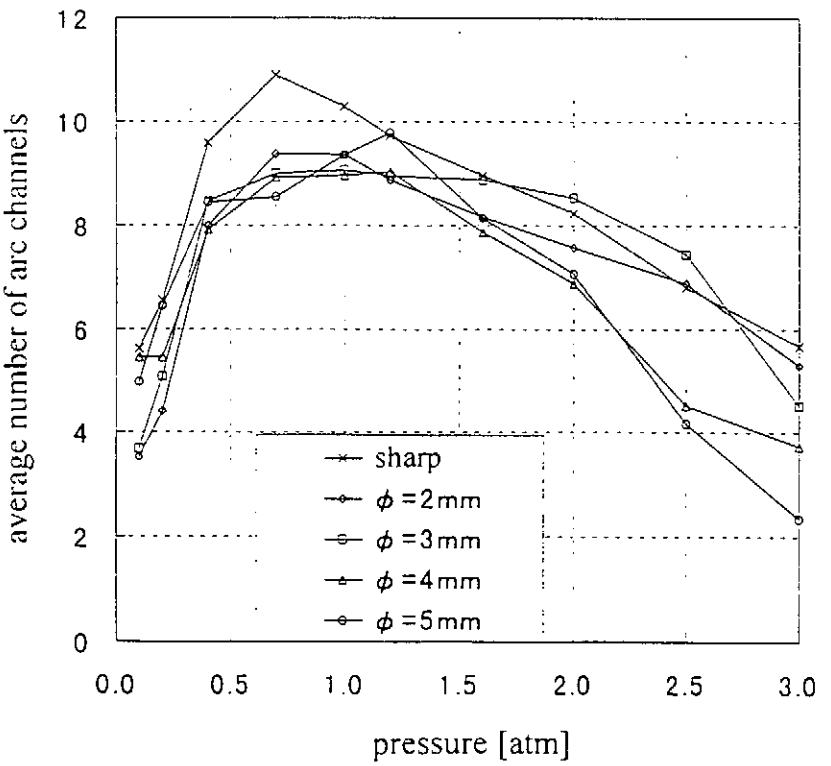

Fig.7 Relations between average number of arc channels and gas pressure with different curvature of needle electrodes

CHARACTERISTICS OF HIGH-PRESSURE, PULSED GLOW DISCHARGE IN GAS DENSITY DEPLETION

Go Imada*, Wataru Masuda[1], and Kiyoshi Yatsui

Extreme Energy Density Research Institute, Nagaoka University of Technology, 1603-1 Kamitomioka, Nagaoka, Niigata 940-2188, Japan

[1] Department of Mechanical Engineering, Nagaoka University of Technology, 1603-1 Kamitomioka, Nagaoka, Niigata 940-2188, Japan

* E-mail: imada@nagaokaut.ac.jp

ABSTRACT

The influences of gas density depletion on the high-pressure, pulsed glow discharge for the excitation of excimer lasers have been investigated eliminating the other factors which may affect the discharge instabilities, such as shock waves, residual ions and discharge products. The gas density depletion is simulated by utilizing a subsonic flow between the curved electrodes. The comparison has been made on the discharge occurred in the presence of the gas density depletion with the second discharge on the double-pulse discharge experiment. We have found that the big gas density non uniformity, $\Delta\rho/\rho_0 \sim 3.6$ % corresponding to an equivalent pulse repetition rate (PRR) of ~ 20 Hz, tends to cause the arc without the other factors. On the other hand, the second discharge on the double-pulse discharge experiment becomes arc in much smaller non uniformity ($\Delta\rho/\rho_0 \sim 1.2$ % corresponding to PRR ~ 3 Hz). The arc in the double-pulse discharge experiment might be driven by the residual ions and/or discharge products other than gas density depletion except for PRR > 20 Hz.

I. INTRODUCTION

In the applications of discharge-pumped excimer laser, a highly-repetitive operation is required to provide the high-average power. The excitation discharge has been known to cause various instabilities in subsequent discharge which collapse the highly-repetitive operation. It has been suggested that the instabilities are induced by the gas density depletion[1),2)], shock waves[3),4)], residual ions[5)] and/or discharge products[6)] produced in the discharge region. The main purpose of this paper is to elucidate the effects of the gas density depletion on the excitation discharge instability eliminating the influences of the shock waves, residual ions and discharge products caused by the previous discharge. We have compared the discharge characteristics occurred in the gas density depletion with that by the double-pulse discharge experiment in a stable gas where the gas density depletion, shocks, residual ions and discharge products are remained in the discharge region.[7)]

II. EXPERIMENTAL SETUP

Figure 1 shows the schematic diagram of experimental setup. On the rupture of the diaphragm of the Ludwieg tube, an unsteady expansion wave propagates upstream into the quiescent high-pressure gas contained within the charge tube, and hence the gas flow starts. The Mach number at the sonic throat comes up to 1 by the choking as soon as the diaphragm is ruptured. Therefore, only the expansion wave is able to propagate into the charge tube.

In the region where the expansion wave passes through, pressure, temperature, density, and velocity will be kept to constant. Consequently, a quasi-steady flow is obtained at the test section. The main electrodes consist of Chang-type anode and cathode where the width, length, gap distance and radius of curvature are 40 mm, 120 mm, 20 mm and 100 mm, respectively. The automatic ultra-violet pre-ionization electrodes consist of 6-pin spark gaps. The excitation circuit is a charge-transfer type circuit (C_1/C_p = 5.3/4.2 nF) where the storage capacitor is charged up to 30 kV. A gas mixture of helium and argon is used to simulate ArF excimer laser. The gas composition is Ar/He = 1/9 with a pressure of 215.4 kPa which corresponds to an initial gas density (ρ_0) of 0.69 kg/m^3.

The gas density depletion is generated by a gas flow between the curved electrodes. The relation between gas density (ρ) and flow cross section (A) in the isentropic flow can be written as

$$\frac{d\rho}{\rho} = \frac{M^2}{(1 - M^2)} \frac{dA}{A}, \tag{1}$$

where M is the Mach number of the flow. The main electrodes compose part of the wall of flow field in our laser head (see Fig. 1(c)). Hence, the gas density depletion is realized in the discharge region, because ρ decreases with decreasing A in the subsonic flow ($M < 1$). A subsonic flow, up to $M \sim 0.93$, is generated by Ludwieg tube.[3)]

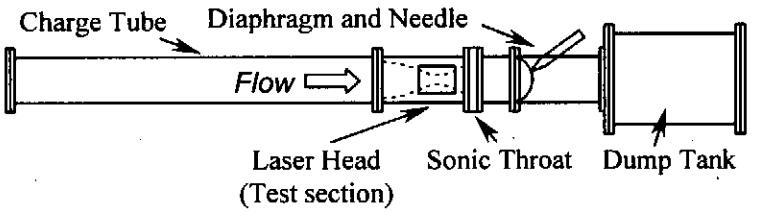

(a)

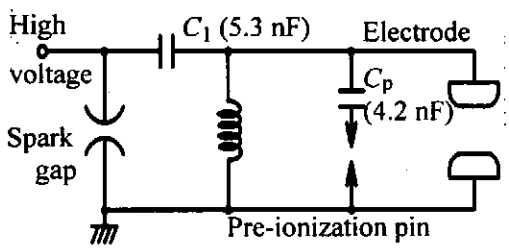

(b)

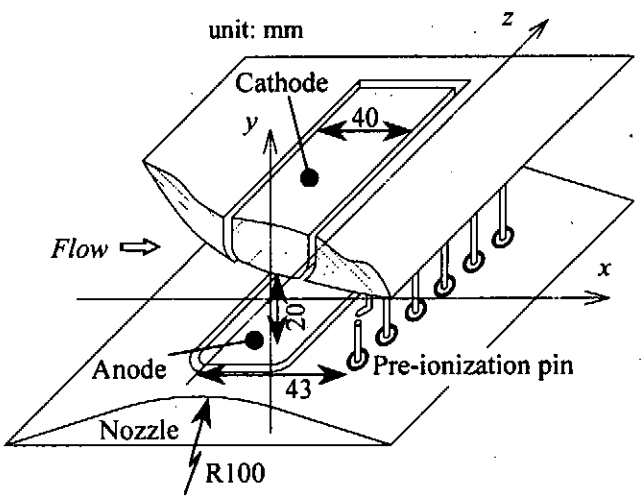

(c)

Fig. 1 Schematic diagrams of (a) experimental setup, (b) excitation circuits and (c) cross-sectional view of flow field and discharge region.

Figure 2 shows the schematic diagram of the Mach-Zehnder interferometer. An argon ion laser, λ = 514.5 nm, is used as a light source. The laser beam is converted into the parallel ray by the lens and the concave mirror. The parallel ray is divided into equal paths by a 50/50 beam splitter, and then passes through the discharge region along the laser axis (L = 200 mm). The interferograms are recorded by a high-speed image-converter camera. This system takes the interferogram of the time-resolved beam-path-integrated spatial gas density distribution. The interferograms have been taken at an exposure time of ~ 750 ns. The infinite-fringe interferogram method is applied to our experiment because it is convenient to obtain the contour lines of density. The density difference between the fringes is calculated to be 0.0146 kg/m^3, where the Gladstone-Dele constant is 0.176 × 10^{-3} m^3/kg.

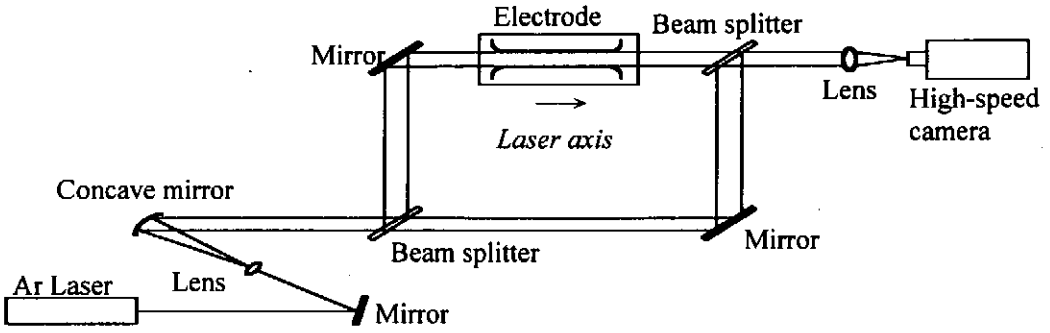

Fig. 2 Schematic diagram of Mach-Zehnder interferometer system.

III. RESULTS AND DISCUSSION

A. Visualization of gas density distribution

Figure 3 shows the time evolution of (a) voltage and current and (b) resistance and power of the single-pulse discharge in a stable gas. We see ~ 18 kV of the breakdown voltage and ~ 2.8 kA of the peak current. The pulse width of the discharge power is ~ 30 ns (FWHM). The discharge energy deposited into the gas is estimated to be ~ 0.7 J.

Figure 4 shows the Mach-Zehnder interferograms after the single-pulse discharge in a stable gas, where t indicates the time after the discharge. It is shown that the instantaneous heating of the gas by the discharge leads to a sudden increase in pressure and a subsequent rapid expansion, which creates a gas density depletion. Thereafter, the gas density depletion spreads out into the surroundings due to the turbulent mixing and then the gas density gradually returns to the initial density.

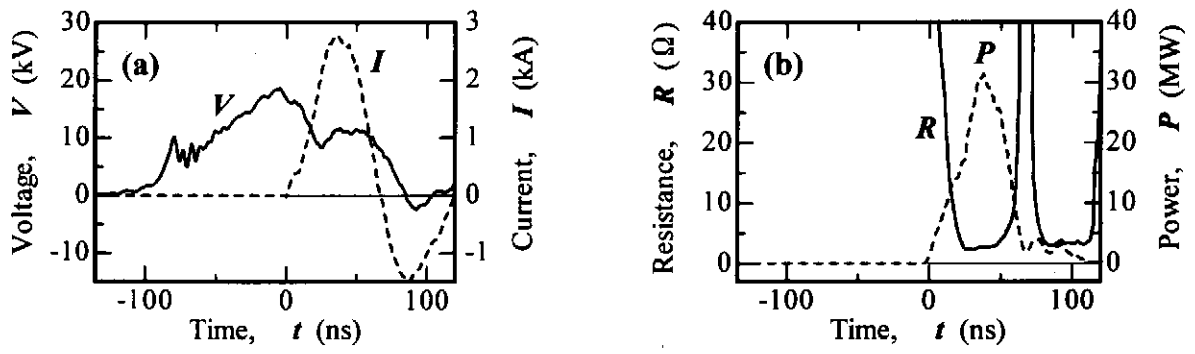

Fig. 3 Time evolution of (a) voltage and current and (b) resistance and power.

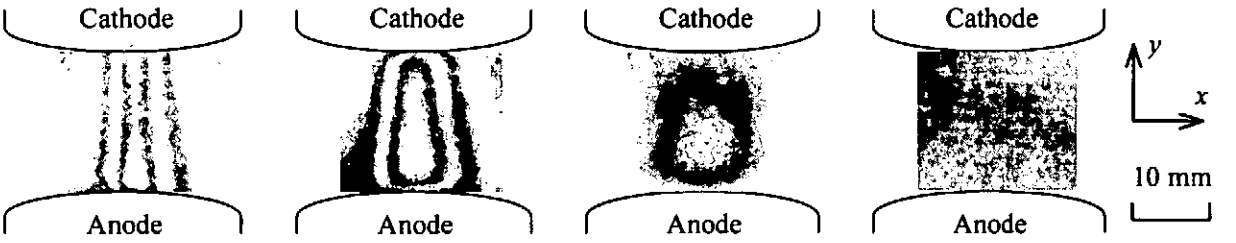

(a) t = 0.1 ms (b) t = 23.7 ms (c) t = 157 ms (d) t = 608 ms

Fig. 4 Interferograms after single-pulse discharge in stable gas.

Figure 5 shows the Mach-Zehnder interferogram of gas density depletion produced by a subsonic gas flow at M = 0.81. It is found that the gas density depletion is generated by subsonic gas flow around the discharge electrode.

Figure 6 shows the typical gas density distributions in the discharge region obtained from the interferograms. The gas density generated by a subsonic flow is also presented in Fig. 6 as broken lines. It is found that the gas density generated by a subsonic flow is similar to that caused by the discharge. To compare the gas density distribution by a subsonic flow with that by the discharge, we define the gas density non uniformity (S) as

$$S = \frac{(\Delta\rho/\rho_0)}{W}, \qquad (2)$$

where $(\Delta\rho/\rho_0)$ is the depth of the gas density depletion and W is the full width at ten-percent-maximum width of the depth of gas density depletion. In the gas density distribution caused by the discharge, S decreases with increasing time because $(\Delta\rho/\rho_0)$ would be reduced with increasing W.

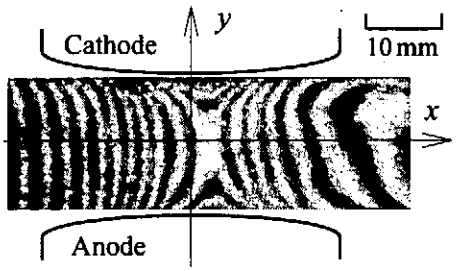

Fig. 5 Interferogram of gas density depletion produced by subsonic gas flow at M = 0.81.

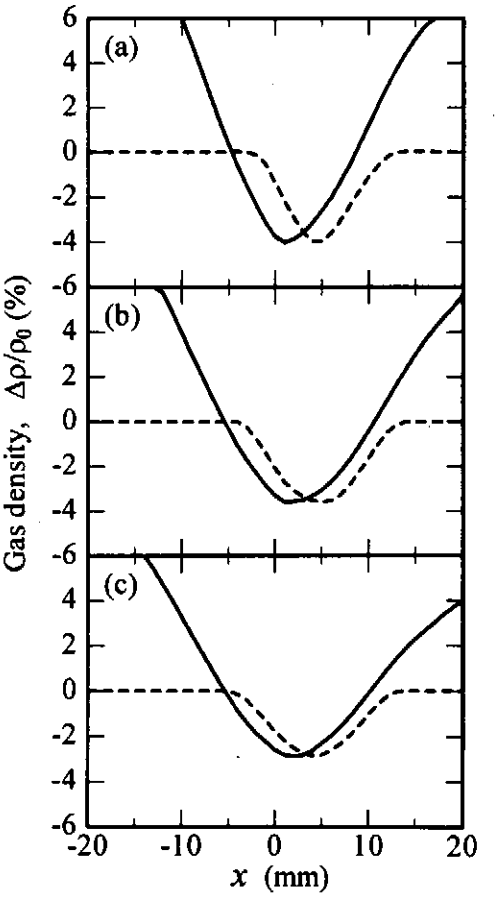

Fig. 6 Spatial distribution of gas density depletion in various gas density non uniformity. (a) S = 3.0 m^{-1} (M = 0.81, t = 6.9 ms), (b) S = 2.4 m^{-1} (M = 0.74, t = 23.7 ms), (c) S = 1.8 m^{-1} (M = 0.67, t = 61.2 ms).

B. Discharge characteristics

Figure 7 shows the time-integrated photographs of the discharge in the double-pulse discharge experiment and in the gas density depletion. The second discharge in the double-pulse discharge experiment occurs in a stable gas where the gas density depletion, shock waves, residual ions, and discharge products are remained. The light emitted from the second discharge superimposes on one from the first discharge. The second discharge tends to turn to arc when the time interval of the double-pulse discharge (Δt) is decreased to ~ 350 ms which corresponds to the equivalent pulse-repetition rate (PRR) of ~ 3 Hz. We have found from Fig.7(b) that the glow are maintained in spite of the presence of the gas density depletion below $\Delta\rho/\rho_0 \sim 3.1$ % ($S = 2.0$ m^{-1}). It is also observed that the discharge becomes arc-like filament in much bigger density depletion in comparison with the double-pulse discharge experiment.

Figure 8 shows (a) discharge resistance (R_d) and (b) probability of arc (η) as a function of the gas density non uniformity (S). Here, R_d is defined as a minimum resistance in the discharge. The arc is evaluated from the photograph of the discharge and the discharge resistance. It is found that R_d in the gas density depletion is reduced from ~ 1 Ω to ~ 0.2 Ω with increasing S. It indicates that the glow changes into the arc gradually. It is shown that the arc occurs through the gas density depletion in case $S > 2.4$ m^{-1} ($\Delta\rho/\rho_0 > 3.6$ %) which corresponds to $\Delta t < 50$ ms in the double-pulse discharge experiment. This result

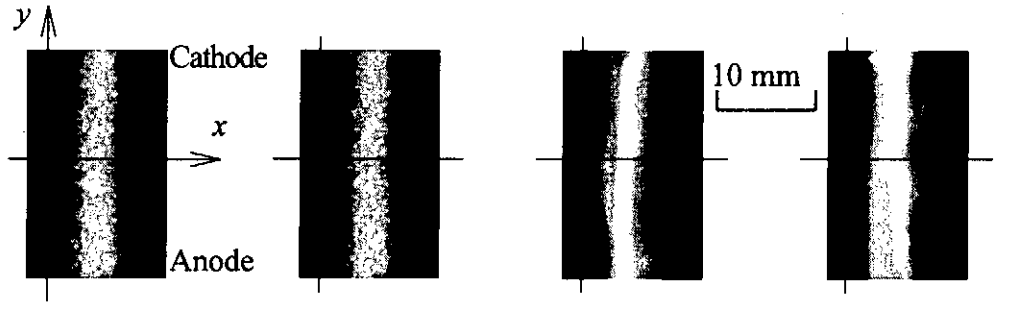

(a) Double-pulse experiment.

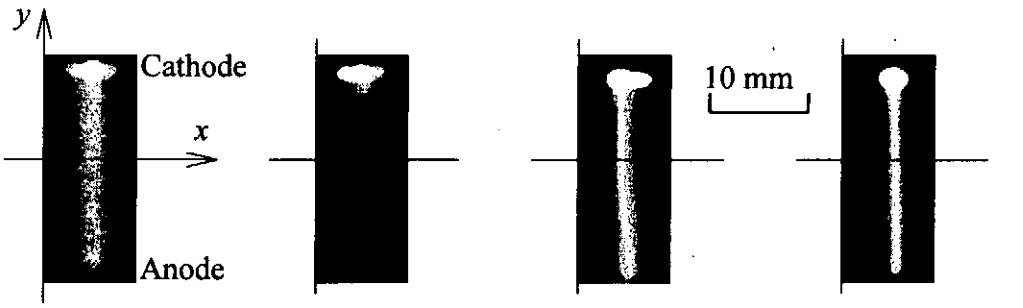

(b) Discharge in gas density depletion.

Fig. 7 Time-integrated photographs of discharge.

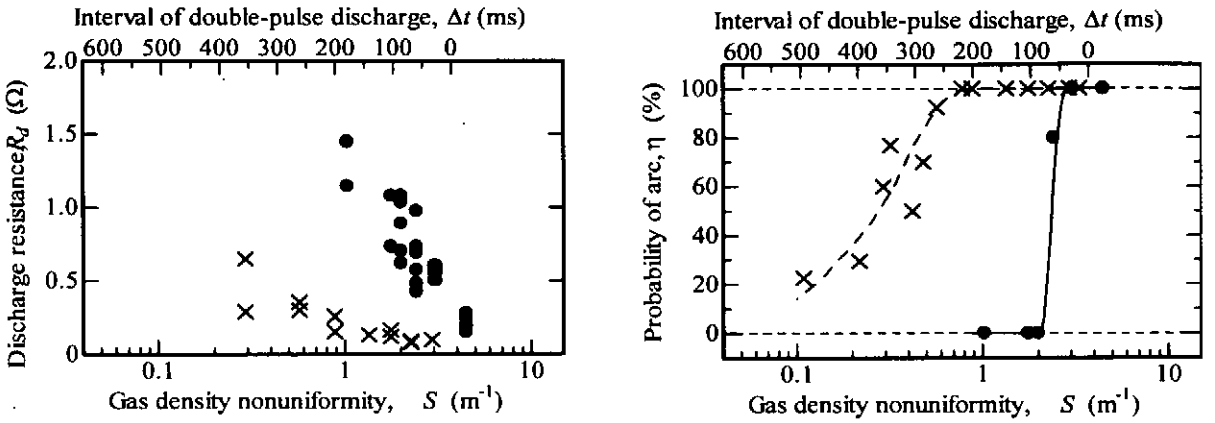

Fig. 8 (a) discharge resistance and (b) probability of arc as a function of gas density non uniformity. ●; single-pulse discharge in a gas density depletion, ×; double-pulse discharge in a stable gas.

clearly demonstrates that the big density non uniformity tends to induce the arc without the shocks, ions and products. The transition from glow to arc with respect to the gas density depletion occurs discontinuously. The second discharge in the double-pulse discharge experiment becomes arc in smaller S. In addition, the transition occurs very slowly. The shock waves generated by the first discharge already leave from the discharge region or will be weakened in magnitude when $\Delta t > 1$ ms.[8] Therefore, it is found that the arc in the double-pulse discharge experiment except for $\Delta t < 50$ ms is induced by the residual ions and/or some products.

IV. CONCLUSION

The effects of the gas density depletion on the excitation discharge in excimer laser eliminating the influences of shock waves, residual ions and discharge products has been studied. The big gas density non uniformity tends to induce the arc without the shock waves, residual ions and discharge products. The second discharge on the double-pulse discharge experiment in a stable gas becomes arc in smaller gas density non uniformity. Therefore, it can be suggested that the discharge instability is also caused by some factors other than the gas density depletion.

ACKNOWLEDGEMENT

This work was partly supported by Grant-in-Aid for Encouragement of Young Scientists from the Ministry of Education, Science, Sports and Culture in Japan. The authors would like to thank Mr. H. Yoshida and Mr. Y. Sato for their collaboration in the experiment and Mr. Y. Sekimoto for mechanical design and experimentation.

REFERENCES

1) S. Kosugi, *et al.*, *Jpn. J. Appl. Phys.*, **32**, 4980, 1993.
2) G. Imada, *et al.*, *Proc. Int'l Symp. on Ultrahigh- and High-Speed Photography and Image-based Motion Measurement*, **SPIE-3173**, 124, 1997.
3) K. Yatsui, *et al.*, *Proc. 10th Int'l Symp. on Gas Flow and Chem. Lasers*, **SPIE-2502**, 134, 1994.
4) M. Sentis, *et al.*, *IEEE J. Quantum Electron.*, **27**, 2332, 1991.
5) M. Osborne and J. Green, *J. Appl. Phys.*, **71**, 3127, 1992.
6) R. Arutyunyan, *et al.*, *Sov. J. Quantum Electron.*, **16**, 1589, 1986.
7) G. Imada, *et al.*, *Proc. 12th Int'l Symp.on Gas Flow and Chem. Lasers*, **SPIE-3574**, 653, 1998.
8) G. Imada, *et al.*, *Metal Vapor and Free-Electron Lasers and Applications, ed. by V. Smiley and F. Tittel*, **SPIE-2118**, 51, 1994.

AN OBSERVATION OF GAS DISCHARGE INDUCED BY HIGH-POWER SHORT-PULSE MICROWAVE USING A HIGH-SPEED CAMERA

M.Onoi, K.Azuma, E.Fujiwara, and M.Yatsuzuka

Himeji Institute of Technology, 2167 Shosha, Himeji, Hyogo 671-2201, Japan

ABSTRACT

A high-power and short-pulse microwave generated by a virtual cathode oscillator was irradiated into the gap of two spherical electrodes being biased by a dc voltage less than a breakdown voltage. The luminescence of discharge was observed with a high-speed camera. Streak pictures show that there are two different discharge processes depending on gas pressure. In the higher region above 300Torr, several local discharges occur by microwave injection and grow to link together, leading to gap breakdown. In the lower region below 300Torr, on the other hand, two-staged gas discharges appear.

1. Introduction

Recent progress of pulse power technologies has allowed us to generate intense relativistic electron beams, leading to development of high-power pulsed microwave (H.P.M.) devices.[1,2] One of high-power microwave applications is a gas discharge by H.P.M. that is important in the fields for measurement and modification of air atmosphere,[3] laser pumping,[3,4] gap switches,[5] microwave-induced lighting,[6] and plasma propulsion.[7] At Himeji Institute of Technology, the high-power microwave with the peak power of 20 MW, frequency of 10-15 GHz, and pulse width of 15-20 ns has generated by a virtual cathode oscillator (vircator) with a pulse power generator, "HARIMA-II".[8,9] The high-power pulsed microwave generated by the vircator was irradiated to a gap biased by a dc voltage less than the breakdown voltage, leading to induced gas discharges.[10-12]

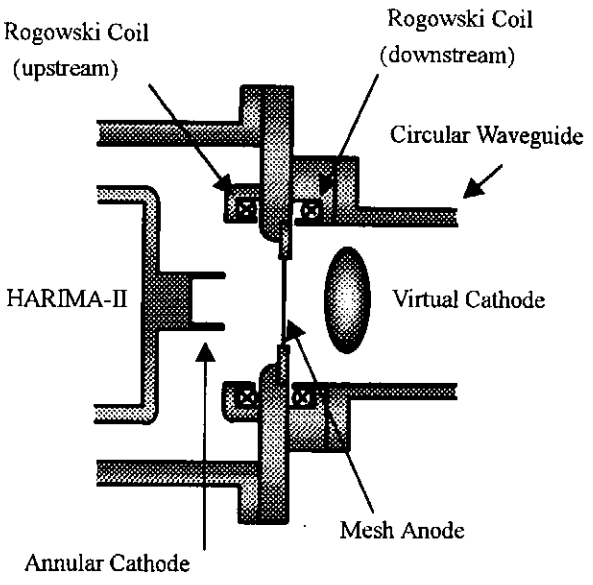

Fig.1. The arrangement of a vircator diode.

2. Microwave generation

The pulsed power generator "HARIMA-II" with the peak power of 400 kV, the pulse duration of 50 ns, and the output impedance of 3 Ω was used for microwave generation by a vircator. The arrangement of vircator diode is shown in Fig.1. The vircator diode consists of a stainless-steel annular cathode (outer radius R_c = 1.5 cm and thickness x = 1.0 mm) and stainless mesh anode with the wire diameter of 0.25 mm and the transmission rate of 67.7%. The A-K gap separation is 3.5 mm. The diode voltage was measured with a resistive divider near the cathode. Electron beam currents were measured with a nano-second-response Rogowski coil at the upstream located at 1.1 cm from the anode and the downstream located at 0.1 cm from the anode.

The electron beam emitted from annular cathode passed through the mesh anode to a circular waveguide (radius : 2.25 cm). When the electron beam at the downstream exceeded a space-charge-limited saturation current, a virtual cathode was formed in the drift space, generating microwaves. The generated microwave was propagated along the circular waveguide and was emitted into free space through a conical horn for power measurement. The microwave power was calculated by integrating the radiation pattern obtained by an open-ended rectangular antenna. The microwave frequency was determined by a 105.7 m waveguide delay line. The monitor signal of microwave was detected with a probe located on the wall of the circular waveguide and observed with a digital

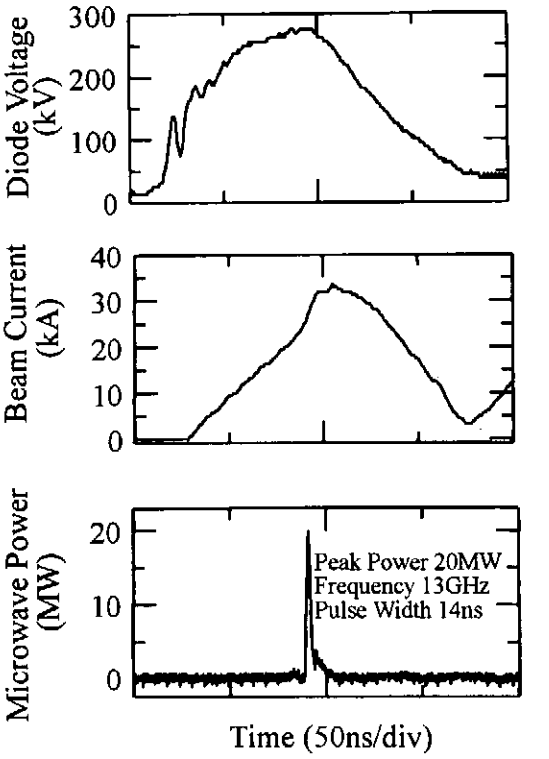

Fig.2. Time history of diode voltage, beam current at the upstream and microwave power.

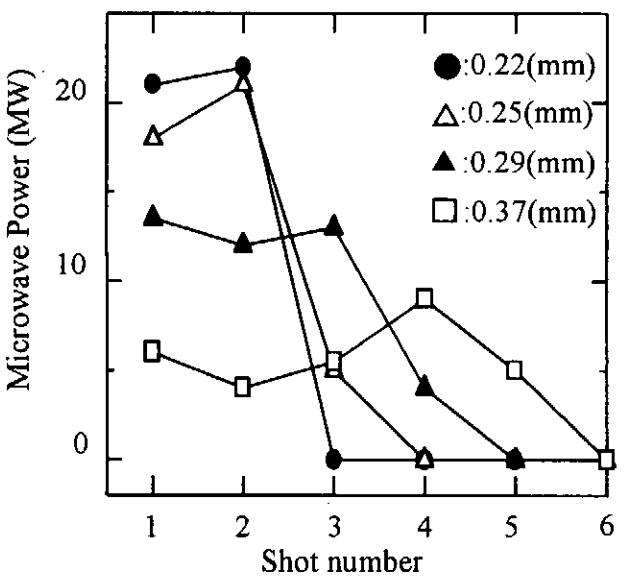

Fig.3. The relation between microwave power to the wire diameter of anode mesh in the repeated operations.

oscilloscope.

Typical time history of the diode voltage, beam current at the upstream, and microwave emission is shown in Fig.2. As seen in Fig.2, the peak diode voltage is 280 kV and the maximum beam current is 35 kA at the upstream. The generated microwave is the peak power of 20 MW, the frequency of 13 GHz, and the pulse width of 14 ns.

The relation between the microwave power to the shot number in repeated operations for various wire diameters of anode mesh is shown in Fig.3, where ●, △, ▲ and □ indicate the wire diameter of 0.22, 0.25, 0.29 and 0.37 mm, respectively and the transparency of each mesh anode was almost constant(63%~71%). As seen in Fig.3, when the wire diameter is the smaller, the higher microwave power is generated, but the number of repeated operations is decreased. No microwave emission appears after a few repeated operations because the mesh anode was broken by strongly pinched electron beams. In this experiment, the anode mesh with the wire diameter of 0.25 mm was used.

3. Experimental setup and procedures for microwave-induced gas discharge

An experimental setup for gas discharge induced by a high-power pulsed microwave is shown in Fig.4. A pulsed microwave from the vircator was injected into a vacuum chamber (stainless steel, diameter : 310 cm, and length : 320 cm) through the circular waveguide, the conical horn, and the dielectric lens. The gap length between two spherical stainless electrodes of 4.1 cm in a diameter was 15 mm, so that the dc electric field between the electrodes is uniform. The irradiated microwave power was also almost uniform in the gap space. The dry air in the pressure region from 50 Torr to 760 Torr was used. A high-power and short-

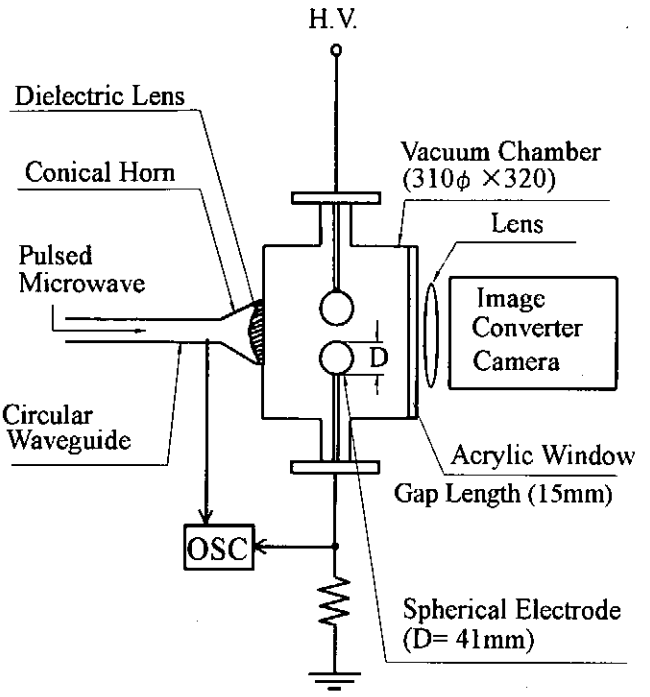

Fig.4. Experimental setup for microwave-induced gas discharge.

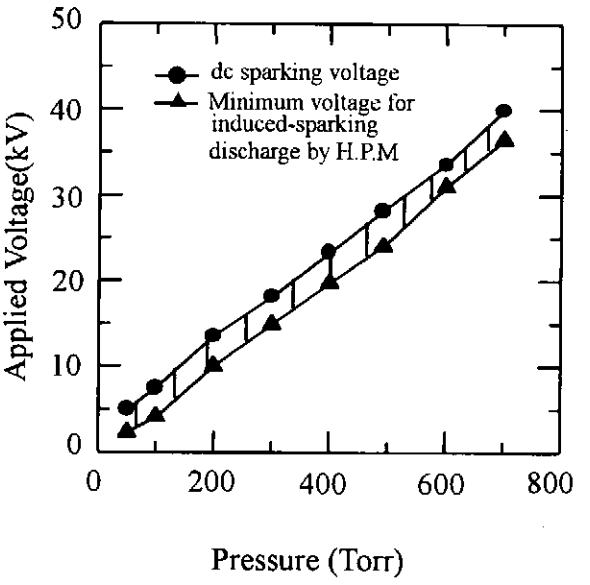

Fig.5. The region induced sparking discharge by high-power pulsed microwave.

pulse microwave was irradiated into the gap biased by the dc voltage less than the breakdown voltage. A luminescence of gas discharge was observed with a high-speed image converter camera (IMACON 792, HADLAND PHOTONICS). The applied dc voltage, the discharge current, and microwave were observed with a digital oscilloscope.

4. Results and Discussion

The region of the gas discharge induced by high-power microwave is shown in Fig.5, where ● indicates the dc breakdown voltage without microwave irradiation and ▲ is the minimum dc voltage for microwave-induced gas discharge. As seen in Fig.5, the induced gas discharge occurs at all pressure regions from 50 Torr to 760 Torr.

Figure 6 shows the streak picture together with the time evolution of discharge current, applied dc voltage, and microwave power for the gas pressure of p=200 Torr, where the initial dc voltage is V_d=13 kV. As seen in Fig.6, two-staged gas discharge appears in the gap by microwave injection. At the first-staged gas discharge, a large single luminescence of discharge is observed in the center of the gap at almost the same time of the microwave injection. Then spiky discharge current flows during the microwave irradiation with the slightly decrease in applied dc voltage. Immediately after, the other discharge luminescences appear between the single large discharge and both electrodes. In first-staged discharge, the large single plasma acts as a conductor in the gap, so that an electrical field between the large single

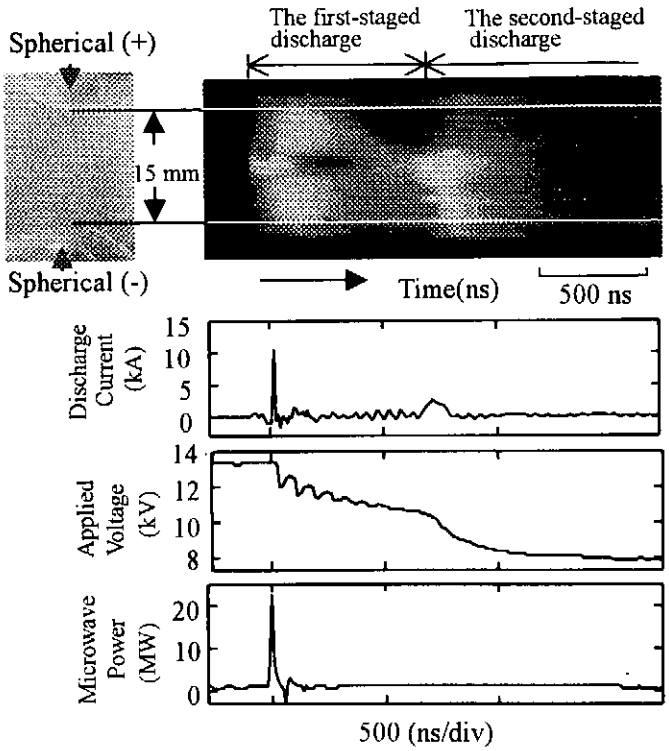

Fig.6. The streak picture of discharge luminescence and time history of discharge current, applied voltage, and microwave power for p=200 Torr and V_d=13 kV.

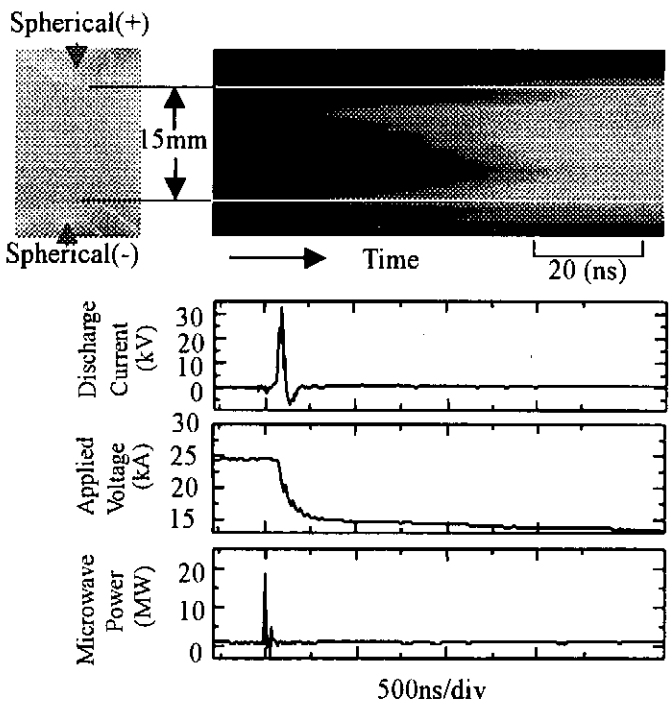

Fig.7. The streak picture of discharge luminescence and time history of discharge current, applied voltage and microwave power for p=400 Torr and V_d=23.7 kV

plasma and the spherical electrodes is increased, leading to the discharge in the gap space between the plasma in the center and both electrodes. At this time there is no detectable discharge current, although the dc voltage is decreased gradually. Before the first-staged gas discharge disappears completely, the second-staged discharge is observed with the discharge current flow and the reduction in dc voltage.

The typical streak picture of discharge in the pressure region above about 300 Torr is shown together with the discharge current, the applied dc voltage, and the microwave in Fig.7, where p=400 Torr and V_d=23.7 kV. After a microwave injection into the gap, several local discharges are observed and grow up to link together. The discharge current flows with the decrease of dc voltage at about 200 ns later after an injection microwave. The observed delay times from an injection of microwave to the start of discharge current for various pressure are shown as a function of applied dc voltage between the gap in Fig.8, where in $p \leq 300$ Torr the delay times of the first-staged and the second-staged discharge are plotted.

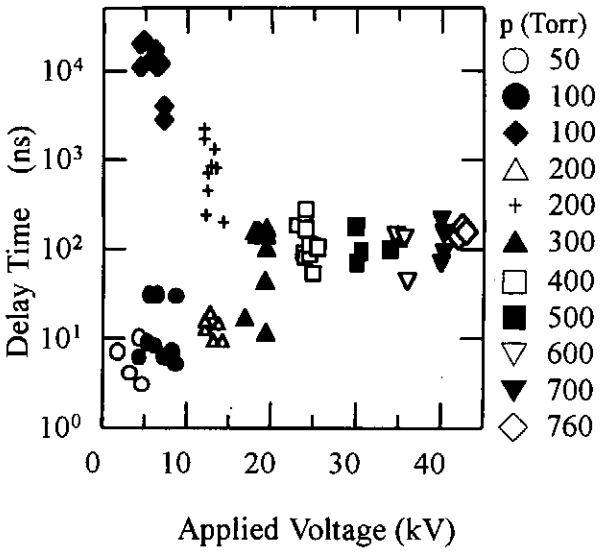

Fig.8. The delay time from an injection of microwave to a start of sparking discharge

A mechanism of discharge in the pressure region above about 300 Torr is studied with a model as follows:

(1) Several local discharges occur at the same time with an equal distance after the microwave injection.

(2) The local discharges grow with an electron drift velocity v_d.

(3) The gap breakdown occurs when the local discharges link together.

Then, the delay time t from an injection of microwave to the gap breakdown is given by

$$t = \frac{d/(N+1)}{v_d},$$

where N is a number of local discharge and d is gap length. The calculated delay time t where d=1.5 cm and the data of v_d[13] is shown in Fig.9 for N= 1, 5, 10, 20, and 50 together with the experimental delay times. In Fig.9 the experimental delay time is 100~150 ns longer than the calculated one since the number of local discharges were N=5~10. This disagreement might be ascribed to the

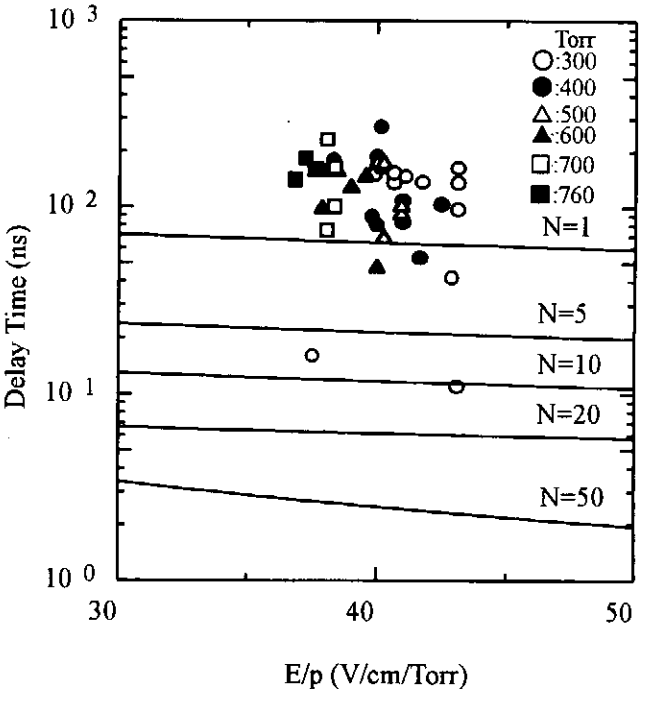

Fig.9. The calculated delay time with a model.

assumption (1). In fact the onset of local discharges is not the same time as shown in Fig.7.

5.Conclusion

The high-power and short pulsed microwave was irradiated to the gap between the spherical electrodes biased by a dc voltage less than the breakdown voltage. There are two different discharges depending on gas pressure. In $p \geq 300$ Torr several discharges occur in the gap and are grown by the electric field of an applied voltage between the gap. When several discharge are linked together each other, the gap breakdown occurs. In $p \leq 300$ Torr, the two-staged discharges are observed. In the first-staged discharge a single large luminescence of gas discharge appears at the center of gap. Immediately after the other luminescence are observed in the gap space between the plasma in the gap center and both electrodes. The second gap breakdown occurs after about 100 ns ~ 10 μ s of the first gap breakdown.

Acknowledgement

This work was supported by the Grant-in-Aid for Scientific Research, The Ministry of Education, Science and Culture of Japan.

References

1) V. L. Granatstein and I. Alexeff, "High-Power Microwave Sources", (Artech House, Boston・London, 1989).
2) J. Benford and J. Swegle, "High-Power Microwaves", (Artech House, Boston・London, 1992).
3) A. V. Gaponov-Grekhov and V. L. Granatstein, "Application of High-Power Microwaves", (Artech House, Boston・London, 1994).
4) A. J. Mendelsohn, R.Normandim, S. E. Harris, and J. F. Young, Appl. Phys. Lett, **38**, 603-605 (1981).
5) N. A. Ridge, P. F. Hirst, A. Maitland, and D. M. Parles, IEEE Trans. Plasma Sci, **24**, 1443-1449(1996).
6) M. Siho. at al.; Nucl. Inst. Meth. In Phys.Res. A8075(1996).
7) L. N. Myrabo, Scientific American, (1999).
8) M. Yatsuzuka, K. Nakayama, Y. Hashimoto, O. Ishihara, and S. Nobuhara, IEEE Trans. Plasma Sci, **22**, 939-944(1994).
9) M.Yatsuzuka, M. Nakayama, M. Tanigawa, S. Nobuhara, D. Young, and O. Ishihara, IEEE Trans. Plasma Sci, **22**, 1314-1321(1998).
10) T.Wakisaka, M. Yatsuzuka, and S. Nobuhara, Proc. of 11th Int'l Conf. on High Power Particle Beams, Vol. 1, (Prague, 1996) pp.465-468.
11) T. Wakisaka, M. Yatsuzuka, and S. Nobuhara, T. IEE Jpn., **116-A**, 378-379 (1996) [in Japanese].
12) M. Onoi, K. Azuma, E. Fujiwara, and M. Yatsuzuka, Proc. IEEJ Workshop on Discharge, ED-98-231, (Kyoto, 1998) pp. 23-28 [in Japanese].
13) H. Raether, "Electron Avalanches and Breakdown in Gases", (Butter Worth, London, 1964).

TWO-STAGE AUTOACCELERATION OF AN INTENSE RELATIVISTIC ELECTRON BEAM USING DOUBLED SECOND STAGE

D. Hasegawa, K. Kamada, A. Kuraku, R. Ando, and M. Masuzaki

Department of Physics, Faculty of Science, Kanazawa University, Kanazawa, 920-1192, Japan

ABSTRACT

It was found that making use of two cavities as the second stage in the two-stage autoacceleration experiment was effective for increase of a gain in energy of the accelerated electrons. An annular electron beam with energy of 550 keV, current of 5 kA, and pulse length of 12 ns was injected into the cavities. The energy of the most accelerated part of the beam electrons increased from 850 keV to 1.1 MeV when two cavities was used instead of a single cavity at the second stage. The pulse length of the most accelerated part remained 3 ns as expected. The transmission line theory that was applicable to multi-stage autoacceleration process was also found to be applicable to this autoacceleration process. These results indicate possibility of producing a sub-nanosecond electron beam with much higher energy by using two or more cavities with the same length at each stage in the multi-stage autoacceleration scheme.

I. Introduction

Generation of a short duration intense relativistic electron beam (IREB) is an interesting subject of study for, for example, application to high-power, short pulse millimeter-wave generation called superradiance.[1] However, it is difficult for conventional pulse-forming-line systems to generate an IREB of short duration on order of 1 ns or less because of their structure. As far as we know, at present only a compact pulsed accelerator based on the RADAN 303[2] modulator equipped with a sub-nanosecond pulse sharpener generates an electron beam with duration of 0.5 ns. The energy and the current of the generated beam are 250 keV and 1-2 kA, respectively. However, the attainable energy and current might be limited because of the small size of the apparatus. We have proposed to compress pulse duration of an IREB after emission from a

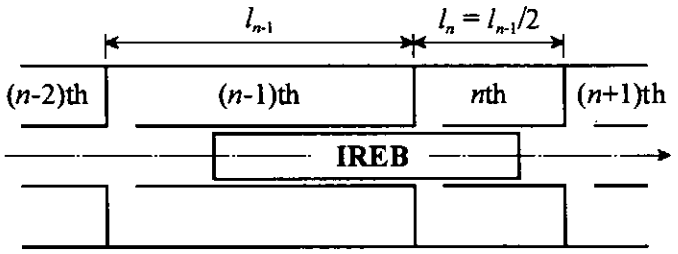

Fig. 1. Schematic of multi-stage autoacceleration.

diode utilizing multi-stage autoacceleration process.[3] Multi-stage autoacceleration process is potentially simple approach to produce a sub-nanosecond electron beam with high particle energies.

One-stage autoacceleration is an energy transfer process for an IREB from the first half of the beam pulse to the second half by only using a passive coaxial cavity structure.[4)-10)] The length of the cavity is equal to a quarter of the incident beam length, and the electrons in the last half of the incident beam length is accelerated. In the multi-stage autoacceleration scheme the autoacceleration process is repeatedly applied to an IREB using cavities connected tandem to accelerate a part of the beam electrons. In this scheme the length of the nth cavity is adjusted to half of the length of the (n–1)th cavity as shown in Fig. 1. The length of the most accelerated part of the IREB after passing through the nth cavity is compressed to $1/2^n$ of its initial length. Only the electrons in the last 2^nth part of the initial beam pulse is accelerated n times by all cavities. The energy increase of the electrons in the most accelerated part of the beam is estimated to be the sum of the products of the beam current and the cavity impedance at each stage. Because the velocity of the electrons in the initial IREB is nearly equal to velocity of light, the current of the accelerated part of the IREB is kept nearly constant after passing through each stage. Therefore, the kinetic energy of the most accelerated beam electrons is expected to increase arithmetically when cavities with the same impedance are used.

The experiments on the four-stage autoacceleration have already been reported.[11] The pulse length of the beam current after the four-stage acceleration was not so narrow as expected as shown in Fig. 2 (a). This is because the beam electrons other than the most accelerated ones could not be taken away. To remove the lower energy electrons, we placed an aluminum foil in front of the Faraday cup used to measure the beam current. An electron beam with pulse length of 0.8 ns, energy of 1.1 MeV and current of 1 kA was obtained at the end of the beam pulse as

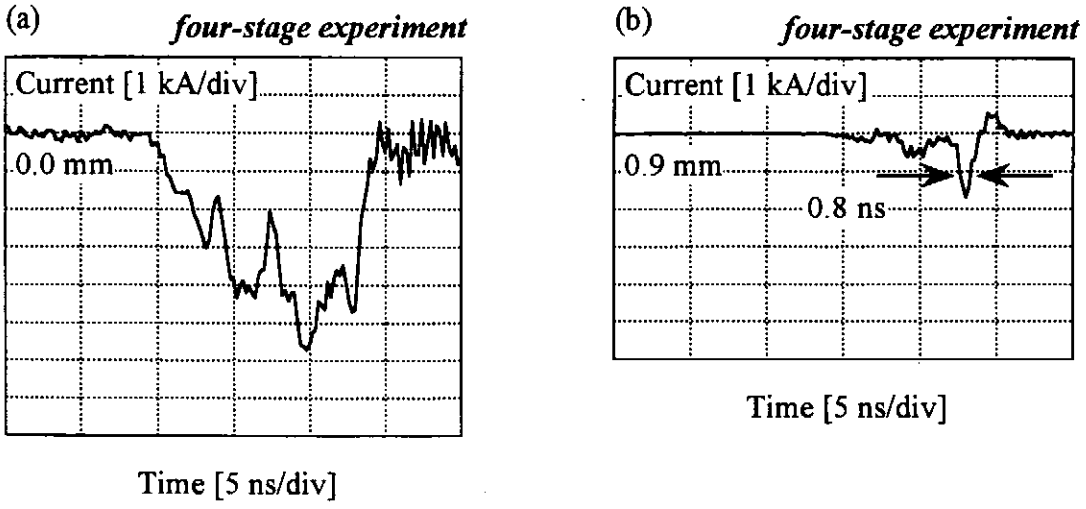

Fig. 2. Typical waveforms of Faraday cup signal obtained from the experiments on the four-stage autoacceleration, (a) the current waveform without aluminum foil and (b) the most accelerated part of the beam transmitted through 0.9 mm aluminum foil.

expected with an aluminum foil with thickness of 0.9 mm [Fig. 2 (b)]. The pulse length agreed well with the round trip time of light in the fourth cavity. However, the energy of beam electrons did not increase arithmetically. To enhance the energy increase at each stage, we carried out two-stage experiments in which two cavities with the same length were used as the second stage.

II. Experimental Setup

A Pulserad 105A of Physics International which utilized a conventional Blumlein line was used as a beam source. A schematic diagram of the experiment and typical pulse forms are shown in Fig. 3. A 550 kV, 5 kA, 12 ns annular electron beam with a diameter of 1.6 cm and a thickness of 1 mm was injected from a foilless diode into a drift tube with an inner diameter of 3 cm. Three solenoid coils of total length of 2.4 m produced an axial magnetic field of 1 T. As the velocity of the beam was nearly equal to that of light, the beam length was calculated to be ~3.6 m. The first cavity with length of 90 cm (= 3.6/4 m) was connected to the drift tube via a gap at 20 cm downstream from the anode. Two cavities with the same length were mounted behind the first cavity. The length of the second and the third cavities were 45 cm. The impedance of three cavities was 76 ohm. The gap space in each cavity was 2 cm. The base pressure of the system was kept below 1×10^{-5} Torr.

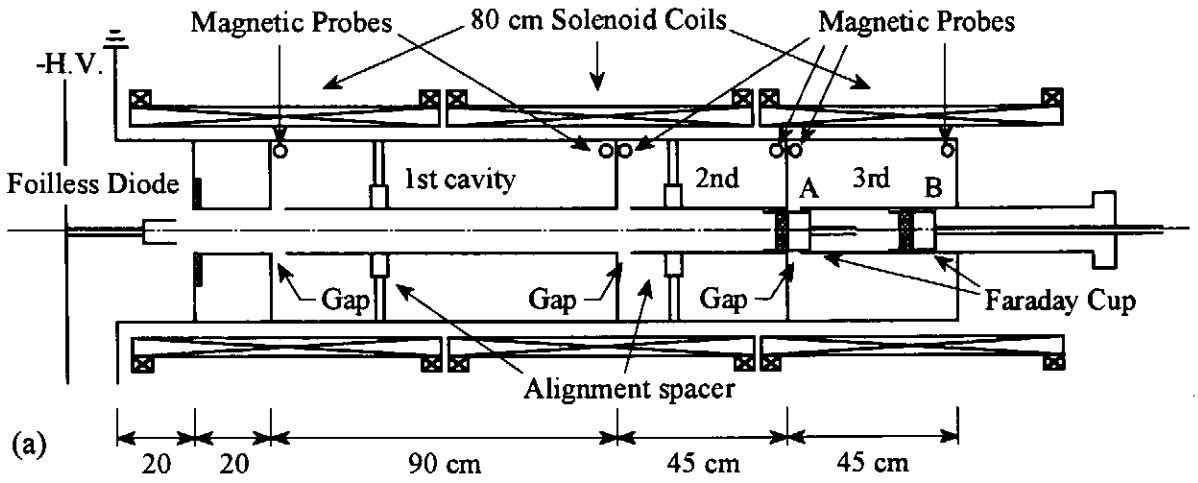

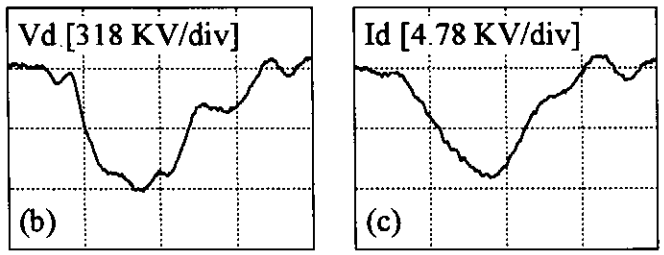

Time [10 ns/div] Time [10 ns/div]

Fig. 3. Schematic diagram of the experiment (a). Typical waveforms of diode voltage (b) and diode current (c).

In the control experiment, the electron beam passed through only the drift tube with inner diameter of 3 cm and length of 2.5 m. In the one-stage experiment, only the first cavity was mounted. The experiments with one cavity as the second stage is called the single second stage experiment in this report, and the experiments with two cavities as the second stage is called doubled second stage experiment.

The beam current was measured by a movable Faraday cup at various locations along the axis in the drift tube. The distance between the Faraday cup and the nearest gap was kept at least 30 cm in order for its presence not to affect the electric field near the gap. It was located at 50 cm downstream from the anode in the control and one-stage experiments. On the other hand it was located in front of the third gap in the single second stage experiment as indicated A in Fig. 3 and behind the third gap in the doubled second stage experiment as indicated B in Fig. 3. Aluminum foils of different thicknesses were placed in front of the Faraday cup to estimate the kinetic energy of the beam electrons.[12]

One-turn magnetic probes were used to detect the currents in the cavities at their entrances and at their ends. The signal detected by each magnetic probe was integrated numerically to obtain the current.

Signals from the Faraday cup and the magnetic probes were monitored by a 1 GHz, 5 sample/ns digitizing oscilloscope, Tektronix TDS 684A.

III. Experimental Results and discussions

The beam currents measured by the Faraday cup with aluminum foils of different thicknesses in the single second stage and the doubled second stage experiments are shown in Fig. 4. Those in the control experiment detected at 50 cm downstream from the anode are also shown in Fig. 4. The aluminum foil to stop the electrons in the most accelerated part of the beam is thicker in the doubled second stage experiment than in the single second stage experiment. The FWHM of the pulse length of the most accelerated part was 3 ns in the doubled second stage experiment. This value agrees well with the round trip time of light in the last cavity. Moreover, the most accelerated part was observed at the end of the beam pulse as expected. The pulse lengths of the beam currents obtained without foil in the single and doubled second stage experiments are not so narrow. This is considered to be due to the beam electrons other than the most accelerated ones which could not be taken away. In comparison with the doubled second stage experiment, the waveform in the single second stage experiment did not clearly show the characteristic pulse length of the most accelerated part. This is also considered to come from the electrons other than the most accelerated ones.

The ratio of the transmitted current through aluminum foils to the current detected without foil is plotted against the thickness of aluminum foils for each experiment as shown in Fig. 5. The range-energy relation method[12] is applied to estimate the kinetic energy of the most accelerated electrons. The highest kinetic energies of electrons in the control, in the one-stage, in the single second stage and in the doubled second stage experiments are estimated to be 550, 750, 850 and 1100 keV, respectively. So increases of the kinetic energies of beam electrons are evaluated to be 100 keV at the second gap and 250 keV at the third gap.

The currents measured by magnetic probes at the gap and at the end of each cavity in the doubled second stage experiment are shown in Fig. 6. According to the transmission line theory, the current at the end of each cavity, $I_0(l, t)$, should be expressed by the current at the gap, $I_0(0, t)$, as below,[10]

$$I_0(l, t) = 2I_0(0, t - t_0/4) - 2I_0(0, t - 3t_0/4) + \cdots, \quad (1)$$

where t_0 is the round trip time for light for each cavity. We try to apply this theory to each stage using measured currents at each gap. Calculated currents $I_0(0, t)$ at the end of each cavity are also shown by dashed lines in Fig. 6. They agree well with the measured waveforms. This result shows that the transmission line theory is applicable to the autoacceleration process described in this report too, so the energy increase of electrons can be estimated from the gap voltage, $V_1(0,$

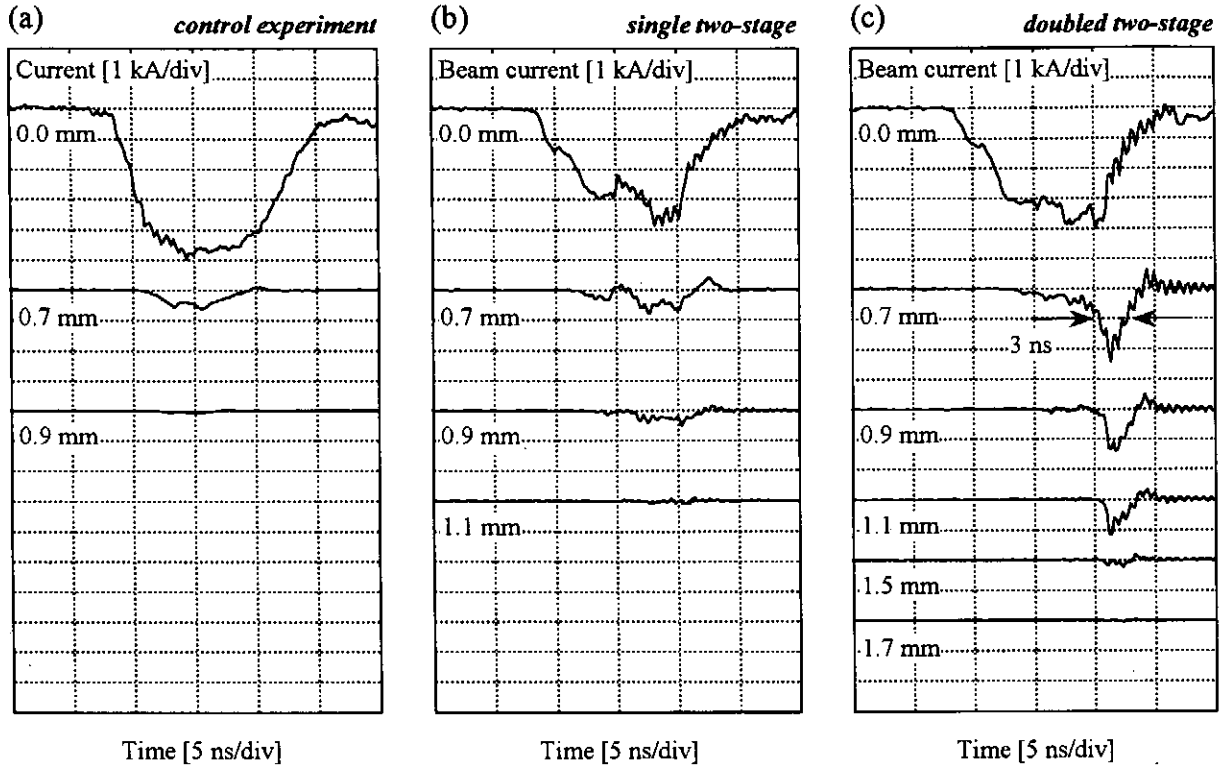

Fig. 4. Typical waveforms of Faraday cup signals with aluminum foil of different thickness, (a) current waveforms of the incident beam, (b) current waveforms of the single second stage experiment, and (c) current waveforms of the doubled second stage experiment.

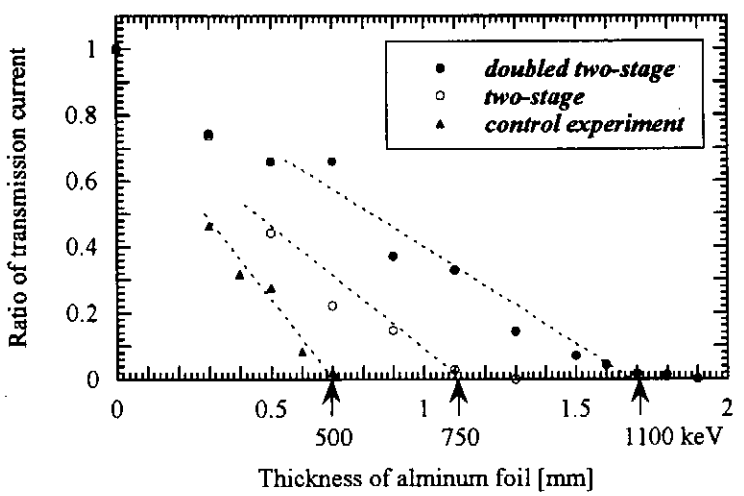

Fig. 5. Ratio of the penetrated current through different thicknesses of aluminum foil.

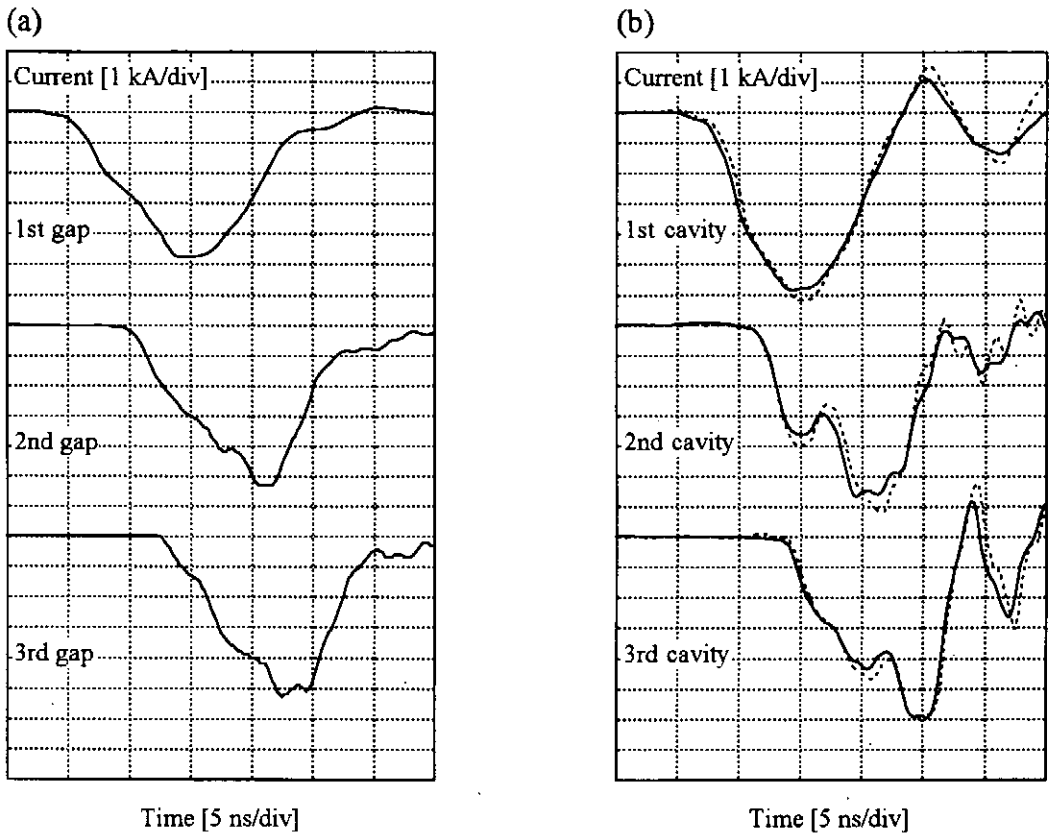

Fig. 6. (a) Beam current waveforms at first, second and third gap measured by magnetic proves, and (b) comparison between measured cavity currents (solid lines) and calculated cavity currents (dashed lines).

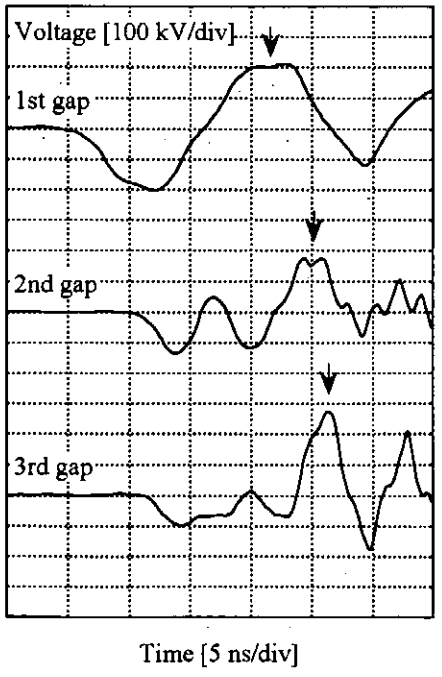

Fig. 7. Calculated voltage waveforms at each gap.

t), using the following equation,[10]

$$V_1(0, t) = Z_c [I_0(0, t) - 2I_0(0, t - t_0/2) + \cdots], \quad (2)$$

where Z_c is the impedance of the cavity. Figure 7 shows the gap voltage waveforms of each cavity constructed using the measured gap currents and Eq. (2). The arrows in Fig. 7 indicate the times around which the most accelerated part passed through each gap. The voltages at arrows are 200 kV, 180 kV and 270 kV at the first, at the second and at the third gap, respectively. The sum of the voltages at arrows is calculated to be 650 keV. These acceleration voltages estimated using the current waveforms agree well with the highest kinetic energy increase derived from the range-energy relation method. This result supports further that the transmission line theory is applicable to multi-stage autoacceleration process described in this report.

The current waveform affects the gap voltage strongly. In the one-stage experiment, the gap voltage estimated from the gap current with triangular waveform is 200 kV, while the expected gap voltage is 342 kV (= 4.5 kA x 76 ohm) if the current waveform is assumed to be square with the same maximum current as that observed in the experiment. As mentioned above, the electrons other than the most accelerated ones arrived at the second and the third gaps as shown also in Fig. 6. These electrons modified the current waveforms at the second and the third gaps. These current modifications caused the difference between the second and the third gap voltages and the increase of the third gap voltage compared with the second gap voltage as shown in Fig. 7. We are now seeking methods to remove the electrons other than the most accelerated ones.

IV. Conclusion

The kinetic energy of the most accelerated electrons was increased in the two-stage autoacceleration by using two cavities as the second stage instead of using a single cavity. Transmission line theory is found to be also applicable for this autoacceleration scheme. If it is possible to generate the square current waveform and scrape off the low energy electrons, we can make the energy increment at each stage to double. We can expect to produce a sub-nanosecond electron beam with much higher energy by using two or more cavities with the same length at each stage in the multi-stage autoacceleration scheme.

References

1) N. S. Ginzburg, I. V. Zotova, A. S . Sergeev, I. V. Konoplev, A. D. R. Phelps, A. W. Cross, S. J. Cooke, V. G. Shpak, M. I. Yalandin, S. A. Shunailov, and M. R. Ulmaskulov, "Experimental observation of cyclotron superradiance under group synchronism conditions," *Phys.*

Rev. Lett., **78**, 2365-2368, (1997).

2) G. A. Mesyats, V. G. Shpak, S. A. Shunailov, and M. I. Yalandin, Proc. SPIE **2154**, 262 (1994).

3) K. Kamada, D. Hasegawa, K. Shimizu, R, Ando, and M. Masuzaki, "Two-stage auto-acceleration using decreasing length cavities," IEEE Trans. Plasma Sci. **27**. 1609-1610, (1999).

4) L. N. Kazanski, A. Kisletsov, and A. N. Lebedev, "Selfacceleration in intense electron beams," *At. Energ.*, **30**, 30-34, (1971).

5) I. A. Grishaev, and A. M. Shenderovich, "Acceleration by interruption of an intense electron beam," *Sov. Phys. Tech. Phys.*, **17**, 1871-1873, (1973).

6) M. Friedman, "Autoacceleration of an intense relativistic electron beam," *Phys. Rev. Lett.*, **31**, 1107-1110, (1973).

7) A. Grishaev, A. N. Debik, V. V. Zakutin, I. I. Magda, Yu. V. Tkach, and A. M. Shenderovich, "Self-acceleration of an intense electron beam," *Sov. Phys. Tech. Phys.*, **19**, 1087-1089, (1975).

8) A. N. Didenko, A. G. Zherlitsyn, V. I. Zelentsov, V. I. Kartin, G. I. Kotlyarevskii, Yu. P. Usov, G. P. Fomenko, Yu. G. Shtein, and Yu. G. Yushkov, "Self-acceleration of electron bunches in resonant systems," *Sov. Phys. Tech. Phys.*, **22**, 612-614, (1977).

9) T. R. Lockner, and M. Friedman, "Collective autoacceleration of electrons using an autoacceleration process," *J. Appl. Phys.*, **51**, 6068-6074, (1980).

10) M. Friedman, "Autoacceleration of high power electron beams," *Appl. Phys. Lett.*, vol. **41**, 419-421, (1982).

11) D. Hasegawa, K. Shimizu, R. Ando, K. Kamada, and M. Masuzaki, "Four-stage autoacceleration of an intense relativistic electron beam," NIFS-PROC-**42**, 81-90, (1999).

12) H. H. Seliger, "Transmission of positrons and electrons," *Phys. Rev.*, **100**, 1029-1037, (1955).

Publication List of NIFS-PROC Series

NIFS-PROC-1 "*U.S.-Japan on Comparison of Theoretical and Experimental Transport in Toroidal Systems Oct. 23-27, 1989*", Mar. 1990

NIFS-PROC-2 "*Structures in Confined Plasmas –Proceedings of Workshop of US-Japan Joint Institute for Fusion Theory Program–* "; Mar. 1990

NIFS-PROC-3 "*Proceedings of the First International Toki Conference on Plasma Physics and Controlled Nuclear Fusion –Next Generation Experiments in Helical Systems– Dec. 4-7, 1989*" Mar. 1990

NIFS-PROC-4 "*Plasma Spectroscopy and Atomic Processes –Proceedings of the Workshop at Data & Planning Center in NIFS–*"; Sep. 1990

NIFS-PROC-5 "*Symposium on Development of Intensed Pulsed Particle Beams and Its Applications February 20 1990*"; Oct. 1990

NIFS-PROC-6 "*Proceedings of the Second International TOKI Conference on Plasma Physics and Controlled Nuclear Fusion , Nonlinear Phenomena in Fusion Plasmas -Theory and Computer Simulation-*"; Apr. 1991

NIFS-PROC-7 "*Proceedings of Workshop on Emissions from Heavy Current Carrying High Density Plasma and Diagnostics*"; May 1991

NIFS-PROC-8 "*Symposium on Development and Applications of Intense Pulsed Particle Beams, December 6 - 7, 1990*"; June 1991

NIFS-PROC-9 *"X-ray Radiation from Hot Dense Plasmas and Atomic Processes"*; Oct. 1991

NIFS-PROC-10 "*U.S.-Japan Workshop on "RF Heating and Current Drive in Confinement Systems Tokamaks" Nov. 18-21, 1991*, Jan. 1992

NIFS-PROC-11 "*Plasma-Based and Novel Accelerators (Proceedings of Workshop on Plasma-Based and Novel Accelerators) Nagoya, Japan, Dec. 1991*"; May 1992

NIFS-PROC-12 "*Proceedings of Japan-U.S. Workshop P-196 on High Heat Flux Components and Plasma-Surface Interactions for Next Devices*"; Mar. 1993

NIFS-PROC-13 「NIFS シンポジウム
「核燃焼プラズマの研究を考える－現状と今後の取り組み方」
1992 年 7 月 15 日、核融合科学研究所」 1993 年 7 月
NIFS Symposium "Toward the Research of Fusion Burning Plasmas -Present Status and Future strategy-", 1992 July 15, National Institute for Fusion Science"; July 1993 (in Japanese)

NIFS-PROC-14 "*Physics and Application of High Density Z-pinches*", July 1993

NIFS-PROC-15 岡本正雄、講義「プラズマ物理の基礎」
平成 5 年度 総合大学院大学1994 年 2 月
M. Okamoto,
*"Lecture Note on the Bases of Plasma Pysics"Graduate University for Advanced Studies*Feb. 1994
(in Japanese)

NIFS-PROC-16 代表者 河合良信
平成 5 年度 核融合科学研究所共同研究
研究会報告書「プラズマ中のカオス現象」
*"Interdisciplinary Graduate School of Engineering Sciences" Report of the meeting on Chaotic Phenomena in Plasma*Apr. 1994 (in Japanese)

NIFS-PROC-17 平成 5 年度 NIFS シンポジウム報告書
「核融合炉開発研究のアセスメント」平成 5 年 11 月 29 日-30 日 於 核融合科学研究所
"Assessment of Fusion Reactor Development" Proceedings of NIFS Symposium held on November 29-30, 1993 at National Insitute for Fusion Science" Apr. 1994(in Japanese)

NIFS-PROC-18 *"Physics of High Energy Density Plasmas Produced by Pulsed Power"* June 1994

NIFS-PROC-19 K. Morita, N. Noda (Ed.),

"*Proceedings of 2nd International Workshop on Tritium Effects in Plasma Facing Components at Nagoya University, Symposion Hall, May 19-20, 1994*", Aug. 1994

NIFS-PROC-20 研究代表者 阿部 勝憲 (東北大学・工学部)
所内世話人 野田信明
平成6年度 核融合科学研究所共同研究[研究会]「金属系高熱流束材料の開発と評価」成果報告書

K. Abe and N. Noda (Eds.),
"Research and Development of Metallic Materials for Plasma Facing and High Heat Flux Components" Nov. 1994(in Japanese)

NIFS-PROC-21 世話人:森田 健治(名大工学部)、金子 敏明(岡山理科大学理学部)
「境界プラズマと炉壁との相互作用に関する基礎過程の研究」研究会報告
K. Morita (Nagoya Univ.), T. Kaneko (Okayama Univ. Science)(Eds.)
"*NIFS Joint Meeting "Plasma-Divertor Interactions" and "Fundamentals of Boundary Plasma-Wall Interactions" January 6-7, 1995 National Institute for Fusion Science*" Mar. 1995 (in Japanese)

NIFS-PROC-22 代表者 河合 良信
プラズマ中のカオス現象
Y. Kawai,
"*Report of the Meeting on Chaotic Phenomena in Plasma,* 1994" Apr. 1995 (in Japanese)

NIFS-PROC-23 K. Yatsui (Ed.),
"*New Applications of Pulsed, High-Energy Density Plasmas*"; June 1995

NIFS-PROC-24 T. Kuroda and M. Sasao (Eds.),
"*Proceedings of the Symposium on Negative Ion Sources and Their Applications, NIFS, Dec. 26-27, 1994*", Aug. 1995

NIFS-PROC-25 岡本 正雄
新古典輸送概論(講義録)
M. Okamoto,
"*An Introduction to the Neoclassical Transport Theory" (Lecture note),* Nov. 1995 (in Japanese)

NIFS-PROC-26 Shozo Ishii (Ed.),
"*Physics, Diagnostics, and Application of Pulsed High Energy Density Plasma as an Extreme State*"; May 1996

NIFS-PROC-27 代表者 河合 良信
プラズマ中のカオスとその周辺非線形現象
Y. Kawai ,
"*Report of the Meeting on Chaotic Phenomena in Plasmas and Beyond, 1995*", Sep. 1996 (in Japanese)

NIFS-PROC-28 T. Mito (Ed.),
"*Proceedings of the Symposium on Cryogenic Systems for Large Scale Superconducting Applications*", Sep. 1996

NIFS-PROC-29 岡本 正雄
講義「核融合プラズマ物理の基礎 - I」
平成8年度 総合研究大学院大学 数物科学研究科 核融合科学専攻 1996年10月
M. Okamoto
"*Lecture Note on the Fundamentals of Fusion Plasma Physics - I" Graduate University for Advanced Studies;* Oct. 1996 (in Japanese)

NIFS-PROC-30 研究代表者 栗下 裕明(東北大学金属材料研究所)
所内世話人 加藤 雄大
平成8年度核融合科学研究所共同研究「被損傷材料の微小体積強度評価法の高度化」研究会 1996年10月 9日 於:核融合科学研究所

H. Kurishita and Y. Katoh (Eds.)
NIFS Workshop on Application of Micro-Indentation Technique to Evaluation of Mechanical Properties of Fusion Materials, Oct. 9, 1996, NIFS ; Nov. 1996 (in Japanese)

NIFS-PROC-31 岡本 正雄
講義「核融合プラズマ物理の基礎 - II」
平成8年度 総合研究大学院大学 数物科学研究科 核融合科学専攻 1997年4月
M. Okamoto
"*Lecture Note on the Fundamentals of Fusion Plasma Physics - II" Graduate University for Advanced*

Studies; Apr. 1997 (in Japanese)

NIFS-PROC-32 代表者 河合 良信
平成8年度 核融合科学研究所共同研究 研究会報告「プラズマ中のカオスとその周辺非線形現象」

Y. Kawai (Ed)
Report of the Meeting on Chaotic Phenomena in Plasmas and Beyond, 1996; Apr. 1997 (mainly in Japanese)

NIFS-PROC-33 H. Sanuki,
Studies on Wave Analysis and Electric Field in Plasmas; July 1997

NIFS-PROC-34 プラズマ対向機器・PSI・熱・粒子制御合同研究会報告
平成9年6月27日（金）9:00 ～16:20 核融合科学研究所・管理棟4F第1会議室
1997年 10月
T. Yamashina (Hokkaido University)
Plasma Facing Components, PSI and Heat/Particle Control June 27, 1997, National Institute for Fusion Science T. Yamashina (Hokkaido University) ; Oct. 1997 (in Japanese)

NIFS-PROC-35 T. Watari,
Plasma Heating and Current Drive; Oct. 1997

NIFS-PROC-36 T. Miyamoto and K. Takasugi (Eds.)
Production and Physics of High Energy Density Plasma; Production and Physics of High Energy Density Plasma; Oct. 1997

NIFS-PROC-37 (Eds.)T. Fujimoto, P. Beiersdorfer,
Proceedings of the Japan-US Workshop on Plasma Polarization Spectroscopy and The International Seminar on Plasma Polarization Spectroscopy January 26-28, 1998, Kyoto; June 1998

NIFS-PROC-38 (Eds.) Y. Tomita, Y. Nakamura and T. Hayashi,
Proceedings of the Second Asian Pacific Plasma Theory Conference APPTC '97, January 26-28, 1998, Kyoto; Aug. 1998

NIFS-PROC-39 (Ed.) K. Hirano,
Production, Diagnostics and Application of High Energy Density Plasmas; Dec. 1998

NIFS-PROC-40 研究代表者 加古 孝（電気通信大学）
所内世話人 渡辺 二太
平成10年度核融合科学研究所共同研究 研究会「プラズマ閉じ込めに関連する数値計算手法の研究」
Ed. by T. Kako and T. Watanabe
Proceeding of 1998-Workshop on MHD Computations "Study on Numerical Methods Related to Plasma Confinement Apr. 1999

NIFS-PROC-41 (Eds.) S. Goto and S. Yoshimura,
Proceedings of The US-Japan Workshop and The Satellite Meeting of ITC-9 on Physics of High Beta Plasma Confinement in Innovative Fusion System, Dec. 14-15, 1998, NIFS, Toki; Apr. 1999

NIFS-PROC-42 (Eds.) H. Akiyama and S. Katsuki,
Physics and Applications of High Temperature and Dense Plasmas Produced by Pulsed Power; Aug. 1999

NIFS-PROC-43 (Ed.) M. Tanaka,
Structure Formation and Function of Gaseous, Biological and Strongly Coupled Plasmas; Sep. 1999

NIFS-PROC-44 (Ed.) T. Kato and I. Murakami,
Proceedings of the International Seminar on Atomic Processes in Plasmas, July 29-30, 1999, Toki, Japan; Jan. 2000

NIFS-PROC-45 (Eds.) K. Yatsui and W. Jiang,
Physics and Applications of Extreme Energy-Density State, Nov. 25-26, 1999, NIFS; Mar. 2000